The physics of the accretion process in the formation and evolution of Young Stellar Objects

Carlo Felice Manara

SIGILL. UNIVERSITAT. LUDOVIC. MAXIM.

München 2014

The physics of the accretion process in the formation and evolution of Young Stellar Objects

Carlo Felice Manara

Dissertation
an der Fakultät für Physik
der Ludwig--Maximilians--Universität
München

vorgelegt von
Carlo Felice Manara
aus Mailand, Italien

München, den 22. Maj 2014

Erstgutachter: Prof. Dr. Barbara Ercolano
Zweitgutachter: Prof. Dr. Andreas Burkert
Tag der mündlichen Prüfung: 8. Juli 2014

To my two girls

This work has been carried out at the European Southern Observatory (ESO) under the supervision of Leonardo Testi and within the ESO/International Max Planck Research School (IMPRS) student fellowship programme.
The members of the Thesis Committee were: Barbara Ercolano, Leonardo Testi, Thomas Preibisch, and Antonella Natta.

Contents

List of Figures

List of Tables

Abstract

The formation of planets is thought to happen in protoplanetary disks surrounding young stars during the first few Myrs of their pre-main-sequence evolution. In order to understand planet formation a detailed knowledge of the disk evolution process is needed. By studying the interaction of the disk with the central star, which includes accretion of matter due to viscous processes in the disk, we can constrain the physical conditions of the inner gaseous disk in which planet formation takes place. With the recent advent of the X-Shooter spectrograph, a second generation instrument of the ESO/VLT, the excess emission due to accretion in the ultraviolet can be studied simultaneously with the accretion signatures in the visible and in the near-infrared, finally giving a complete view of this phenomenon.

In this Thesis I have studied various X-Shooter datasets of young stars to determine the intensity and the properties of the accretion process at various phases of disk evolution and as a function of the central star mass and age. To fully exploit the potential of the X-Shooter spectra, I have developed an innovative method of analysis to derive accretion and stellar parameters with an automatic algorithm. This is based on a set of models, composed of a set of photospheric templates of young stars that I gathered and characterized, a set of slab models, that I have coded, to reproduce the emission due to the accretion shock, and a reddening law to take into account extinction effects. This method allows to accurately determine for the first time the stellar and accretion parameters of the targets self-consistently and with no prior assumptions, a significant improvement with respect to previous studies. I have applied this methodology to determine the correct stellar parameters of two objects in the Orion Nebula Cluster that were reported in the literature to have an anomalous old age. My analysis has shown why previous investigations could not resolve the degeneracy between various parameters, while the methodology developed in this Thesis could.

I have applied my methodology to a relatively large sample of transitional disks, which are thought to be evolved disks with a large gap in the dusty disk between the outer disk and the central star. I showed that, when accretion is present, their properties are similar to those of less evolved disks. Under steady-state assumptions this implies the presence of an efficient mechanism to transport gas from the outer disk to the inner regions of the system through the dust depleted gap. In order to investigate the evolution of accretion, I have then used a combined sample of all the $\sim$90 X-Shooter spectra I have studied of young stars with disks. My sample covers a range of environments and stellar masses, and my accurate analysis method allows for a much better determination of the accretion versus stellar mass relation. The slope of this relation is in good agreement with the predictions of X-ray photoevaporation models. On the other hand, the significantly smaller spread in values that I find compared to previous works can be explained as a small spread of initial conditions, such as initial core rotation rates. By removing the dependence of the accretion rates with the stellar mass I have been able to search for a purely evolutionary trend of accretion. In general, viscous evolution models can reproduce the observed trend with small variations of the fiducial disk parameters.

To follow the path marked by this Thesis, future accretion studies should focus on complete samples in various star forming regions. These will be then coupled with on-going surveys with other observational tools, such as ALMA in the sub-mm wavelength range, targeting other properties of protoplanetary disks, for example disk masses.

Zusammenfassung

Es wird angenommen, dass Planeten in protoplanetaren Scheiben von jungen Sternen entstehen. Diese jungen Sterne befinden sich in den ersten Millionen Jahren ihrer Entwicklung bevor sie die Hauptreihe erreichen. Um Planetenentstehung zu verstehen, muss der Entwicklungsprozess der Scheibe im Detail verstanden werden. Indem man die Wechselwirkungen zwischen der Scheibe und dem zentralen Stern, zu denen zum Beispiel Massenakkretion auf den Stern durch Reibungsprozesse in der Scheibe gehören, untersucht, kann man die physikalischen Eigenschaften der inneren Gasscheibe, in der die Planeten entstehen, abschätzen. Mit Hilfe des kürzlich installierten X-Shooter Spektrographen, einem ESO/VLT Instrument der zweiten Generation, kann die zusätzliche Emission im ultravioletten Bereich, die durch die Akkretion entsteht, mit den Akkretionsmerkmalen im optischen und nahinfraroten Bereich verglichen werden. Dadurch erhält man ein umfassenderes Bild dieses Prozesses als zuvor.

In dieser Doktorarbeit habe ich verschiedene X-Shooter Daten von jungen Sternen untersucht, um die Intensität und die Eigenschaften des Akkretionsprozesses, abhängig von der Masse und des Alters des zentralen Sterns und von den verschiedenen Phasen der Scheibenentwicklung, herauszufinden. Um das volle Potential der X-Shooter Spektren auszunutzen, habe ich eine innovative Methode zur Analyse entwickelt, um daraus Akkretions- und Sterneigenschaften mit einem automatischen Algorithmus abzuleiten. Diese Methode basiert auf einer Reihe von Modellen, die ich aus photosphärischen Vorlagen für junge Sterne ausgewrtet habe, aus ``slab'' Modellen, die ich programmiert habe um die Emission des Akrretionsschocks zu reproduzieren, und einer Annahme für die Rötung des Lichts durch Extinktion. Diese Methode ermöglicht es zum ersten Mal die stellaren und Akkretions-parameter der Objekte einheitlich und ohne vorige Annahmen zu bestimmen. Dies ermöglicht eine signifikante Verbesserung, verglichen mit vorangegangenen Studien. Ich habe diese Methode angewandt, um die korrekten stellaren Parameter von zwei Objekten im Orion Nebel zu bestimmen, die in der Literatur mit stark abweichendem hohen Alter angegeben wurden. Meine Analyse hat gezeigt, warum vorherige Untersuchungen diese Widersprüche nicht auflösen konnten, aber warum meine Methode, die ich in dieser Arbeit entwickelt habe, dies ermöglicht.

Ich habe meine Methode auf ein relativ große Auswahl von Scheiben im Übergangsstadium angewandt, für die man annimmt, dass sie weit entwickelte Scheiben sind, weil deren Staubscheibe große Lücken zwischen der äußerer Scheibe und dem Zentralstern aufweist. Ich habe gezeigt, dass, in Anwesenheit von Akkretion, die Eigenschaften der weit entwickelten Übergangsscheiben gleich derer in weniger entwickelten Scheiben sind.

Unter der Annahme von steady-state Bedingungen, impliziert dies einen effizienten Mechanismus, der Gas von der äußeren Scheibe durch die staubarme Lücke in die innere Region der Scheibe transportiert. Um die Entwicklung der Akkretion zu untersuchen, habe ich alle 90 aufgenommenen X-Shooter Spektren von jungen Sternen mit Scheiben verwendet. Diese Spektren umfassen verschiedene stellare Umgebungen und Sternmassen und meine genaue Methode zur Analyse ermöglicht eine deutlich verbesserte Bestimmung der Akkretions-Sternenmasse-Relation. Die von mir bestimmte Steigung dieser Relation stimmt gut mit den Vorhersagen der Röntgenstrahlungs-Evaporationsmodelle überein. Außerdem kann die signifikant kleinere Streuung der Werte im Vergleich mit früher gefun-

denen größeren Streuungen, mit einer kleinen Streuung der Anfangsbedingungen, wie zum Beispiel anfängliche Kernrotation, erklärt werden. Durch das Entfernen der Abhängigkeit der Akkretionsrate von der Sternmasse, war es mir möglich nach rein evolutionären Trends in der Akkretion zu suchen. Allgemein können Entwicklungsmodelle, die die Viskosität berücksichtigen, den beobachteten Trend der Scheibenparameter mit kleinen Abweichungen gut reproduzieren.

Um die in dieser Arbeit aufgezeigte Methode fortzusetzen, sollten zukünftige Akkretionsstudien sich möglichst auf eine vollständige Auswahl an Objekten aus verschiedenen Sternentstehungsgebieten fokussieren. Diese können dann mit Daten, die andere Eigenschaften von protoplanetarischen Scheiben untersuchen, von anderen aktuellen Beobachtungen, zum Beispiel im ALMA sub-mm Wellenlängenbereich, kombiniert werden.

List of Acronyms

YSO	Young stellar object
PMS	Pre-Main-Sequence
cTTs	Classical TTauri star
wTTs	Weak lined TTauri star
TD	Transitional disk
HRD	Hertzsprung-Russell diagram
SpT	Spectral type
$T_{\rm eff}$	Effective temperature
$L_\star$	Stellar (bolometric) luminosity
$M_\star$	Stellar mass
$R_\star$	Stellar radius
A_V	Extinction in V-band
$L_{\rm line}$	Line luminosity
$L_{\rm acc}$	Accretion luminosity
$\dot{M}_{\rm acc}$	Mass accretion rate
$L_{\rm acc,noise}$	Noise on the accretion luminosity due to chromospheric activity
$\dot{M}_{\rm acc,noise}$	Noise on the mass accretion rate due to chromospheric activity
ONC	Orion Nebula Cluster
UV	Ultraviolet
UVB	Ultraviolet arm of the X-Shooter spectrograph ($\lambda\lambda$ 300-559.5 nm)
VIS	Visible arm of the X-Shooter spectrograph ($\lambda\lambda$ 559.5-1024 nm)
NIR	Near-infrared arm of the X-Shooter spectrograph ($\lambda\lambda$ 1024-2480 nm)
VLT	Very Large Telescope
GTO	Guaranteed time observations

1
Introduction

When looking at the night sky and staring at the multitude of stars big questions have always arose in mankind, from the questions of what stars are and how they have formed, to ultimate questions such as: ``Are we alone in the Universe?'' or ``*A che tante facelle?*'' (``*Wherefore so many lights?*'', G. Leopardi). Astronomy is the science that aims at answering the scientific questions that come to our mind when looking at the night sky. But we do not have only questions, we also have evidence. In particular, if we have one evidence, this is that planets form. We live on a planet, the only planet known, so far, that is hosting life. Somehow $\sim$4.5 billion years ago something happened and this beautiful planet was formed. We also know that other planets exist, in the Solar System but also beyond. In recent years, we are discovering that extra Solar System planets (exoplanets) not only exist, but are common around Main Sequence stars (e.g., Mayor & Queloz, 2012). We know that planets form in the disks surrounding forming stars, the so-called ``protoplanetary disk'', but how this whole process of star and planet formation in fact works is still to be understood.

This Thesis aims at understanding the processes that lead to the formation of a star, its interaction with the surrounding protoplanetary disk, and ultimately how this affects how planets are formed. In particular, I will focus on what we can learn from the study of the accretion of matter from the protoplanetary disk to the central forming star. Here I introduce the context in which this Thesis sets, starting from a general introduction of the process of star and planet formation, then discussing in detail the process of accretion, and finally explaining the path of this Thesis, which will be discussed in the next chapters.

1.1 Setting the scene: the evolutionary path from molecular cloud cores to stars and planets

The process of star formation starts from the gravitationally induced collapse of a dense molecular cloud core (e.g., Shu et al., 1987, top panel of Fig. 1.1). Each collapsing core results in the formation of one or more protostars still embedded in the parental cloud. During this stage, the just formed protostar is referred to as a Class 0 object. Any small initial rotational velocity of the cloud is magnified by its rapid collapse, and to conserve the angular momentum the system evolves forming a disk around the central protostar.

The protostar-disk system is still too embedded to be observed at optical wavelength, but the disk is detected at mm-wavelength using high resolution interferometry (e.g., Tobin et al., 2013). As the envelope falls onto the protostar and onto the disk it becomes more optically thin and the system enters in the so-called Class I stage. During the Class 0 and Class I phases the system originates powerful jets that disperse a large amount of angular momentum (e.g., Frank et al., 2014). Indeed, at the beginning of the collapse the angular momentum of the cloud core is orders of magnitude larger than the total angular momentum of the star(s) that will be the outcome of the process. This excess momentum is dispersed by the system possibly by jet launching or disk winds, and by viscous processes which drive accretion of material from the disk onto the star. This accretion process starts already in these first phases at a high pace, and decreases with time as I will describe in Sect. 1.2.

As the envelope is dissipated the young stellar object (YSO) is observable at visible wavelengths and is referred to as a Class II object, or classical TTauri star (cTTs). During this phase the protoplanetary disk, composed of dust and gas, is optically thick and evolves viscously (cf. Sect. 1.3). This is an important phase for accretion studies, as all the signatures of accretion and the spectral features useful to determine the stellar properties of the central object are observable. During this stage the luminosity ($L_\star$) and temperature ($T_{\rm eff}$) of the central protostar[1] are such that the location of these objects is above the Main Sequence on the Hertzsprung-Russel diagram (HRD), i.e. $L_\star$ is larger than typical Main Sequence stars of the same $T_{\rm eff}$. This is due to the larger radii of these objects, which still contract due to gravitational collapse until they reach the Main Sequence. Due to this location on the HRD, YSOs in this and later phases are usually called Pre-Main-Sequence (PMS) objects. The time usually needed by these PMS stars to reach the Main Sequence can be even longer than $\sim$100 Myr, depending on the $T_{\rm eff}$ of the object. On the other hand, the Class II phase, i.e. the stage in which the protoplanetary disk is still optically thick, is found observationally to last typically $\sim$3-5 Myr (e.g., Haisch et al., 2001; Hernández et al., 2007; Fedele et al., 2010, see Fig. 1.2). This finding, obtained with different proxies for detecting disks (e.g., IR-excess, accretion signatures), has been recently challenged by the discovery of optically thick disks around older objects (e.g., Beccari et al., 2010). Also, Bell et al. (2013) showed that the typical timescale of the optically thick disk phase could be longer due to incorrect estimate of the ages of some star forming regions. This will be discussed in more detail in Chapter 4. However, it is true that *in general* the fraction of objects still surrounded by an optically thick disk in a given region diminishes with time following an exponential decrease. This is a stringent constraint on the available time to form a planet in a protoplanetary disk, and a better understanding of this timescale is crucial for planet formation theories.

Before the disk is dissipated, (at least) a fraction of the objects undergo a phase where they present an optically thin region, i.e. significantly dust depleted, thus called *hole* or *gap*, while the outer part is still optically thick. The YSOs in this phase are referred to

---

[1] During the course of this Thesis I could also refer to this class of objects as *stars*. However, it is worth mentioning that protostars, unlike main sequence stars, are not yet burning hydrogen.

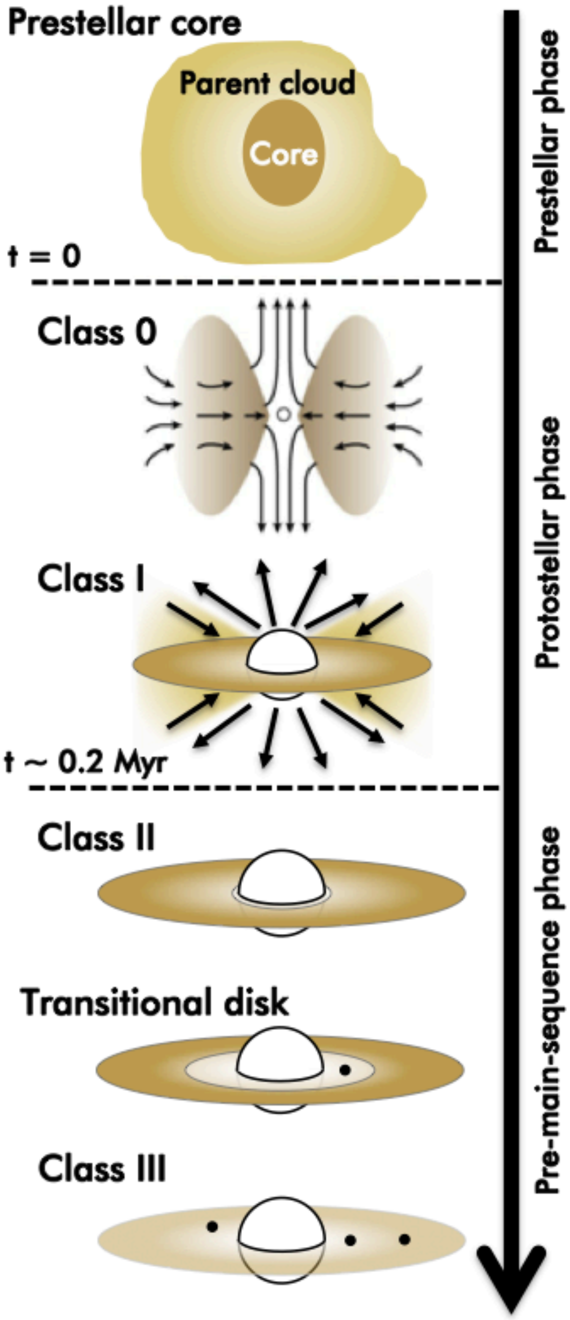

Figure 1.1: Current picture of the evolutionary sequence of young stellar objects. The thick arrow shows increasing time. Cartoons are not on scale. Adapted from André (2002).

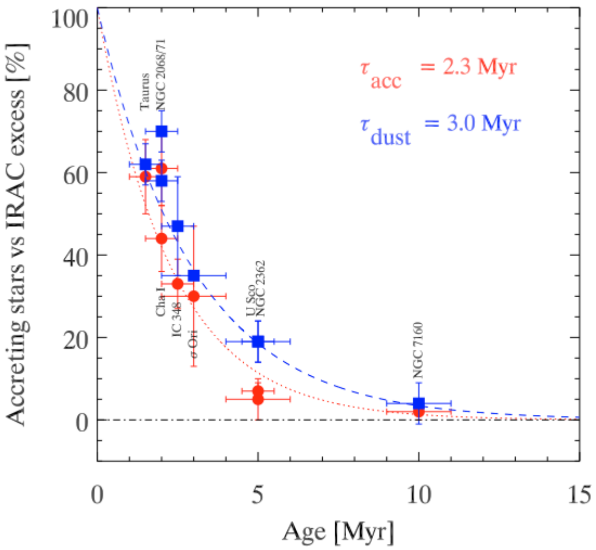

Figure 1.2: Fraction of young stellar objects surrounded by protoplanetary disks in different star forming regions as a function of the age of the regions. The blue line refers to the fraction of objects with optically thick inner disk detected from mid-infrared observations, that is from dust emission. The red line is the fraction of accreting objects, thus with a significantly dense inner gaseous disk. From Fedele et al. (2010).

as transitional disks (TDs, e.g., Espaillat et al., 2014), but whether all the objects undergo this phase is not clear, as well as the properties of the disks in this class of objects. I refer to Chapter 5 of this Thesis for a detailed analysis of these objects. I just report here that a possible explanation for the depletion of dust in the inner part of these disks is the formation of a planet. However, it is still unclear whether these *gaps* in the disks are created by planets already formed or actually promote planet formation. The final phase of evolution, the Class III stage, refers to YSOs whose circumstellar disk has become optically thin due to its evolution. In this phase the interaction with the central star through accretion is not occurring anymore. Their emission lines, which are related to the accretion process as I discuss in Sect. 1.2, are therefore weaker and due only to chromospheric emission at this stage. Non-accreting (Class III) YSOs are also referred to as weak lined TTauri stars (wTTs). These YSOs are of great interest for several reasons, in particular because they are great photospheric templates of YSOs, as I will discuss in Chapter 3.

During these phases planet formation takes place. It is still not clear when this happens, either in these first few Myrs of evolution or even in the hypothetical case of a second disk formation event (Scicluna et al., submitted) at later stages. In any case, the current idea is that no planets can form without the presence of a gas and/or dust rich disk. Indeed, planet formation is thought to happen either by growth of solid particles in the disks which accrete other particles until they become a planet (*core accretion* scenario), or by fragmentation of massive and gravitationally unstable disks (*disk instability* scenario). In this context, a better understanding on the evolutionary processes and of the properties of the protoplanetary disk at every phase of evolution is of help for planet formation theories. In the next Section

I discuss in detail why the process of accretion is of particular interest in this context.

1.2 Star-disk interaction: accretion

As introduced in the previous Section, protoplanetary disks are one of the most important means by which YSOs dissipate angular momentum. This happens through turbulent processes in the disk which result in viscous accretion. The seminal work of Lynden-Bell & Pringle (1974) describes this process with the idea that infinitesimal mass particles carry all the angular momentum on a circular orbit at an infinitely large radius, while the remaining mass drifts inwards after transferring all its angular momentum to the aforementioned particles. The material drifting inwards is accreted on the central star. In this picture the particles in the disk need to have some kind of turbulent interaction through which angular momentum is exchanged. This is thought to be a consequence of the development of magneto-hydro-dynamic (MHD) instabilities, and in particular of magneto-rotational instabilities (MRI). Other possibilities for driving turbulences are gravitational instability or baroclinic vortices. However, at present time none of these processes alone can produce strong and stable turbulences in the whole disk (e.g., Turner et al., 2014). It is usual to model viscosity through the simple and successful parametrization in terms of an unknown dimensionless parameter, the Shakura-Sunyaev α parameter (Shakura & Sunyaev, 1973). From dimensional analysis it is possible to scale the kinematic viscosity in terms of a characteristic length and a turbulent velocity (Hartmann, 2009). It is also generally assumed that the length scale of the turbulence in a disk is less than the scale height (H), and that the eddy velocity is less than the sound speed (c_s), since otherwise these would be dissipated through shocks. According to this prescription, the kinematic viscosity (ν) has the following form: $\nu = \alpha c_s H$. The value of α is constrained to be $\alpha \leq 1$ for the two previously stated upper limits. I stress that this form is just a parametrization based on dimensional analysis, not a theory of viscosity.

In fact, accretion is known to happen and viscous evolution of disks is commonly observed (see Sect. 1.4.1). The main observational signatures of accretion present in the spectra of cTTs are the strong excess continuum emission in the ultraviolet (UV) part of the spectrum and the wealth of strong emission lines at all wavelengths. Those are mostly hydrogen series lines, such as Balmer (Hα, Hβ, etc.), Paschen (e.g., Paβ), or Brackett (e.g., Brγ) series lines, but also helium (e.g., He I line at λ 587.6 nm) and calcium lines (e.g., Ca II infrared triplet at $\lambda\lambda$ 849.8-854.2-866.2 nm). These signatures are originated in the region where there is interaction of the disk with the central forming star. The current and widely accepted paradigm describing how the material is accreted from the disk onto the star is the *magnetospheric accretion* scenario, which I introduce in the next subsection.

1.2.1 Magnetospheric accretion

To explain the observational signatures of accretion different models have been developed. In the description of Lynden-Bell & Pringle (1974) the disk extends down to the stellar

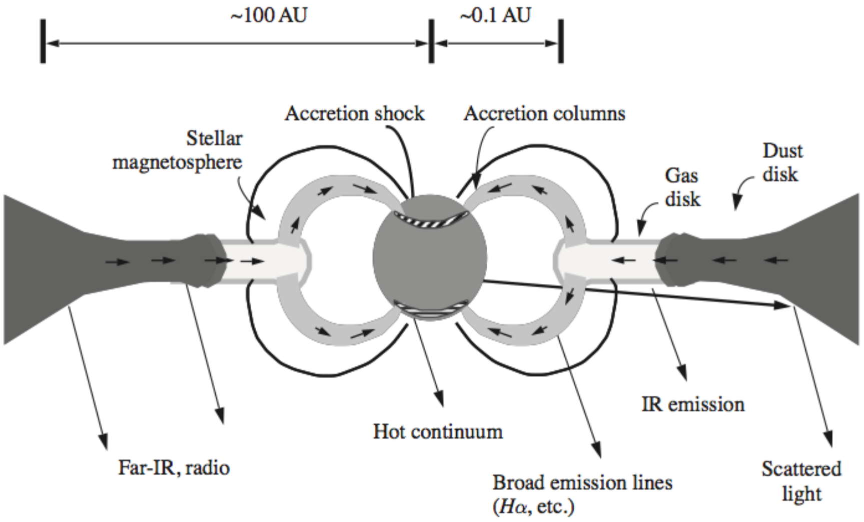

Figure 1.3: Scheme of the magnetospheric accretion scenario. The material is channeled from the disk onto the star by the strong magnetic fields of the young stellar objects. From Hartmann (2009).

surface and the innermost part of the disk - the so-called *boundary layer* - emits a radiation which is strong in the UV part of the spectrum. This picture, which I discuss in more detail in Sect. 2.1, is known not to be valid given that the strong magnetic fields of these YSOs (e.g., Johns-Krull, 2007; Johnstone et al., 2014) disrupt the disk at few stellar radii. Moreover, the strong emission lines observed in the spectra of cTTs have also very broad line profiles ($\gtrsim$200 km/s) which are thought to be connected with material moving at high velocity (e.g., Muzerolle et al., 2003). Finally, this process of accretion is known to be highly variable (e.g., Costigan et al., 2012, 2014) and the surface of these stars present various non-axisymmteric hot spots (e.g., Bouvier et al., 2007). The magnetospheric accretion model is, so far, the only model that can explain all these observables in a qualitative way.

In Fig. 1.3 I show a schematic view of the inner disk in the context of magnetospheric accretion (e.g., Hartmann, 2009). Inside the dust sublimation radius the disk is composed only of gas, which is mostly ionized by the strong radiation of the central star. This ionized material is channeled by the interaction with the stellar magnetic fields to fall on the central object on hot spots, which are thought to be located away from the stellar equator in the case in which the magnetic field is simply dipolar. The distance from which the material is accreted on the star is commonly assumed to be $\sim$5 stellar radii ($R_\star$), but this value depends on the strength of the magnetic field and, to lesser extent, to the mass accretion rate ($\dot{M}_{\rm acc}$) and the mass ($M_\star$) of the star, as I discuss in Chapter 5. The material channeled along the magnetic field lines is accelerated and reaches almost free-fall velocity, giving raise to the broad emission lines observed in the spectra. When the material impacts the stellar surface, the kinetic energy is dissipated locally creating a hot spot ($T \gtrsim$ 8000-10000 K), that is responsible of the continuum excess emission in the UV part of the cTTs spectra. Depending on the geometry of the system, this model could explain the variability of the accretion tracers (lines, continuum), even in a steady state accretion configuration, as a change of the line of sight of the object, where in some cases the accretion shocks and funnels are visible, while they are not in other rotational period phases (e.g., Costigan et al., 2014).

In this context, the gravitational potential energy released is converted in accretion luminosity ($L_{\rm acc}$) according to the following relation:

$$L_{\rm acc} = \frac{GM_\star \dot{M}_{\rm acc}}{R_\star}\left(1 - \frac{R_\star}{R_m}\right), \tag{1.1}$$

where R_m is the radius at which the disk is truncated by the magnetic field. Assuming $R_m = 5R_\star$ (e.g., Gullbring et al., 1998), the amount of material accreted on the star is:

$$\dot{M}_{\rm acc} = \frac{L_{\rm acc} R_\star}{0.8\, GM_\star}. \tag{1.2}$$

1.3 Accretion as a tracer of protoplanetary disk evolution

As I discussed so far, accretion is a process present at all the early stages of star and planet formation. It starts as accretion onto the star-disk system from the parental envelope, and then proceed as accretion from the disk onto the star driven by viscous processes. This process is known to have strong impact on the properties of the disk. In particular, it is important to stress that planets are forming in *evolving* disks, where the amount of gas and dust, the chemical composition, the total mass, and many other parameters are not constant with time. The process of accretion governs and keeps track of this evolution, and for this reason it is crucial to understand how it works. A clear connection between the strength of the accretion process and the disk composition is given by the amount of gas present in the innermost region of the disk. As I also discuss in Chapter 5, the density of the gas in the inner disk depends directly on $\dot{M}_{\rm acc}$. Moreover, recent studies are showing that accretion bursts change the chemical composition of the disk, for example by influencing the chemistry of the gaseous phase of ices in protoplanetary disks (e.g., Banzatti et al., 2012, 2014).

To better understand this process and its dependence with disk evolution it is important to study how accretion evolves with time, i.e. with the age of the central object, and how it depends on the properties of the central YSO, such as its mass. This will be the path of this Thesis, as I describe in Sect. 1.4, while I discuss the current models adopted to explain some of these properties of accretion in the following two subsections.

1.3.1 Evolution of accretion rates with time in a viscous disk

The evolution of an infinitesimally thin viscuous Keplerian disk with time is described with the basics equations of viscous fluid dynamics: the continuity equation and the Navier-Stokes equations. Being the disk assumed to be infinitesimally thin, these equations can be written in cylindrical polar coordinates centered on the star. With the further assumption that the disk is axisymmetric, the **continuity equation** has the following expression:

$$\frac{\partial \Sigma}{\partial t} + \frac{1}{R}\frac{\partial}{\partial R}(R\Sigma v_R) = 0, \tag{1.3}$$

where Σ is the surface density, R the radius of the disk, and v_R the radial velocity.

As shown by, e.g., Lodato (2008), the general equation describing the evolution of the surface density in a Keplerian disk is derived by solving the momentum equation including viscous forces, known as Navier-Stokes equation, for a geometrical thin disk in the azimuthal direction. The expression of the conservation of angular momentum equation is derived to be the following:

$$\frac{\partial}{\partial t}(\Sigma \Omega R^2) + \frac{1}{R}\frac{\partial}{\partial R}(\Sigma v_R R^3 \Omega) = \frac{1}{R}\frac{\partial}{\partial R}\left(\nu \Sigma R^3 \frac{\mathrm{d}\Omega}{\mathrm{d}r}\right), \tag{1.4}$$

where Ω is the orbital frequency. By combining the latter equation with Eq. (1.3), the term v_R is eliminated and, using $\Omega = \sqrt{GM_\star/R^3}$, the **disk evolution equation** is obtained in the form:

$$\frac{\partial \Sigma}{\partial t} = \frac{3}{R}\frac{\partial}{\partial R}\left[R^{1/2}\frac{\partial}{\partial R}(\nu \Sigma R^{1/2})\right]. \tag{1.5}$$

This is a diffusive partial differential equation which is, in general, not linear. However, if the viscosity ν is not a function of Σ, then this equation is linear and solutions can be obtained. Therefore, the evolution of a viscous disk depends upon the form of the viscosity ν, which in turn could have a complicated dependence on the disk properties. In the following I derive some simple solutions under some general assumptions on the kinematic viscosity.

Steady state solution

First of all, it is useful to derive a solution of Eq. (1.5) which is independent on ν. This can be done assuming that the flow in the disk is steady. As I show below, also similarity solutions suggest that the mass flow is nearly constant with the disk radius at a given time, so this can be a reasonable assumption.

Considering that the mass in an infinitesimal disk annulus is $\mathrm{d}M = 2\pi R \Sigma \mathrm{d}R$, the mass flow in the disk ($\dot{M}$) is:

$$\dot{M} = \frac{\mathrm{d}M}{\mathrm{d}t} = -2\pi R \Sigma v_R, \tag{1.6}$$

where the mass flux is assumed to be inward (i.e. a negative v_R implies a positive $\dot{M}$). In the case of steady surface density evolution, the continuity equation (Eq. (1.3)) implies:

$$R\Sigma v_R = const, \tag{1.7}$$

since $\partial\Sigma/\partial t$ vanishes by hypothesis. This implies that $\dot{M}$ is constant with radius. The solution of Eq. (1.5) is then obtained from Eq. (1.4), assuming that the $\partial/\partial t$ term is zero,

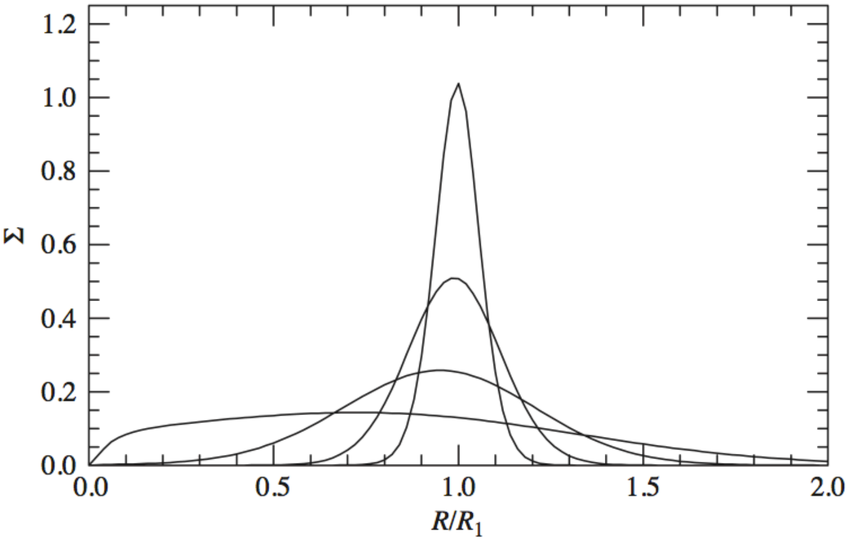

Figure 1.4: Evolution of the disk surface density (Σ) in the case where ν is a constant and the initial surface density distribution is a thin ring centered at $R = R_1$ (spreading ring). Various plots show the distribution of Σ for different values of τ, starting from the most peaked distribution at τ = 0 and spreading out with time. From Hartmann (2009).

that $\dot{M} = -2\pi R \Sigma v_R$ (Eq. (1.6)), integrating over R, assuming that at $R = R_{\rm in}$ there is no torque (i.e., $\mathrm{d}\Omega/\mathrm{d}R|_{R_{\rm in}} = 0$), and substituting $\Omega = \sqrt{GM_\star/R^3}$. This solution has the form:

$$\Sigma(R) = \frac{\dot{M}}{3\pi\nu}\left(1 - \sqrt{\frac{R_{\rm in}}{R}}\right). \tag{1.8}$$

At radii $R \gg R_{\rm in}$, this equation implies that $3\pi\nu\Sigma \sim \dot{M}$ that means, since $\dot{M}$ is constant, that Σ and ν are inversely proportional. In this work I will measure $\dot{M}$ on the star, i.e. $\dot{M}_{\rm acc}$= $\dot{M}(R \rightarrow 0)$. Given that it is not yet possible to measure $\dot{M}(R)$ along the disk, it is not yet possible to constrain whether this steady state case is plausible.

Spreading ring

The easiest assumption on the viscosity is that ν is constant with time and independent of R and Σ. In this case, the solution of Eq. (1.5) is known as the *spreading ring* (e.g., Lynden-Bell & Pringle, 1974), as the disk is expanding both inwards (accreting on the star) and outwards (transferring angular momentum) under the action of viscous forces. This spreading permits the conservation of angular momentum while dissipating this quantity from the central star to outer disk radii. This solution is obtained assuming as initial condition an infinitesimally thin ring of mass m, whose shape is described with a δ function centered at the radius R_1, that is:

$$\Sigma(R, t = 0) = \frac{m}{2\pi R_1}\delta(R - R_1). \tag{1.9}$$

The solution of Eq. (1.5) with this initial condition has been derived by Lynden-Bell & Pringle (1974) to be:

$$\Sigma(x,\tau) = \frac{m}{\pi R_1^2}\frac{x^{-1/4}}{\tau}e^{-\frac{(1+x^2)}{\tau}}I_{1/4}\left(\frac{2x}{\tau}\right), \tag{1.10}$$

where $I_{1/4}$ is a modified Bessel function, $x = R/R_1$, $\tau = 12\nu t/R_1^2 = t/t_\nu$, with the viscous timescale (t_ν) defined as:

$$t_\nu \sim \frac{R_1^2}{\nu}. \tag{1.11}$$

The evolution of Σ described by Eq. (1.10) is shown in Fig. 1.4. As I introduced above, it is clear that the disk is spreading with time. The material moving inwards loses angular momentum and accretes on the star, while materials moving outwards get the excess angular momentum and bring it far from the central star. The radius at which there is the transition between material moving inwards and outwards is $R_{\rm tr} \sim t_\nu/R_1 \sim R_1\,(t/t_\nu)$. This moves outwards with time, thus implying that the angular momentum will be transferred to an infinite radius by a negligible fraction of mass.

Similarity-solution

The most interesting assumption on the viscosity, however, is to assume that this depends on the disk radius as a power-law, i.e. $\nu \propto R^\gamma$. When solving Eq. (1.5) with this assumption on the viscosity, the solutions are usually referred as *self-similar solutions*. The initial conditions for this solution are described as:

$$\Sigma(R, t=0) = \frac{C}{3\pi\nu_1 r^\gamma}\,\text{exp}\left(-r^{(2-\gamma)}\right) \tag{1.12}$$

where $r \equiv R/R_1$ and $\nu_1 \equiv \nu(R_1)$, being R_1 the cut-off radius, and C is a scaling constant. These solutions have been derived in the general case by Lynden-Bell & Pringle (1974) to be:

$$\Sigma(R,t) = \frac{C}{3\pi\nu_1 r^\gamma}T^{-(5/2-\gamma)/(2-\gamma)}\,\text{exp}\left(-\frac{r^{(2-\gamma)}}{T}\right), \tag{1.13}$$

where the dimensionless time T is:

$$T = t/t_\nu + 1, \tag{1.14}$$

with the viscous timescale being, in this case:

$$t_\nu = \frac{1}{3(2-\gamma)^2}\frac{R_1^2}{\nu_1}. \tag{1.15}$$

From Eq. (1.13) it is possible to derive the equation for the mass flux through the disk:

$$\dot{M}(R,t) = -2\pi R v_R \Sigma = C T^{-(5/2-\gamma)/(2-\gamma)}\,\text{exp}\left(-\frac{r^{(2-\gamma)}}{T}\right)\left[1 - \frac{2(2-\gamma)r^{(2-\gamma)}}{T}\right]. \tag{1.16}$$

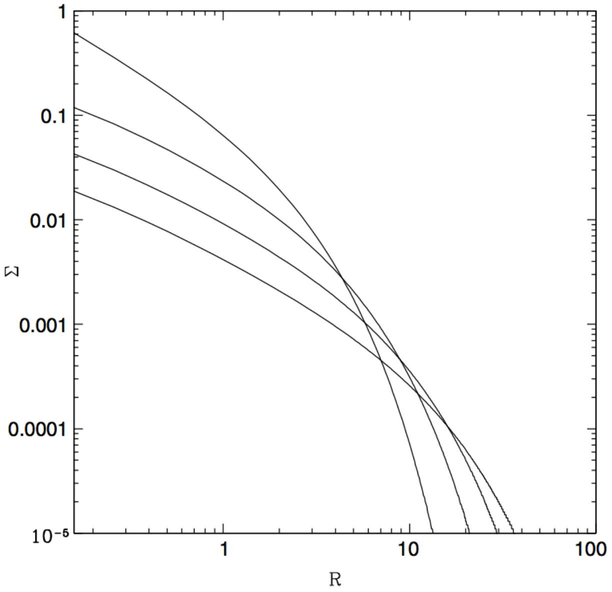

Figure 1.5: Evolution of the disk surface density according to similarity solutions in the case where $\nu \propto R$. The lines show, from top to bottom, the self-similar solution at increasingly large times. (From Lodato (2008))

In the case $T \gg 1$, that is when the time is much longer than the viscous timescale, where the disk has evolved and thus is independent from the initial conditions, the mass accretion rate on the star ($\dot{M}_{\rm acc}$), i.e. the limit $r \rightarrow 0$, has this form:

$$\dot{M}_{\rm acc}(t) \propto t^{-(5/2-\gamma)/(2-\gamma)} \propto t^{-\eta}, \tag{1.17}$$

and this equation is valid only when $\gamma < 2$ for existence conditions. In this framework $\dot{M}_{\rm acc}$ decreases with time as a power-law, where the new parameter $\eta = (5/2-\gamma)/(2-\gamma)$ is the exponent. This value can be determined from observations, as I will describe in Sect. 1.4.1. This can in turn constrain the dependence of viscosity on the radius, i.e. γ, in the context of similarity solutions, from the following relation:

$$\gamma = \frac{2\eta - 5/2}{\eta - 1}. \tag{1.18}$$

It is easily understood that the mass of the disk should decrease with time, i.e. $M_{\rm disk} \propto t^{-\alpha}$ with $\alpha > 0$. This decrease of mass of the disk is due to accretion onto the central star, i.e. $\dot{M}_{\rm acc}$= d$M_{\rm disk}$/d$t \propto t^{-(\alpha+1)}$. This implies that $\eta = \alpha + 1$ which results in the condition $\eta > 1$ if $\alpha > 0$.

I show in Fig. 1.5 the evolution of the disk surface density predicted by the similarity solution in the simple (but not too unrealistic) case where $\gamma = 1$, i.e. $\nu \propto R$. This would imply that $\dot{M}_{\rm acc}$ decreases with time as a power-law with exponent η=1.5. The solutions in this case, derived by e.g., Hartmann (2009), lead to some simple expressions useful to describe the evolution of a typical TTauri star disk. Assuming that the main source of

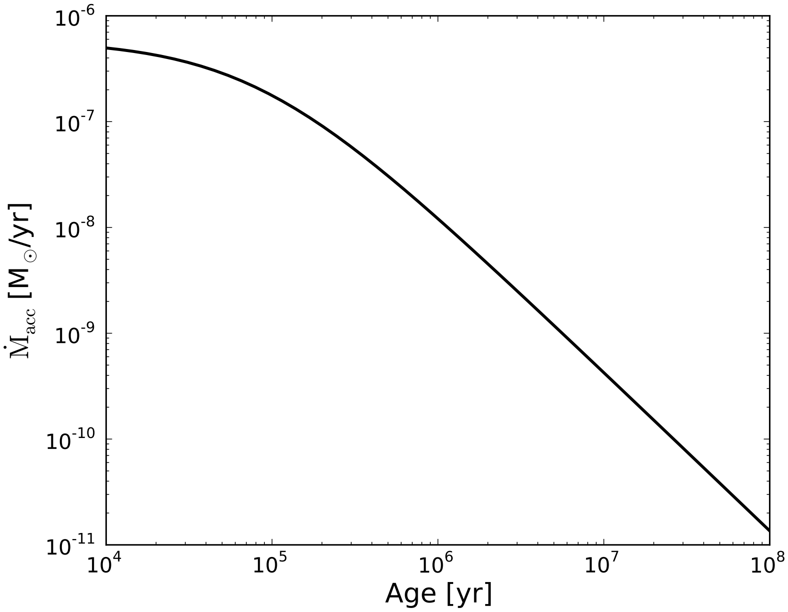

Figure 1.6: Evolution of mass accretion rates with time according to similarity solution viscous models. This is calculated using the expressions of Eq. (1.23), $R = 5R_\star$, and the fiducial parameters of Hartmann (2009).

irradiation of the disk is the central star, that the disk is ``flared'' in such a way that its temperature can be described as:

$$T(R) \sim 10 \left(\frac{100\text{AU}}{R}\right)^{1/2} \text{K}, \tag{1.19}$$

and that the disk had an ``initial'' radius R_0[2], the evolution of the surface density is:

$$\Sigma \sim 1.4 \times 10^3 \frac{e^{-R/(R_0 t_d)}}{(R/R_0) t_d^{3/2}} \left(\frac{M_d(0)}{0.1 M_\odot}\right) \left(\frac{R_0}{10\text{AU}}\right)^{-2} \text{g cm}^{-2}, \tag{1.20}$$

with $M_d(0)$ being the initial disk mass, and t_d is related to the age of the source t by:

$$t_d = 1 + \frac{t}{t_s}, \tag{1.21}$$

where the scaling time t_s is:

$$t_s \sim 8 \times 10^4 \left(\frac{R_0}{10\text{AU}}\right) \left(\frac{\alpha}{10^{-2}}\right)^{-1} \left(\frac{M_\star}{0.5 M_\odot}\right)^{1/2} \left(\frac{T_{100}}{10\text{K}}\right)^{-1} \text{yr}. \tag{1.22}$$

---

[2] R_0 is the length scale of the initial density distribution of the disk, i.e. the radius at which 60% of the mass resides initially.

Also $\dot{M}$ can be expressed in the following simple term under the aforementioned assumptions:

$$\dot{M} \sim 6 \times 10^{-7} \, \frac{e^{-R/(R_0 t_d)}}{t_d^{3/2}} \left(1 - \frac{2R}{R_0 t_d}\right) \left(\frac{M_d(0)}{0.1 M_\odot}\right) \left(\frac{R_0}{10\text{AU}}\right)^{-1} \\ \times \left(\frac{\alpha}{10^{-2}}\right) \left(\frac{M_\star}{0.5 M_\odot}\right)^{-1/2} \left(\frac{T_{100}}{10\text{K}}\right) M_\odot \, \text{yr}^{-1}, \tag{1.23}$$

with T_{100} being the disk temperature at 100 AU.

The evolution of $\dot{M}_{\text{acc}}$, i.e. $\dot{M}$ calculated at $R = 5R_\star$, with time according to this description is shown in Fig. 1.6 using the fiducial parameters of Hartmann (2009).

According to this description of the evolution of viscous disks, observational constraints on the slope of the relation between $\dot{M}_{\text{acc}}$ and the age of the objects can be translated in general properties of the protoplanetary disk. In particular, the evolution of the surface density in the disk, that means of the amount of material available to form planets at various radii, is derived from this observation. As I describe in Sect. 1.4.1, determining the exponent of this power-law decay has been one of the first tasks of observers in the last fifteen years. I will then discuss in Chapter 6 the constraints I can put on this model and on the physical conditions of the disks from the data analyzed in this Thesis.

1.3.2 Evolution of accretion rates with time due to photoevaporation

Another important process governing the evolution of protoplanetary disks is photoevaporation. This process, in particular, is thought to be one of the main driver of the final dispersal of disks. In particular, internal photoevaporation from the central star is probably present in most, if not all, the YSOs, at least at later stages of PMS evolution, i.e. in the Class II phase and in TDs. This is driven by the high-energy radiation coming from the central star, which can be UV and/or X-rays, heating the gas on the surface of the disk to sufficiently high temperatures to unbound it from the gravitational well of the star. This happens at sufficiently large radii where the thermal energy of the heated layer exceeds the gravitational binding energy. Under this condition the heated gas escapes the disk in a photoevaporative wind (e.g., Armitage, 2010; Alexander et al., 2014). Here I do not discuss the details of the various photoevaporation models, but I stress what is the general qualitative prediction of all the models, which is that the disk is cleared via an inside-out process. The quantitative differences between the models are discussed, e.g., by Alexander et al. (2014, and references therein).

In general, the evolution of a viscous disk under the effects of photoevaporation is described by the evolution equation Eq. (1.5) with the addition of a term describing the removal of mass due to this process:

$$\frac{\partial \Sigma}{\partial t} = \frac{3}{R} \frac{\partial}{\partial R} \left[R^{1/2} \frac{\partial}{\partial R} (\nu \Sigma R^{1/2}) \right] + \dot{\Sigma}_{\text{wind}}(R, t), \tag{1.24}$$

where this mass loss term ($\dot{\Sigma}_{\text{wind}}$) varies according to the different models of photoevaporation. The reason for which it is possible to include this term in the evolution equation

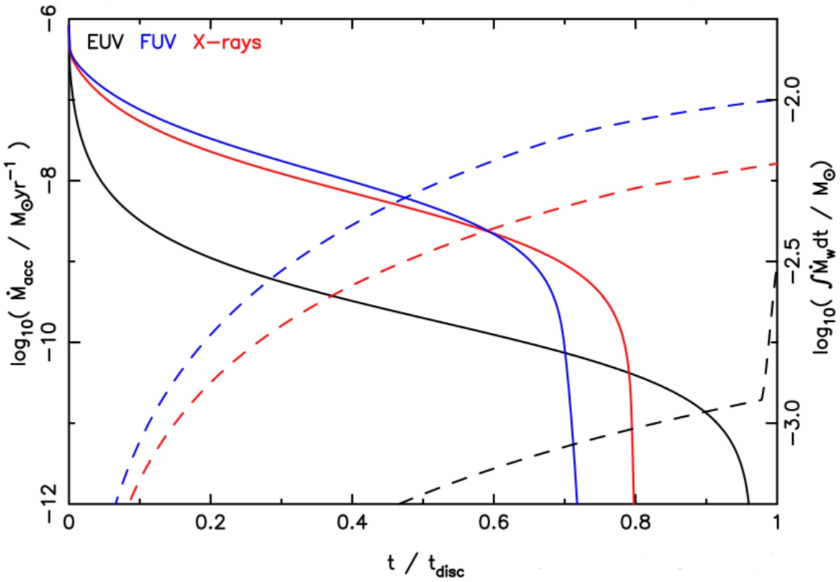

Figure 1.7: Evolution of mass accretion rates according to different photoevaporation models. The solid lines refer to values of $\dot{M}_{\rm acc}$ reported on the left axis, while dashed lines to values of the mass loss rate, that are reported on the right axis. These quantities are shown as a function of time. The *black lines* are for the EUV photoevaporation model, the *blue lines* for the FUV photoevaporation one, while the *red linse* for X-ray model. From Alexander et al. (2014).

is that the flow leaving the disk has the same specific angular momentum as the disk at the launch point (e.g., Armitage, 2010). According to photoevaporation models there are three phases of the disk evolution. In the first phase the inward mass flow in the disk due to viscous evolution is much larger than the mass loss in the wind due to photoevaporation ($\dot{M}_{\rm acc}\gg$ $\dot{M}_{\rm wind}$). In this phase the effects of photoevaporation are negligible. Eventually, $\dot{M}_{\rm acc}$, which decreases with time as expected by Eq. (1.17), becomes comparable to the wind mass loss rate. At this stage, the material drifting inwards from the outer radius is detached from the disk at the gravitational radius $R_g = GM_\star/c_s$, which is the location where the sound speed (c_s) of the ionized gas is equal to the orbital velocity in the disk. At this disk radius there is the development of an annular gap in the gas surface density, as all the material inflowing from the outer disk is diverted into the photoevaporated flow. From this point, the inner disk is cut off from its outer disk mass reservoir and rapidly accretes onto the central star. The timescale on which this draining of the inner disk happens is the viscous timescale, which, for this radius, is $\sim 10^5$ yr. Finally, the outer disk is directly irradiated by high-energy radiation. This results in an increased rate of mass loss due to photoevaporation, and in a fast dispersal of the outer disk on similar timescales (e.g., Owen et al., 2012). Following Alexander et al. (2014), I show in Fig. 1.7 the expected evolution of $\dot{M}_{\rm acc}$ and $\dot{M}_{\rm wind}$ according to the three main models of photoevaporation (FUV, EUV, X-rays). In this plot is clear that the evolution of $\dot{M}_{\rm acc}$ is the same as the one expected from viscous evolution models until $\dot{M}_{\rm acc}\sim$ $\dot{M}_{\rm wind}$, when a rapid decrease of $\dot{M}_{\rm acc}$, due to the rapid disk dispersal, happens.

This inside-out mechanism is one of the claimed mechanism to explain transitional disks (see Sect. 1.1 and Chapter 5), but still cannot explain all the observations. Surely, this process is known to happen but also to coexist with other mechanisms, and the interplay between these various processes is still under debate (e.g., Rosotti et al., 2013). For example, I discuss in Chapter 5 that the transitional disks analyzed in this Thesis are still accreting at a rate similar to cTTs, thus have still a gaseous inner disk. Possibly some of these disks have not evolved due to photoevaporation.

1.3.3 The dependence of accretion rates with the mass of the central star

The dependence of $\dot{M}_{\rm acc}$ on $M_\star$ was initially not explored in detail from a theoretical point of view. The basic reason was that in a viscous disk where viscosity is driven by MRI turbulence there is no dependence between the two quantities according to theory. For example, using the layered accretion disk theory, Gammie (1996) showed that $\dot{M}_{\rm acc}$ in the inner disk is:

$$\dot{M}_{\rm acc} = 1.8 \times 10^{-8} \left(\frac{\alpha}{10^{-2}}\right)^2 \left(\frac{\Sigma_a}{100 \text{ g} \cdot \text{cm}^{-2}}\right)^3 M_\odot \text{ yr}^{-1}, \tag{1.25}$$

where Σ_a is the surface density in the active layer of the disk, and α the usual parameter to describe the disk viscosity. In this result there is no explicit dependence upon $M_\star$, and no further theoretical arguments were available at that time to predict any dependence between these two observables. As I describe in Sect. 1.4.1 in detail, the first observational works aimed at studying accretion in cTTs were all focused on objects with $M_\star \sim 0.5 - 1\ M_\odot$ (e.g., Valenti et al., 1993; Kenyon & Hartmann, 1995; Hartmann et al., 1998). In the next years more efforts were done to study lower mass objects, and, in particular, it became clear that brown dwarfs (BDs) posses circumstellar disks like cTTs, with infrared excess (e.g., Natta & Testi, 2001; Jayawardhana et al., 2003a) and accretion signatures (e.g., Jayawardhana et al., 2003b; Natta et al., 2004; Mohanty et al., 2005). The initial idea was that, if BD formation is just a scaled-down version of star formation, $\dot{M}_{\rm acc}$ should scale proportionally to $M_\star$ down to the BD regime. However, thanks to the sufficiently large interval of $M_\star$ accessible to observations (roughly 2 orders of magnitude when including BDs) the $\dot{M}_{\rm acc}$-$M_\star$ relation could be observationally investigated, and, strikingly, this dependence was found to be $\dot{M}_{\rm acc} \propto M_\star^2$, with a considerably large spread in the values of $\dot{M}_{\rm acc}$ at any $M_\star$ (e.g., Muzerolle et al., 2003; Natta et al., 2004; Mohanty et al., 2005; Natta et al., 2006). These results called for an explanation, and different possibilities have been explored in the next years. In particular, it became clear that, given that $M_\star$ changes negligibly during the Class II phase, the $\dot{M}_{\rm acc}$-$M_\star$ plane is a diagnostic tool for the evolution of accretion during this phase, yielding information on the relative amount of time spent in various regions of the plane by the objects (Clarke & Pringle, 2006). So far, no final solution of this problem has been found. Here I discuss the possible scenarios introduced to explain the $\dot{M}_{\rm acc}$-$M_\star$ dependence, while I discuss the observational results and the still open issues on this relation at the beginning of this Thesis in Sect. 1.4.1.

Bondi-Hoyle accretion

An early explanation for the observed $\dot{M}_{\rm acc}$-$M_{\star}$ relation was suggested by Padoan et al. (2005), who explained this as a consequence of Bondi-Hoyle accretion. They suggested that, given that the origin of disk turbulence driving the viscous evolution is not yet clear, the only possibility to compare viscous evolution models with observation is to assume ``ad hoc'' values for the viscosity. Moreover, all YSOs are still associated with their parental cloud, so the assumption that disks evolve in isolation could be incorrect. Their proposed evolution of YSOs is divided in two phases. In the first one the core collapses and there is spherical accretion which ends with the formation of a central PMS object surrounded by a disk. This very massive disk is gravitationally unstable and rapidly accretes onto the central object in less than 1 Myr. In the second phase the system accretes material from the large-scale gas distribution in the parent cloud, and the disk acts as a short-term buffer between the large-scale structure and the central PMS star. The accretion of material from the parent cloud is driven by Bondi-Hoyle accretion, whose rate is:

$$\dot{M}_{\rm BH} = \frac{4\pi G^2 \rho_\infty}{(c_\infty^2 + v_\infty^2)^{3/2}} M_\star^2, \tag{1.26}$$

where ρ_∞ is the gas density of the parental cloud, c_∞ its sound speed, v_∞ the gas velocity relative to the star, and all these quantities depend on the environment, therefore are independent on the properties of each individual YSO. If the values of $\dot{M}_{\rm acc}$ are assumed to be the same as expected from Bondi-Hoyle accretion, than the order-of-magnitude of the observation is matched and the dependence of $\dot{M}_{\rm acc}$ with $M_\star$ is a power-law with exponent 2, as expected.

However, there are several caveats to this description. First, the assumption that $\dot{M}_{\rm acc} \sim \dot{M}_{\rm BH}$ means that all the mass which is accreted on the star+disk system steady flows in the disk to the central PMS star. In fact, the actual rate of accretion on the star could be lower (e.g., Mohanty et al., 2005). Then, this description implies that $\dot{M}_{\rm acc}$ itself should depend strongly on the environment in which the YSO is located. This was, however, never observed, as described by, e.g., Mohanty et al. (2005), Hartmann et al. (2006), and Alexander & Armitage (2006). Finally, explaining the evolution of protoplanetary disks without angular momentum transport is a questionable assumption that could not explain, for example, the fact that TTauri stars posses large disks (e.g., Hartmann et al., 2006) and that disks in the early phases are very small (e.g., Miotello et al., 2014), so they have to expand afterwards. Therefore, this explanation is not thought to be descriptive of the phenomenon.

Initial conditions and basic viscous evolution

Alexander & Armitage (2006) firstly proposed an explanation for the $\dot{M}_{\rm acc} \propto M_\star^2$ relation as a consequence of properties of the disks at formation, followed by classical viscous evolution. From the solution of the surface density evolution in the context of similarity solution ($\nu \propto R^\gamma$, Eq. 1.13), by expressing the constant C, that is:

$$C = \frac{3\ M_d(0)(2-\gamma)\nu_1}{2R_1^2}, \tag{1.27}$$

they derive:

$$\Sigma(R,t) = \frac{M_d(0)(2-\gamma)}{2\pi R_1^2 r^\gamma} T^{-(5/2-\gamma)/(2-\gamma)} \exp\left[-\frac{r^{(2-\gamma)}}{T}\right], \tag{1.28}$$

where M_d(0) is the initial disk mass, $r = R/R_1$ is a dimensionless radius, R_1 is the scale radius that sets the initial disk size, and $T = t/t_\nu + 1$ is the dimensionless time. As the viscous timescale is:

$$t_\nu = \frac{R_1^2}{3(2-\gamma)^2\nu_1}, \tag{1.29}$$

they derive that $\dot{M}_{\rm acc}$, i.e. the accretion rate onto the star ($r \to 0$) is:

$$\dot{M}_{acc} = \frac{M_d(0)}{2(2-\gamma)t_\nu} T^{-(5/2-\gamma)/(2-\gamma)}, \tag{1.30}$$

which is the same as in Eq. (1.17), but with the proportionality constant expressed. Their assumption is that the $\dot{M}_{\rm acc} \propto M_\star^2$ relation is valid already for the initial accretion rates. Given that observations show that in BDs the disk-to-star mass ratio is comparable to that of cTTs, they assume that $M_d(0) \propto M_\star$, thus their assumption is fullfilled if the viscous timescale depends on $M_\star$ in the following way:

$$t_\nu \propto \frac{1}{M_\star}. \tag{1.31}$$

This has strong implications on possible observables. First of all, Eq. (1.31) implies that the viscous timescale is longer for BDs than for TTauri stars, with typically $t_\nu \sim 10^6$ yr for BDs if $t_\nu \sim 10^4 - 10^5$ yr for cTTs (e.g., Hartmann et al., 1998). Lower mass objects will thus evolve more slowly with time than higher mass ones. As a consequence, the spread in the values of $\dot{M}_{\rm acc}$ on the $\dot{M}_{\rm acc}$-$M_\star$ plane should be smaller at lower $M_\star$. Then, from the expression of the viscous timescale and the viscosity itself they derive that, typically, the initial disk radius for BDs are larger than for cTTs, with scale radii R_0 for BDs $\sim$ 50-100 AU. However, the fact that the viscous timescale is shorter for higher mass stars implies that disks around these objects will spread for viscous evolution faster than those around BDs, so there would be no observable differences at later stages. Implicit in their discussion there is the suggestion that the observed spread of values of $\dot{M}_{\rm acc}$ at any $M_\star$ is due to age differences.

A similar approach of suggesting that the observed spread is due to the imprint of the initial conditions at formation has been used by Dullemond et al. (2006) to explain the $\dot{M}_{\rm acc}$-$M_\star$ relation. They model the collapse of various rotating molecular cloud cores and the subsequent viscous evolution of the disk which forms. By assuming that cores with significantly different masses have similar rotation rates to breakup rate ratios they find a trend of $\dot{M}_{\rm acc}\propto M_\star^{1.8\pm0.2}$. The observed spread can be then interpreted as a spread in the initial core rotation rates. This simple but descriptive solution has some observable consequences, as well. First, the process of star formation is similar for higher mass stars and BDs. Then, the mass of the disk should depend strongly on $M_\star$, roughly $M_d \propto M_\star^2$, and, in particular, should be a tightly correlated with $\dot{M}_{\rm acc}$.

Assumptions on disk viscosity

A possible explanation could be that the viscosity of the disk, which drives accretion, depends on $M_\star$. If MRI is driving the disk turbulence, Mohanty et al. (2005) suggest that the amount of ionization, and thus the turbulence, is lower for cooler, i.e. lower-mass, objects. This qualitative argument has been later on somehow developed by Hartmann et al. (2006), who suggest that $\dot{M}_{\rm acc}$ depends on $M_\star$ if irradiation by the central star is taken into account in a layer accretion model (Gammie, 1996). Basically, $\dot{M}_{\rm acc}$ is given by the accretion rate of the layered model at a critical radius (R_C) where the temperature is high enough to enhance MRI in the disk. They assume this critical radius to be the inner edge of the dusty disk, which is frontally illuminated by the central star. By fixing the dust destruction temperature they derive that $R_C \propto L_\star^{1/2}$. Assuming a classical alpha-viscosity description of the disk, i.e. $\nu = \alpha c_s/\Omega$, they obtain that:

$$\dot{M} \propto \nu\Sigma \propto \alpha c_s^2 \Omega^{-1}\Sigma_a \propto \alpha\Sigma_a L_\star^{3/4} M_\star^{-1/2}, \tag{1.32}$$

where also in this case Σ_a is the surface density of the active layer of the disk. In PMS stars, at least for $M_\star \lesssim 2M_\odot$, the dependence of the stellar luminosity with the mass is $L_\star \propto M_\star^2$, so, if the disk is purely internally irradiated, the accretion rate at R_C would be:

$$\dot{M} \propto \alpha\Sigma_a M_\star. \tag{1.33}$$

With this description the mass accretion rate depends on the stellar mass, but the slope of this dependence is not as steep as observed. However, this description could represent the upper envelope of accretion rates observed (Hartmann et al., 2006). The suggestion would be that the upper envelope is composed by objects whose disk is described by the layered accretion disk model with irradiation from the central star, while the other objects falling well below this upper envelope in the $\dot{M}_{\rm acc}$-$M_\star$ plane (mostly BDs and low-mass TTauri stars) have a small and magnetically active disk that substantially evolved viscously and has now a lower rate of accretion. This implies that lower-mass objects evolve faster than solar-mass cTTs, so the evolution of $\dot{M}_{\rm acc}$ with time should be different for the two classes of objects, with $\dot{M}_{\rm acc}$ slowly decreasing for higher mass cTTs with respect to BDs and low-mass stars.

Self-gravitation

Some efforts have been made in the literature to explain the evolution of protoplanetary disks under self-regulated disks which experience gravitational instabilities driving the disk turbulence and the subsequent accretion process. In particular, Vorobyov & Basu (2008) discuss how $\dot{M}_{\rm acc}$ would depend on $M_\star$ in systems where gravitational instabilities are the only driver of disk turbulence, and hence accretion. By carrying out several simulations on the first 3 Myr of evolution of low- and intermediate-mass TTauri stars ($0.25 M_\odot < M_\star < 3.0 M_\odot$), they derive a $\dot{M}_{\rm acc}$-$M_\star$ relation with a power-law of exponent 1.7. At the same time, they predict that $\dot{M}_{\rm acc}$ should correlate almost linearly with the disk mass. Finally, they discuss that there could be a bimodality in the observed $\dot{M}_{\rm acc}$-$M_\star$ relation, with different behaviors in the very-low-mass end and in the $M_\star > 0.2 M_\odot$ range. Following this work, Vorobyov & Basu (2009) developed a set of models to describe the evolution of both objects with $M_\star > 0.2 M_\odot$ and of lower $M_\star$. In order to be able to describe both classes of objects they include in their description also an effective turbulent α-viscosity with α=0.01 to allow for accretion in the lower mass objects, where the disk is not massive enough to drive substantial gravitational instabilities. Also in this case the values of $\dot{M}_{\rm acc}$ predicted by their models are similar to those observed. The $\dot{M}_{\rm acc}$-$M_\star$ relation is clearly reproduced, with an exponent of the power-law which is 1.8 when including all the time-averaged models at all $M_\star$. They also suggest that the large spread of $\dot{M}_{\rm acc}$ at any given $M_\star$ is partly due to intrinsic variability during the evolution and partly to object-to-object variations due to different initial conditions. Finally, they predict with their models a strong bimodality in the $\dot{M}_{\rm acc}$-$M_\star$ relation, with values of the exponent of the power-law varying from 2.9 for YSOs with $M_\star < 0.2 M_\odot$ to 1.5 for objects with $0.2 M_\odot \leq M_\star < 3.0 M_\odot$.

Photoevaporation

As I discussed in Sect. 1.3.2, protoplanetary disks are subject to photoevaporation from the central star. Under this description, Clarke & Pringle (2006) suggested that the lowest accretion rate measurable at a given mass is set by the onset of photoevaporation. As the decrease of $\dot{M}_{\rm acc}$ with time is a power-law decay, young stars spend most of their time at the lowest possible accretion rates, and this is the situation at which it is more plausible to observe them. Therefore, the $\dot{M}_{\rm acc}$-$M_\star$ relation could be driven in large samples by these low-accretors. Following on this path, if the lowest accretion is set by photoevaporation (see Sect. 1.3.2), then the most plausible accretion rate of a star is $\dot{M}_{\rm acc}$=$\dot{M}_{\rm wind}$, with $\dot{M}_{\rm wind}$ being the mass-loss rate due to photoevaporation. Clarke & Pringle (2006) compute the expected $\dot{M}_{\rm acc}$-$M_\star$ relation in the case in which UV radiation dominates the photoevaporative flow, which results in the following mass-loss rate dependence of $M_\star$:

$$\dot{M}_{\rm wind} \propto (M_\star \phi)^{1/2}, \tag{1.34}$$

where ϕ is the ionizing flux. In the UV photoevaporation case ϕ simply scales with stellar luminosity, implying that $\dot{M}_{\rm wind} \propto M_\star^{1.35}$. This power-law exponent, however, is much lower than what is observed.

On the other hand, steeper dependence on $M_\star$ is found when considering X-ray driven photoevaporation, as recently shown by Ercolano et al. (2014). In the case of X-ray photoevaporation, Owen et al. (2012) derived that the mass-loss rate is described as:

$$\dot{M}_{\text{wind}} = 6.25 \times 10^{-9} \left(\frac{L_X}{10^{30}\ \text{ergs}^{-1}} \right)^{1.14} M_\odot\ \text{yr}^{-1}, \tag{1.35}$$

where L_X is the X-ray luminosity, and the very weak ($\sim M_\star^{-0.068}$) dependence on the stellar mass is ignored. With this description the $\dot{M}_{\text{acc}}$-$M_\star$ relation is driven by the $M_\star$-L_X one, which can be constrained observationally. Observations of various objects in Orion (Preibisch et al., 2005) and in Taurus (Güdel et al., 2007) suggest that $L_X \sim M_\star^{1.5-1.7}$ for objects with $M_\star < 1M_\odot$, which results in a dependence $\dot{M}_{\text{acc}} \sim M_\star^{1.5-1.7}$ in agreement with most of the observations, as I discuss in the next section.

1.4 The role of this Thesis

The main aim of this Thesis is to understand the properties of protoplanetary disks and their evolution by studying observationally the interaction with the central forming stars through accretion. As I introduced in the previous sections, accretion on TTauri stars has been a subject of study since many years but many questions remain open. More stringent constraint on the evolution of circumstellar disks can be obtained only analyzing large samples of objects with different intrinsic properties, such as age, mass, or evolutionary stage, and with accurate methodologies.

1.4.1 The state of the art at the beginning of this Thesis

The first observational works in this field (e.g. Valenti et al., 1993; Gullbring et al., 1998; Calvet & Gullbring, 1998; Hartmann et al., 1998) have mostly been focused on one nearby low-mass star-forming region, Taurus, which was easily accessible in the northern sky and included many strong accretors. Thanks to these works the general picture of the evolution of disks was obtained: typical $\dot{M}_{\text{acc}}$ are of the order of $\sim 10^{-8} M_\odot$/yr for objects 1-3 Myr old and decrease with age as a power-law ($\dot{M}_{\text{acc}} \propto t^{-\eta}$) with exponent η ~1.5 (Hartmann et al., 1998, see Fig. 1.8). This result would imply that, according to similarity solution models (see Section 1.3.1, in particular the equations 1.17 and 1.18), the disk viscosity scales linearly with the disk radius ($\nu \propto R$). Therefore, viscous evolution model have been shown with these work to be able to reproduce the general evolution of disks.

These early works were all based on the observation of the UV-excess due to accretion by means of low-resolution spectroscopy or U-band photometry and the subsequent modeling of this excess to derive L_{acc} (see Fig. 1.9). Measurements of this excess could be carried out only with instruments and telescopes with high-sensitivity at $\lambda \lesssim 4000$ Å, such as large ground-based telescopes (more than 4m, e.g. Lick, Palomar, MMT at that time) or the Hubble Space Telescope. As both UV-excess and strong emission lines are originated in the accretion flow (see Section 1.2.1), it became clear that a less telescope-time demanding method to derive accretion rates for large sample of objects would be to

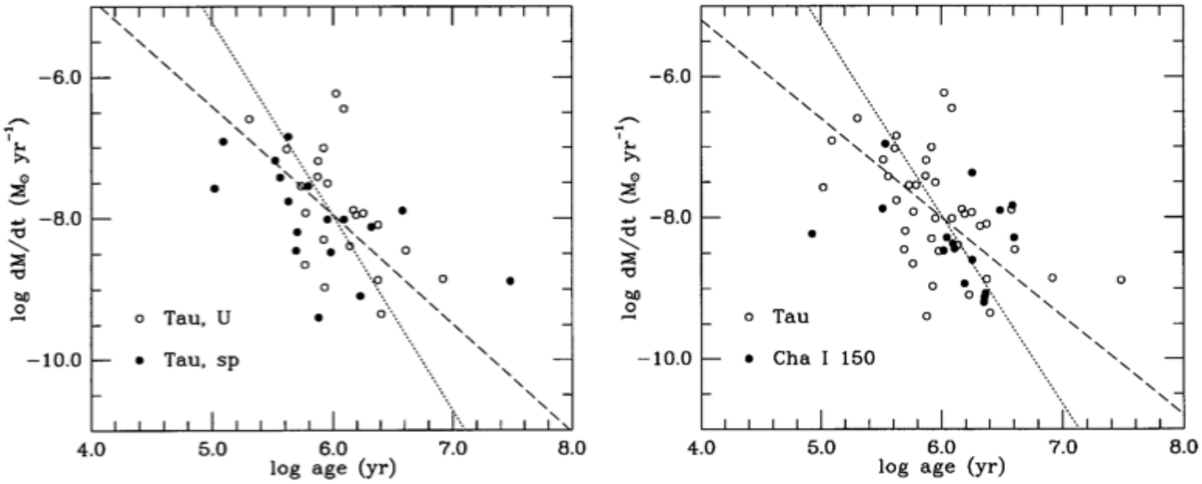

Figure 1.8: First observations of the mass accretion rate as a function of age from Hartmann et al. (1998). The overplotted lines are the linear best fit assuming different uncertainties on the two quantities. The dashed line represents a fit with slope 1.5.

study the luminosity of emission lines ($L_{\rm line}$) at optical wavelengths. The relations between the $L_{\rm acc}$ measured directly from the UV-excess and $L_{\rm line}$ have then been calibrated in various works (e.g., Gullbring et al., 1998; Calvet et al., 2004; Natta et al., 2006; Herczeg & Hillenbrand, 2008; Dahm, 2010). This opened the possibility to study larger samples and different star forming regions, such as Orion (Robberto et al., 2004; Fang et al., 2009; Rigliaco et al., 2011a; Manara et al., 2012), ρ-Ophiucus (e.g., Natta et al., 2004, 2006; Gatti et al., 2006), the Cepheus OB2 region (e.g. Sicilia-Aguilar et al., 2005, 2010), the Chameleon clouds (e.g., Biazzo et al., 2012), and even star forming regions in the Magellanic Clouds (e.g., Spezzi et al., 2012). The analysis of these regions confirmed in most of the cases the general behavior predicted by viscous evolution models (e.g., Robberto et al., 2004; Sicilia-Aguilar et al., 2010; Manara et al., 2012, see Fig. 1.10 and 1.11), but started to show the limits of this description, which cannot explain some of the observed effects, such as the presence of many non-accreting objects at any age (Sicilia-Aguilar et al., 2010), the large spread of values of $\dot{M}_{\rm acc}$ at any age, or the low values of η derived when analyzing large samples, which have been found to be even below the physical limit $\eta > 1$ (see discussion after Eq. 1.18) in some cases (Manara et al., 2012).

At the same time, the awareness that stellar ages determined with pre-main-sequence evolutionary models are highly uncertain grew (e.g. Hartmann, 2003; Soderblom, 2010; Baraffe & Chabrier, 2010; Preibisch, 2012) and researcher started to put more effort in exploring other relations, such as the relation between $\dot{M}_{\rm acc}$ and $M_\star$, claimed firstly to be $\dot{M}_{\rm acc}\sim M_\star^2$ in Muzerolle et al. (2003). Many following works (e.g. Natta et al., 2006; Fang et al., 2009; Rigliaco et al., 2011a; Manara et al., 2012) confirmed observationally the existence of this relation and derived values of the exponent ~1.5-2 (see, e.g., Fig. 1.11). The last works carried out on significantly large and homogeneous samples of objects before this Thesis, however, noted that this exponent is not the same at all masses. The differ-

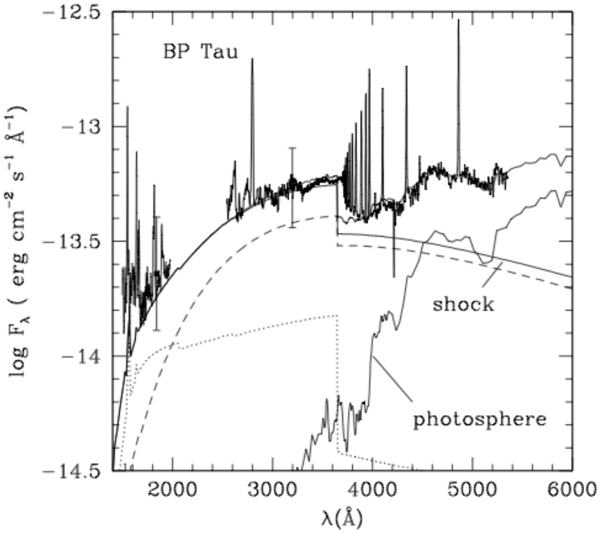

Figure 1.9: Observation and modeling of the UV-excess of young stellar objects due to accretion. The observed spectrum is more intense in this range than a pure photosphere spectrum. The excess emission is modeled with a shock model. From Gullbring et al. (2000).

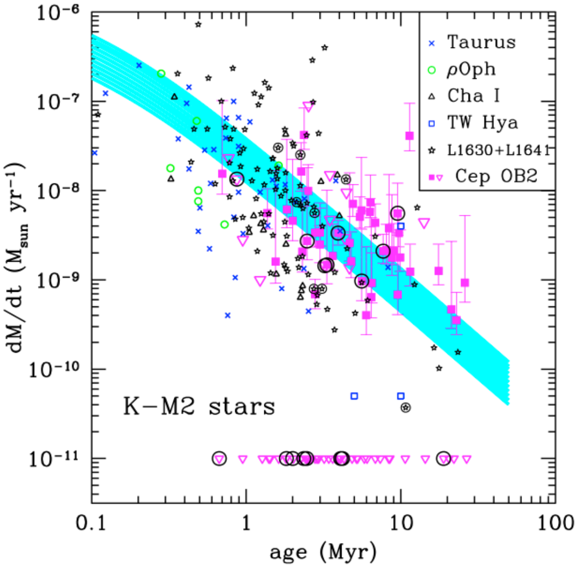

Figure 1.10: Observations of the mass accretion rates as a function of age in various regions from Sicilia-Aguilar et al. (2010). The overplotted blue lines represent various similarity solution models that reproduce the observed trend. At any age various objects with undetectable accretion are found and are shown as open downwards triangles.

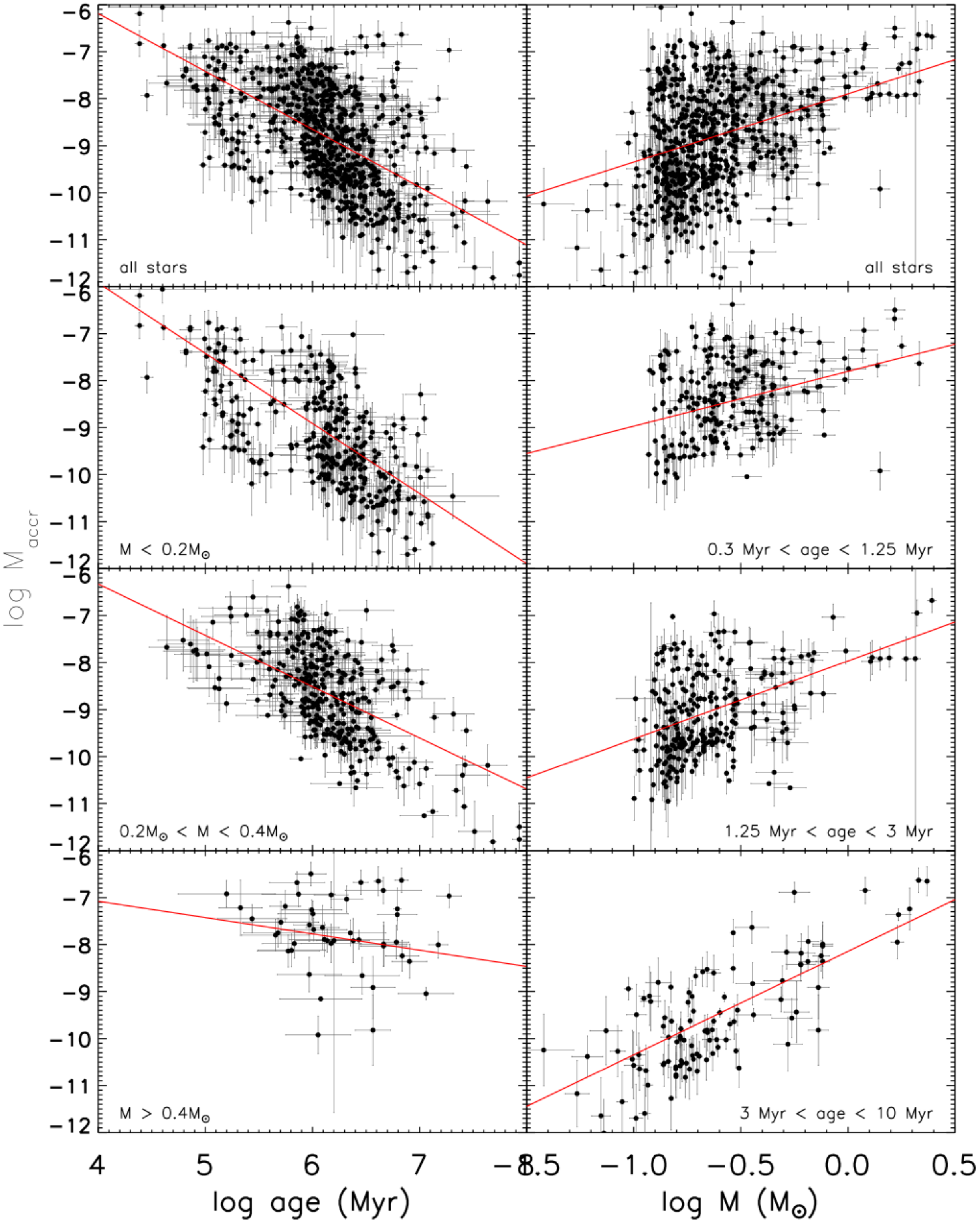

Figure 1.11: Observations of the mass accretion rates ($\dot{M}_{\rm acc}$) as a function of age and mass in the Orion Nebula Cluster obtained from U-band and Hα photometry by Manara et al. (2012). On the left-hand side $\dot{M}_{\rm acc}$ is reported as a function of the age of the objects, while on the right hand side as a function of $M_\star$. Different panels refer to different mass or age ranges reported on the plot. The red line is the best fit.

ent slopes in different mass bins imply that intermediate-mass stars ($M \sim 1 M_\odot$) evolve on longer timescales than lower-mass ones (Rigliaco et al., 2011a; Manara et al., 2012), as it can be seen from the steepening of the $\dot{M}_{\rm acc}$-$M_\star$ relation in Fig. 1.11. This was somehow predicted by some theoretical works (see Sect. 1.3.3) but the small samples and high uncertainties of previous works prevented to study this effect in detail. In all the works, regardless the methodology used or the region analyzed, a large scatter of the values of $\dot{M}_{\rm acc}$ at any $M_\star$ ($\sim$ 2-3 dex, e.g., Natta et al. 2006; Manara et al. 2012) was always observed. It was not clear, however, whether this spread was due to observational uncertainties, to different methodologies, to variability of accretion, or real. Moreover, the lack of complete samples suggested that this relation could be driven by selection effects (Clarke & Pringle, 2006), given that low accretion rates are hardly measured and the spectrum of strong accretors is too strongly veiled to determine their stellar properties. Finally, all these results depend strongly on the evolutionary models used to derive the stellar properties, in particular $M_\star$, and all these uncertainties had been an obstacle for theoreticians to better constrain the physical mechanism driving this relation.

1.4.2 Open issues at the beginning of this Thesis

All the works presented in the previous section suggested that the main driver of the evolution of protoplanetary disk is the disk viscosity, but this cannot be the only driver and other effects, such as photoevaporation or environmental effects, have to be included. Obstacles against a better understanding of the importance of these effects had been the high uncertainties in the measurements of $\dot{M}_{\rm acc}$ available in the literature and the lack of large and homogeneous samples. In particular, the main issues that I address in this Thesis are reported here.

■ **What are the observational uncertainties on the estimate of $\dot{M}_{\rm acc}$ due to chromospheric activity?**
Young stars are known to be strongly chromospherically active, but the effect of this emission on the estimates of accretion in YSO was not clear. In particular, the question was to determine what is the minimum observable accretion rate in accreting YSO and whether this threshold depends on the mass of the YSO. The initial part of my Thesis is dedicated to establishing this intrinsic limit due to chromospheric activity (cf. Chapter 3).

■ **What is the effect of veiling due to accretion and of extinction on the estimate of stellar parameters of young stellar objects?**
When determining stellar parameters of YSOs various effects that modify the observed spectrum should be taken into account, in particular veiling due to accretion and extinction. In the past these effects were usually considered independently, and the question was to estimate how much this would have affected the stellar parameters determination, and how to better constrain these properties altogether. As part of this Thesis I develop a self consistent method to accurately derive the mass accretion rates and the photospheric

parameters from broad band intermediate resolution spectroscopic data (cf. Chapter 4).

- **Is accretion similar at all evolutionary stages of protoplanetary disks?**

The properties of accretion in the Class II phase of YSO evolution has been studied in many cases, but few studies have been focused on more evolved stages of evolution, such as the transitional disk phase. The question was then whether the properties of accretion in these disks are the same of less evolved objects when studied in detail. If the later phases of disk evolution are photoevaporation dominated while the early stages are viscosity dominated, then a change in properties is expected as photoevaporation severs the link between the inner disk and the outer mass reservoire. As part of my work, I apply the original methodology developed in the first part of this Thesis to a sample of transition disks to address this evolutionary aspect (cf. Chapter 5).

- **Is the large observed spread of accretion rates real?**

All the aforementioned studies always found a large spread of values of $\dot{M}_{\rm acc}$ at any $M_\star$ and age, but it was not clear whether this was a real effect or only an observational bias. Stronger constraint on the extent of this spread is needed to understand the $\dot{M}_{\rm acc}$-$M_\star$ relation, and thus the properties of protoplanetary disks in general. The accurate method developed in this Thesis to derive accretion and photospheric parameters is then applied to a large sample of accreting young stellar objects in order to evaluate whether the large spread is intrinsic or not (cf. Chapter 6).

- **What is the dependence of accretion with the mass of the central objects and with its age?**

As discussed in the previous sections, different models predict different behaviors of $\dot{M}_{\rm acc}$ as a function of the stellar mass and age. The observational data were affected by large uncertainty and scatter in the measurements of $\dot{M}_{\rm acc}$ and the photospheric properties. One of the goals of this Thesis is to improve significantly on the measurements and attempt to derive more stringent constraints for the models (cf. Chapter 6).

1.4.3 The structure of this Thesis

In the context presented above I started the work of my Thesis aiming at putting stronger observational constraints on our understanding of protoplanetary disk evolution. For this reason I have developed a model for the accretion spectrum, collected reliable photospheric templates, and designed an analysis method to obtain robust results on large samples of objects. This method is applied in this Thesis to spectra obtained with a second generation ESO/VLT instrument, the X-Shooter spectrograph. This instrument covers simultaneously the spectral range from $\lambda \sim 300$ nm to $\lambda \sim 2500$ nm with high-sensitivity and medium resolution (up to R$\sim$9900 in the UV part of the spectrum, up to more than 18000 in the optical part, Vernet et al. 2011). Thanks to the large wavelength coverage of this instrument the excess emission in the near-UV region can be studied simultaneously with the effects of veiling of the photospheric features at all wavelengths, giving an unprecedented view of the accretion phenomenon to get a much better understanding of the inner disk evolution. I analyze in the following samples of objects with different stellar properties ($L_\star$, $M_\star$, age), at different evolutionary stages, and located in different regions. The structure of the Thesis is the following.

In **Chapter 2** I describe the model for the accretion spectrum that I have developed and that I use in my analysis of YSO spectra. Then, in **Chapter 3** I present the analysis of a sample of 24 spectra of non-accreting (Class III) YSOs. In particular, I discuss how I have derived with different methods their stellar properties in order to be able to use them in my analysis as photospheric templates. I also explain how I use these spectra to determine the bias introduced by the strong chromospheric emission of these young objects in the determination of accretion rates based solely on line luminosity.

The model for the accretion spectrum and the photospheric templates are then used in the rest of the Thesis to study the properties of accretion as a function of the stellar properties of the young stellar objects and as a function of the evolutionary stage of the protoplanetary disk. In particular, the above described model and templates are the main ingredient of the automatic fitting procedure I have developed to determine simultaneously stellar and accretion properties of the observed YSOs from broad-band spectra. This procedure is described in detail in **Chapter 4**, where I apply it to two apparently old objects still surrounded by protoplanetary disks in the Orion Nebula Cluster. My analysis shows how these objects have been misclassified in the literature because the effects of veiling and extinction have not been considered properly. The stellar parameters I determine prove that these objects have an age compatible with the rest of the population of the cluster, thus showing that they are typical cTTs and not age outliers.

With the method I have developed I also study the properties of more evolved stages of disk evolution. In particular, in **Chapter 5** I present the analysis of spectra for a sample of 22 transitional disks (see Section 1.1). In this Chapter I show that the typical accretion rates for the transitional disks in my sample are compatible with those of less evolved accreting YSOs (cTTs) with similar stellar parameters. With the knowledge of their accretion properties I am able to determine the properties of their inner disk, in particular to determine the amount of gas present in the inner disk of these objects. This estimate is needed for disk evolution models to determine what mechanism is driving the evolution of transitional disks.

The methodology and the knowledge acquired in this Thesis allow to study objects in various regions and with different stellar properties. With my method I have contributed to the study of a large number of cTTs located in the Lupus clouds (36 Class II YSOs Alcalá et al., 2014) and 8 objects in the σ-Orionis region (Rigliaco et al., 2012). In **Chapter 6** I analyze a sample of 17 objects in the young ρ-Ophiucus cluster together with 3 more targets in the older Upper Scorpius region. In this Chapter I then analyze all the aforementioned targets and the other ones studied in this Thesis to constrain the properties of accretion as a function of the stellar properties ($L_\star$, $M_\star$) and of their ages. I show how my methodology allows to achieve a significantly smaller spread of accretion rate at any value of the stellar properties, and how viscous evolution models can reproduce the general properties of the targets analyzed here.

Finally, in **Chapter 7** I summarize my findings and discuss the future perspective of this work.

2

Modeling the accretion spectrum

The disk accretion process gives rise to a strong continuum emission at all wavelengths, in particular in the ultraviolet part of the electromagnetic spectrum, but also at optical wavelengths. As outlined in the Introduction, in this Thesis I constrain the evolution of protoplanetary disks through observations of spectra of young stellar objects by determining the intensity and properties of the accretion process. In this Chapter I present the physical background of the slab model I use to derive the continuum emission due to accretion from the observed spectra. I first start in Section 2.1 with a short description of the models adopted in the literature and to evidence their similarities and differences. Then, in Section 2.2 I report the equations needed to properly model an accretion spectrum with a slab model. Finally, I describe in Section 2.3 the dependence of the some important features in the model on the input parameters.

2.1 Accretion spectrum models in the literature

In the description of viscous accretion disks by Lynden-Bell & Pringle (1974), which is discussed in Section 1.2, the disk extends down to the stellar surface. In the innermost part of such disk there is a *boundary layer* of infinitesimal radius. This is a region where the angular velocity of the particles in the disk (Ω) has a continuous transition to the angular velocity of the star ($\Omega_\star$), as it is shown in Figure 2.1. This region is very narrow, as can be derived from the axisymmetric momentum equation:

$$v_r \frac{\mathrm{d}v_r}{\mathrm{d}r} - \frac{v_\Phi^2}{r} = -\frac{1}{\rho}\frac{\mathrm{d}P}{\mathrm{d}r} - \frac{GM}{r^2}, \tag{2.1}$$

where P is the pressure. Inside the boundary layer gravity is not balanced by the rotational support and the radial velocity is small in most cases. The requirement to, instead, having the radial pressure forces to balance the force of gravity, is:

$$\frac{1}{\rho}\frac{\mathrm{d}P}{\mathrm{d}r} \sim \frac{c_s^2}{\Delta R} \sim \frac{GM}{r^2} \sim \Omega_\mathrm{K}^2 r, \tag{2.2}$$

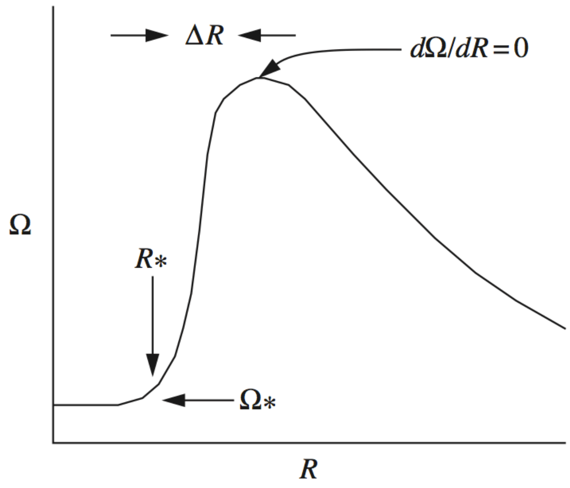

Figure 2.1: Scheme of the angular velocity as a function of the radius in the innermost region of a disk extending down to the stellar surface. The angular velocity varies from the Keplerian velocity to the angular velocity of the star ($\Omega_\star$) over a narrow region. This is known as the boundary layer. From Hartmann (2009)

where c_s is the sound speed in the boundary layer, ΔR its radial extent, and $\Omega_{\rm K}$ the Keplerian angular velocity. Since the vertical scale-heigt is $H = c_s/\Omega_{\rm K}$, I obtain that:

$$\frac{\Delta R}{R} \sim \left(\frac{H}{R}\right)^2 , \tag{2.3}$$

that implies $\Delta R \ll R$ for the assumption that the disk is thin, i.e. $H \ll R$.

The energy released by particles moving from one point in the boundary layer to rest on the stellar surface is the same as the one released by a particle getting to a circular orbit close to the stellar surface from an orbit far from the central star, i.e. $GM_\star/2R_\star$. For this reason, the boundary layer emits a luminosity comparable to that released by the whole disk. This higher luminosity on a very narrow regions leads to the conclusion that the temperature of the boundary layer is much hotter than the maximum temperature of the disk, so it emits radiation at wavelengths shorter than the central star. For this reason the excess emission in the UV observed in young stars surrounded by a disk was thought to be originated in this boundary layer (e.g., Lynden-Bell & Pringle, 1974). Within this picture the emission responsible for the excess due to accretion is well reproduced with a *slab of hydrogen* at high temperatures ($\sim 10^4$ K). Therefore, the first models used to reproduce the accretion spectrum of TTauri stars were slab models. In particular, Valenti et al. (1993, and reference therein) reproduced the observed UV-excess in the spectra of various accreting YSOs with this model.

As I discussed in Section 1.2.1, instead, the current paradigm adopted to describe the geometry of the inner disk, and thus of the region where accretion takes place, is the *magnetospheric accretion* model. In this description the disk is truncated at few stellar radii by the strong magnetic fields (e.g., Hartmann, 2009), so the boundary layer is not present. To describe in detail the emission arising from this magnetospheric region more detailed modeling than a simple slab is needed. Calvet & Gullbring (1998) developed a model which takes into account the shocks originated by the material falling onto the stellar surface at free-fall velocities. In this model the heated photosphere below the shock is optically thick and emits mostly in the Paschen and Brackett continua. On the other hand, the emission coming from the preshock and attenuated postshock regions is optically thin and dominates the spectrum in the Balmer jump region and at shorter wavelengths. This model has been shown to reproduce with good accuracy both the UV-excess (e.g. Calvet & Gullbring, 1998; Calvet et al., 2004; Ingleby et al., 2013) and the shape of the emission lines (e.g. Muzerolle et al., 1998a) of accreting TTauri stars.

Nevertheless, in the present days both models are still used. On one hand, the shock models have a more robust physical relevance in the sense that they aim at reproducing the shock on the stellar surface produced by the accretion flow. However, the geometry of the inner disk region is not completely understood and also these models lack in matching the observation of the veiling due to accretion at longer wavelengths in spectra of accreting TTauri stars (e.g., Ingleby et al., 2013). On the other hand, slab models, which are based on the old assumption on the geometry of the star-disk boundary, are fast and easy to compute and can reproduce with good agreements the observations (e.g., Valenti et al., 1993; Herczeg & Hillenbrand, 2008). Moreover, it should be noted that the most important reason for which these models are needed is to estimate the bolometric correction to derive the total excess emission due to accretion. Most of this excess emission arises in the regions covered by the optical-UV spectra, but a non negligible fraction is emitted at wavelengths $\lesssim$300nm, in a spectral region that is not accessible with ground-based telescopes. Comparison of the bolometric correction factors on different objects shows that the derived values are similar with the two models (e.g., Calvet & Gullbring, 1998; Herczeg & Hillenbrand, 2008). Also results obtained in this Thesis using the slab model, for example the values of $\dot{M}_{\rm acc}$ obtained for 5 TDs in Chapter 5 (TW Hya, LkCa15, CS Cha, GM Aur, DM Tau), are compatible with those derived for the same objects by Ingleby et al. (2013) using shock models. This confirms that both models describe the typical emission due to accretion with similar accuracy. The slab model is thus a good enough description of the process, and I will use this simpler description in this Thesis to model the observed spectra of accreting YSOs. However, being the geometrical assumptions at the base of the slab model inaccurate, I decide to use only the flux of the slab to measure $L_{\rm acc}$, while I never report in the following the values of the physical quantities adopted in the model, such as the temperature of the slab.

2.2 The slab model

Here I model the continuum emission arising from a plane-parallel slab composed of pure hydrogen and assumed in LTE. The input parameters needed to describe the system are the temperature of the slab ($T_{\rm slab}$), the electron density (n_e), and the slab length ($L_{\rm slab}$). The latter can be substituted with the optical depth at a given wavelength (τ_{λ_0}), as these two quantities are related by the following relation:

$$L_{\rm slab} = \frac{\tau_{\lambda_0} \cdot B_{\lambda_0}(T_{\rm slab})}{j_{{\rm H},\lambda_0}}, \tag{2.4}$$

where $B_{\lambda_0}(T_{\rm slab})$ is the value of the blackbody of temperature equal to the slab temperature at the given wavelength, and $j_{{\rm H},\lambda_0}$ the emissivity of hydrogen at that wavelength. Given that the optical depth is one of the physical quantities that governs the slab emissivity, I consider as a set of input parameters the temperature, the electron density, and the optical depth of a pure hydrogen slab (one of the two components of my slab, the other being the H$^-$) at 300 nm (τ_{300}). This particular wavelength is chosen to be close to the Balmer jump, so this parameter is strictly related to the optical depth of the hydrogen component of the slab at the jump.

In the following I derive the emissivity of the slab ($j_{{\rm slab},\nu}$) including both the emissivity from hydrogen ($j_{{\rm H},\nu}$) and that from H$^-$ ($j_{{\rm H}^-,\nu}$), which is an important source of opacity at densities higher than $\sim 10^{13}$ cm^{-3}. From the emissivity I then derive the intensity of the slab ($I_{{\rm slab},\nu}$), which is then converted in observed flux ($F_{{\rm slab},\nu}$) assuming the emission to arise at a distance D from a slab with area $Area_{\rm slab}$ using the following relation:

$$F_{{\rm slab},\nu} = I_{{\rm slab},\nu} \times \frac{Area_{\rm slab}}{D^2}. \tag{2.5}$$

2.2.1 The hydrogen emission

The continuum spectrum of hydrogen is composed by the following two emissions: the free-bound emission, which originates from radiative recombination, and the free-free radiation, which arises from electron transitions in the encounters with protons. I will discuss the equations governing the emission from these two components in the next two subsections.

Free-bound emissivity

Free-bound emission arises from photons emitted when a free electron is captured by an ion. This process, also known as radiative recombination, is the reverse of the photoionization process. This is described by the following reaction:

$${\rm H}^+ + 2e^- \leftrightarrow {\rm H}(n) + e^-. \tag{2.6}$$

In this description the detail balance law (Kirchoff's law) can be used to relate the emissivity to the cross-section for photoionization:

$$\begin{aligned} j_{{\rm H},\nu,{\rm fb}} &= \kappa_{\nu,fb} B_\nu(T) \\ &= [n_b]_{\rm LTE} \cdot \sigma_{b,pi}(\nu) \left[1 - e^{-h\nu/k_B T}\right] B_\nu(T) \end{aligned} \tag{2.7}$$

where $\kappa_{\nu,fb}$ is the absorption coefficient, $[n_b]_{\rm LTE}$ is the number density of atoms in bound state with the assumption of LTE, and $\sigma_{b,pi}(\nu)$ the cross-section of photoionization. The number density of atoms in bound state, i.e. the population of the n-th level, can be derived considering the photoionization reaction (Eq. 2.6) and the law of mass action, and is:

$$[n_b]_{\mathrm{LTE}} = \frac{h^3}{(2\pi k_B T)^{3/2}} \left(\frac{m_{\mathrm{H}}}{m_p m_e}\right)^{3/2} \frac{g[\mathrm{H}(n)]}{g(e^-)g(\mathrm{H}^+)} e^{h\nu_0/n^2 k_B T} n_e n(\mathrm{H}^+), \tag{2.8}$$

where $\nu_0 = 3.28795 \cdot 10^{15}$ Hz is the ionization frequency for hydrogen. Given that electrons and protons have spin 1/2, the value of $g(e^-)$ and $g(\mathrm{H}^+)$ is in both cases 2, while for the hydrogen atom $g[\mathrm{H}(n)] = 4n^2$. I thus derive that:

$$[n_b]_{\mathrm{LTE}} = \frac{h^3}{(2\pi m_e k_B)^{3/2}} n^2 T^{-3/2} e^{h\nu_0/n^2 k_B T} n_e n_i. \tag{2.9}$$

According to Draine (2011), the cross-section of photoionization can be approximated reasonably as:

$$\sigma_{b,pi}(\nu) \sim \sigma_0 \left(\frac{h\nu}{Z_i^2 I_{\mathrm{H}}}\right)^{-3}, \tag{2.10}$$

where I_{H} is the ionization potential for hydrogen, and σ_0 is the cross section at threshold, given by:

$$\sigma_0 \equiv \frac{2^9 \pi}{3e^4} Z_i^{-2} \alpha \pi a_0^2 = 6.304 \times 10^{-18} Z_i^{-2}\ \mathrm{cm}^2. \tag{2.11}$$

Inserting these expressions in Eq. (2.7) I obtain:

$$\begin{aligned} j_{\mathrm{H},\nu,\mathrm{fb}} &= \frac{8}{3}\left(\frac{2\pi}{3}\right)^{1/2} \frac{Z_i^2 e^6}{m_e^{3/2} c^3 (k_B T)^{1/2}} n_e n_i e^{-h\nu/k_B T} \cdot g_{fb} \\ &= 5.44 \cdot 10^{-39} \frac{Z_i^2}{T^{1/2}} n_e n_i e^{-h\nu/k_B T} g_{fb}\ \mathrm{erg\ cm^{-3}\ s^{-1}\ Hz^{-1}\ sr^{-1}}, \end{aligned} \tag{2.12}$$

where g_{fb} is the free-bound Gaund factor, whose expression is:

$$g_{fb}(\nu, T) = \frac{2h\nu_0 Z_i^2}{k_B T} \sum_{n=m}^{\infty} n^{-3} e^{h\nu_0/n^2 k_B T} g_n(\nu), \tag{2.13}$$

with m being the quantum number of the lower final state of the free-bound transition, whose expression is:

$$m = integer \left(\frac{\nu_0 Z_i^2}{\nu}\right)^{1/2} + 1. \tag{2.14}$$

According to Seaton (1960), $g_n(\nu)$ can be approximated as:

$$\begin{aligned} g_n(\nu) = 1 + 0.1728 \cdot &\left[\left(\frac{\nu}{\nu_0 Z_i^2}\right)^{1/3} - \frac{2}{n^2}\left(\frac{\nu}{\nu_0 Z_i^2}\right)^{-2/3}\right] + \\ -0.0496 \cdot &\left[\left(\frac{\nu}{\nu_0 Z_i^2}\right)^{2/3} - \frac{2}{3n^2}\left(\frac{\nu}{\nu_0 Z_i^2}\right)^{-1/3} + \frac{2}{3n^4}\left(\frac{\nu}{\nu_0 Z_i^2}\right)^{-4/3}\right]. \end{aligned} \tag{2.15}$$

Free-free emissivity

When electrons interact with an ion without being captured they emit free-free radiation, also known as bremsstrahlung radiation. In our system there are free electrons whose velocity distribution is described with a Maxwell-Boltzman distribution. Within this assumption the free-free emission, according to classical theory, is nearly independent of frequency except for the exponential cutoff resulting from the Maxwellian distribution of electron velocities. Following, e.g., Spitzer (1978), the emissivity for this free-free transition is:

$$\begin{aligned} j_{\mathrm{H},\nu,\mathrm{ff}} &= \frac{8}{3}\left(\frac{2\pi}{3}\right)^{1/2} \frac{Z_i^2 e^6}{m_e^{3/2} c^3 (k_B T)^{1/2}} n_e n_i e^{-h\nu/k_B T} \cdot g_{ff} \\ &= 5.44 \cdot 10^{-39} \frac{Z_i^2}{T^{1/2}} n_e n_i e^{-h\nu/k_B T} g_{ff} \text{ erg cm}^{-3}\text{ s}^{-1}\text{ Hz}^{-1}\text{ sr}^{-1}, \end{aligned} \tag{2.16}$$

where $Z_i e$ is the charge of the protons interacting with the electrons and n_i their density; g_{ff} is the Gaunt factor for free-free transition. It is interesting to note that also in this case, as in the free-bound emission, there is a dependence of the emissivity with $n_e \cdot n_i$, which is typical of binary interactions. According to Seaton (1960), g_{ff} can be expressed with the following asymptotic expansion:

$$\begin{aligned} g_{ff}(\nu, T) = 1 + 0.1728 \cdot \left(\frac{\nu}{\nu_0 Z_i^2}\right)^{1/3} \left(1 + \frac{2 k_B T}{h\nu}\right) + \\ -0.0496 \cdot \left(\frac{\nu}{\nu_0 Z_i^2}\right)^{2/3} \left[1 + \frac{2}{3}\frac{k_B T}{h\nu} + \frac{4}{3}\left(\frac{k_B T}{h\nu}\right)^2\right]. \end{aligned} \tag{2.17}$$

Total emission

Given that the modeled slab is composed solely of hydrogen, I assume Z_i=1 and $n_i = n_p$ in the previous formulas. Moreover, I assume that the medium is neutral, so $n_e = n_p$. The total emissivity of hydrogen is thus obtained adding together Eq. (2.12) and Eq. (2.16). The result is the following:

$$j_{\mathrm{H},\nu} = 5.44 \cdot 10^{-39} e^{-h\nu/k_B T} T^{-1/2} [g_{ff}(\nu, T) + g_{fb}(\nu, T)] n_e^2 \text{ erg cm}^{-3}\text{ s}^{-1}\text{ Hz}^{-1}\text{ sr}^{-1} \tag{2.18}$$

From the total emissivity of Hydrogen I then derive the intensity:

$$I_{\mathrm{H},\nu} = j_{\mathrm{H},\nu} L_{\mathrm{slab}} \beta_{\mathrm{H},\nu}, \tag{2.19}$$

where $\beta_{\mathrm{H},\nu}$ is the escape probability at the frequency ν:

$$\beta_{\mathrm{H},\nu} = \frac{1 - e^{-\tau_{\mathrm{H},\nu}}}{\tau_{\mathrm{H},\nu}}, \tag{2.20}$$

and $\tau_{\mathrm{H},\nu}$ is the optical depth. This is obtained from the following equation:

$$\tau_{\mathrm{H},\nu} = \kappa_{\mathrm{H},\nu} L_{\mathrm{slab}} = \sum_{n=m}^{\infty} \sigma_{n,pi}(\nu) n_b L_{\mathrm{slab}}, \tag{2.21}$$

with m calculated with the expression of Eq. (2.14) and $\sigma_{n,pi}(\nu)$ being the photoionization cross section from level n. Under the assumption of LTE I can compute κ_ν using detail balance as:

$$\kappa_{\mathrm{H},\nu} = j_{\mathrm{H},\nu}/B_\nu(T), \tag{2.22}$$

and thus the optical depth at any frequency can be calculated as:

$$\tau_{\mathrm{H},\nu} = j_{\mathrm{H},\nu} L_{\mathrm{slab}}/B_\nu(T). \tag{2.23}$$

2.2.2 The H$^-$ emission

The negative hydrogen ion (H$^-$) is a major source of continuous absorption in dense regions, such as stellar atmospheres. The main reactions where H$^-$ is involved are the photo-detachment mechanism:

$$h\nu + \mathrm{H}^- \rightarrow \mathrm{H} + e^-, \tag{2.24}$$

which is a bound-free transition that contributes up to the ionization threshold λ_0 = 1.6419 μm, and the free-free mechanism:

$$h\nu + e^- + \mathrm{H} \rightarrow \mathrm{H} + e^-. \tag{2.25}$$

Absorption coefficients for H$^-$

The calculation of the absorption coefficients for these transitions has been presented in John (1988), and the total absorption coefficient ($\kappa_{\mathrm{H}^-,\lambda,\mathrm{tot}}$) per unit electron pressure per hydrogen atom is the sum of the absorption coefficients of the two transitions. In particular, the coefficient of absorption from H$^-$ photo-detachment is:

$$\kappa_{\mathrm{H}^-,\lambda,\mathrm{fb}}(\lambda, T) = 0.750\ T^{-5/2} e^{\alpha/\lambda_0 T}(1 - e^{-\alpha/\lambda T})\sigma_\lambda\ \mathrm{cm}^4\ \mathrm{dyne}^{-1}, \tag{2.26}$$

where $\lambda_0 = 1.6419$ μm is the photo-detachment threshold wavelength for H$^-$ and $\alpha = 1.439 \cdot 10^8$ Å·K, wavelengths are assumed in μm, temperatures in K, and σ_λ is the photo-detachment cross-section, whose expression is:

$$\sigma_\lambda = 10^{-18}\lambda^3 \left(\frac{1}{\lambda} - \frac{1}{\lambda_0}\right)^{3/2} f(\lambda)\ \mathrm{cm}^2, \tag{2.27}$$

valid for $\lambda < \lambda_0$. In the latter $f(\lambda)$ is a function with the following form:

$$f(\lambda) = \sum_{n=1}^{6} C_n \left(\frac{1}{\lambda} - \frac{1}{\lambda_0}\right)^{(n-1)/2}\ \mathrm{cm}^2. \tag{2.28}$$

The parameters C_n are reported in Table 2.1 and are valid in the range 0.125$\leq \lambda(\mu\mathrm{m}) \leq$ 1.6419 for any temperature.

Table 2.1: Parameters for generating photo-detachment cross sections for H$^-$

n	C_n
1	152.519
2	49.534
3	−118.858
4	92.536
5	−34.194
6	4.982

Notes. From John (1988).

Table 2.2: Parameters for generating free-free absorption coefficient for H$^-$ in the wavelength range 0.182 μm $< \lambda <$ 0.3645 μm

n	A_n	B_n	C_n	D_n	E_n	F_n
1	518.1021	−734.8667	1021.1775	−479.0721	93.1373	−6.4285
2	473.2636	1443.4137	−1977.3395	922.3575	−178.9275	12.3600
3	−482.2089	−737.1616	1096.8827	−521.1341	101.7963	−7.0571
4	115.5291	169.6374	−245.6490	114.2430	−21.9972	1.5097
5	0.0000	0.0000	0.0000	0.0000	0.0000	0.0000
6	0.0000	0.0000	0.0000	0.0000	0.0000	0.0000

Notes. From John (1988).

The free-free absorption coefficient for H$^-$, instead, is fitted by the following formula:

$$\kappa_{\mathrm{H}^-,\lambda,\mathrm{ff}}(\lambda, T) = 10^{-29} \sum_{n=1}^{6} \left(\frac{5040}{T}\right)^{(n+1)/2} \times \\ \times \left\{\lambda^2 A_n + B_n + C_n/\lambda + D_n/\lambda^2 + E_n/\lambda^3 + F_n/\lambda^4\right\} \ \mathrm{cm}^4\ \mathrm{dyne}^{-1}. \tag{2.29}$$

Also in this case wavelengths are assumed in μm and temperatures in K. The coefficients of this expression are reported in Table 2.2 for the wavelength range 0.182 μm $< \lambda <$ 0.3645 μm and in Table 2.3 for wavelengths greater than 0.3645 μm, and are valid in the range 0.5$\leq$ $(5040/T[\mathrm{K}])$ $\leq$3.6, which is the range in which I calculate the models.

Table 2.3: Parameters for generating free-free absorption coefficient for H$^-$ for $\lambda \geq$ 0.3645 μm

n	A_n	B_n	C_n	D_n	E_n	F_n
1	0.0000	0.0000	0.0000	0.0000	0.0000	0.0000
2	2483.3460	285.8270	−2054.2910	2827.7760	−1341.5370	208.9520
3	−3449.8890	−1158.3820	8746.5230	−11485.6320	5303.6090	−812.9390
4	2200.0400	2427.7190	−13651.1050	16755.5240	−7510.4940	1132.7380
5	−696.2710	−1841.4000	8624.9700	−10051.5300	4400.0670	−655.0200
6	88.2830	444.5170	−1863.8640	2095.2880	−901.7880	132.9850

Notes. From John (1988).

The total absorption coefficient for H$^-$ is then obtained in the following way:

$$\kappa_{\mathrm{H}^-,\lambda,\mathrm{tot}} = [\kappa_{\mathrm{H}^-,\lambda,\mathrm{bf}} + \kappa_{\mathrm{H}^-,\lambda,\mathrm{ff}}] \cdot n_e n_\mathrm{H} k_B T \ \mathrm{cm}^{-1}, \tag{2.30}$$

where the factor $n_e n_\mathrm{H} k_B T$ takes into account the units of the calculations above. The value of n_H is derived in the same way as $[n_b]_\mathrm{LTE}$ (see Eq. (2.9)), while n_e and $T = T_\mathrm{slab}$ are input parameters.

Total emission of H$^-$

The emissivity of the H$^-$ emission is derived using the law of detail balance:

$$j_{\mathrm{H}^-,\nu} = \kappa_{\mathrm{H}^-,\nu,\mathrm{tot}} B_\nu(T). \tag{2.31}$$

To derive the intensity of the emission, whose expression is:

$$I_{\mathrm{H}^-,\nu} = j_{\mathrm{H}^-,\nu} L_\mathrm{slab} \beta_{\mathrm{H}^-,\nu}, \tag{2.32}$$

I need to calculate the optical depth as:

$$\tau_{\mathrm{H}^-,\nu} = \kappa_{\mathrm{H}^-,\nu,\mathrm{tot}} L_\mathrm{slab}, \tag{2.33}$$

and I insert this expression in Eq. (2.20) replacing $\tau_{\mathrm{H},\nu}$ to derive $\beta_{\mathrm{H}^-,\nu}$.

2.2.3 The total emission of the slab model

The total emission from the slab can be derived in LTE by computing the total optical depth ($\tau_{\mathrm{slab},\nu}$) as the sum of the optical depths of the two components, H and H$^-$, simply adding the results of Eq. (2.23) and (2.33) to derive $\tau_{\mathrm{slab},\nu} = \tau_{\mathrm{H},\nu} + \tau_{\mathrm{H}^-,\nu}$. Then, the total intensity of the slab emission is obtained as:

$$I_{\mathrm{slab},\nu} = \tau_{\mathrm{slab},\nu} B_\nu(T_\mathrm{slab}) \beta_{\mathrm{slab},\nu}, \tag{2.34}$$

where $\beta_{\mathrm{slab},\nu}$ is obtained using Eq. (2.20) and the total optical depth of the slab $\tau_{\mathrm{slab},\nu}$.

Finally, the flux emitted by the slab is obtained using Eq. (2.5), where the factor $Area_\mathrm{slab}$ is derived when fitting the spectrum of an object. I show in Fig. 2.2 an example of the output spectrum of the model.

2.3 Dependence of selected features on the input parameters

In the emission spectrum of the slab model (see Fig. 2.2 for an example) there are several features that are of great interest for our analysis. Those are, in particular, the value of the Balmer jump, the ratio of the emission in the Balmer continuum and Paschen continuum

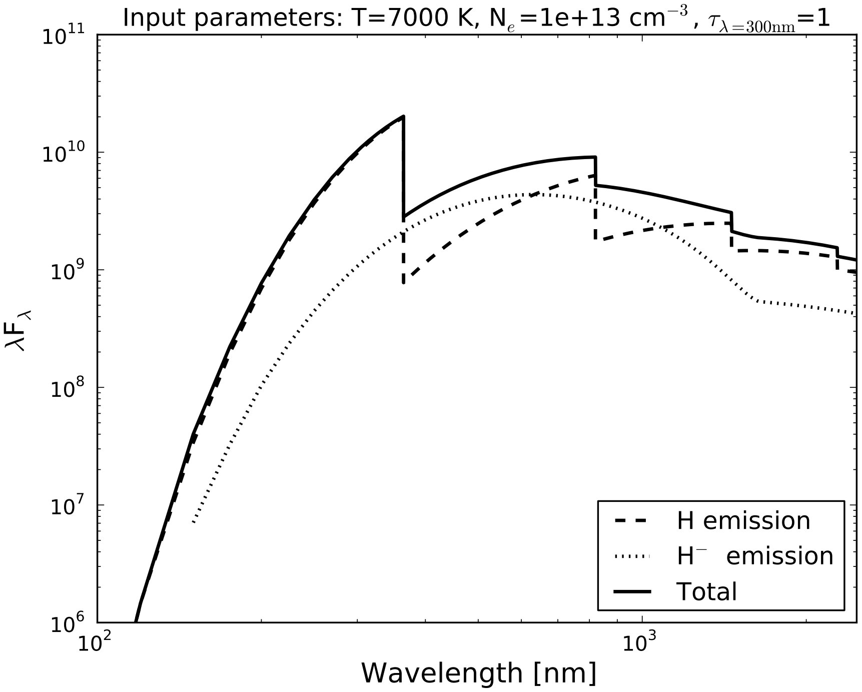

Figure 2.2: Example of the emission of a slab model with input parameters T_{slab}= 7000 K, $n_e = 10^{13}$ cm^{-3}, and $\tau_{\lambda=300\mathrm{nm}}$ = 1. The total emission is represented by the solid line, while the dashed line is the emission from the H component and the dotted line the one from the H$^-$. The H$^-$ emission is modeled only from $\lambda >$ 125 nm as explained in Sect. 2.2.2.

regions, and the slopes of the Balmer and Paschen continua. Here I discuss the dependence of these features on the input parameters. I will also consider the separate contribution of H and H$^-$ emission to these features. In this context it is interesting to understand what are the ratio of these two components as a function of the model parameters, and I will start by discussing this aspect.

2.3.1 Contribution of H and H$^-$ to the total emission

In Fig. 2.3 the ratio of the H to H$^-$ emission is shown as a function of the three input parameters of the slab model. The four panels show the value of this ratio vs T_{slab} for different densities, where each panel refers to a value of the optical depth of the H slab at λ=300 nm. From these plots it is clear that the contribution of H is dominant in most of the parameter space described by our model. The H$^-$ emission has the largest contribution to the total slab emission at any density when $T_{\mathrm{slab}} \lesssim$ 6000 K, and for higher slab temperatures for increasing densities. At $n_e \sim 10^{16}$ cm^{-3} H$^-$ is the dominant source of emission almost for all value of T_{slab}. The relative contribution of H$^-$ with respect to the one of H decreases with increasing optical depth of the hydrogen component. These findings are compatible with what Valenti et al. (1993) reported, as they state that the contribution of H$^-$ in their

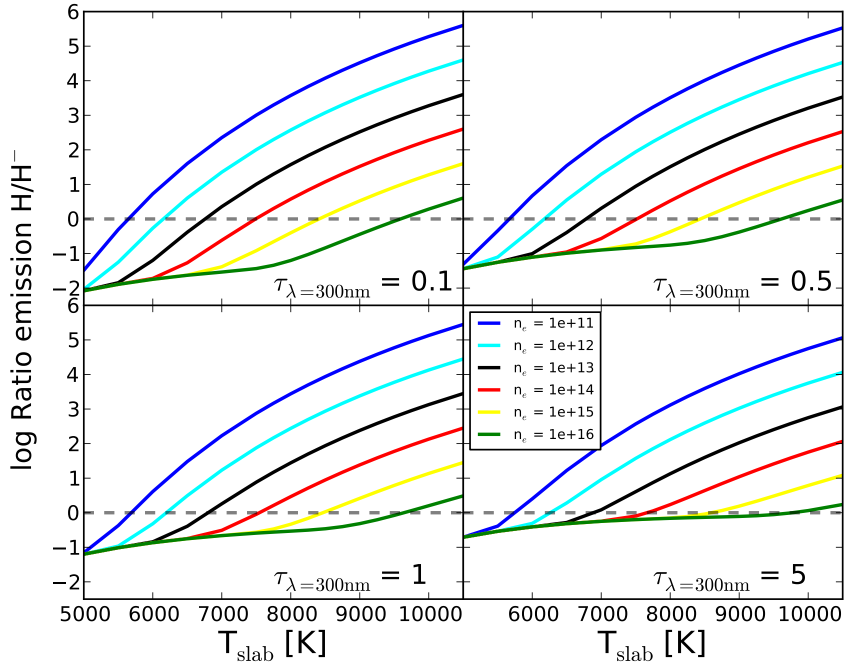

Figure 2.3: Ratio of the emission due to H to that due to H^- in the slab model as a function of the input parameters. The four panels represent models with increasing input hydrogen optical depth at λ=300 nm. In each panel, where the logarithmic value of the ratio of the H over H^- emission is showed vs the slab temperature, the colored lines correspond to increasing electron densities as reported in the legend.

slab models is basically negligible at densities $\lesssim 10^{13}\mathrm{cm}^{-3}$, while this becomes a dominant source of emission at densities $\gtrsim 10^{15}\mathrm{cm}^{-3}$.

2.3.2 Balmer jump

I define the value of the Balmer jump as the ratio between the flux at $\lambda \sim$360 nm over the flux at $\lambda \sim$ 400 nm. This is the same definition that I will use in the next chapters, such as in Chapter 4. The logarithm of this value is shown as a function of the various input slab parameters in Fig. 2.4. In those plots we see that in a pure H slab model (*dashed lines* in the plots) the value of the Balmer jump would decrease monotonically with T_{slab}, would be independent on the electron density, and would decrease with increasing optical depth. The reason for the monotonically decrease of the jump with T_{slab} is that the population of the second level in the hydrogen atom decreases more slowly than in the higher levels (e.g., Valenti et al., 1993). On the other hand, the H^- emission does not have any Balmer jump, therefore its contribution (*dotted lines* in Fig. 2.4) is almost constant and independent on the density and the optical depth. These effects, together with the relative contribution of H and H^- to the total emission discussed above, result in the fact that the Balmer jump of the output slab, when considering both components together (*solid lines* in Fig. 2.4), follows

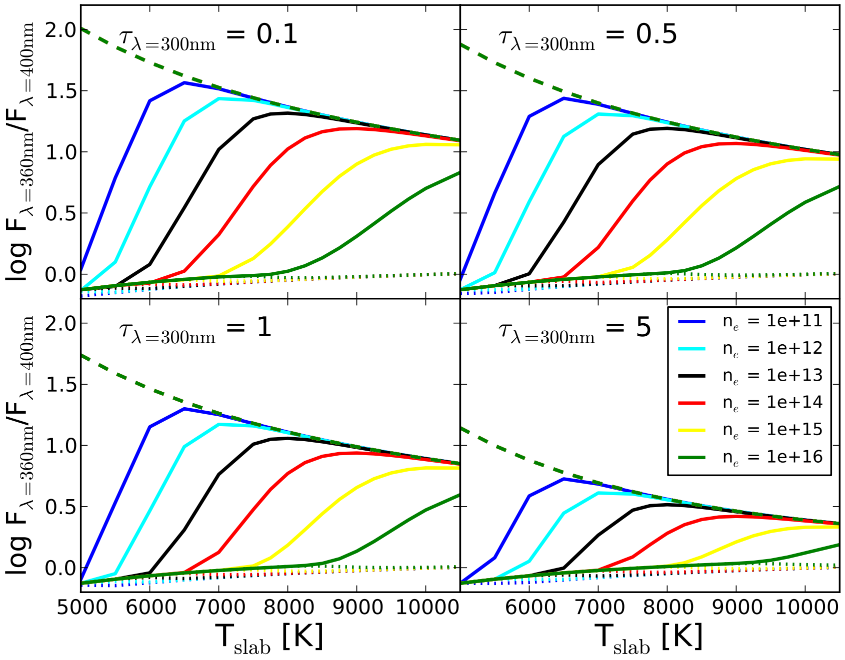

Figure 2.4: Balmer jump obtained with the slab model as a function of the input parameters. The four panels represent models with increasing input hydrogen optical depth at λ=300 nm. In each panel, where the value of the Balmer jump is showed vs the slab temperature, the colored lines correspond to increasing electron densities. The solid lines represent the value obtained from the total emission, while the dashed line is obtained from the hydrogen emission alone, and the dotted lines from the H^- emission.

the behavior of the pure H emission at low densities and higher temperatures, while it is different in regions of the parameter space where the H^- contribution is stronger. The fact that the Balmer jump of the slab is smaller than the pure H one due to the H^- emission is in agreement with the results reported by Herczeg & Hillenbrand (2008).

2.3.3 Balmer and Paschen continua

The ratio of the contribution of the emission from the Balmer continuum with respect to that arising from the Paschen continuum is shown in Fig. 2.5. It is clear that the emission is dominated by the Balmer continuum region for low optical depth, while the two emissions become comparable at higher optical depth. The shape of the H^- contribution, which peaks in the Paschen continuum region, and its relative importance to the H emission (see above) results in a stronger Balmer to Paschen continuum ratio with increasing T_{slab} and at lower densities.

The Balmer continuum slope is strictly connected with deriving the contribution to the total excess emission due to accretion at the wavelengths not covered by ground-based UV spectra, i.e. at $\lambda \lesssim 310$ nm. A large fraction ($\sim$ 30-40%) of the excess emission due

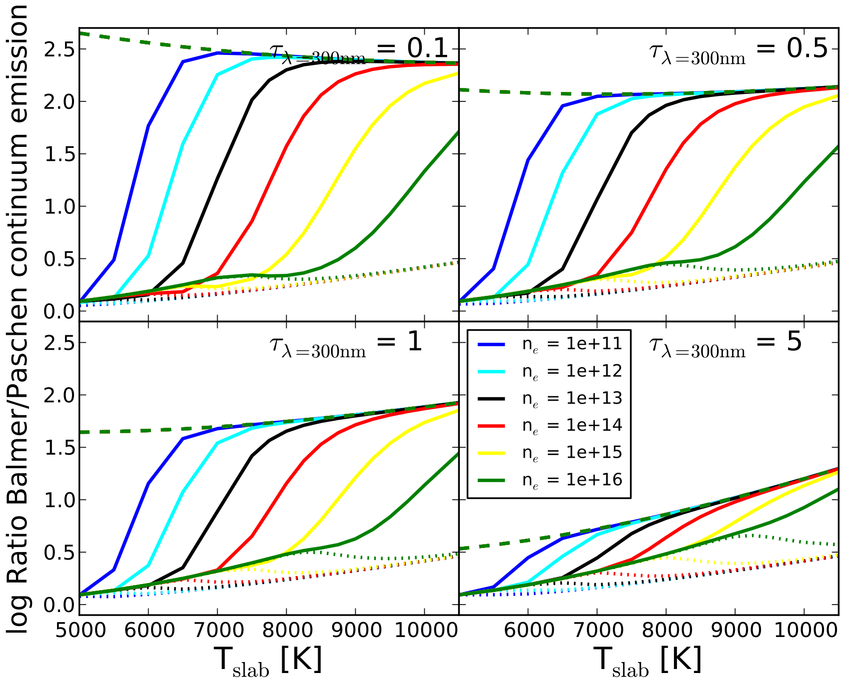

Figure 2.5: Ratio of the emission from the Balmer and Paschen continua obtained with the slab model as a function of the input parameters. Symbols as in Fig. 2.4

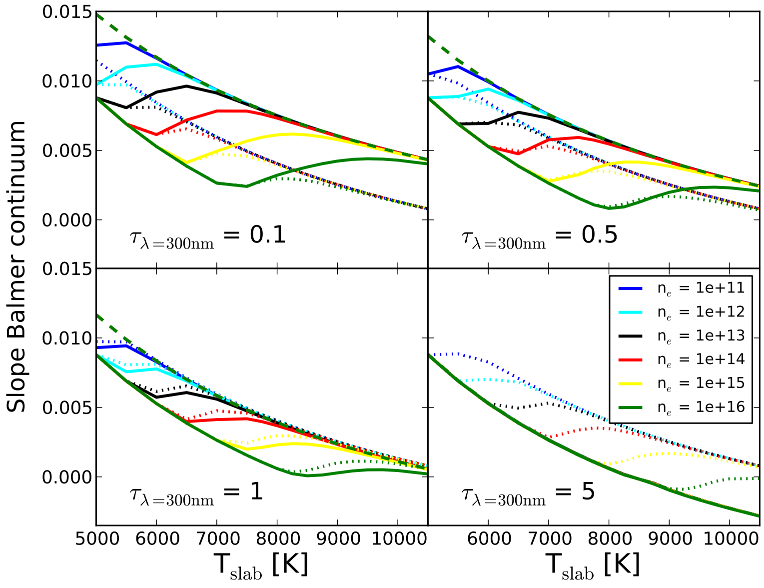

Figure 2.6: Balmer continuum slope obtained with the slab model as a function of the input parameters. Symbols as in Fig. 2.4

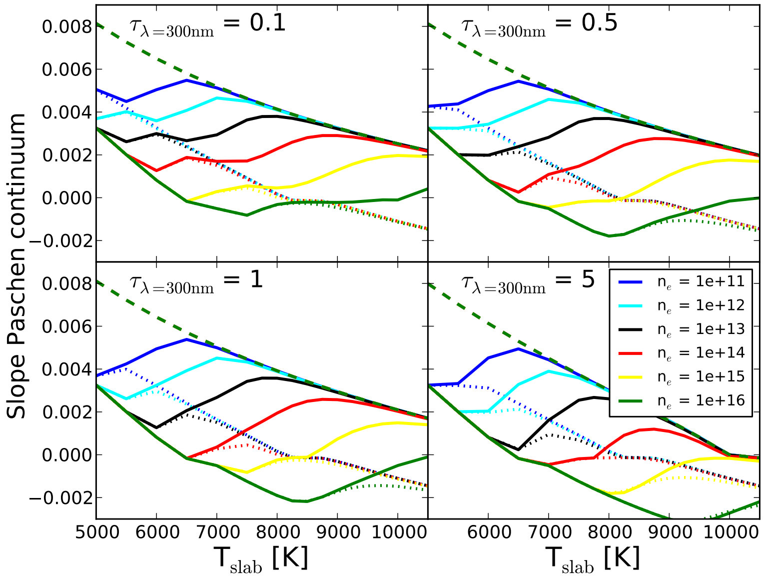

Figure 2.7: Paschen continuum slope obtained with the slab model as a function of the input parameters. Symbols as in Fig. 2.4

to accretion arises shortward the Balmer jump, and the exact amount of this emission is related with this slope, which is defined here as the slope of the spectrum between ∼330 nm and ∼ 360 nm. In Fig. 2.6 this quantity is shown as a function of the various input parameters. Similarly to the Balmer jump, also the Balmer continuum slope of the pure H emission is independent on the density and becomes less steep, i.e. bluer, with increasing temperature and optical depth, similarly to what found by Herczeg & Hillenbrand (2008). The contribution of H^- makes the slope of this continuum bluer in all cases, being more important in the regions of the parameters space discussed above.

Similar trends are found also for the Paschen continuum slope, defined as the slope between ∼400 nm and ∼ 477 nm, which is shown in Fig. 2.7, as also Herczeg & Hillenbrand (2008) noted. In this case the slope is important for the effects of veiling of absorption features in the redder part of the spectrum. It is important to note that the slope of this continuum is close to zero, which is what is assumed in various studies to model the veiling in the red part of the optical spectrum (e.g. Ingleby et al., 2013; Herczeg & Hillenbrand, 2014). Nevertheless, this slope is not zero in many part of the parameter space, and this will be shown to be a good model for the veiling of the photospheric features across the spectrum (see, e.g., Chapter 4). In comparison to the Balmer continuum slope the Paschen slope depends slightly on the optical depth of H at λ=300 nm.

3

Photospheric templates of young stellar objects and the impact of chromospheric emission on accretion rate estimates

Published as Manara, Testi, Rigliaco, Alcalà, Natta, Stelzer et al., A&A, 2013, 551, 107;
``X-Shooter spectroscopy of young stellar objects:
II. Impact of chromospheric emission on accretion rate estimates''[*]

Abstract

Context: The lack of knowledge of photospheric parameters and the level of chromospheric activity in young low-mass pre-main sequence stars introduces uncertainties when measuring mass accretion rates in accreting (Class II) young stellar objects. A detailed investigation of the effect of chromospheric emission on the estimates of mass accretion rate in young low-mass stars is still missing. This can be undertaken using samples of young diskless (Class III) K and M-type stars.
Aims: Our goal is to measure the chromospheric activity of Class III pre main sequence stars to determine its effect on the estimates of the accretion luminosity ($L_{\rm acc}$) and mass accretion rate ($\dot{M}_{\rm acc}$) in young stellar objects with disks.
Methods: Using VLT/X-Shooter spectra, we analyzed a sample of 24 nonaccreting young stellar objects of spectral type between K5 and M9.5. We identified the main emission lines normally used as tracers of accretion in Class II objects, and we determined their fluxes in order to estimate the contribution of the chromospheric activity to the line luminosity.
Results: We have used the relationships between line luminosity and accretion luminosity derived in the literature for Class II objects to evaluate the impact of chromospheric activity on the accretion rate measurements. We find that the typical chromospheric activity would bias the derived accretion luminosity by $L_{\rm acc,noise}< 10^{-3}L_\odot$, with a strong dependence on the T$_{\rm eff}$ of the objects. The noise on $\dot{M}_{\rm acc}$ depends on stellar mass and age, and the typical

---

[*] This chapter depends on collaborative work which I had the opportunity to take the lead of. In particular I was responsible for part of the data reduction, in particular for the flux calibration and the telluric correction of the spectra, the interpretation, and the discussion. Finally, I was responsible of the composition of the manuscript.

values of log($\dot{M}_{\rm acc,noise}$) range between ~ -9.2 to $-11.6 M_\odot$/yr.
Conclusions: Values of $L_{\rm acc} \lesssim 10^{-3} L_\odot$ obtained in accreting low-mass pre main sequence stars through line luminosity should be treated with caution because the line emission may be dominated by the contribution of chromospheric activity.

3.1 Introduction

Circumstellar disks are formed as a natural consequence of angular momentum conservation during the gravitational collapse of cloud cores (e.g. Shu et al., 1987). In the early phases of star formation, the disk allows for the dissipation of angular momentum channeling the accretion of material from the infalling envelope onto the central young stellar object (YSO). At later stages, when the envelope is dissipated, planetary systems form in the disk, while the star-disk interaction continues through the inner disk and the stellar magnetosphere. This phenomenon constrains the final stellar mass build-up (e.g. Hartmann et al., 1998), and its typical timescales are connected with the timescales on which disks dissipate and planet formation occurs (e.g. Hernández et al., 2007; Fedele et al., 2010; Williams & Cieza, 2011).

Accretion can be observed using typical signatures in the spectra of YSOs, such as the continuum excess in the blue part of the visible spectrum (e.g. Gullbring et al., 1998) and the prominent optical and infrared emission lines (e.g. Muzerolle et al., 1998a; Natta et al., 2004; Herczeg & Hillenbrand, 2008; Rigliaco et al., 2012). The measurements used to determine the bolometric accretion luminosity ($L_{\rm acc}$) are either direct or indirect. Direct measurements are obtained by measuring the emission in excess of the photospheric one in the Balmer and Paschen continua and adopting a model to correct for the emission at the wavelengths not covered by the observations, which originates mostly below the U-band threshold (e.g. Valenti et al., 1993; Gullbring et al., 1998; Calvet & Gullbring, 1998; Herczeg & Hillenbrand, 2008; Rigliaco et al., 2012) or by line profile modeling (e.g. Muzerolle et al., 1998a). Indirect measurements are obtained using empirical correlations between emission line luminosity ($L_{\rm line}$) and $L_{\rm acc}$ (e.g. Muzerolle et al., 1998b; Natta et al., 2004, 2006; Mohanty et al., 2005; Rigliaco et al., 2011a).

Measurements of mass accretion rate ($\dot{M}_{\rm acc}$) are subjected to many uncertainties, because this quantity depends on $L_{\rm acc}$ and on the mass-to-radius ($M_\star/R_\star$) ratio. This ratio is normally determined from the position of the object on the HR diagram and a set of evolutionary models. Uncertainties on spectral type (SpT) of the objects affect the determination of effective temperature ($T_{\rm eff}$), while those on the extinction (A_V) and the distance mainly affect the estimate of stellar luminosity ($L_\star$). It is not trivial to determine those parameters in accreting stars because of accretion shocks on the stellar surface producing veiling in the photospheric lines (e.g. Calvet & Gullbring, 1998) and modifying the photometric colors (e.g. Da Rio et al., 2010a). Moreover, the derivation of $L_{\rm line}$, from which $L_{\rm acc}$ is determined, is affected by another stellar property, namely the chromospheric activity of the YSOs (Houdebine et al., 1996; Franchini et al., 1998). Chromospheric line emission is usually smaller than the accretion-powered emission, but it can become important when accretion decreases at later evolutionary stages (Ingleby et al., 2011) and in lower mass stars, where accretion rates are lower (Rigliaco et al., 2012). Therefore, this is an important source of uncertainty that has not been investigated in detail so far.

Part of the INAF consortium's Guaranteed Time Observations (GTO) of X-Shooter, a broad-band, medium-resolution, high-sensitivity spectrograph mounted on the ESO/VLT, has been allocated for star formation studies, in particular to investigate accretion, outflows, and chromospheric emission in low-mass Class II young stellar and substellar objects (Alcalá et al., 2011). The targets observed during the GTO were chosen in nearby (d $<$ 500 pc) star forming regions with low extinction and with many very low-mass (VLM) YSO ($M_\star < 0.2$ $M_\odot$). Generally, those YSOs for which measurements in many photometric bands were available, both in the IR (e.g. Hernández et al., 2007; Merín et al., 2008) and in the visible part of the spectrum (e.g. Merín et al., 2008; Rigliaco et al., 2011a), were selected. To derive $L_{\rm acc}$ of a given Class II YSO, a Class III template of the same SpT as the Class II is needed. Therefore, during this GTO survey 24 Class III targets in the range K5-M9.5 were observed, providing the first broad-band grid of template spectra for low-mass stars and brown dwarfs (BDs). Since these spectra have a very wide wavelength range ($\sim$350 - 2500 nm) covering part of the UV spectrum (UVB), the whole visible (VIS), and the near infrared (NIR), this sample allows us to determine the stellar parameters of the targets, derive the chromospheric emission line fluxes and luminosities, hence determine the implications of chromospheric emission on the indirect accretion estimates in Class II objects.

The paper is structured as follows. In Sect. 3.2 we discuss the sample selection, the observation strategy, and the data reduction procedure. In Sect. 3.3 we describe how SpTs of our targets have been determined, while in Sect. 3.4 we derive their main stellar parameters. In Sect. 3.5 we identify the main lines present in the spectra and derive their intensities. In Sect. 3.6 we discuss the implications of the line luminosity found for studies of $\dot{M}_{\rm acc}$ in Class II YSOs. Finally, in Sect. 3.7 we summarize our conclusions.

3.2 Sample, observations, and data reduction

Among the objects observed in the GTO survey, we selected only those that have been classified as Class III objects using *Spitzer* photometric data. The sample comprises Class III YSOs in the σ-Orionis, Lupus III, and TW Hya associations. In the end, the number of targets is 24: 13 objects are members of the TW Hya association, 6 of the Lupus III cloud, and 5 of the σ-Orionis region. Their SpTs range between K5 and M9.5 (see Sect. 3.3). Three BDs, namely Par-Lup3-1, TWA26, and TWA29, are included in our sample, with SpT M6.5, M9, and M9.5, respectively. Data available from the literature for these objects are reported in Table 3.1. Six YSOs in our sample are components of three known wide visual binary systems. In all cases we were able to resolve them, given that their separations are always larger than 6$''$.

All the observations were made in the slit-nodding mode, in order to achieve a good sky subtraction. Different exposure times and slit dimensions were used for different targets to have enough S/N and to avoid saturation. The readout mode used in all the observations was ``100,1x1, hg", while the resolution of our spectra is R = 9100, 5100, and 3300 in the UVB arm for slits 0.5″, 1.0″, and 1.6″, respectively; R = 17400, 8800, and 5400 in the VIS arm for slits 0.4″, 0.9″, and 1.5″, respectively; R = 11300, 5600, and 3500 in the NIR arm for slits 0.4″, 0.9″, and 1.5″, respectively. We report in Table 3.2 the details of all observations for this work.

The data were reduced using two versions of the X-Shooter pipeline (Modigliani et al., 2010), run through the *EsoRex* tool, according to the period in which the data were acquired. Version 1.0.0 was used for the data of December 2009 and May 2010, while version 1.3.7 was used for data gathered in January 2011, April 2011, and April 2012. The two versions led to results that are very similar. The reduction was done independently for each spectrograph arm. This also takes the flexure compensation and the instrumental profile into account. We used the pipeline recipe *xsh_scired_slit_nod*, which includes bias and flat-field correction, wavelength calibration, order-tracing and merging, and flux calibration. Regarding the last point, by comparing the response functions of different flux standards observed during the same night, we estimated an intrinsic error on the flux calibration of less than 5%. Given that some observations were done with poor weather conditions (seeing ∼3.5″) or with narrow slits, we then checked the flux calibration of each object using the available photometric data, usually in the U, B, V, R, I, J, H, K bands, as reported in Table 3.1. We verified that all the spectra match the photometric spectral energy distribution (SED) well and adjusted the flux-calibrated spectra to match the photometric flux. Binaries were reduced in stare mode. Telluric removal was done using standard telluric spectra obtained in similar conditions of airmass and instrumental set-up of the target observations. This correction was accomplished with the IRAF[1] task *telluric*, using spectra of telluric standards from which photospheric lines were removed using a multigaussian fitting. The correction is very good at all wavelengths, with only two regions in the NIR arm ($\lambda\lambda$ 1330-1550 nm, $\lambda\lambda$ 1780-2080 nm) where the telluric absorption bands saturate. More detail about the reduction will be reported in Alcalá et al. (2014).

---

[1] IRAF is distributed by National Optical Astronomy Observatories, which is operated by the Association of Universities for Research in Astronomy, Inc., under cooperative agreement with the National Science Foundation.

Table 3.1: Known parameters from the literature

Name	Other names	RA (J2000)	DEC (J2000)	Region	D	SpT	U	B	V	R	I	J	H	K	Ref
TWA9A	CD −36 7429A	11 48 24.22	−37 28 49.15	TW Hya	68	K5	...	12.52	11.26	...	6.94	8.68	8.03	7.85	1,2,3
SO879	...	05 39 05.42	−02 32 30.34	σ-Ori	360	K5	17.09	14.70	14.44	13.53	12.83	11.55	10.86	10.67	3,4,5,6,7,8,9
TWA6	Tyc 7183 1477 1	10 18 28.70	−31 50 02.85	TW Hya	51	M0	...	13.39	11.81	...	9.94	8.87	8.18	8.04	1,3,10
TWA25	Tyc 7760 283 1	12 15 30.71	−39 48 42.56	TW Hya	54	M0	...	12.85	11.44	...	9.50	8.17	7.50	7.31	1,3,11,12
TWA14	UCAC2 12427553	11 13 26.22	−45 23 42.74	TW Hya	96	M0.5	...	...	13.80	...	10.95	9.15	8.73	8.50	2,3,13
TWA13B	RX J1121.3−3447S	11 21 17.24	−34 46 45.50	TW Hya	59	M1	...	12.88	11.46	...	9.57	8.43	7.73	7.49	1,3,11,12
TWA13A	RX J1121.3−3447N	11 21 17.40	−34 46 50.00	TW Hya	59	M1	...	13.43	11.96	...	9.88	8.43	7.68	7.46	1,3,11,12
TWA2A	CD −29 8887A	11 09 13.81	−30 01 39.80	TW Hya	47	M2	...	12.55	11.07	...	9.20	7.63	6.93	6.71	1,2,3
Sz122	...	16 10 16.42	−39 08 05.07	Lup III	200	M2	...	15.33	13.73	13.28	12.12	10.89	10.12	9.93	3,14,15,16
TWA9B	CD −36 7429B	11 48 23.73	−37 28 48.50	TW Hya	68	M1	...	15.43	14.00	...	11.45	9.98	9.38	9.15	1,2,3
TWA15B	...	12 34 20.47	−48 15 19.50	TW Hya	111	M2	...	13.30	12.20	13.41	11.80	10.49	9.83	9.56	3,17,18,19
TWA7	Tyc 7190 2111 1	10 42 30.06	−33 40 16.62	TW Hya	28	M2	...	12.21	10.91	...	9.10	7.79	7.12	6.90	1,3,10
TWA15A	...	12 34 20.65	−48 15 13.50	TW Hya	111	M1.5	...	13.30	12.20	13.51	11.90	10.56	9.93	9.67	3,18,19
Sz121	...	16 10 12.19	−39 21 18.11	Lup III	200	M3	...	15.70	14.06	13.88	11.84	10.08	9.31	9.03	3,15,16
Sz94	...	16 07 49.59	−39 04 28.79	Lup III	200	M4	...	16.31	16.00	14.76	12.90	11.45	10.81	10.56	3,15,16
SO797	...	05 38 54.92	−02 28 58.35	σ-Ori	360	M4	21.05	19.84	18.61	17.26	15.50	13.80	13.20	12.87	3,5,20,21
SO641	...	05 38 38.58	−02 41 55.86	σ-Ori	360	M5	21.65	...	...	18.28	16.36	14.56	13.97	13.65	3,5,22,23
Par−Lup3−2	...	16 08 35.78	−39 03 47.91	Lup III	200	M6	...	16.88	15.49	15.02	13.09	11.24	10.73	10.34	3,15,24
SO925	...	05 39 11.39	−02 33 32.78	σ-Ori	360	M5.5	22.57	...	...	...	16.54	14.45	13.93	13.57	3,5,9,22
SO999	...	05 39 20.23	−02 38 25.87	σ-Ori	360	M5.5	21.41	21.12	18.97	17.57	15.56	13.61	13.04	12.78	3,5,21,22
Sz107	...	16 08 41.79	−39 01 37.02	Lup III	200	M5.5	...	17.31	16.06	15.42	13.20	11.25	10.62	10.31	3,15,16,25
Par−Lup3−1	...	16 08 16.03	−39 03 04.29	Lup III	200	M7.5	...	17.74	19.92	18.15	15.28	12.52	11.75	11.26	3,15,24
TWA26	2M J1139511−315921	11 39 51.14	−31 59 21.50	TW Hya	42	M9	...	20.10	...	18.10	15.83	12.69	12.00	11.50	3,26,27
TWA29	DENIS−P J124514.1−442907	12 45 14.16	−44 29 07.70	TW Hya	79	M9.5	...	...	...	...	18.00	14.52	13.80	13.37	28,29

References. (1) Torres et al. (2006); (2) Barrado Y Navascués (2006); (3) Cutri et al. (2003); (4) Caballero et al. (2010); (5) Rigliaco et al. (2011a); (6) Morrison et al. (2001); (7) Hernández et al. (2007); (8) Sacco et al. (2008); (9) Caballero (2008); (10) Høg et al. (2000); (11) Zuckerman & Song (2004); (12) Messina et al. (2010); (13) Riaz et al. (2006); (14) Gómez & Mardones (2003); (15) Merín et al. (2008); (16) Cieza et al. (2007); (17) Shkolnik et al. (2011); (18) Samus' et al. (2003); (19) Zuckerman et al. (2001); (20) Oliveira et al. (2006); (21) Sherry et al. (2004); (22) Rigliaco et al. (2012); (23) Burningham et al. (2005); (24) Comerón et al. (2003); (25) Hughes et al. (1994); (26) Reid et al. (2008); (27) DENIS Consortium (2005); (28) Kirkpatrick et al. (2008); (29) Looper et al. (2007);

Notes. Distances to TW Hya objects are obtained by Weinberger et al. (2013), by Torres et al. (2008), and by Mamajek (2005), to σ-Ori by Brown et al. (1994), and to Lupus III by Comerón (2008).

Table 3.2: Details of the observations

Name		SLITS		t_{exp}	Observation
	UVB	VIS	NIR		date
TWA9A	0.5″	0.4″	0.4″	150s	16-17 May 2010
SO879	1.0″	0.9″	0.9″	3600s	11-12 Jan 2011
TWA6	0.5″	0.4″	0.4″	100s	12 Jan 2011
TWA25	0.5″	0.4″	0.4″	120s	16-17 May 2010
TWA14	0.5″	0.4″	0.4″	400s	12 Jan 2011
TWA13B	0.5″	0.4″	0.4″	150s	16-17 May 2010
TWA13A	0.5″	0.4″	0.4″	150s	16-17 May 2010
TWA2A	0.5″	0.4″	0.4″	100s	16-17 May 2010
Sz122	1.0″	0.9″	0.9″	600s	18 Apr 2012
TWA9B	0.5″	0.4″	0.4″	800s	16-17 May 2010
TWA15B	0.5″	0.4″	0.4″	600s	16-17 May 2010
TWA7	0.5″	0.4″	0.4″	100s	12 Jan 2011
TWA15A	0.5″	0.4″	0.4″	600s	16-17 May 2010
Sz121	1.0″	0.9″	0.9″	500s	18 Apr 2012
Sz94	1.0″	0.9″	0.9″	600s	16-17 May 2010
SO797	1.0″	0.9″	0.9″	2400s	23-24 Dec 2009
SO641	1.0″	0.9″	0.9″	3600s	23-24 Dec 2009
Par−Lup3−2	1.0″	0.9″	0.9″	1200s	16-17 May 2010
SO925	1.0″	0.9″	0.9″	3600s	21-22 Dec 2009
SO999	1.0″	0.9″	0.9″	2400s	24-25 Dec 2009
Sz107	1.0″	0.9″	0.9″	600s	22 Apr 2011
Par−Lup3−1	1.0″	0.9″	0.9″	600s	16-17 May 2010
TWA26	1.0″	0.9″	0.9″	3600s	22 Mar 2010
TWA29	1.6″	1.5″	1.5″	3600s	22 Mar 2010

The fully reduced, flux-, and wavelength-calibrated spectra are available on Vizier[2].

3.3 Spectral type classification

A careful SpT classification of the sample is important in order to provide correct templates for accretion estimates of Class II YSOs. Moreover, the procedure used to derive the SpT of Class II and Class III YSOs should be as homogeneous as possible. In this section we describe two different methods of deriving SpT for these objects. First, we use the depth of various molecular bands in the VIS part of the spectrum. Then, we describe the second method, which consists of using spectral indices in the VIS and in the NIR part of the spectrum. These provide us with a reliable, fast, and reddening-free method for determining SpT for large samples of YSOs.

3.3.1 Spectral typing from depth of molecular bands

For the SpT classification of the objects, we used the analysis of the depth of several molecular bands in the spectral region between 580 nm and 900 nm (Luhman, 2004; Allen & Strom, 1995; Henry et al., 1994). This region includes various TiO ($\lambda\lambda$ 584.7-605.8, 608-639, 655.1-685.2, 705.3-727, 765-785, 820.6-856.9, 885.9-895 nm), VO ($\lambda\lambda$ 735-755,

---

[2] http://vizier.u-strasbg.fr/viz-bin/VizieR-3?-source=J/A%2bA/551/A107/spectra

785-795, 850-865 nm), and CaH ($\lambda\lambda$ 675-705 nm) absorption bands, and a few photospheric lines (the CaII IR triplet at $\lambda\lambda$ 849.8, 854.2, 866.2 nm, the NaI doublet at λ 589.0 and 589.6 nm, the CaI at λ 616.2 nm, a blend of several lines of BaII, FeI and CaI at λ 649.7 nm, the MgI at λ 880.7 nm, and the NaI and KI doublets at $\lambda\lambda$ 818.3 nm and 819.5 and $\lambda\lambda$ 766.5 nm and 769.9, respectively.

In Figs. 3.1, 3.2, and 3.3 we show the VIS spectra of the objects in the wavelength range between 580 and 900 nm. All the spectra are normalized at 750 nm and, for the sake of clarity, smoothed to a resolution of R$\sim$2500 at 750 nm and vertically shifted. The depth of the molecular features increases with SpT almost monotonically, and by comparing the spectra of the targets using together different wavelength subranges and different molecular bands, we can robustly assign a SpT to our objects thanks to the differences in the depth of the bands, with uncertainties estimated to be 0.5 subclasses.

With this spectral typing procedure, we classified all the objects in our sample with SpT earlier than M8. The agreement between the SpTs derived here and those in the literature is good, with only three cases where the difference is two spectral subclasses. We assume the SpT available from the literature for the two YSOs with SpT later than M8 (Reid et al., 2008; Kirkpatrick et al., 2008), because the classification by comparing molecular bands depth with other spectra in the sample is not possible because our sample has a gap between M6.5 and M9. We can only confirm that these objects have a SpT later than the other targets in the sample and that their SpT differ by 0.5 subclass. The SpT obtained here are listed in Table 3.3 and in the first column of Table 3.4, and they are used for the rest of the analysis. The distribution of SpT for the sample is shown in Fig. 3.4. The range of the M-type is almost entirely covered, providing a good sample for the goals of this paper and a solid library of templates that can be used for $L_{\rm acc}$ estimates of Class II YSOs.

In Appendix 3.C the NIR and UVB spectra of all the sources are shown. Also in these cases a trend with SpT can be seen.

3.3.2 Spectral indices for M3-M8 stars

Spectral indices provide a fast method of determining SpT for large samples of objects. Here we test some of these indices for M-type objects. Riddick et al. (2007) tested and calibrated various spectral indices in the VIS part of the spectrum for pre main sequence (PMS) stars with SpT from M0.5 to M9. In fact, they suggest using some reliable spectral indices that are valid in the range M3-M8. We find that the best SpT classification can be achieved by combining results obtained using the set of indices that we report in Table 3.5. We proceeded as follows. For each object we calculated the SpT with all these indices, and then assigned the mean SpT using those results that are in the nominal range of validity of each index. Typical dispersions of the SpT derived with each index are less than half a subclass. We report the final results obtained with these indices in the second column (VIS_ind) of Table 3.4. Comparing these results with those derived in the previous section, we report an agreement within one subclass for all the objects in the range M3-M8, as expected. However, there are four YSOs classified M1-M2 from the depth of molecular

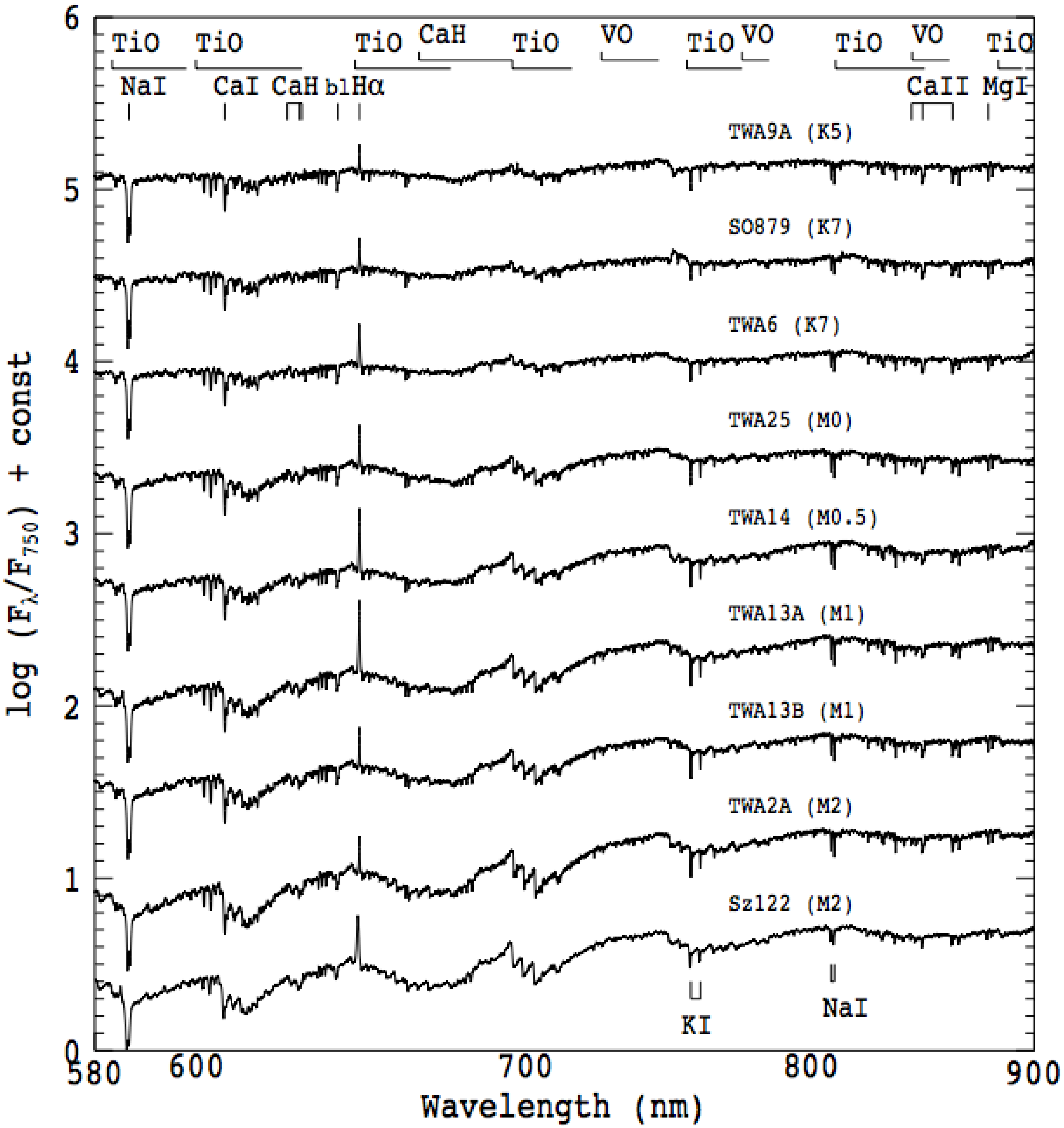

Figure 3.1: Spectra of Class III YSOs with SpT earlier than M3 in the wavelength region where the spectral classification has been carried out (see text for details). All the spectra are normalized at 750 nm and offset in the vertical direction by 0.5 for clarity. The spectra are also smoothed to the resolution of 2500 at 750 nm to make the identification of the molecular features easier.

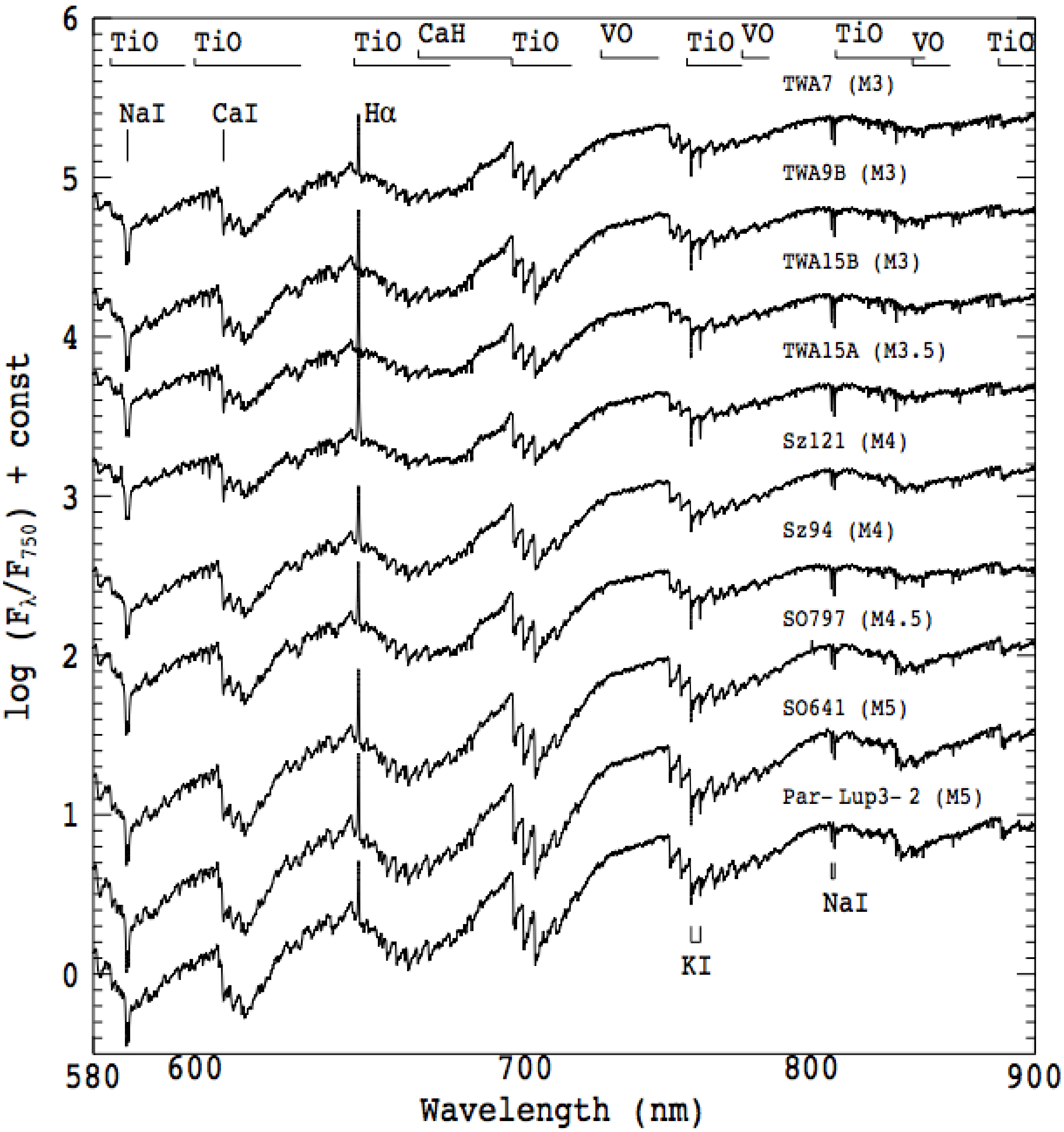

Figure 3.2: Same as Fig. 3.1, but for SpTs between M3 and M5.

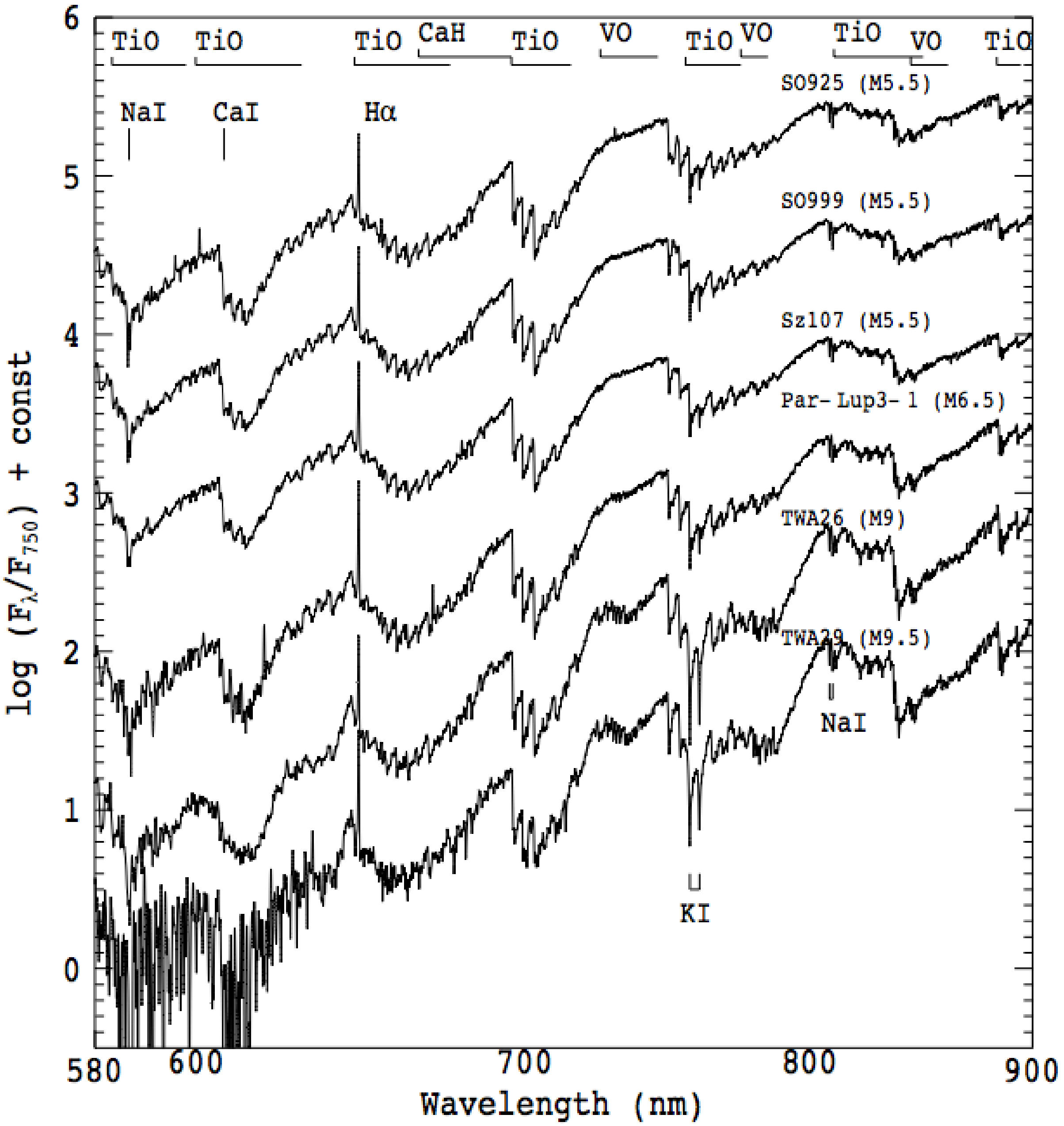

Figure 3.3: Same as Fig. 3.1, but for SpTs later than M5.

Table 3.3: Stellar parameters derived for the objects in our sample

Name	SpT	$T_{\rm eff}$ [K]	$\log(L_\star/L_\odot)$	$M_\star[M_\odot]$	$<\log(L_{acc,noise}/L_\odot)>$
TWA9A	K5	4350	−0.61	0.81	−3.38
SO879	K7	4060	−0.29	1.07	−2.88
TWA6	K7	4060	−0.96	0.66	−3.37
TWA25	M0	3850	−0.61	0.84	−3.04
TWA14	M0.5	3780	−0.83	0.73	−3.23
TWA13B	M1	3705	−0.70	0.68	−3.32
TWA13A	M1	3705	−0.61	0.70	−2.85
TWA2A	M2	3560	−0.48	0.55	−3.36
Sz122	M2	3560	−0.60	0.54	−2.57
TWA9B	M3	3415	−1.17	0.37	−3.93
TWA15B	M3	3415	−0.96	0.37	−3.45
TWA7	M3	3415	−1.14	0.37	−3.84
TWA15A	M3.5	3340	−0.95	0.30	−3.23
Sz121	M4	3270	−0.34	0.37	−3.25
Sz94	M4	3270	−0.76	0.28	−3.38
SO797	M4.5	3200	−1.26	0.19	−4.27
SO641	M5	3125	−1.53	0.12	−4.51
Par−Lup3−2	M5	3125	−0.75	0.18	−3.89
SO925	M5.5	3060	−1.59	0.10	−4.65
SO999	M5.5	3060	−1.28	0.13	−4.30
Sz107	M5.5	3060	−0.79	0.16	−3.69
Par−Lup3−1	M6.5	2935	−1.18	0.10	−4.74
TWA26	M9	2400	−2.70	0.02	−6.54
TWA29	M9.5	2330	−2.81	0.02	−6.64

Notes. The spectral type-$T_{\rm eff}$ relation is adopted from Luhman et al. (2003) for M-type objects and from Kenyon & Hartmann (1995) for K-type objects.

Table 3.4: Spectral types obtained using the method based on the spectral indices described in Sect. 3.3 and in Appendix 3.B

Name	SpT[a]	VIS_ind[b]	H_2O_K2	H_2O	sH_2O^J	sH_2O^K	sH_2O^{H1}	I_J	I_H	HP
TWA9A	K5	...	...	...	...	...	...	...	...	...
SO879	K7	...	...	...	...	...	...	...	...	...
TWA6	K7	...	...	...	...	...	...	...	...	...
TWA25	M0	...	...	...	...	...	...	...	...	...
TWA14	M0.5	...	...	...	...	...	...	...	...	...
TWA13B	M1	M3.3	...	...	...	M1.0	M1.2	...	M0.5	...
TWA13A	M1	M3.3	...	...	...	M1.0	M0.7	...	M0.7	...
TWA2A	M2	M3.3	M2.0	...	M2.6	M1.5	M0.1	M1.4	M0.5	...
Sz122	M2	M3.4	M2.2	...	M2.6	M2.7	M2.4	M2.5	M2.0	...
TWA9B	M3	M3.7	M4.0	...	M5.1	M3.1	M3.4	M4.4	M3.4	...
TWA15B	M3	M3.8	M4.5	...	M6.7	M3.8	M3.3	M5.0	M2.1	...
TWA7	M3	M3.8	M2.6	...	M3.5	M4.3	M3.3	M3.3	M3.7	...
TWA15A	M3.5	M3.8	M3.8	...	M7.2	M4.1	M4.0	M5.3	M2.5	...
Sz121	M4	M4.3	M3.0	...	M3.6	M1.2	M5.8	M2.9	M2.1	...
Sz94	M4	M3.7	M4.3	...	M4.9	M3.7	M3.0	M4.9	M4.0	...
SO797	M4.5	M4.7	M2.3	...	M2.1	M6.0	M5.0	M3.6	M5.9	...
SO641	M5	M5.2	M5.3	M5.8	M4.7	M4.2	M5.1	M5.9	M6.6	...
Par−Lup3−2	M5	M5.0	M5.7	M5.7	M5.8	M4.0	M4.5	M6.1	M5.0	...
SO925	M5.5	M5.5	M7.3	M6.3	M3.9	M1.5	M5.0	M6.2	M7.3	...
SO999	M5.5	M5.4	M3.6	M5.8	M3.9	M5.7	M5.4	M6.1	M6.5	...
Sz107	M5.5	M5.5	M5.7	M5.9	M6.1	M6.1	M5.6	M6.4	M4.5	...
Par−Lup3−1	M6.5	M6.4	M6.6	M7.1	L0.8	M5.7	M8.6	L0.0	M5.5	...
TWA26	M9	...	M8.4	M8.3	L0.0	M7.7	M9.9	L0.4	M6.8	M9.1
TWA29	M9.5	...	M9.4	M8.7	M9.3	M8.2	L0.8	L0.2	M7.2	M9.5

Notes. (a) SpT derived in this work as explained in Sect. 3.3.1. (b) Results obtained using the spectral indices in the VIS part of the spectrum, as explained in Sect. 3.3.2. All the other columns refer to the results obtained using NIR spectral indices, as explained in Appendix 3.B. SpT are reported only in the range of validity of each index.

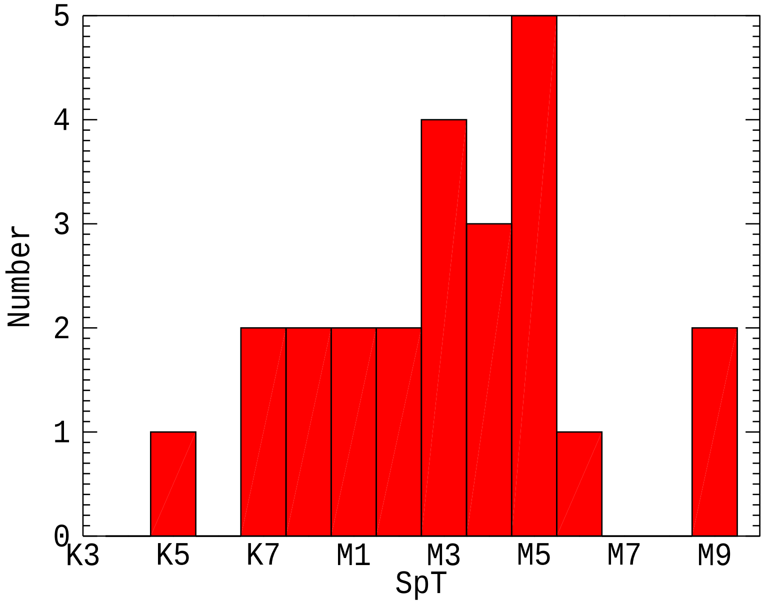

Figure 3.4: Distribution of spectral types of the Class III YSOs discussed in this work. Each bin corresponds to one spectral subclass.

Table 3.5: Spectral indices from Riddick et al. (2007, et reference therein) adopted in our analysis for spectral type classification

Index	Range of validity	Numerator [nm]	Denominator [nm]
VO 7445	M5-M8	0.5625 (735.0-740.0) + 0.4375 (751.0−756.0)	742.0−747.0
VO 2	M3-M8	792.0−796.0	813.0−815.0
c81	M2.5-M8	811.5−816.5	(786.5−791.5)+(849.0−854.0)
R1	M2.5-M8	802.5−813.0	801.5−802.5
R2	M3-M8	814.5−846.0	846.0−847.0
R3	M2.5-M8	(802.5−813.0)+(841.5−846.0)	(801.5−802.5)+(846.0−847.0)
TiO 8465	M3-M8	840.5−842.5	845.5−847.5
PC3	M3-M8	823.5−826.5	754.0−758.0

bands that would be classified M3 from the values of the Riddick's indices. This suggests that spectral classification M3 obtained with spectral indices could, in fact, be earlier by more than one subclass.

There are also indices based on features in the NIR part of the spectrum (e.g Testi et al., 2001; Testi, 2009; Allers et al., 2007; Rojas-Ayala et al., 2012). In Appendix 3.B we compare the results obtained with these NIR indices with the SpT derived in the previous section to confirm the validity of some of these indices for the classification of M-type YSOs.

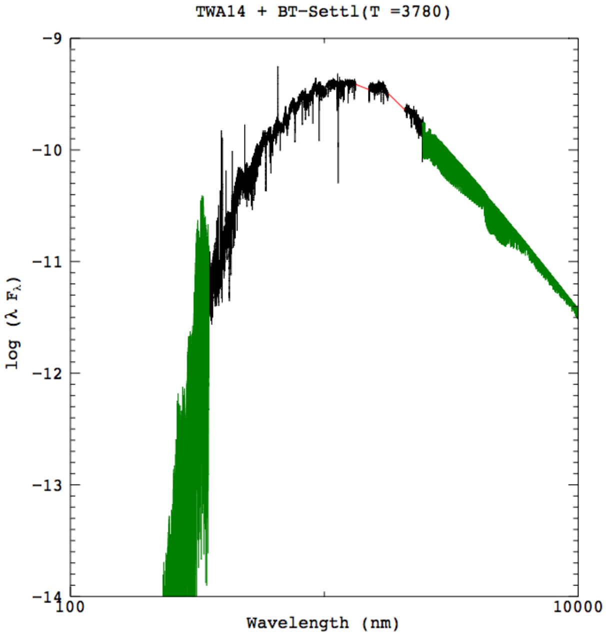

Figure 3.5: Example of the combination of a flux-calibrated and telluric removed X-Shooter spectrum (black) with model spectra with the same effective temperature (green), which is normalized at the red and blue edges of the X-Shooter spectrum and only shown outside the X-Shooter range. The telluric bands in the NIR are replaced with a linear interpolation (red). In this figure we show the example of TWA14.

3.4 Stellar parameters

To estimate the mass ($M_\star$), radius ($R_\star$) and age for each target we compare the photospheric parameters ($L_\star$,T$_{\rm eff}$) with the theoretical predictions of the Baraffe et al. (1998) PMS evolutionary tracks. We derive the T$_{\rm eff}$ of each star from its SpT using the Luhman et al. (2003) SpT-T$_{\rm eff}$ scale, while the procedure for estimating $L_\star$ is described in the next paragraph. We then use ($L_\star$,T$_{\rm eff}$) to place the stars on the HR diagram and estimate ($M_\star$, age) by interpolating the theoretical evolutionary tracks. These parameters are reported in Table 3.3. Finally, we obtain $R_\star$ from $L_\star$ and T$_{\rm eff}$.

3.4.1 Stellar luminosity

Given the broad wavelength coverage (∼300-2500 nm) of the X-Shooter spectra, for objects with 2300 < T$_{\rm eff}$ < 4400 K only a low percentage of the stellar flux ($\lesssim$ 10-30%) arises from spectral regions outside the X-Shooter spectral range. We use, therefore, the following procedure to estimate the total flux of our objects: first, we integrate the whole X-Shooter spectrum from 350 nm to 2450 nm, excluding the last 50 nm of spectra on each side, which are very noisy, and the regions in the NIR between the J, H and K-bands ($\lambda\lambda$ 1330-1550 nm, $\lambda\lambda$ 1780-2080 nm, see Sect. 3.2), where we linearly interpolate across the telluric absorption regions. We then use the BT-Settl synthetic spectra from Allard et al. (2011) with the same T$_{\rm eff}$ as our targets (see Table 3.3), assuming log$g$=4.0, which is typical of low-mass

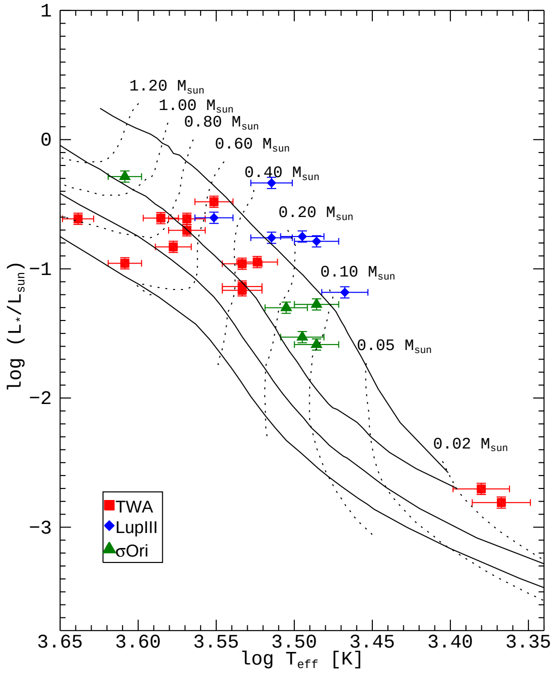

Figure 3.6: Hertzsprung-Russell Diagram of the Class III YSOs of this work. Data points are compared with the evolutionary tracks (dotted lines) by Baraffe et al. (1998). Isochrones (solid lines) correspond to 2, 10, 30, and 100 Myr.

YSOs, and normalized with our spectra at 350 and 2450 nm to estimate the contribution to the total flux emitted outside the observed range. The match of the normalization factors at the two ends is very good in all cases. We show in Fig. 3.5 an example of this procedure.

The main source of uncertainty in $L_\star$ comes from the uncertainty in the spectroscopic flux. For the objects observed in excellent weather conditions, this matches the fotometric fluxes to better than a factor $\lesssim$1.5. It is then reasonable to assume such an uncertainty for all the objects in our sample, after normalizing the spectroscopic flux to the photometry (see Sect. 3.2). This would lead to an uncertainty of less than 0.2 dex in log$L_\star$.

To convert the bolometric fluxes obtained in this way in $L_\star$ we adopt these distances: we assume that YSOs in the σ-Ori region have a distance of 360 pc (Brown et al., 1994), those in TW Hya the distances listed in Weinberger et al. (2013), in Torres et al. (2008), and in Mamajek (2005), and those in Lupus III of 200 pc (Comerón, 2008), as reported in Table 3.1. The derived stellar luminosities are listed in Table 3.3. These values are comparable to those obtained with photometric data in the literature, with a typical difference $\lesssim$ 0.2 dex. As a result, they are consistent with our determinations, within the errors.

3.4.2 Stellar mass and age

In Fig. 3.6 we show the Hertzsprung-Russell diagram (HRD) of our PMS stars, built using T_{eff} as reported in Table 3.3 and $L_{\star}$ derived in Sec 3.4.1. We assign $M_{\star}$ and age to our PMS stars by interpolating evolutionary tracks from Baraffe et al. (1998) in the HRD. The resulting $M_{\star}$ are reported in Table 3.3. For four objects (Sz107, Sz121, TWA26, and TWA29) the position in the HRD implies an age <1 Myr, where theoretical models are known to be very uncertain and, in fact, are typically not tabulated (Baraffe et al., 1998). We estimate the mass of these objects by extrapolating from the closest tabulated points, but we warn the reader that the values are affected by high uncertainty.

Our YSOs are distributed along different isochrones; Lupus YSOs appear to be younger than the others (age$\lesssim$2 Myr), while σ-Ori YSOs are distributed in isochronal ages in the range 2$\lesssim$age$\lesssim$10 Myr; finally, TW Hya targets appear generally close to the 10 Myr isochrone. This is in general agreement with what is found in the literature; indeed, Lupus has an estimated age of ~1-1.5 Myr (Hughes et al., 1994; Comerón, 2008), while the σ-Ori region is usually considered to be slightly older (~3 Myr in average), and ranges from $\lesssim$1 Myr to several Myr (Zapatero Osorio et al., 2002; Oliveira et al., 2004). For the TW Hya association, the age estimates are $\gtrsim$10 Myr (Mamajek, 2005; Barrado Y Navascués, 2006; Weinberger et al., 2013).

3.5 Line classification

The spectra of our objects are characterized by photospheric absorption lines that depend on the SpT and, in some cases, on the age. To assess the PMS status of the objects in our sample, we check that the lithium absorption feature at λ 670.8 nm, which is related to the age of the YSOs (e.g. Mentuch et al., 2008), is detected in all but one (Sz94) of the objects. We discuss in more detail the implications of the nondetection in Sz94 in Appendix 3.A, and we explain why this object could be considered in our analysis as YSO anyway. The values of the lithium equivalent width (EW_{LiI}) for the other objects in the sample are $\sim$ 0.5 Å. A detailed analysis of this line and the other photospheric absorption lines of the objects in our sample will be carried out by Stelzer et al. (2013).

In addition to these, we detect many emission lines, typically H, He, and Ca lines, that originate in the chromosphere of these stars. In this work we concentrate on the emission lines characterization, since we are interested in the chromospheric activity.

3.5.1 Emission lines identification

To understand the contribution of the chromospheric emission to the estimate of L_{acc} through the luminosity of accretion-related emission lines, we first identified in our spectra the lines typically related to accretion processes in Class II YSOs. Here, we describe which lines we detected and report their fluxes and equivalent widths in Tables 3.6 and 3.7.

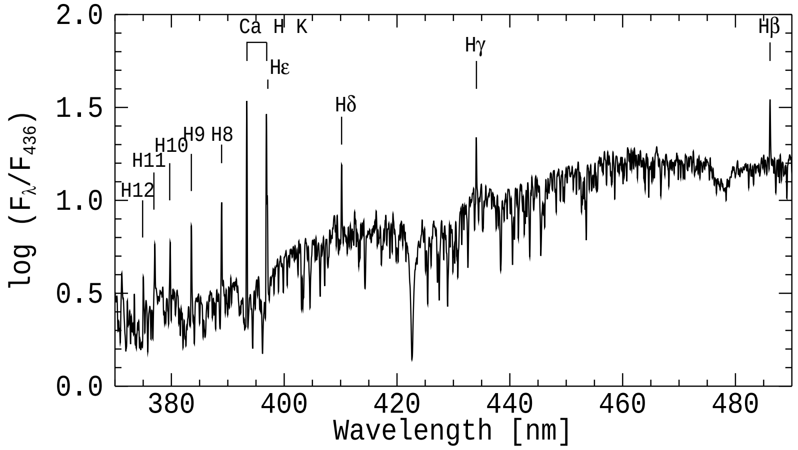

Figure 3.7: Portion of the spectrum, showing emission in all Balmer lines from Hβ up to H12, as well as the CaII H and K lines, of the YSO TWA13B. The spectrum has been smoothed to a resolution R = 3750 at 375 nm.

The most common line detected in YSOs is the Hα line at 656.28 nm, which is present in the spectra of all our objects. Emission in this line has been used as a proxy for YSO identification and has been related to accretion processes (e.g. Muzerolle et al., 1998a; Natta et al., 2004). This line is also generated in chromospherically active YSOs (e.g. White & Basri, 2003). Similarly, the other hydrogen recombination lines of the Balmer series are easily detected in almost all of our Class III objects up to the H12 line (λ 374.9 nm). It is not easy, nevertheless, to determine the continuum around Balmer lines beyond the H9 line (λ 383.5 nm), and the Hϵ line (λ 397 nm) is blended with the CaII-K line. An example of a portion of the spectrum from Hβ to H12 is shown in Fig. 3.7.

The hydrogen recombination lines of the Paschen and Brackett series, in particular the Paβ (λ 1281.8 nm) and Brγ (λ 2166 nm) lines, have been shown to be related to accretion by Muzerolle et al. (1998a). These lines have subsequently been used to survey star forming regions with high extinction (Natta et al., 2004, 2006) in order to obtain accretion rate estimates for very low-mass objects. We do not detect any of these lines in our Class III spectra, confirming that chromospheric activity is not normally detectable with these lines.

The calcium II emission lines at $\lambda\lambda$ 393.4, 396.9 nm (Ca HK) and at $\lambda\lambda$ 849.8, 854.2, 866.2 nm (Ca IRT) are related to accretion processes (e.g. Mohanty et al., 2005; Herczeg & Hillenbrand, 2008; Rigliaco et al., 2012), but also to chromospheric activity (e.g. Montes, 1998). The CaII H and K lines are detected in 90% of our objects. The CaII IRT lines are detected in 11 out of 13 objects with SpT earlier than M4. These emission lines appear as a reversal in the core of the photospheric absorption lines. For all 11 objects with SpT M4 or later, the CaII IRT lines are not detected.

The HeI line at λ 587.6 nm is also known to be associated with accretion processes (Muzerolle et al., 1998a; Herczeg & Hillenbrand, 2008), but in Class III YSOs it is known to be of chromospheric origin (e.g. Edwards et al., 2006). The line is indeed detected in

22 (92%) objects. Other HeI lines at $\lambda\lambda$ 667.8, 706.5, and 1083 nm are usually associated with accretion processes (Muzerolle et al., 1998a; Herczeg & Hillenbrand, 2008; Edwards et al., 2006). We detect only in Sz122 the HeI lines at $\lambda\lambda$ 667.8, 706.5 nm, while we detect in 8 (33%) of the objects the HeI line at λ 1083 nm.

Finally, there is no trace of forbidden emission lines in any of our X-Shooter spectra, consistent with the expected absence of circumstellar material in Class III YSOs.

3.5.2 Hα equivalent width and 10% width

A commonly used estimator for the activity in PMS stars is the EW of the Hα line (e.g. White & Basri, 2003). This is useful especially when dealing with spectra that are not flux-calibrated or with narrow-band photometric data. The absolute values of this quantity as a function of the SpT of the objects are plotted in Fig. 3.8, and the values are reported in Table 3.6. We observe a well-known dependence of EW$_{H\alpha}$ with SpT that is due to decreasing continuum flux for cooler atmospheres. With respect to the threshold to distinguish between accreting and nonaccreting YSOs proposed by White & Basri (2003), all our targets satisfy the criteria of White & Basri (2003) for being nonaccretors.

Another diagnostic to distinguish between accreting and nonaccreting YSOs is the full width of the Hα line at 10% of the line peak (White & Basri, 2003). This diagnostic has been shown to be correlated with $\dot{M}_{\rm acc}$, but with a large dispersion (Natta et al., 2004). Figure 3.9 shows the EW$_{H\alpha}$ absolute values versus the 10% Hα width. We see that for most of our objects the 10% Hα width is in the ~100-270 km/s range, and for only three objects this value is significantly above the threshold suggested by White & Basri (2003) of 270 km/s (TWA6, Sz122, and Sz121). In Appendix 3.A we discuss these objects, and we explain why TWA6 and Sz121 can be considered in our analysis, while Sz122 should be excluded because it is probably an unresolved binary. This is probably due either to high values of $v\sin i$ for these objects, which broaden the line profile, or to unresolved binarity. For BDs, the threshold for distinguishing accretors from nonaccretors is set at values of the 10% Hα width of 200 km/s (Jayawardhana et al., 2003a). This is satisfied for all the BDs in the sample. The values of 10% Hα width are listed in Table 3.6.

3.5.3 Line luminosity

We measure the flux of each line by estimating the continuum in the proximity of the line with the IDL astrolib outlier-resistant mean task *resistant_mean*. We then subtract the continuum from the observed flux and calculate the integral, checking that the whole line, including the wings, is included in the computation. To compute $L_{\rm line}$ we adopt the distances reported in Table 3.3.

For the CaII IRT lines, where the emission appears in the core of the absorption feature, we subtract the continuum from our spectrum following the prescription given by Soderblom et al. (1993). Using a BT-Settl synthetic spectrum (Allard et al., 2011) of the same $T_{\rm eff}$ smoothed at the same resolution of our observed spectrum, we obtain an esti-

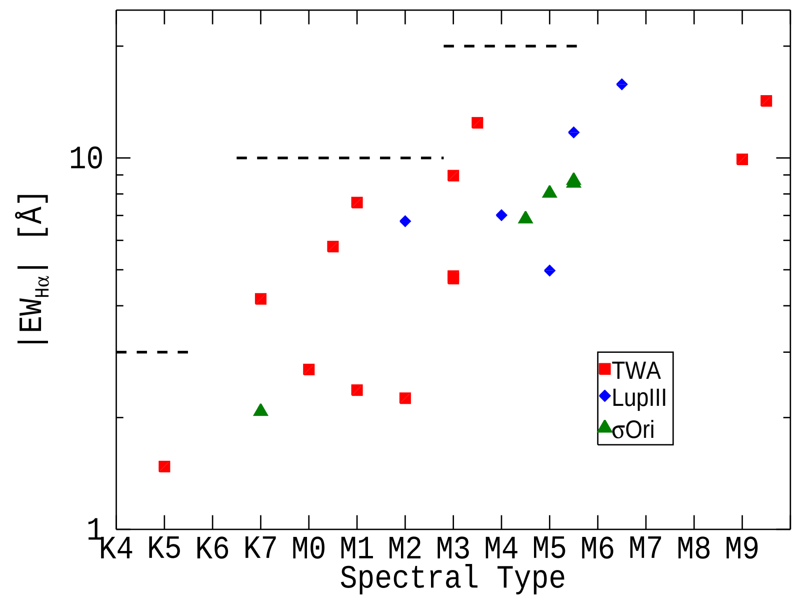

Figure 3.8: Hα equivalent width as a function of spectral type. The dashed lines represent the boundary between accretors and non accretors proposed by White & Basri (2003) for different SpT.

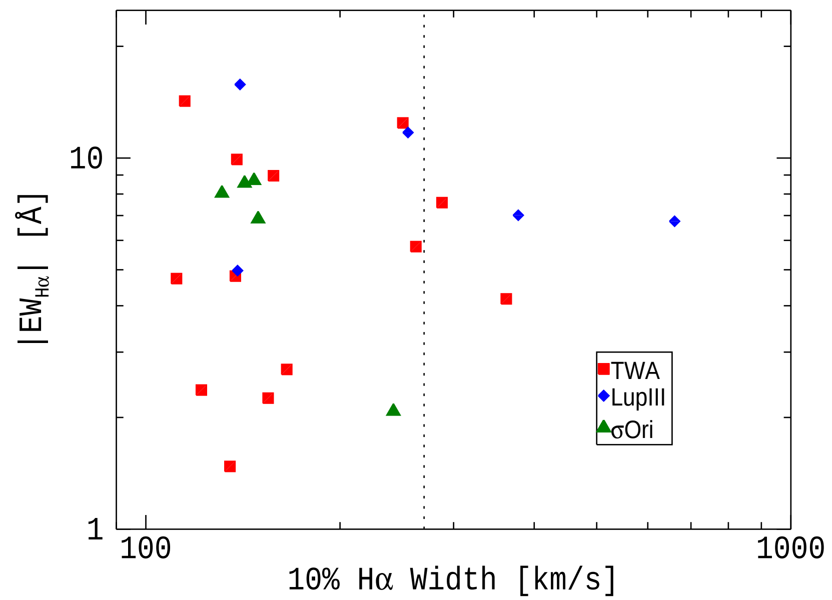

Figure 3.9: Hα equivalent width as a function of the 10% Hα width. The vertical dashed line rerpesents the White & Basri (2003) criterion for the boundary between accretors and nonaccretors. The objects with 10% Hα width bigger than 270 km/s are, from right to left: Sz122, Sz121, TWA6, and TWA13A.

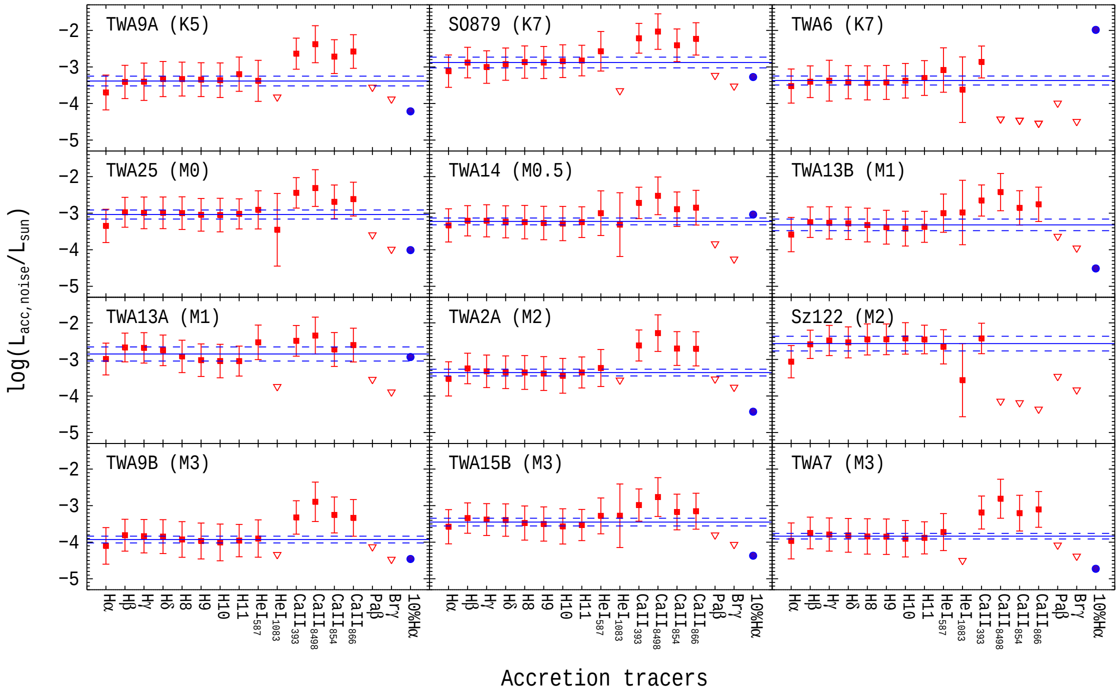

Figure 3.10: $\log(L_{\rm acc,noise}/L_\odot)$ obtained using different accretion tracers and the relations between $L_{\rm line}$ and $L_{\rm acc}$ from Alcalá et al. (2014). The mean values obtained using the Balmer and HeI$_{\lambda587.6}$ lines are shown with the blue solid lines, and the 1σ dispersion is reported with the blue dashed lines. Upper limits are reported with red empty triangles. The 10% Hα width is reported with a blue filled circle.

mate of the line absorption feature that is then subtracted in order to isolate the emission core of the line; finally, we integrate over the continuum subtracted spectrum. We report in Tables 3.6 and 3.7 the values obtained for the fluxes and the line EWs.

We include in Table 3.6 the values of the observed Balmer jump, defined as the ratio between the flux at ~360 nm and at ~400 nm. Typical values found in the literature for ClassIII YSOs range between ~0.3 and 0.5 (Herczeg & Hillenbrand, 2008; Rigliaco et al., 2012). In ClassII YSOs, instead, the observed Balmer jump values are usually higher, up to ~6 (Hartigan et al., 1991; Herczeg & Hillenbrand, 2008; Rigliaco et al., 2012). For the objects in our sample, this quantity ranges between ~0.35 and ~ 0.55 (see Table 3.6), with the exception of Sz122. The values of the Balmer jump ratio for the three BDs in the sample are not reported, because the SNR of the UVB spectrum of these sources is too low to estimate this quantity.

3.6 Implications for mass accretion rates determination

The physical parameter that is used to estimate the accretion activity in Class II YSOs is $\dot{M}_{\rm acc}$, which is derived from $L_{\rm acc}$ and the stellar parameters using the following relation

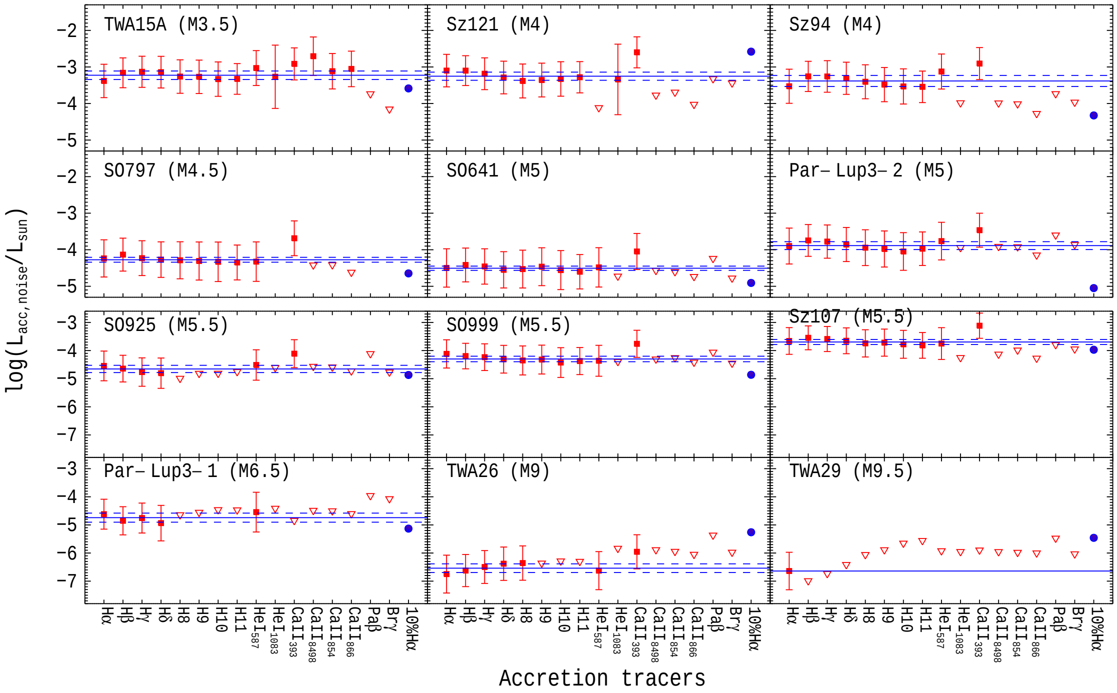

Figure 3.11: $\log(L_{\rm acc,noise}/L_{\odot})$ obtained using different accretion tracers as Fig. 3.10.

(Hartmann et al., 1998):

$$\dot{M}_{\rm acc} = \left(1 - \frac{R_\star}{R_m}\right)^{-1} \frac{L_{\rm acc} R_\star}{G M_\star} = \frac{L_{\rm acc} R_\star}{0.8 G M_\star}\,, \tag{3.1}$$

where the factor 0.8 is due to the assumption that the accretion flows arise from a magnetospheric radius $R_{\rm m} \sim 5R_\star$ (Shu et al., 1994).

When estimating $L_{\rm acc}$ in Class II YSOs with the direct method of UV-excess fitting (e.g. Valenti et al., 1993), the contribution to the continuum excess emission due to chromospheric activity is probably negligible, and it is normally taken into account using a Class III YSO of the same SpT as a template for the analysis (e.g. Herczeg & Hillenbrand, 2008; Rigliaco et al., 2011b, 2012). However, $L_{\rm acc}$ is often derived using spectral lines luminosity and appropriate empirical relations (see e.g. Muzerolle et al., 1998a; Natta et al., 2004; Herczeg & Hillenbrand, 2008, and references therein). Several of the lines normally used for these studies are influenced by chromospheric activity (Sect. 3.5), which should be estimated and subtracted from the line emission before computing $L_{\rm acc}$. This procedure is not trivial, since it is difficult to properly disentangle the two emission processes in each object and each line. All the $L_{\rm acc} - L_{\rm lines}$ relations are always based on the uncorrected values of $L_{\rm line}$. This correction, as shown in Ingleby et al. (2011) and Rigliaco et al. (2012), can be important in objects with low $L_{\rm acc}$ and, in particular, in VLM stars. Therefore, the chromospheric emission acts as a systematic ``noise" that affects the $L_{\rm acc}$ measurements.

Table 3.6: Fluxes and equivalent widths of Balmer lines

Name	Hα	Hβ	Hγ	Hδ	H8	H9	H10	H11	10%Hα	F$_{360}$/F$_{400}$
TWA9A	14.0 ± 1.1	4.7 ± 1.8	2.7 ± 1.5	2.2 ± 1.0	1.4 ± 0.2	1.0 ± 0.1	0.82 ± 0.07	0.91 ± 0.47	135.0	0.38
	−1.48	−0.68	−0.62	−0.59	−0.80	−0.83	−0.43	−0.65		
SO879	1.8 ± 0.2	0.52 ± 0.15	0.23 ± 0.08	0.20 ± 0.06	0.15 ± 0.01	0.11 ± 0.01	0.10 ± 0.00	0.078 ± 0.022	242.0	0.38
	−2.08	−1.17	−0.70	−1.12	−1.62	−1.57	−1.74	−0.77		
TWA6	36.4 ± 4.0	8.4 ± 2.1	5.1 ± 3.9	3.3 ± 0.7	2.0 ± 0.1	1.5 ± 0.1	1.4 ± 0.1	1.3 ± 0.7	362.0	0.41
	−4.17	−1.68	−1.02	−1.43	−1.47	−1.54	−1.67	−1.36		
TWA25	47.3 ± 3.7	18.8 ± 3.4	10.4 ± 2.6	7.5 ± 1.4	4.8 ± 0.2	3.4 ± 0.2	2.7 ± 0.2	2.2 ± 0.3	165.4	0.42
	−2.69	−1.94	−1.86	−1.81	−2.26	−1.97	−1.14	−1.15		
TWA14	15.4 ± 1.1	3.6 ± 0.5	2.1 ± 0.5	1.4 ± 0.2	0.87 ± 0.02	0.63 ± 0.02	0.50 ± 0.02	0.41 ± 0.07	262.2	0.45
	−5.77	−3.18	−3.03	−2.91	−3.30	−2.73	−1.28	−1.87		
TWA13B	23.8 ± 1.9	8.8 ± 1.4	4.8 ± 1.1	3.3 ± 0.5	1.9 ± 0.1	1.3 ± 0.1	0.95 ± 0.08	0.81 ± 0.12	121.9	0.39
	−2.37	−1.94	−1.88	−1.75	−2.07	−1.65	−0.51	−0.94		
TWA13A	85.7 ± 5.5	30.2 ± 4.0	17.0 ± 3.4	10.6 ± 1.3	4.8 ± 0.1	3.0 ± 0.1	2.3 ± 0.1	1.7 ± 0.2	287.8	0.45
	−7.58	−6.07	−5.48	−5.11	−4.30	−3.41	−1.28	−1.68		
TWA2A	42.0 ± 5.0	13.9 ± 2.1	6.6 ± 1.5	4.4 ± 0.8	2.8 ± 0.1	2.0 ± 0.1	1.4 ± 0.1	1.3 ± 0.2	154.7	0.38
	−2.25	−1.88	−1.56	−1.36	−1.64	−1.38	−0.43	−0.84		
Sz122	6.4 ± 0.8	3.2 ± 0.3	2.3 ± 0.6	1.5 ± 0.4	1.2 ± 0.1	1.0 ± 0.1	0.86 ± 0.05	0.59 ± 0.08	660.3	0.74
	−6.76	−8.67	−10.00	−8.02	−11.57	−11.69	−10.02	−6.27		
TWA9B	5.9 ± 0.6	2.0 ± 0.1	1.0 ± 0.1	0.71 ± 0.06	0.37 ± 0.01	0.24 ± 0.01	0.18 ± 0.01	0.16 ± 0.01	137.6	0.39
	−4.81	−4.83	−4.20	−3.50	−3.09	−2.49	−0.71	−1.54		
TWA15B	6.8 ± 0.3	2.0 ± 0.1	1.1 ± 0.1	0.72 ± 0.06	0.38 ± 0.01	0.27 ± 0.02	0.19 ± 0.01	0.16 ± 0.01	157.7	0.45
	−8.96	−7.94	−7.19	−6.48	−6.20	−5.18	−1.60	−3.11		
TWA7	46.7 ± 3.9	13.3 ± 0.9	6.8 ± 0.6	4.5 ± 0.4	2.6 ± 0.1	1.8 ± 0.1	1.4 ± 0.1	1.1 ± 0.1	111.6	0.41
	−4.73	−4.53	−3.82	−3.36	−2.97	−2.36	−0.48	−1.68		
TWA15A	10.4 ± 0.6	3.0 ± 0.2	1.8 ± 0.1	1.3 ± 0.1	0.62 ± 0.02	0.47 ± 0.02	0.33 ± 0.02	0.25 ± 0.03	250.3	0.55
	−12.43	−10.34	−10.80	−9.68	−6.33	−8.07	−3.36	−4.06		
Sz121	5.9 ± 0.8	1.1 ± 0.1	0.50 ± 0.10	0.28 ± 0.06	0.15 ± 0.01	0.12 ± 0.01	0.10 ± 0.01	0.087 ± 0.020	377.9	0.38
	−7.01	−5.06	−3.79	−2.90	−2.33	−2.39	−2.32	−2.02		
Sz94	2.3 ± 0.2	0.75 ± 0.05	0.42 ± 0.04	0.27 ± 0.02	0.14 ± 0.01	0.087 ± 0.006	0.064 ± 0.006	0.047 ± 0.008	188.9	0.39
	−5.67	−5.79	−5.49	−4.43	−3.91	−2.73	−2.66	−1.18		
SO797	0.16 ± 0.02	0.035 ± 0.003	0.016 ± 0.002	0.0099 ± 0.0015	0.0057 ± 0.0006	0.0037 ± 0.0011	0.0030 ± 0.0011	0.0022 ± 0.0007	149.3	0.43
	−6.85	−6.83	−5.23	−3.89	−5.95	−3.71	−3.47	−1.48		
SO641	0.090 ± 0.009	0.019 ± 0.001	0.0097 ± 0.0010	0.0053 ± 0.0006	0.0033 ± 0.0003	0.0025 ± 0.0003	0.0018 ± 0.0003	0.0012 ± 0.0002	131.2	0.38
	−8.04	−9.08	−8.38	−5.42	−6.91	−5.98	−5.97	−1.74		
Par−Lup3−2	1.1 ± 0.2	0.26 ± 0.03	0.14 ± 0.02	0.080 ± 0.011	0.041 ± 0.003	0.026 ± 0.003	0.019 ± 0.005	0.017 ± 0.005	138.7	0.36
	−4.97	−4.88	−4.07	−2.67	−1.90	−1.38	−0.65	−1.39		
SO925	0.081 ± 0.009	0.012 ± 0.001	0.0050 ± 0.0011	0.0030 ± 0.0013	<0.0012	<0.0011	<0.000975	<0.000877	142.2	0.68
	−8.55	−6.81	−5.59	−4.29	...	...	...	...		
SO999	0.20 ± 0.02	0.031 ± 0.003	0.016 ± 0.002	0.0091 ± 0.0020	0.0050 ± 0.0011	0.0036 ± 0.0006	0.0024 ± 0.0005	0.0021 ± 0.0007	147.1	0.45
	−8.70	−7.99	−7.80	−5.31	−4.23	−4.18	−2.43	−1.35		
Sz107	1.8 ± 0.2	0.40 ± 0.03	0.21 ± 0.02	0.13 ± 0.02	0.064 ± 0.010	0.049 ± 0.007	0.036 ± 0.006	0.025 ± 0.008	254.9	0.38
	−11.72	−11.77	−9.88	−6.91	−4.28	−4.23	−2.57	−2.07		
Par−Lup3−1	0.22 ± 0.02	0.024 ± 0.007	0.016 ± 0.007	0.0073 ± 0.0060	<0.0082	<0.0066	<0.0072	<0.0055	140.0	1.43
	−15.78	−16.82	−29.99	−9.01	...	...	...	...		
TWA26	0.052 ± 0.008	0.012 ± 0.002	0.0085 ± 0.0016	0.0068 ± 0.0017	0.0038 ± 0.0007	<0.0020	<0.0022	<0.0018	138.4	1.55
	−9.91	−27.07	−66.62	−35.39	−97.42	...	...	...		
TWA29	0.019 ± 0.003	<0.0016	<0.0014	<0.0018	<0.0021	<0.0017	<0.0028	<0.0028	114.9	1.56
	−14.24	...	...	...	...	...	...	...		

Notes. Fluxes (10^{-14} erg s^{-1} cm^{-2}) are reported in the first rows for each object with their errors, with equivalent widhts (Å) in the second rows. The Hα 10% width is in km/s. The last column refers to the Balmer jump ratio, intened as the ratio between the flux at ∼360 nm to the flux at ∼400 nm. Upper limits are reported with <.

Table 3.7: Fluxes and equivalent widths of helium and calcium lines

Name	HeI$_{\lambda 587.6}$	HeI$_{\lambda 1083}$	CaII$_{\lambda 393.4}$	CaII$_{\lambda 849.9}$	CaII$_{\lambda 854.2}$	CaII$_{\lambda 866.2}$
TWA9A	5.71e-15 ± 3.31e-15	<1.10e-14	9.59e-14 ± 7.44e-16	4.53e-13 ± 3.21e-15	2.27e-13 ± 4.47e-15	2.59e-13 ± 4.36e-15
	−0.08	...	−13.46	0.16	0.38	0.46
SO879	1.08e-15 ± 6.52e-16	<5.63e-16	9.82e-15 ± 1.57e-16	4.04e-14 ± 3.13e-16	1.78e-14 ± 3.74e-16	2.26e-14 ± 3.65e-16
	−0.15	...	−18.79	-0.04	0.28	0.37
TWA6	1.87e-14 ± 1.47e-14	2.99e-14 ± 9.97e-15	9.66e-14 ± 4.87e-15	<3.54e-15	<4.89e-15	<2.85e-15
	−0.25	−0.39	−12.29	...	...	...
TWA25	2.39e-14 ± 1.14e-14	3.80e-14 ± 3.85e-14	2.46e-13 ± 1.60e-15	8.53e-13 ± 6.41e-15	3.86e-13 ± 9.47e-15	3.73e-13 ± 7.90e-15
	−0.19	−0.16	−20.04	0.01	0.23	0.35
TWA14	6.27e-15 ± 5.04e-15	1.61e-14 ± 5.51e-15	3.92e-14 ± 1.13e-15	1.54e-13 ± 1.29e-15	7.35e-14 ± 2.48e-15	6.42e-14 ± 1.05e-15
	−0.31	−0.44	−19.84	0.02	0.41	0.49
TWA13B	1.66e-14 ± 7.83e-15	8.55e-14 ± 5.30e-14	1.22e-13 ± 7.24e-16	5.33e-13 ± 4.54e-15	2.13e-13 ± 6.06e-15	2.16e-13 ± 4.83e-15
	−0.24	−0.61	−21.91	0.01	0.22	0.32
TWA13A	4.33e-14 ± 1.21e-14	<1.73e-14	1.83e-13 ± 1.18e-14	6.50e-13 ± 5.87e-15	2.93e-13 ± 1.01e-14	3.18e-13 ± 7.42e-15
	−0.61	...	−15.88	-0.12	0.15	0.26
TWA2A	1.61e-14 ± 5.31e-15	<3.93e-14	2.10e-13 ± 7.81e-16	1.23e-12 ± 1.05e-14	4.94e-13 ± 1.38e-14	3.84e-13 ± 9.01e-15
	−0.16	...	−21.62	0.08	0.32	0.42
Sz122	2.93e-15 ± 6.09e-16	2.18e-15 ± 2.18e-15	1.88e-14 ± 7.91e-16	<4.84e-16	<6.36e-16	<2.94e-16
	−0.44	−0.06	−19.58	...	...	...
TWA9B	1.96e-15 ± 2.73e-16	<3.74e-15	1.72e-14 ± 1.44e-16	1.15e-13 ± 1.33e-15	5.84e-14 ± 1.57e-15	3.64e-14 ± 9.35e-16
	−0.37	...	−20.82	0.02	0.18	0.32
TWA15B	2.63e-15 ± 5.10e-16	1.30e-14 ± 4.50e-15	1.51e-14 ± 3.17e-16	6.10e-14 ± 8.13e-16	2.69e-14 ± 1.36e-15	2.19e-14 ± 5.98e-16
	−0.69	−0.58	−27.41	-0.20	0.03	0.19
TWA7	1.66e-14 ± 2.82e-15	<1.57e-14	1.42e-13 ± 8.57e-16	8.47e-13 ± 9.56e-15	3.90e-13 ± 1.19e-14	3.91e-13 ± 6.34e-15
	−0.35	...	−25.00	-0.10	0.07	0.22
TWA15A	4.40e-15 ± 6.80e-16	1.32e-14 ± 4.04e-15	1.79e-14 ± 8.08e-16	7.13e-14 ± 9.30e-16	3.11e-14 ± 1.59e-15	2.84e-14 ± 7.04e-16
	−1.05	−0.70	−19.29	-0.31	-0.02	0.16
Sz121	<1.45e-16	3.50e-15 ± 3.22e-15	1.22e-14 ± 5.84e-16	<1.30e-15	<2.23e-15	<7.06e-16
	...	−0.11	−23.33	...	...	...
Sz94	1.12e-15 ± 1.41e-16	<9.13e-16	5.64e-15 ± 1.53e-16	<7.37e-16	<9.93e-16	<3.70e-16
	−0.59	...	−18.92	...	...	...
SO797	2.92e-17 ± 7.82e-18	<3.02e+02	2.48e-16 ± 2.09e-17	<7.25e-17	<1.11e-16	<4.69e-17
	−0.35	...	−20.54	...	...	...
SO641	2.12e-17 ± 3.81e-18	<5.96e-17	1.00e-16 ± 2.47e-18	<4.89e-17	<6.87e-17	<3.47e-17
	−0.65	...	−16.82	...	...	...
Par−Lup3−2	3.00e-16 ± 7.21e-17	<9.93e-16	1.39e-15 ± 4.54e-17	<9.00e-16	<1.25e-15	<5.15e-16
	−0.46	...	−9.30	...	...	...
SO925	1.98e-17 ± 3.89e-18	<7.64e-17	8.55e-17 ± 7.46e-18	<4.93e-17	<7.12e-17	<3.54e-17
	−0.79	...	−18.79	...	...	...
SO999	2.70e-17 ± 8.90e-18	<1.19e-16	2.05e-16 ± 3.06e-17	<9.80e-17	<1.65e-16	<7.89e-17
	−0.42	...	−15.56	...	...	...
Sz107	3.08e-16 ± 1.66e-16	<5.19e-16	3.34e-15 ± 1.76e-16	<5.03e-16	<1.06e-15	<3.70e-16
	−0.57	...	−25.26	...	...	...
Par−Lup3−1	6.02e-17 ± 5.72e-17	<3.71e-16	<4.40e-17	<1.97e-16	<2.86e-16	<1.58e-16
	−2.35	...	...	...	...	...
TWA26	1.89e-17 ± 9.96e-18	<4.28e-16	6.20e-17 ± 1.82e-17	<1.10e-16	<1.69e-16	<8.50e-17
	−1.88	...	−56.20	...	...	...
TWA29	<2.27e-17	<9.49e-17	<2.02e-17	<2.59e-17	<4.37e-17	<2.73e-17
	...	...	...	...	...	...

Notes. Fluxes are reported in [erg s^{-1} cm^{-2}] in the first rows, equivalent widths (Å) are reported in the second rows. Upper limits are shown with $<$.

In the following, we characterize this effect using the $L_{\rm line}$ derived in Sect. 3.5 and the most recent $L_{\rm acc} - L_{\rm line}$ relations for Class II YSOs derived by Alcalá et al. (2014). These relations have been derived using the same method as described in Rigliaco et al. (2012), where $L_{\rm acc}$is obtained from the continuum excess emission and then compared with the $L_{\rm line}$ of the several emission line diagnostics in every object. In Alcalá et al. (2014) the sample is composed of 36 YSOs located in the Lupus I and Lupus III clouds, together with eight additional YSOs located in the σ-Ori region from Rigliaco et al. (2012). These relations are not quantitatively different from those in the literature, but have significantly smaller uncertainties and have been derived for stars with similar properties than the Class III analyzed here. For each Class III object, we compute $L_{\rm acc}$ from a number of different lines, as described in the following. This provides a measurement of the ``noise'' introduced in the determination of $L_{\rm acc}$ from line luminosities in Class II. It represents a typical threshold for determining $L_{\rm acc}$ in Class II objects by chromospheric activity, assuming that this is approximately the same in the two different classes of objects, with and without ongoing accretion. We define it in the following as $L_{\rm acc,noise}$.

3.6.1 Accretion luminosity noise

Alcalá et al. (2014) use a sample of Class II YSOs in the Lupus star forming region observed with X-Shooter to refine the $L_{\rm acc} - L_{\rm line}$ relations. We adopt their relations to estimate the $L_{\rm acc,noise}$ for our Class III YSOs, using in particular the Hα, Hβ, Hγ, Hδ, H8, H9, H10, H11, HeI ($\lambda\lambda$587.6, and 1083 nm), CaII (λ393 nm), CaII (λ849.8 nm), CaII (λ854.2 nm), and CaII (λ866.2 nm) lines. Moreover, we use the relation from Natta et al. (2004) between $\dot{M}_{\rm acc}$ and the 10% Hα width to estimate $L_{\rm acc,noise}$ from this indicator.

We show in Fig. 3.10-3.11 the values of $L_{\rm acc,noise}$ for every object obtained using the different indicators. The uncertainties on these values are dominated by the errors in the relations between $L_{\rm line}$ and $L_{\rm acc}$. Upper limits for undetected lines indicate the 3σ upper limits. Each Balmer line leads to values of $L_{\rm acc,noise}$ that always agree with the other Balmer lines by less than ~0.2 dex, and similarly the HeI$_{\lambda587.6}$ line almost in all cases. The HeI$_{\lambda1083}$ and the CaII lines, instead, in various cases do not agree with the result obtained using the Balmer and HeI$_{\lambda587.6}$ lines, with differences even larger than 0.6 dex. It should be considered that the exact value of the CaII IRT lines luminosity is subject to many uncertainties, owing to the complicated procedure for estimating the excess luminosity (see Sect. 3.5.3).

The Paschen and Brackett HI emission lines are not detected in our spectra, as pointed out in Sect. 3.5.1. We report in Figs. 3.10-3.11 the 3σ upper limits for $L_{\rm acc,noise}$ obtained using the Paβ and Brγ line luminosities and the relations from Alcalá et al. (2014). These values are always below the mean $L_{\rm acc,noise}$ value obtained with the Balmer and HeI$_{\lambda587.6}$ lines. This implies that those lines are less sensitive to chromospheric activity than the Balmer lines.

The 10% Hα width is the accretion indicator that leads to values of $L_{\rm acc,noise}$ that are more discrepant from the mean (Figs. 3.10-3.11). This clearly does not follow in more than 50% of the cases the results obtained using the other indicators. This is not surprising

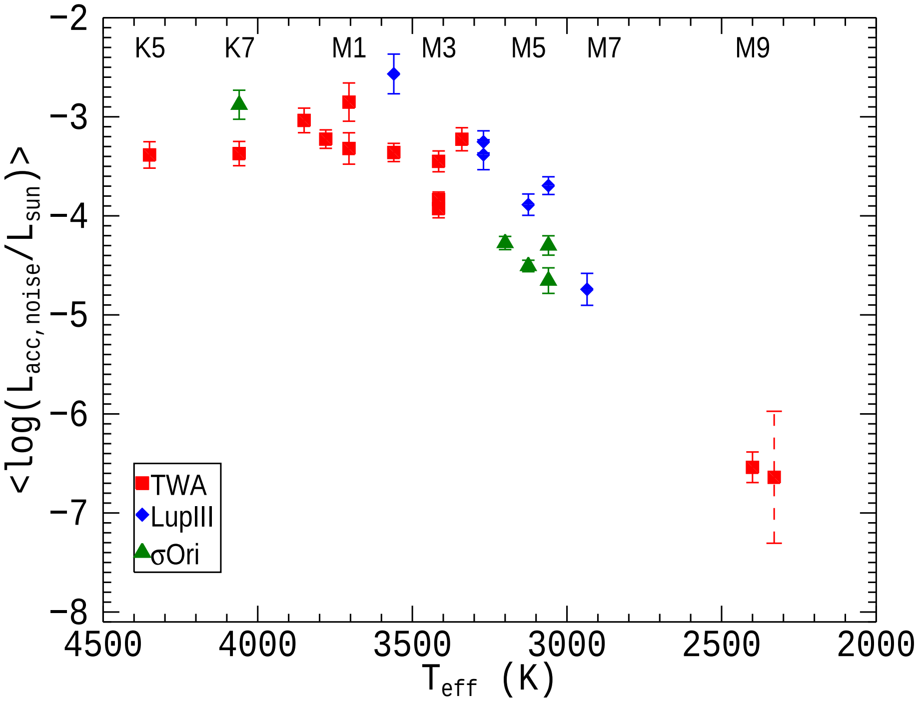

Figure 3.12: Mean values of $\log(L_{\rm acc,noise}/L_\odot)$ obtained with different accretion diagnostics as a function of $T_{\rm eff}$. Error bars represent the standard deviation around the mean $\log(L_{\rm acc,noise}/L_\odot)$. These data should be intended as the noise in the values of $L_{\rm acc}$ due to chromospheric emission flux.

since the Hα width is mainly a kinematics measurement, unlike $L_{\rm line}$ measurements. It is to be expected that the application of a method calibrated for accretion processes to chromospheric activity would result in inconsistencies. We know that the broadening of the Hα line and the other accretion-related lines is due to the high-velocity infall of material in the accretion flows, while the intensity of the emission lines is due to emission from the high-temperature region. The latter can be either accretion shocks on the stellar surface or chromospheric emission. That in our sample of non-accreting objects relations converting $L_{\rm line}$ to $L_{\rm acc}$ lead to similar results when using line fluxes, while the result is quite different when using line broadening seems to confirm that the Hα 10% width we detect is only due to thermal broadening in the chromosphere of these stars and not to the gas flow kinematics associated with the accretion onto the central object.

For all objects, the mean $L_{\rm acc,noise}$ value is always below $\sim 10^{-3}L_\odot$, and this value decreases monotonically with the SpT. In Fig. 3.12 these mean values of $\log(L_{\rm acc,noise}/L_\odot)$ obtained with the Balmer and HeI$_{\lambda587.6}$ lines are plotted as a function of the $T_{\rm eff}$ of the objects. The error bars on the plot represent the standard deviation of the derived values of $L_{\rm acc,noise}$[3]. These values should be intended as the noise in the $L_{\rm acc}$ values arising from

---

[3] For the object TWA29, where only the Hα line is detected, we report the error on the estimate of

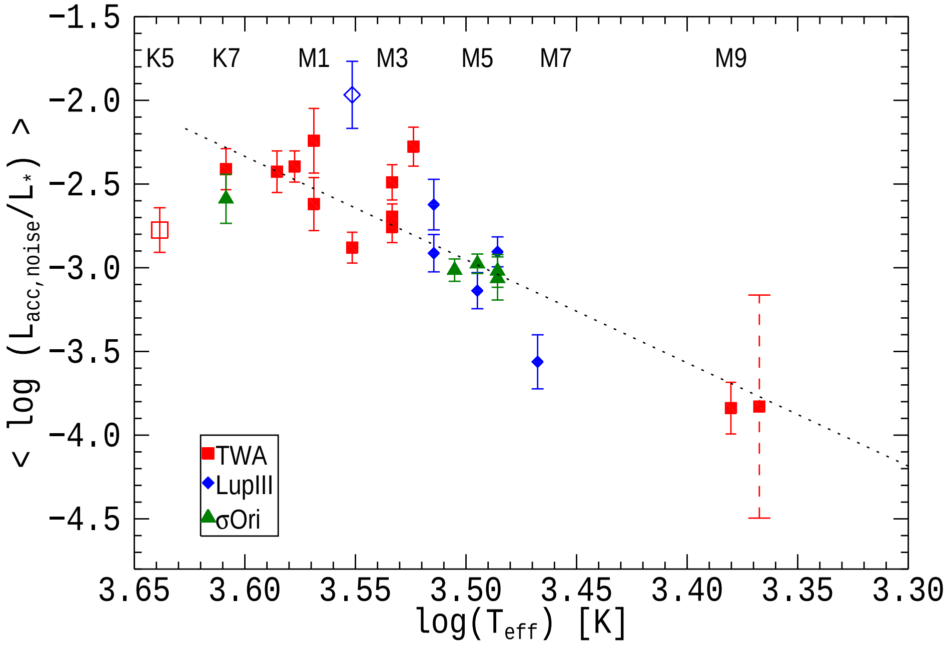

Figure 3.13: Mean values of $\log(L_{\mathrm{acc,noise}}/L_\star)$ obtained with different accretion diagnostics as a function of $\log T_{\mathrm{eff}}$. The dashed line is the best fit to the data, whose analytical form is reported in Eq. (3.2). Two objects (Sz122 and TWA9A) are excluded from the fit (empty symbols), as explained in the text.

the chromospheric activity. In Fig. 3.13 we show the mean values of the logarithmic ratio $L_{\mathrm{acc,noise}}/L_\star$ obtained using the Balmer and $\mathrm{HeI}_{\lambda 587.6}$ lines as a function of the T_{eff}. Unlike Fig. 3.12, the quantity $L_{\mathrm{acc,noise}}/\mathrm{L}_\star$ is unbiased by uncertainties on distance values or by different stellar ages, leading to smaller spreads. We see that from the K7 objects down to the BDs, the values of $\log(L_{\mathrm{acc,noise}}/L_\star)$ decrease with the T_{eff} of the YSOs. After fitting the $L_{\mathrm{acc,noise}}$- T_{eff} relation with a powerlaw, using only the objects in the range K7-M9.5, and excluding Sz122 (see Appendix 3.A for details), we obtain the following analytical relation (Fig. 3.13):

$$\log(L_{\mathrm{acc,noise}}/L_\star) = (6.17 \pm 0.53) \cdot \log T_{\mathrm{eff}} - (24.54 \pm 1.88). \tag{3.2}$$

The only clear deviation from the general trend, apart from Sz122, is the K5 YSO TWA9A, which shows a value of $\log(L_{\mathrm{acc,noise}}/L_\star)$ lower by ~0.6 dex with respect to what should be expected by the extrapolation of the previous relation. Unfortunately, our sample is too small, and we do not have other objects with earlier SpT to verify whether this low value is actually a different trend due to different chromospheric activity for earlier SpT YSOs or if the source is peculiar. There are also signatures of different chromospheric activity intensity among objects with the same SpT and located in the same region; for

---

$L_{\mathrm{acc,noise}}/L_\odot$ from this line in Figs. 3.12-3.13 with a dashed line.

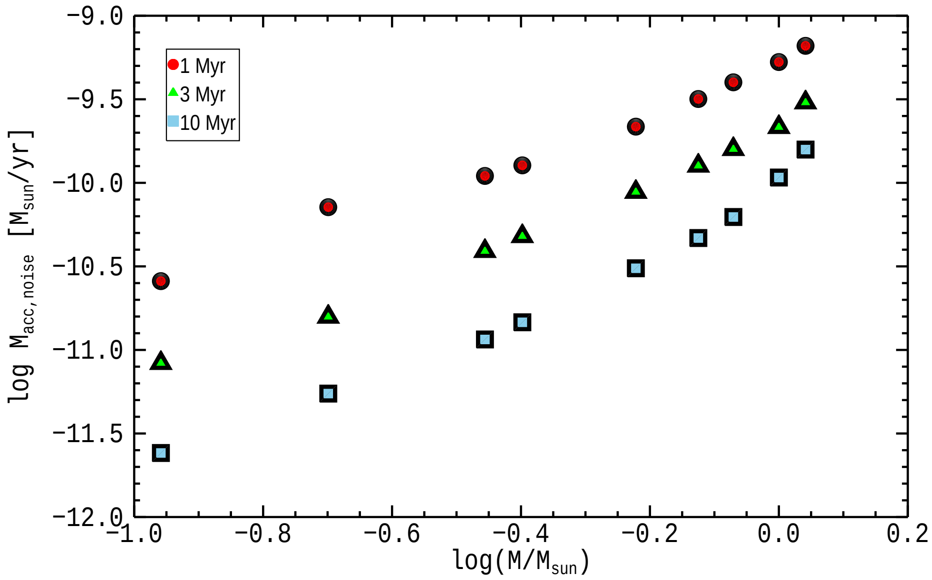

Figure 3.14: $\log\dot{M}_{\rm acc,noise}$ as a function of $\log M_\star$, with values of $\dot{M}_{\rm acc,noise}$ obtained using three different isochrones from Baraffe et al. (1998) and the values of $L_{\rm acc,noise}/L_\star$ derived from the fit in Eq. (3.2) at any $T_{\rm eff}$. Results using the 1 Myr isochrone are reported with filled circles, those using the 3 Myr isochrone with filled triangles, and those using the 10 Myr isochrone with filled squares.

example, the two TW Hya M1 YSOs, which are two components of a binary system, thus coeval objects, have a spread in $\log(L_{\rm acc,noise}/L_\star)$ of $\sim$0.5 dex.

Values of $L_{\rm line}$ and $L_{\rm acc}$ in Class II YSOs that are close to those estimated in this work should be considered very carefully, because the chromospheric activity could be an important factor in the excess luminosity in the line and could produce misleading results.

3.6.2 Mass accretion rate noise

In this section, we determine what the typical ``chromospheric noise" on $\dot{M}_{\rm acc}$ would be when derived from indirect methods if the chromospheric emission is not subtracted before computing $L_{\rm line}$. We refer to this quantity as $\dot{M}_{\rm acc,noise}$.

The procedure is the following. We select three isochrones (1, 3, and 10 Myr) from Baraffe et al. (1998) models and nine different YSOs masses (0.11, 0.20, 0.35, 0.40, 0.60, 0.75, 0.85, 1.00, and 1.10 $M_\odot$), which always correspond to $T_{\rm eff}$ in the range 2500-4000 K, where our results are applicable. Then, for each $T_{\rm eff}$ we derive $L_{\rm acc,noise}/L_\star$ using the fit reported in Eq. (3.2). Finally, we use Eq. (3.1), adopting the proper $R_\star$, $M_\star$, and $L_\star$ at any age from the Baraffe et al. (1998) tracks, in order to determine the typical $\dot{M}_{\rm acc,noise}$ at different ages as a function of $M_\star$. The results are shown in Fig. 3.14, where a strong correlation between the two parameters is evident, with increasing $\dot{M}_{\rm acc,noise}$ with $M_\star$. At the same time, the variation in $\dot{M}_{\rm acc,noise}$ with age at any given $M_\star$ is large, up to 0.5 dex

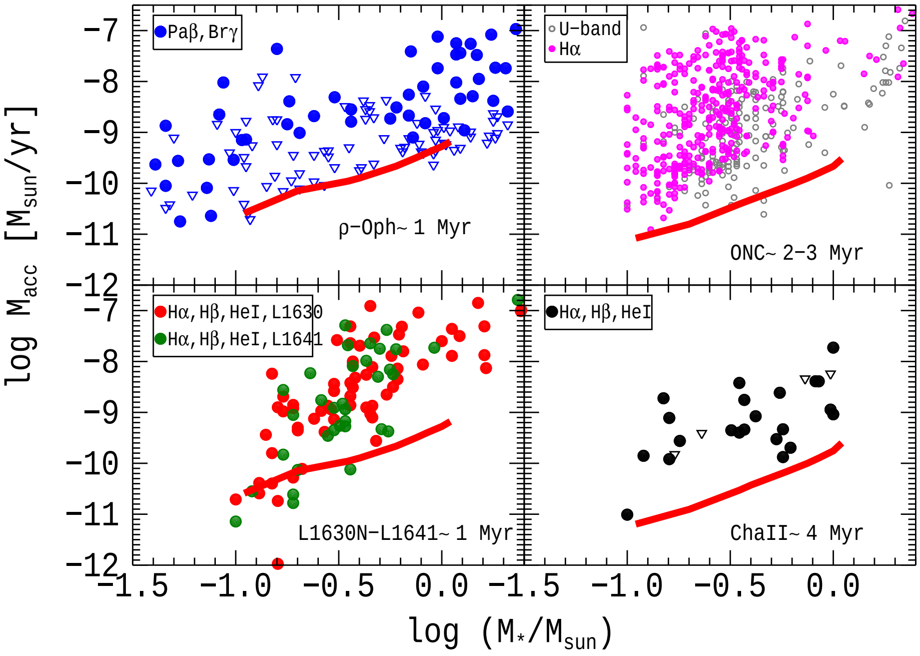

Figure 3.15: $\log\dot{M}_{\rm acc}$ as a function of $\log M_\star$ for Class II objects located in different star forming regions. Data for ρ-Oph are from Natta et al. (2006), corrected for new distance measurements by Rigliaco et al. (2011a); ONC points are from Manara et al. (2012), data for L1630N and L1641 are from Fang et al. (2009), and those for ChaII from Biazzo et al. (2012). $\dot{M}_{\rm acc}$ values obtained with indirect methods are shown with colored, filled points, while measurements based on the direct U-band excess method are shown with gray empty points as a reference. Downwards triangles refer to upper limits. The thick red solid line is the lower limit to the measurements of $\dot{M}_{\rm acc}$ set by chromospheric activity in the line emission. We use the values for the correct isochrone according to the mean value of the age for each region, as reported on the plot.

for differences of 2 Myr at the H-burning limit, but decreases with increasing $M_\star$. Similar results are obtained when using other evolutionary models.

We derive a limit on the detectable $\dot{M}_{\rm acc}$ of $\sim 6.6 \cdot 10^{-10}$ $M_\odot$/yr for solar-mass, young (1 Myr) objects, decreasing to $2.5 \cdot 10^{-12}$ $M_\odot$/yr for low-mass, older (10 Myr) objects. We report these $\dot{M}_{\rm acc,noise}$ values for the three isochrones analyzed in Table 3.8.

Comparison with literature data

As discussed, $\dot{M}_{\rm acc,noise}$ is a lower limit to the values of $\dot{M}_{\rm acc}$ that can be derived from the luminosity of lines emitted by stellar chromospheres. In this section, we compare this chromospheric limit with estimates of $\dot{M}_{\rm acc}$ based on $L_{\rm line}$ from the literature. We show in Fig. 3.15 values of $\dot{M}_{\rm acc}$ as a function of $M_\star$ obtained with optical or NIR emission lines as accretion diagnostic for objects located in four star forming regions with different ages: ρ-Ophiucus, the Orion Nebula Cluster, the L1630N and L1641 regions, and the Chameleon II region. We overplot the locii of $\dot{M}_{\rm acc,noise}$ obtained using the proper isochrone for the mean age of each region. In this way we do not address possible differences in $\dot{M}_{\rm acc}$ due to

Table 3.8: Values of log$\dot{M}_{\rm acc,noise}$ at different $M_\star$ and ages

$M_\star$	Age [Myr]		
[$M_\odot$]	1	3	10
0.11	−10.59	−11.08	−11.62
0.20	−10.15	−10.80	−11.26
0.35	−9.96	−10.41	−10.94
0.40	−9.90	−10.32	−10.83
0.60	−9.66	−10.05	−10.51
0.75	−9.50	−9.90	−10.33
0.85	−9.40	−9.80	−10.20
1.00	−9.28	−9.67	−9.97
1.10	−9.18	−9.52	−9.80

Notes. Values of log$\dot{M}_{\rm acc,noise}$ at different $M_\star$ and different ages obtained using isochrones from Baraffe et al. (1998) and the procedure explained in Sect. 3.6.2.

age spreads in these regions, but these spreads, if present, are $\lesssim$1-2 Myr (see e.g. Reggiani et al., 2011). The effect of a similar age spread on the $\dot{M}_{\rm acc,noise}$ threshold would be ~0.5 dex for low-mass objects and ~0.3 dex for solar-mass stars (see Fig. 3.14).

We consider in this analysis $\dot{M}_{\rm acc}$ values obtained using optical emission lines. In Fig. 3.15 we show the values for the ~1 Myr old regions L1630N and L1641 (Fang et al., 2009), where the Hα, Hβ, and HeI lines were used, those for the ~ 2-3 Myr old Orion Nebula Cluster (Manara et al., 2012) obtained with photometric narrow-band Hα luminosity estimates[4], and those obtained with the Hα, Hβ, and HeI lines for the ~4 Myr old Chameleon II region (Biazzo et al., 2012). In all these cases, the vast majority of datapoints are found, as expected, well above the $\dot{M}_{\rm acc,noise}$ threshold, confirming that the chromospheric contribution to the line emission is negligible for strongly accreting YSOs. Nevertheless, there are a few (11) objects in L1630N and L1641, where measured values of $\dot{M}_{\rm acc}$ are lower than the expected $\dot{M}_{\rm acc,noise}$. One possibility to explain this result is variable accretion in these objects, which has been found to vary as much as 0.4 dex on time scales of one year (Costigan et al., 2012). Still, this does not explain why only lower mass objects happen to be below the threshold. In any case, these points should be considered with caution, since the measured $L_{\rm line}$ could be completely due to chromospheric emission, leading to erroneous estimates of $\dot{M}_{\rm acc}$.

For the ~1 Myr old ρ-Ophiucus region we consider the $L_{\rm line}$ derived through Paβ and Brγ lines (Natta et al., 2006), corrected for a more recent estimate of the distance (see Rigliaco et al., 2011a). As we noted in Sects. 3.5.1 and 3.6.1, Paβ and Brγ lines are not detected in our Class III YSOs spectra. In Fig. 3.15, all the detections are located well above the $\dot{M}_{\rm acc,noise}$ locus, while the upper limits are distributed also at the edge of the $\dot{M}_{\rm acc,noise}$ threshold. This confirms the validity of these NIR lines as good tracers of accretion and the fact that they are most likely less subject to chromospheric noise than the Balmer and HeI$_{\lambda 587.6}$ lines.

---

[4] We also report the values of $\dot{M}_{\rm acc}$ obtained through U-band excess by Manara et al. (2012), which are shown as a comparison.

3.7 Conclusion

In this paper, we presented the analysis of 24 diskless, hence nonaccreting, Class III YSOs, observed with the broad-band, medium-resolution, high-sensitivity VLT/X-Shooter spectrograph. The targets are located in three nearby star forming regions (Lupus III, σ-Ori, and TW Hya) and have SpT in the range from K5 to M9.5. We checked the SpT classifications, using both spectral indices and broad molecular bands. Moreover, using the flux calibrated spectra, we derived the stellar luminosity. Then, we analyzed the emission lines related to accretion processes in accreting objects that are present in these spectra and, from their luminosities, we studied the implications of chromospheric activity for $\dot{M}_{\rm acc}$ determination in accreting (Class II) objects. This was done by deriving the parameter $L_{\rm acc,noise}$, which is the systematic ``noise" introduced by chromospheric emission in the measurements of $L_{\rm acc}$ from line emission in Class II objects. For this analysis we assumed a similar chromospheric activity in the two classes of objects.

Our main conclusions are:

1. All hydrogen recombination emission lines of the Balmer series are detected in our sample of Class III YSOs spectra when the S/N is high enough. In contrast, Paschen and Brackett series lines are not detected in emission, and they are significantly weaker, when compared to Balmer lines, than in Class II objects. The chromospheric ``noise'' in these lines is lower than in the optical lines (see Figs. 3.10-3.11), and they are very good tracers of accretion in low-mass, low accretion rate objects.

2. Using Balmer and HeI$_{\lambda 587.6}$ lines and the calibrated relations between $L_{\rm line}$ and $L_{\rm acc}$ from the literature, we derived $L_{\rm acc,noise}$ values that always show good agreement among all the lines.

3. Calcium emission lines in the NIR spectral range ($\lambda\lambda$ 849.8, 854.2, 866.2 nm) are detected in 11 objects (45% of the sample) superposed on the photospheric absorption lines. This results in a more complicated line flux measurement than for other lines. Their behavior with respect to the hydrogen line luminosities is different; in particular, the values of $L_{\rm acc,noise}$ obtained using these lines often do not agree well with those obtained using Balmer and HeI$_{\lambda 587.6}$ lines.

4. The mean values of $L_{\rm acc,noise}$ for the objects in our sample are lower than $\sim 10^{-3} L_\odot$ and have a clear dependence with $T_{\rm eff}$ for K7-M9.5 objects. Therefore, $L_{\rm acc}$ of this order or smaller measured in Class II objects using line luminosity as a proxy of accretion may be significantly overestimated if the chromospheric contribution to the line luminosity is not taken into account.

5. Our results show that the ``noise" due to chromospheric activity on the estimate of $\dot{M}_{\rm acc}$ in Class II YSOs obtained using secondary indicators for accretion has a strong dependence on $M_\star$ and age. Typical values of log($\dot{M}_{\rm acc,noise}$) for M-type YSOs are in the range from ~ -9.2 for solar-mass young (1 Myr) objects to -11.6 $M_\odot$/yr for low-mass, older (10 Myr) objects. Therefore, derived accretion rates below this threshold

should be treated with caution because the line emission may be dominated by chromospheric activity.

Aknowledgements C.F.M. acknowledges the PhD fellowship of the International Max-Planck-Research School. We thank Aleks Scholz, Greg Herczeg, and Luca Ricci for insightful discussions.
This research made use of the SIMBAD database and of the VizieR catalog access tool, operated at the CDS, Strasbourg, France.

3.A Comments on individual objects

Sz94

Sz94 was discovered as an Hα emitting star in the survey by Schwarz (1977). Since then, it has been considered as a PMS star in reviews and investigations (Krautter, 1992; Hughes et al., 1994; Comerón, 2008; Mortier et al., 2011), but nothing has been mentioned about the presence of the lithium absorption line at 670.8 nm. Based on its spectral energy distribution, Sz94 has been classified as a Class III IR YSO by Merín et al. (2008). For all these reasons, we included the star in our program as a Class III template of M4 SpT. Notwithstanding the high quality of the X-Shooter data in terms of S/N and resolution, the Li I λ 670.8 nm line is not present in the spectrum, and we determine an upper limit of $\mathrm{EW_{Li}} < 0.1$Å. The question then rise whether lithium may have already been depleted in the star. However, lithium is significantly depleted by large factors only after several tens of Myr, inconsistently with the average age of a few Myr of the Lupus members. Analysis of the radial velocity of this object shows that its value is in the typical range for Lupus sources (Stelzer et al., 2013). We consider here the source as a PMS, given its position in the HRD, the Hα emission, and the radial velocity measurement, but more analysis should be done to confirm its PMS status.

Sz122

Sz122 is a Class III object classified with *Spitzer* (Merín et al., 2008). All the lines of this object appear very broadened. Nevertheless, the spectrum cannot be fitted with synthetic spectra broadened at reasonable values of $v \sin i$, meaning that this is not a single fast rotator. We think, therefore, that this object is a binary system. This could explain the very faint LiI line ($\mathrm{EW_{Li}} < 0.25$ Å) and the lack of emission in the CaII IRT absorption features, which is usually found in other early M-type objects of our sample. Even the presence of a broad Hα line (10% width > 600 km/s) can be explained by the presence of two objects. We do not consider this object in the analysis of the implications of chromospheric activity on $\dot{M}_{\mathrm{acc}}$ measurements, because the effect of its binarity cannot be accounted for.

Sz121

Similar to Sz122, the lines of this object appear very broadened. Also in this case, the object is classified with *Spitzer* as a Class III (Merín et al., 2008). We can fit the spectrum with a synthetic spectrum of the same $T_{\rm eff}$, $\log g$=4.0, and $v \sin i$ = 70 km/s. This value of $v \sin i$ is rather high for a typical M4-type YSO. If true, it would be an extreme ultrafast rotator. The large 10% Hα width ($\sim$380 km/s) is then due to its very high rotational velocity. Another possibility is that this object may also be an unresolved spectroscopic binary.

TWA6

This object has been discovered and classified as a young nonaccreting object by Webb et al. (1999). It is a member of the TWA association, and it is a known fast rotator ($v \sin i$=72 km/s, Skelly et al. (2008)). We measure a 10% Hα width of 362 km/s. This is larger than the threshold to distinguish the accreting and nonaccreting objects proposed by White & Basri (2003). Nevertheless, this object can be considered a Class III YSO for the small $EW_{H\alpha}$, the small Balmer jump, and in particular, the IR classification. For these reasons we consider this object in our analysis.

3.B NIR spectral indices

Spectral indices in the NIR part of the spectrum are particularly useful for classifying VLM stars and BDs, which emit most of their radiation in this spectral region. Therefore, various analyses to calibrate reliable NIR indices to classify late M-type objects and BDs have been carried out in the past (e.g. Kirkpatrick et al., 1999). With our sample, we are able to verify the validity of various NIR indices for M-type YSOs, comparing the SpT obtained through optical spectroscopy (Sect. 3.3). We consider in this analysis different NIR indices that have been calibrated using either dwarfs or young stars (subgiants) for objects with SpT M or later. In particular, Rojas-Ayala et al. (2012) calibrated the $H_2O - K2$ index using a sample of M dwarfs, and derived a relation valid for the whole M class. Allers et al. (2007) calibrated the gravity-independent spectral index H_2O on a sample of young BDs and dwarfs. This is valid for objects with SpT in the range M5-L0. Testi et al. (2001) and Testi (2009) proposed various spectral indices (sH_2O^J, sH_2O^K, sKJ, sHJ, sH_2O^{H1}, sH_2O^{H2}, I_J, I_H, and I_K) to classify M-, L-, and T-type BDs, calibrating those on a large sample of dwarfs; finally, Scholz et al. (2012) used a sample of VLM YSOs to calibrate the HP index, which is valid for objects with SpT in the range M7-M9.5. We report those indices in Table 3.9.

Figure 3.16 shows the results of this analysis. The SpTs obtained in Sect. 3.3 are reported as a function of each spectral index for our objects. For the spectral indices derived in Testi et al. (2001) and Testi (2009), we report also the data for the sample of L- and M-type dwarfs they adopted in the analysis. We stress that the latter sample should be considered with

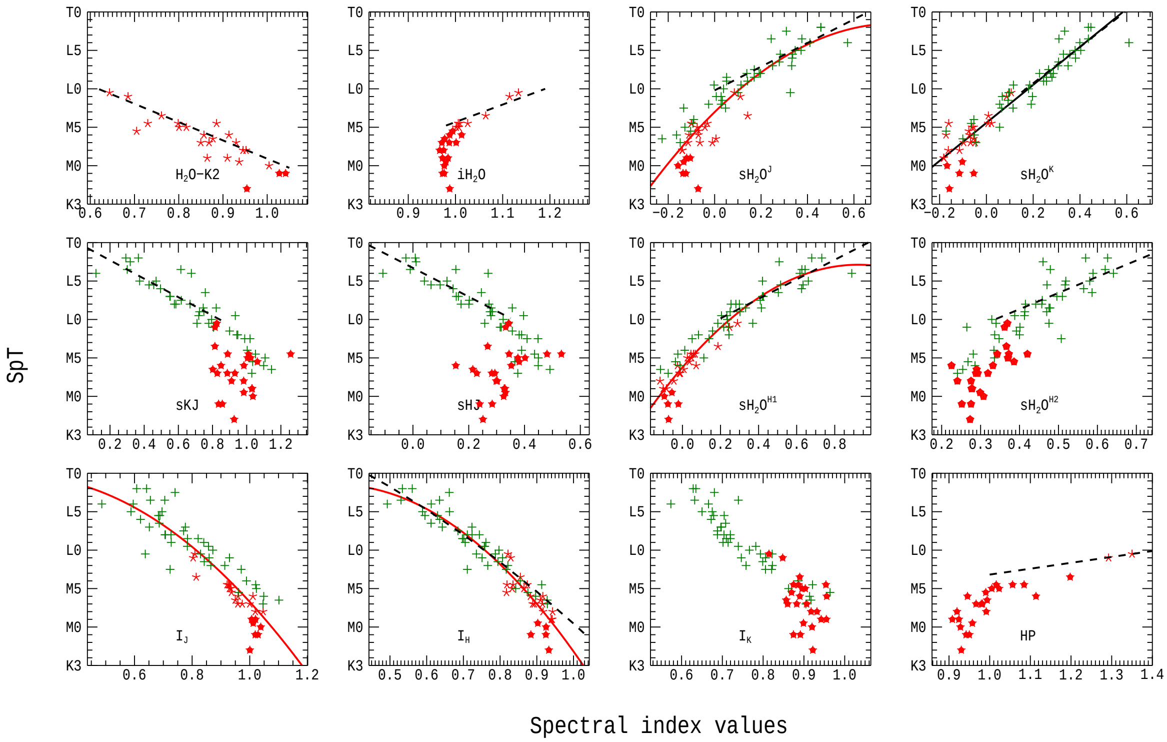

Figure 3.16: Spectral type of the objects as a function of the spectral index values obtained with different NIR indices (Table 3.9). Red symbols are values from this work, while green crosses are from Testi et al. (2001) and Testi (2009). Red stars are used for objects with SpT in the range of validity of the index, while red pentagons for those not in the range of validity of the index. Dashed lines are the best fit from the reference cited in Table 3.9 for each index, when available. No published relations are available for the indices I_J and I_K. Black and red solid lines are the best fits (black = linear, red = polynomial) from this work, considering both our sample and the values from the literature.

caution, since gravity dependent spectral indices calibrated using samples of dwarfs may not be reliable for YSOs, which are subgiants.

We see that the indices sH$_2$O^{H2}, sKJ, sHJ, and I$_K$ cannot be used to classify YSOs of M-type class. In contrast, we find a good correlation with the indices sH$_2$O^K, sH$_2$O^J, sH$_2$O^{H1}, I$_J$, and I$_H$. For these indices we decide to fit our objects and those from the literature together in all cases, using either a linear or a second-degree polynomial fit. We show the best fit obtained in Fig. 3.16. Using these relations, we derived the SpT for each of our YSOs, and we report these results in Table 3.4. We thus propose new SpT-spectral index relations for the following five indices from Testi et al. (2001) and Testi (2009). The first three are valid for objects with SpT later and equal to M1:

$$\text{SpT} - \text{code} = 0.55 + 2.48 \cdot sH_2O^K \tag{3.3}$$

$$\text{SpT} - \text{code} = 0.38 + 2.89 \cdot sH_2O^{H1} - 1.56 \cdot (sH_2O^{H1})^2 \tag{3.4}$$

$$\text{SpT} - \text{code} = 1.11 + 3.92 \cdot I_H - 5.35 \cdot (I_H)^2. \tag{3.5}$$

The following two indices are valid for objects with SpT later and equal to M2:

$$\text{SpT} - \text{code} = 0.70 + 2.90 \cdot sH_2O^J - 1.78 \cdot (sH_2O^J)^2 \tag{3.6}$$

$$\text{SpT} - \text{code} = 1.83 + 1.08 \cdot I_J - 2.59 \cdot (I_J)^2 \tag{3.7}$$

where the SpT are coded in the following way: M0 $\equiv$ 0.0, M9 $\equiv$ 0.9, L5 $\equiv$ 1.5, and a variation of 0.1 corresponds to a step of one subclass. For these spectral indices we conclude that results for objects with SpT in the nominal range of validity of each index are reliable within a typical uncertainty of about one subclass.

A good correlation is also found for the spectral index $H_2O - K2$. Using the analytical relation between SpT and spectral index from the literature, we obtain for 13 out of 22 objects with M SpT results that are compatible within one subclass with the correct SpT (see Table 3.4). The differences can be due to the imperfect telluric removal in the first interval of interest of this index. Moreover, we confirm that the H$_2$O index is valid for YSOs with SpT in the range M5-M9.5, finding agreement within one subclass for all our objects (see Table 3.4). Regarding the HP index, we confirm that it is not valid for YSOs with SpT earlier than M7, and we observe that the SpT obtained with this index confirm those from the literature for our two later SpT objects (see Table 3.4).

Table 3.9: NIR spectral indices analyzed in Appendix 3.B

Index	Range of validity	Numerator [nm]	Denominator [nm]	Reference
H_2O-K2	M0-M9	(2070-2090) / (2235-2255)	(2235-2255) / (2360-2380)	Rojas-Ayala et al. (2012)
I_J	M0-T9	(1090-1130) + (1330-1350)	2·(1265-1305)	Testi (2009)
I_H	M0-T9	(1440-1480) + (1760-1800)	2·(1560-1600)	Testi (2009)
I_K	M0-T9	(1960-1990) + (2350-2390)	2·(2120-2160)	Testi (2009)
H_2O	M5-L5	1550-1560	1492-1502	Allers et al. (2007)
sHJ	L0-L9	(1265-1305) - (1600-1700)	0.5·[(1265-1305) + (1600-1700)]	Testi et al. (2001)
sKJ	L0-L9	(1265-1305) - (2120-2160)	0.5·[(1265-1305) + (2120-2160)]	Testi et al. (2001)
sH_2O^J	L0-L9	(1265-1305) - (1090-1130)	0.5·[(1265-1305) + (1090-1130)]	Testi et al. (2001)
sH_2O^{H1}	L0-L9	(1600-1700) - (1450-1480)	0.5·[(1600-1700) + (1450-1480)]	Testi et al. (2001)
sH_2O^{H2}	L0-L9	(1600-1700) - (1770-1810)	0.5·[(1600-1700) + (1770-1810)]	Testi et al. (2001)
sH_2O^K	L0-L9	(2120-2160) - (1960-1990)	0.5·[(2120-2160) + (1960-1990)]	Testi et al. (2001)
HIP	M7-M9.5	(1675-1685)	(1495-1505)	Scholz et al. (2012)

3.C On-line material

NIR spectra

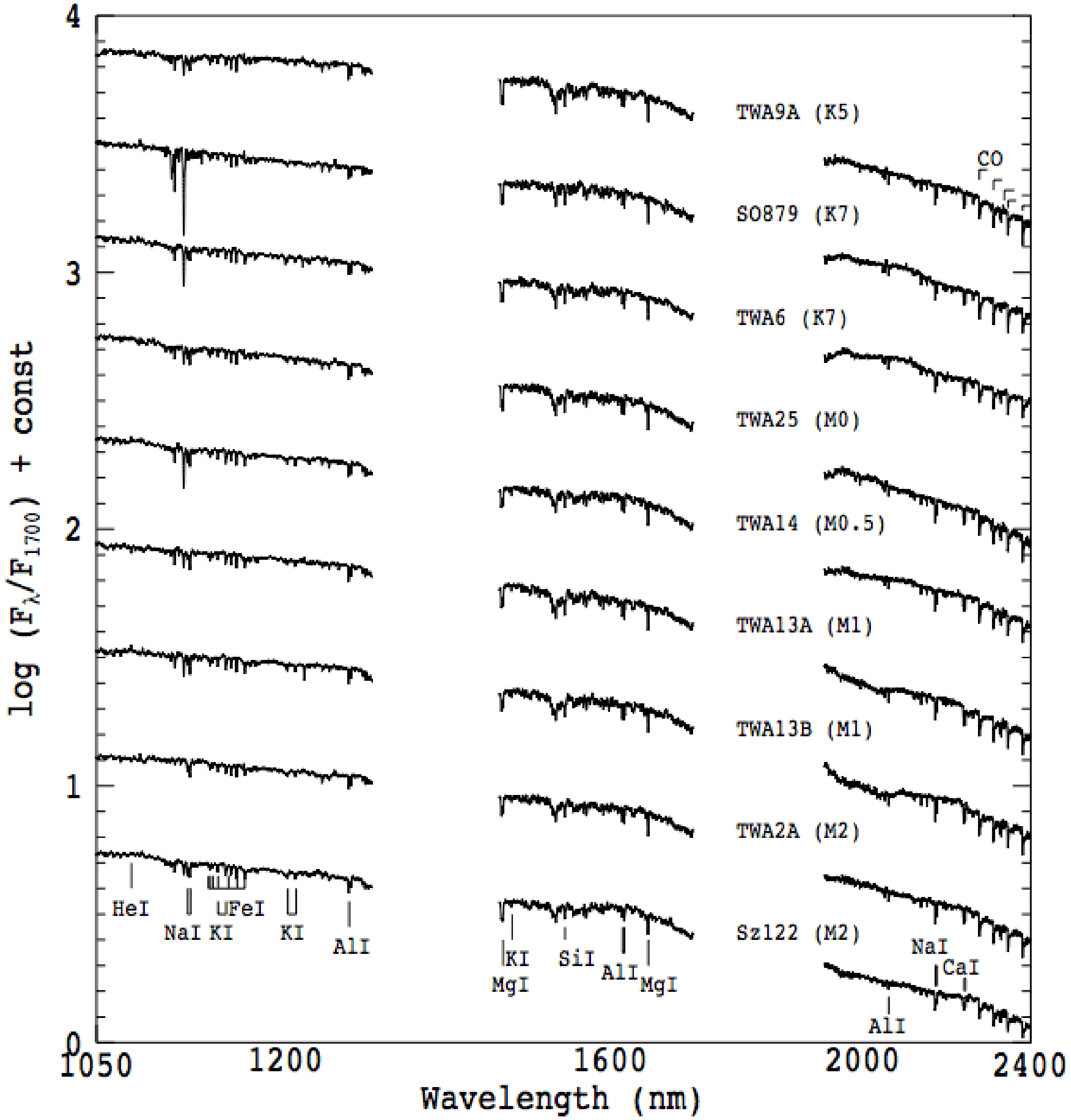

Figure 3.17: Spectra of Class III YSOs with spectral type earlier than M3 in the NIR arm. All the spectra are normalized at 1700 nm and offset in the vertical direction by 0.5 for clarity. The spectra are also smoothed to the resolution of 2000 at 2000 nm to make identification of features easier.

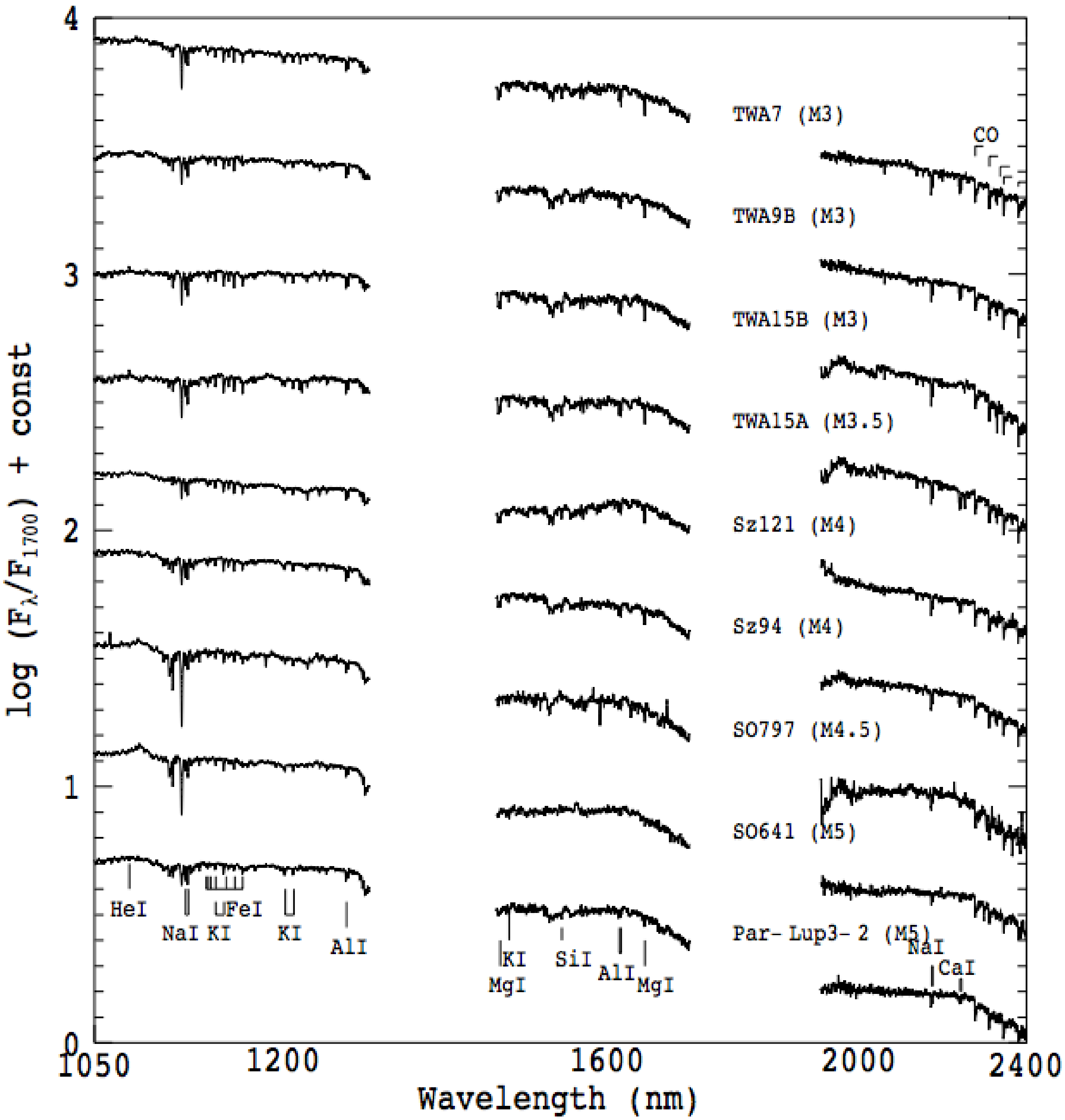

Figure 3.18: Same as Fig. 3.17, but for spectral types between M3 and M5.

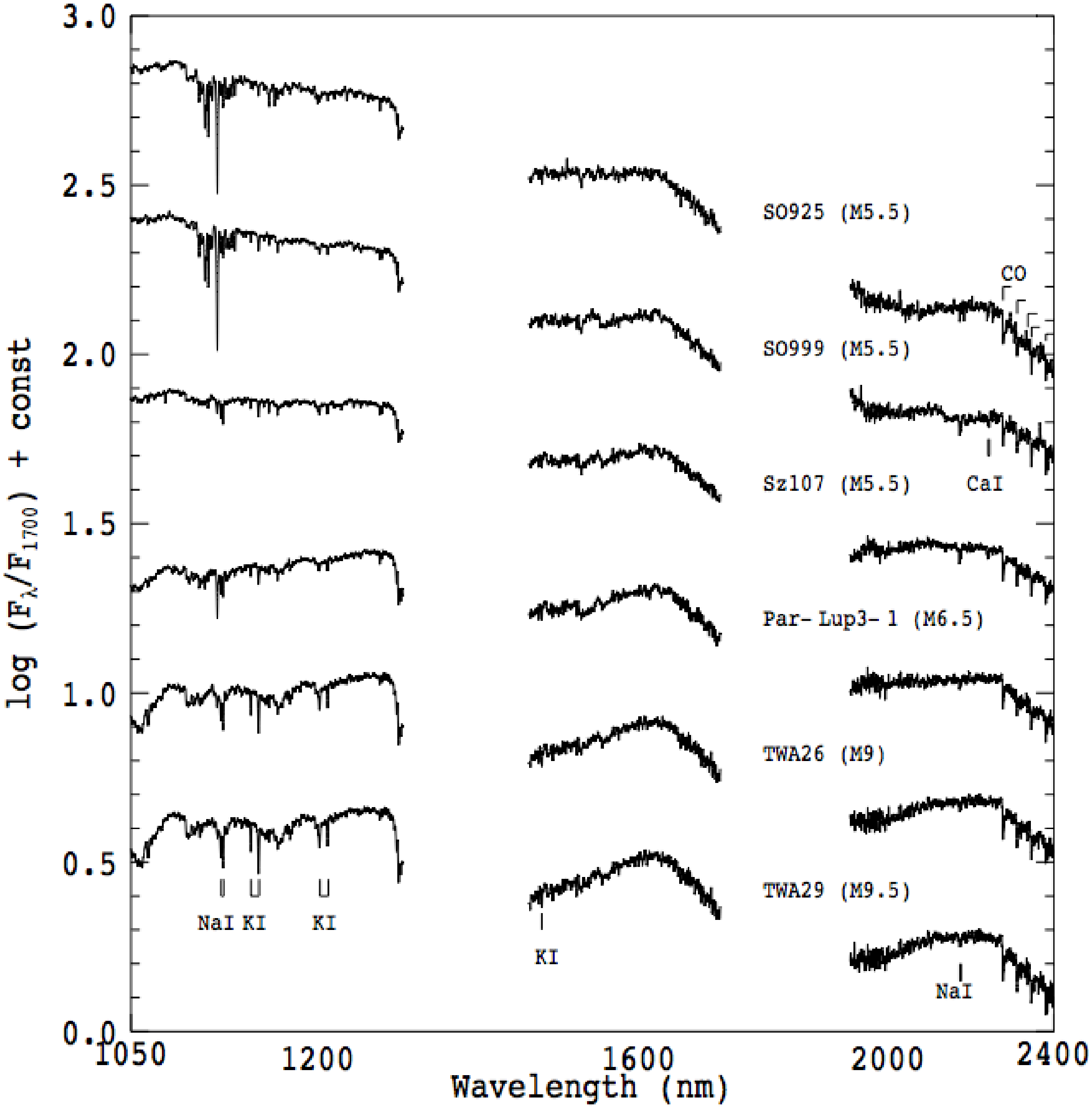

Figure 3.19: Same as Fig. 3.17, but for spectral types later than M5.

UVB spectra

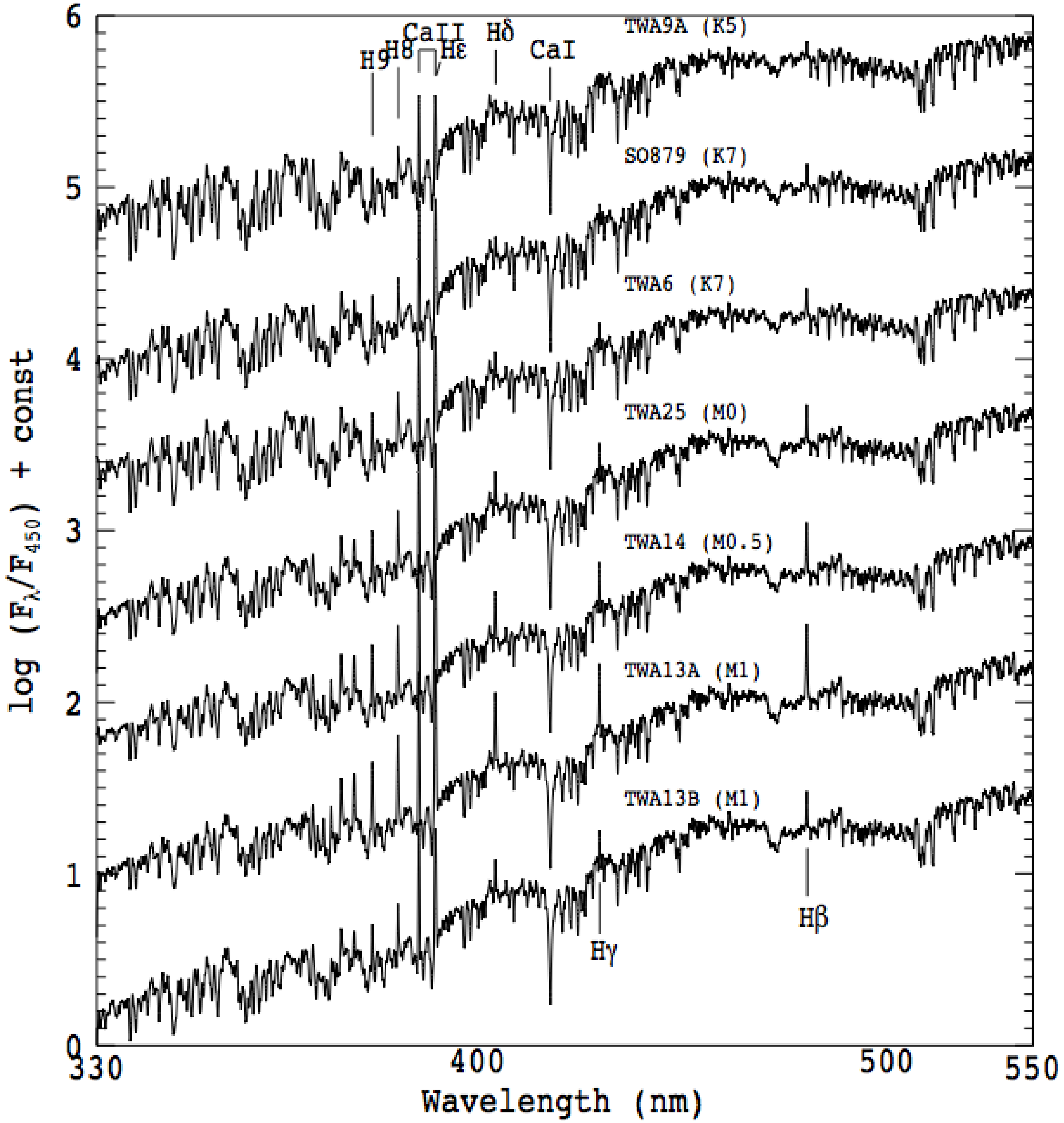

Figure 3.20: Spectra of Class III YSOs with spectral type earlier than M2 in the UVB arm. All the spectra are normalized at 450 nm and offset in the vertical direction for clarity. The spectra are also smoothed to the resolution of 1500 at 400 nm to make identification of features easier.

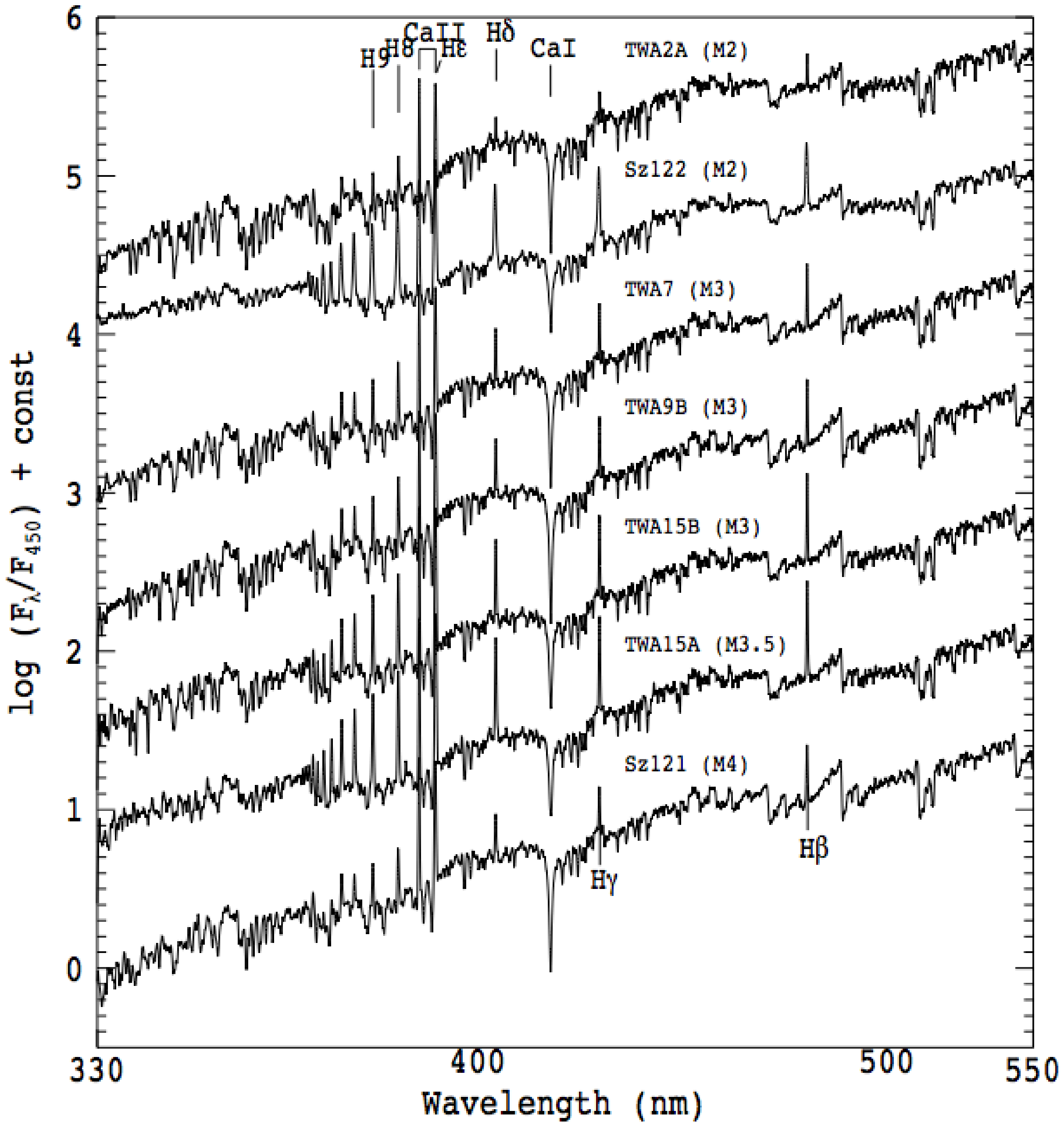

Figure 3.21: Same as Fig. 3.20, but for spectral types between M2 and M4.

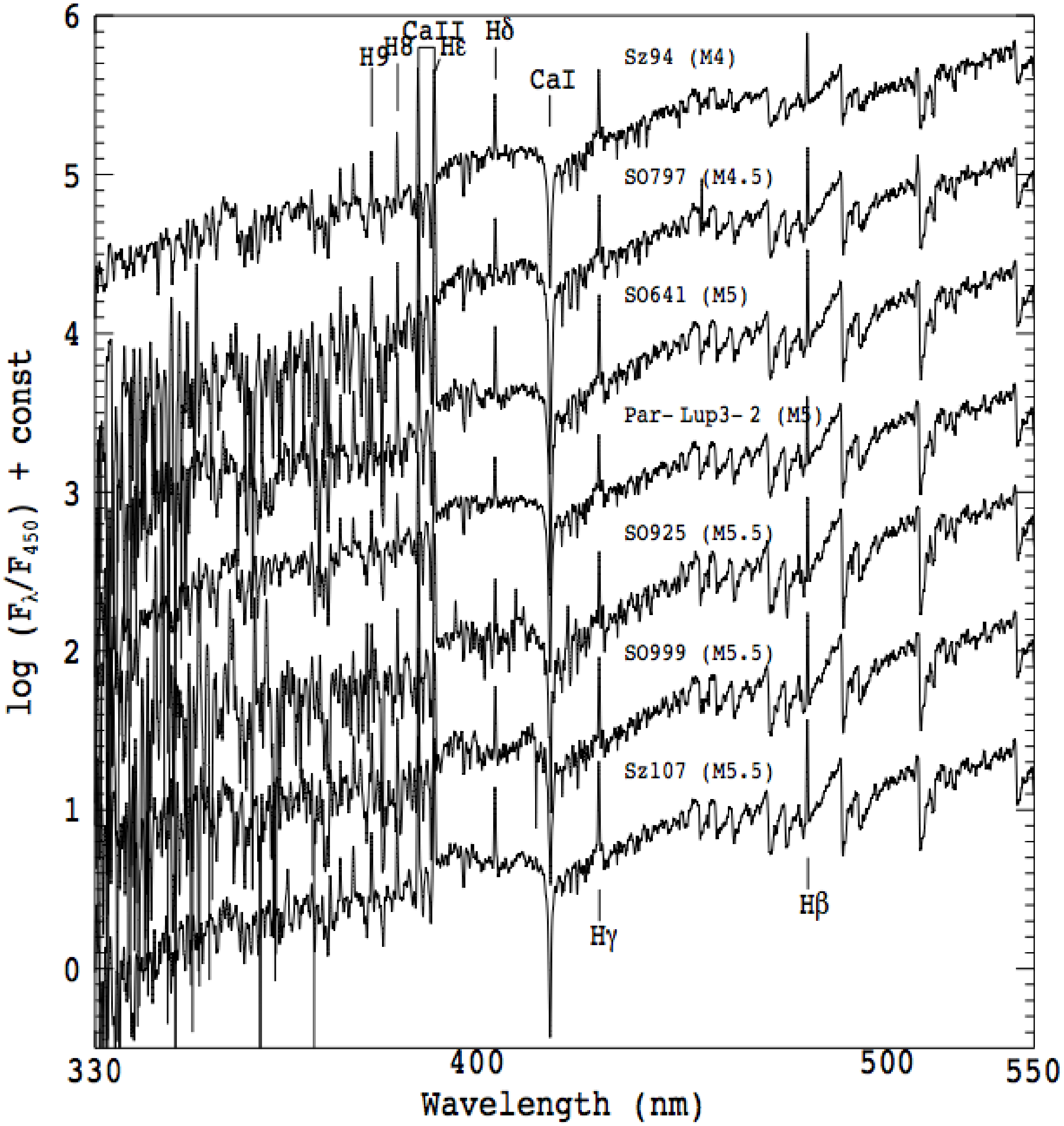

Figure 3.22: Same as Fig. 3.20, but for spectral types later than M4.

4

Accurate determination of accretion and photospheric parameters in young stellar objects

Published as Manara, Beccari, Da Rio, De Marchi, Natta, Ricci, Testi A&A, 2013, 558, 114; ``Accurate determination of accretion and photospheric parameters in young stellar objects: The case of two candidate old disks in the Orion Nebula Cluster''

Abstract

Context: Current planet formation models are largely based on the observational constraint that protoplanetary disks have a lifetime of ~3 Myr. Recent studies, however, report the existence of pre-main-sequence stars with signatures of accretion (strictly connected with the presence of circumstellar disks) and photometrically determined ages of 30 Myr or more.
Aims: Here, we present a spectroscopic study of two major age outliers in the Orion Nebula Cluster. We use broadband, intermediate resolution VLT/X-Shooter spectra combined with an accurate method to determine the stellar parameters and the related age of the targets to confirm their peculiar age estimates and the presence of ongoing accretion.
Methods: The analysis is based on a multicomponent fitting technique, which derives simultaneously spectral type, extinction, and accretion properties of the objects. With this method, we confirm and quantify the ongoing accretion. From the photospheric parameters of the stars, we derive their position on the H-R diagram and the age given by evolutionary models. With other age indicators like the lithium-equivalent width, we estimate the age of the objects with high accuracy.
Results: Our study shows that the two objects analyzed are not older than the typical population of the Orion Nebula Cluster. While photometric determination of the photospheric

---

[*] This chapter is the result of a collaborative work that I started and lead. In particular I wrote the DDT proposal to ask for the observing time to collect the data. I then prepared the observations that have been carried out in service mode. I also carried out all the data reduction of the spectra, I developed the methodology to analyze the data, and I have then interpreted the data. Finally, I was responsible of the composition of the manuscript, where the coauthors helped with several comments and suggestions.

parameters are an accurate method to estimate the parameters of the bulk of young stellar populations, our results show that those of individual objects with high accretion rates and extinction may be affected by large uncertainties. Broadband spectroscopic determinations should thus be used to confirm the nature of individual objects.
Conclusions: The analysis carried out shows that this method allows us to obtain an accurate determination of the photospheric parameters of accreting young stellar objects in any nearby star-forming region. We suggest that our detailed, broadband spectroscopy method should be used to derive accurate properties of candidate old and accreting young stellar objects in star-forming regions. We also discuss how a similarly accurate determination of stellar properties can be obtained through a combination of photometric and spectroscopic data.

4.1 Introduction

The formation of planetary systems is strongly connected to the presence, structure, and evolution of protoplanetary disks in which they are born. In particular, the timescale of disk survival sets an upper limit on the timescale of planet formation, becoming a stringent constraint for planet formation theories (Haisch et al., 2001; Wolf et al., 2012). As the observed timescale for the evolution of the inner disk around pre-Main Sequence (PMS) stars is on the order of a few Myr (e.g., Williams & Cieza, 2011), all models proposed to explain the gas giant planet formation (core accretion, gravitational instability) are generally constrained to agree with a disk lifetime of much less than 10 Myr.

Observations of nearby young clusters (age $\lesssim$ 3 Myr) show the presence of few outliers with derived isochronal ages of more than 10 Myr. For example, this is found in the Orion Nebula Cluster (ONC) (Da Rio et al., 2010a, 2012) and in Taurus (White & Hillenbrand, 2005). The age of the objects is derived from their position on the H-R diagram (HRD) and thus subject to several uncertainties, which are either observational (e.g., spectral type, extinction), intrinsic to the targets (e.g., strong variability, edge-on disk presence, Huélamo et al. 2010), or related to the assumed evolutionary models (e.g., Da Rio et al., 2010b; Baraffe & Chabrier, 2010; Barentsen et al., 2011). On the other hand, observations of far (d >1 kpc) and extragalactic more massive clusters revealed the presence of a large population of accreting objects older (ages>30 Myr) than the typical ages assumed for the cluster ($\sim$ 3-5 Myr). Examples of these findings are the studies of NGC 3603 (Beccari et al., 2010), NGC 6823 (Riaz et al., 2012) and of various regions of the Magellanic Clouds (De Marchi et al., 2010, 2011; Spezzi et al., 2012). Observations in these clusters are dominated by solar- and intermediate-mass stars, for which the age determination is subject to the same uncertainties as for nearby clusters, but also to other uncertainties: For example, the age of these more massive targets is more sensitive to assumptions on the birthline (Hartmann, 2003).

These findings challenge the present understanding of protoplanetary disk evolution and can imply a entirely new scenario for the planet formation mechanism. On one side, the existence of one or few older disks in young regions does not change the aforementioned disk evolution timescales but represents a great benchmark of a possible new class of objects, where planet formation is happening on longer timescales. In contrast, the presence of a large population of older objects, representing a significant fraction of the total cluster members, could imply a totally different disk evolution scenario in those environments.

We thus want to verify the existence and the nature of older and still active protoplanetary disks in nearby regions. For this reason we have developed a spectroscopic method, which allows us to consistently and accurately determine the stellar and accretion properties of the targeted objects. Here, we present a pilot study carried out with the ESO/VLT X-Shooter spectrograph targeting two major age outliers with strong accretion activity in the ONC. This is an ideal region for this study, given its young mean age ($\sim$2.2 Myr, Reggiani et al. 2011), its vicinity (d = 414 pc, Menten et al. 2007), the large number of objects (more than 2000, Da Rio et al. 2010a), and the large number of previous studies (e.g., Hillenbrand, 1997; Da Rio et al., 2010a, 2012; Megeath et al., 2012; Robberto et al., 2013). Our objectives are therefore a) to verify the previously derived isochronal ages of these two objects by using different and more accurate age indicators and b) to assess the presence of an active disk with ongoing accretion.

The structure of the paper is the following. In Sect. 4.2, we report the targets selection criteria, the observation strategy, and the data reduction procedure. In Sect. 4.3, we describe the procedure adopted to derive the stellar parameters of the objects; and in Sect. 4.4, we report our results. In Sect. 4.5, we discuss the implications of our findings. Finally, we summarize our conclusions in Sect. 4.6.

4.2 Sample, observations, and data reduction

4.2.1 Targets selection and description

We have selected the two older PMS candidates from the sample of the HST Treasury Program on the ONC (Robberto et al., 2013). Our selection criteria were as follows: clear indications of ongoing accretion and of the presence of a protoplanetary disk; an estimated isochronal age much larger than the mean age of the cluster, i.e. $\gtrsim$ 30 Myr; a location well outside the bright central region of the nebula to avoid intense background contamination, which corresponds to a distance from θ^1 Orionis C larger than 5′($\sim$0.7 pc); and low foreground extinction ($A_V \lesssim 2$ mag). To find the best candidates, we have combined HST broadband data (Robberto et al., 2013) with narrow-band photometric and spectroscopic data (Hillenbrand, 1997; Stassun et al., 1999; Da Rio et al., 2010a, 2012) with mid-infrared photometric data (Megeath et al., 2012). According to Da Rio et al. (2010a, 2012), the total number of PMS star candidates in the ONC field with a derived isochronal age $\gtrsim$ 10 Myr, which is derived using various evolutionary models (D'Antona & Mazzitelli, 1994; Siess et al., 2000; Palla & Stahler, 1999; Baraffe et al., 1998), is $\sim$165 including both accreting and non-accreting targets, which corresponds to $\sim$10% of the total population. Among these, $\sim$ 90 objects ($\sim$5%) have ages $\gtrsim$30 Myr. The presence of ongoing accretion has been estimated through the Hα line equivalent width (EW$_{\mathrm{H}\alpha}$) reported in Da Rio et al. (2010a). We

Table 4.1: Parameters available in the literature for the objects analyzed in this work

Name	Other names	RA (J2000)	DEC (J2000)	SpT	$T_{\rm eff}$ [K]	A_V [mag]	$L_\star$ [$L_\odot$]	$M_\star$ [$M_\odot$]	age [Myr]
OM1186	MZ Ori	05:35:20.982	-05:31:21.55	K5	4350	2.40	0.13	0.66	64
OM3125	AG Ori	05:35:21.687	-05:34:46.90	G8	5320	1.47	0.63	0.95	25

Notes. Data taken from Da Rio et al. (2010a, and references therein).

use a threshold value of $\mathrm{EW}_{\mathrm{H}\alpha} > 20$ Å, which implies non negligible mass accretion rates ($\dot{M}_{\rm acc} \gtrsim 10^{-9} M_\odot$/yr). This is a high threshold that leads to select stronger accretors. Following White & Basri (2003) and Manara et al. (2013a), objects with $\mathrm{EW}_{\mathrm{H}\alpha} < 20$ Å can still be accretors but with a lower accretion rate. The available *Spitzer* photometry (Megeath et al., 2012) has been used to confirm the presence of an optically thick circumstellar disk, which is already suggested by the strong Hα emission. This is performed by looking at the spectral energy distribution (SED) of the targets to see clear excess with respect to the photospheric emission in the mid-infrared wavelength range. Among the objects with isochronal age $\gtrsim$10 Myr, there are ten objects (<1%) showing very strong Hα excess, or $\mathrm{EW}_{\mathrm{H}\alpha} > 20$ Å. Very striking, two PMS star candidates, each with an isochronal age $\gtrsim$30 Myr, have clear indications of Hα excess and the presence of the disk from IR photometry. These two extreme cases of older-PMS star candidates are selected for this work.

The two targets selected are OM1186 and OM3125, and we report their principal parameters available from Da Rio et al. (2010a, and reference therein) in Table 4.1. Both targets are located on the HRD almost on the main sequence, as we show in Fig. 4.1, where the position of these sources is reported using green stars. We also plot the position of other PMS star candidates in the ONC field, as shown with blue circles if their $\mathrm{EW}_{\mathrm{H}\alpha} < 20$ Åand with red diamonds if $\mathrm{EW}_{\mathrm{H}\alpha} \geq 20$ Å. Their position on the HRD clearly indicates that they have an isochronal age much larger than the bulk of the ONC population with ages between $\sim$ 60 Myr and $\sim$ 90 Myr for OM1186, according to different evolutionary tracks, and between $\sim$ 25 Myr and $\sim$ 70 Myr for OM3125. The spectral type (SpT) of the two targets has been determined in Hillenbrand (1997) to be K5 for OM1186 and G8-K0 for OM3125.

4.2.2 Observations and data reduction

Observations with the ESO/VLT X-Shooter spectrograph have been carried out in service mode between February and March 2012 (ESO/DDT program 288.C-5038, PI Manara). This instrument covers the wavelength range between $\sim$300 nm and $\sim$ 2500 nm simultaneously, dividing the spectrum in three arms - namely, the UVB arm in the region $\lambda\lambda \sim$ 300-550 nm, the VIS arm between $\lambda\lambda \sim$ 550-1050 nm, and NIR from $\lambda \sim$ 1050 nm to $\lambda \sim$ 2500 nm (Vernet et al., 2011). The targets have been observed in slit-nodding mode to have a good sky subtraction in the NIR arm. For both targets we used the same slit widths (0.5″ in the UVB arm and 0.4″ in the other two arms) and the same exposure times (300s x 4 in all three arms) to ensure the highest possible resolution of the observations (R=9100,

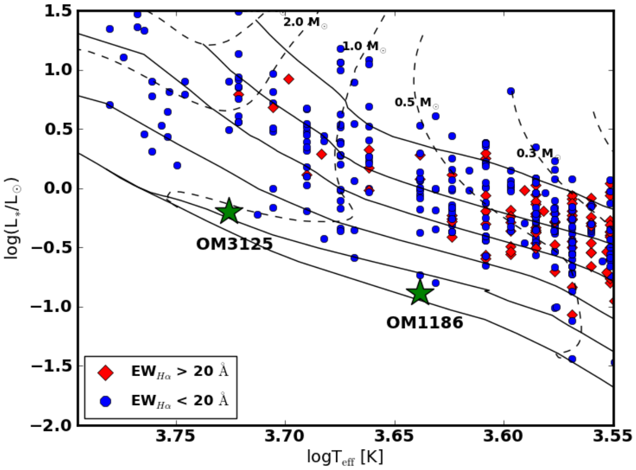

Figure 4.1: Hertzsprung-Russell diagram diagram of the ONC from Da Rio et al. (2012) with green stars showing the positions of the two targets of this study. The overplotted evolutionary tracks are from D'Antona & Mazzitelli (1994). We plot (from top to bottom) the 0.3, 1, 3, 10, 30, and 100 Myr isochrones.

17400, and 10500 in the UVB, VIS, and NIR arms, respectively) and enough S/N in the UVB arm. The readout mode used in both cases was ``100,1x1,hg''. The seeing conditions of the observatory during the observations were 1″ for OM1186 and 0.95″ for OM3125.

Data reduction has been carried out using the version 1.3.7 of the X-Shooter pipeline (Modigliani et al., 2010), which is run through the *EsoRex* tool. The spectra were reduced independently for the three spectrograph arms. The pipeline with the standard reduction steps (i.e., bias or dark subtraction, flat-fielding, spectrum extraction, wavelength calibration, and sky subtraction) also considers the flexure compensation and the instrumental profile. Particular care has been paid to the flux calibration and telluric removal of the spectra. Flux calibration has been carried out within the pipeline and then compared with the available photometry (Robberto et al., 2013) to correct for possible slit losses. We have also checked the conjunctions between the three arms. The overall final agreement is very good. Telluric removal has been carried out using the standard telluric spectra that have been provided as part of the X-Shooter calibration plan on each night of observations. The correction has been accomplished using the IRAF[1] task *telluric*, using the procedure explained in Alcalá et al. (2014).

4.3 Method

The determination of SpT and stellar properties in accreting young stellar objects (YSOs) is not trivial for a variety of reasons. First, YSOs are usually still embedded in their parental

---

[1] IRAF is distributed by National Optical Astronomy Observatories, which is operated by the Association of Universities for Research in Astronomy, Inc., under cooperative agreement with the National Science Foundation.

molecular cloud, which originates differential reddening effects in the region. This with the presence of a circumstellar disk surrounding the star can modify the actual value of the extinction (A_V) on the central YSO from one object to another. Second, YSOs may still be accreting material from the protoplanetary disk on the central star. This process affects the observed spectrum of a YSO - producing excess continuum emission in the blue part of the spectrum, veiling of the photospheric absorption features at all optical wavelengths and adding several emission lines (e.g., Hartmann et al., 1998). The two processes modify the observed spectrum in opposite ways: Extinction toward the central object suppresses the blue part of the spectrum, making the central object appear redder and thus colder, while accretion produces an excess continuum emission, which is stronger in the blue part of the spectrum, making the observed central object look hotter.

For these reasons, SpT, A_V, and accretion properties should be considered together in the analysis of these YSOs. Here, we present the minimum $\chi^2_{\rm like}$ method that we use to determine SpT, A_V, and the accretion luminosity ($L_{\rm acc}$) simultaneously. With this procedure, we are able to estimate $L_\star$, which is used to derive $M_\star$, the age of the target using different evolutionary models, and the mass accretion rate ($\dot{M}_{\rm acc}$). Finally, we determine the surface gravity ($\log g$) for the input object by comparison to synthetic spectra.

4.3.1 Parameters of the multicomponent fit

To fit the optical spectrum of our objects, we consider three components: a set of photospheric templates, which are used to determine the SpT and therefore the effective temperature ($T_{\rm eff}$) of the input spectrum; different values of the extinction and a reddening law to obtain A_V; and a set of models, which describe the accretion spectrum that we use to derive $L_{\rm acc}$.

Photospheric templates. The set of photospheric templates is obtained from the one collected in Manara et al. (2013a). This is a sample of 24 well-characterized X-Shooter spectra of non-accreting (Class III) YSOs which are representative of objects of SpT classes from late K to M. We extend this grid with two new X-Shooter observations of non-accreting YSOs from the ESO programs 089.C-0840 and 090.C-0050 (PI Manara): one object with SpT G4 and the other one with SpT K2. In total, our photospheric templates grid consists of 26 non-accreting YSOs with SpT between G4 and M9.5. We use Class III YSOs as a photospheric template, because synthetic spectra or field dwarfs spectra would be inaccurate for this analysis for the following reasons. First, YSOs are highly active, and their photosphere is strongly modified by this chromospheric activity in both the continuum and the line emission (e.g., Ingleby et al., 2011; Manara et al., 2013a). Second, field dwarf stars have a different surface gravity with respect to PMS stars, which are sub-giants. Using spectra of non-accreting YSOs as templates mitigates these problems.

Extinction. In the analysis we consider values of A_V in the range [0-10] mag with steps of 0.1 mag in the range A_V = [0-3] mag and 0.5 mag at higher values of A_V. This includes all the possible typical values of A_V for non embedded objects in this region (e.g., Da Rio et al., 2010a, 2012). The reddening law adopted in this work is from Cardelli et al. (1989)

with R_V=3.1, which is appropriate for the ONC region (Da Rio et al., 2010a).

Accretion spectrum. To determine the excess emission due to accretion and thus $L_{\rm acc}$, we use a grid of isothermal hydrogen slab models, which has already been used and proven to be adequate for this analysis (e.g., Valenti et al., 1993; Herczeg & Hillenbrand, 2008; Rigliaco et al., 2012; Alcalá et al., 2014). We describe the emission due to accretion with the slab model to have a good description of the shape of this excess and to correct for the emission arising in the spectral region at wavelengths shorter than the minimum wavelengths covered by the X-Shooter spectra at $\lambda \lesssim 330$ nm. In these models, we assume local thermodynamic equilibrium (LTE) conditions, and we include both the H and H^- emission. Each model is described by three parameters: the electron temperature ($T_{\rm slab}$) , the electron density (n_e), and the optical depth at λ=300 nm (τ), which is related to the slab length. The $L_{\rm acc}$ is given by the total luminosity emitted by the slab. The grid of slab models adopted covers the typical values for the three parameters: $T_{\rm slab}$ are selected in the range from 5000 to 11000 K, n_e varies from 10^{11} to 10^{16} cm^{-3}, and τ has values between 0.01 and 5.

Additional parameters. In addition to the five parameters just introduced - namely, the photospheric template, A_V, and the three slab model parameters ($T_{\rm slab}$, n_e, τ), there is the need to also include two normalization constant parameters: one for the photospheric template ($K_{\rm phot}$) and one for the slab model ($K_{\rm slab}$). The first rescales the emitted flux of the photospheric template to the correct distance and radius of the input target, while the latter converts the slab emission flux as it would have been emitted at the stellar surface by a region with the area given by the slab parameters.

4.3.2 Determination of the best fit

To consider the three components (SpT, A_V, $L_{\rm acc}$) together, we develop a Python procedure, which determines the model that best fits the observed spectrum. We calculate a likelihood function for each point of the model grid, which can be compared to a χ^2 distribution, by comparing the observed and model spectra in a number of spectral features. These are chosen in order to consider both the region around the Balmer jump, where the emitted flux mostly originates in the accretion shock, and regions at longer wavelengths, where the photospheric emission dominates the observed spectrum. The form of this function that is addressed as $\chi^2_{\rm like}$ function is the following:

$$\chi^2_{\rm like} = \sum_{features} \left[\frac{f_{\rm obs} - f_{\rm mod}}{\sigma_{\rm obs}}\right]^2, \qquad (4.1)$$

where f is the value of the measured feature, obs refers to measurements operated on the observed spectrum, mod refers to those on the model spectrum, and $\sigma_{\rm obs}$ is the error on the value of the feature in the observed spectrum. The features considered here are the Balmer jump ratio, defined as the ratio between the flux at ∼360 nm and ∼ 400 nm; the slope of the Balmer continuum between ∼335 nm and ∼ 360 nm; the slope of the Paschen continuum between ∼ 400 nm and ∼ 475 nm; the value of the Balmer continuum at ∼360 nm; that

Table 4.2: Spectral features used to calculate the best-fit in our multicomponent fit procedure

Name	Wavelength range [nm]
Balmer Jump ratio	(355-360)/(398-402)
Balmer continuum (slope)	332.5-360
Paschen continuum (slope)	398-477
Continuum at $\sim$ 360	352-358
Continuum at $\sim$ 460	459.5-462.5
Continuum at $\sim$ 703	702-704
Continuum at $\sim$ 707	706-708
Continuum at $\sim$ 710	709-711
Continuum at $\sim$ 715	714-716

of the Paschen continuum at $\sim$ 460 nm; and the value of the continuum in different bands at $\sim$ 710 nm. The exact wavelength ranges of these features are reported in Table 4.2. The best fit model is determined by minimizing the $\chi^2_{\rm like}$ distribution. The exact value of the best fit $\chi^2_{\rm like}$ is not reported, because this value itself should not be considered as an accurate estimate of the goodness of the fit. Whereas a fit with a value of $\chi^2_{\rm like}$ which is much larger than the minimum leads to a very poor fit of the observed spectrum, this function is not a proper χ^2, given that it considers only the errors on the observed spectrum and only some regions in the spectrum.

The procedure is as follows. For each photospheric template we deredden the observed spectrum with increasing values of A_V. Considering each slab model, we then determine the value of the two normalization constants $K_{\rm phot}$ and $K_{\rm slab}$ for every value of A_V. This is done matching the normalized sum of the photosphere and the slab model to the observed dereddened spectrum at $\lambda \sim 360$ nm and at $\lambda \sim 710$ nm. After that, we calculate the $\chi^2_{\rm like}$ value using Eq. (4.1). This is done for each point of the grid (SpT, A_V, slab parameters). After the iteration on each point of the grid terminates, we find the minimum value of the $\chi^2_{\rm like}$ and the correspondent values of the best fit parameters (SpT, A_V, slab parameters, $K_{\rm phot}$, $K_{\rm slab}$).

We also derive the uncertainties on these two parameters and thus on $L_{\rm acc}$ from the $\Delta\chi^2_{\rm like}$ distribution with respect to the SpT of the photospheric templates and the different values of A_V. Indeed, these are the main sources of uncertainty in the determination of $L_{\rm acc}$, which is a measurement of the excess emission with respect to photospheric emission due to accretion. Most of the accretion excess ($\gtrsim$70%) is emitted in regions covered by our X-Shooter spectra and originates mostly in the wavelength range of $\lambda \sim 330$-1000 nm, while most of the excess emission at longer wavelengths is due to disk emission and is not considered in our analysis. To derive the total excess due to accretion, we need a bolometric correction for the emission at wavelengths shorter than those in the X-Shooter range at $\lambda \lesssim$330 nm. This is calculated with the best fit slab model. Our analysis of the slab models lead to the conclusion that this contribution accounts for less than 30% of the excess emission and that the shape of this emission is well constrained by the Balmer continuum slope. Different slab model parameters with reasonable Balmer continuum slopes that would imply similarly good fits as the best one would lead to values of $L_{\rm acc}$ always within 10% of each other, as it has also been pointed out by Rigliaco et al. (2012). Therefore, once SpT and A_V are constrained, the results with different slab parameters are similar. With our procedure, we can very well constrain all the parameters. Typically, the solutions with $\chi^2_{\rm like}$ values closer to the best-fit are those within one spectral subclass of difference in the photospheric template at ±0.1-0.2 mag in extinction values and with differences of $L_{\rm acc}$ of less than ~10%. Other sources of uncertainty on the estimate of $L_{\rm acc}$ are the noise in the observed and template spectra, the uncertainties in the distances of the target, and the uncertainty given by the exclusion of emission lines in the estimate of the excess emission (see e.g., Herczeg & Hillenbrand 2008; Rigliaco et al. 2012; Alcalá et al. 2014). Typical errors altogether on estimates of $L_{\rm acc}$ with our method are of 0.2-0.3 dex.

As previously mentioned, the accretion emission veils the photospheric absorption features of the observed YSO spectrum. These veiled features can be used to visually verify the agreement of the best fit obtained with the $\chi^2_{\rm like}$ minimization procedure. To do this, we always plot the observed spectrum and the best fit in the Balmer jump region, in the Ca I absorption line region at λ ~420 nm, in the continuum bands at $\lambda \sim$ 710 nm, and in the spectral range of different photospheric absorption lines, which depends mainly on the temperature of the star ($T_{\rm eff}$) - namely, TiO lines at $\lambda\lambda$ 843.2, 844.2, and 845.2 nm, and the Ca I line at $\lambda \sim$ 616.5 nm. The agreement between the best fit and the observed spectrum in the Balmer jump region at $\lambda \sim 420$ nm and in the continuum bands at $\lambda \sim 710$ nm is usually excellent. Similarly, the best fit spectrum also reproduces the photospheric features of the observed one at longer wavelengths very well.

4.3.3 Comparison to synthetic spectra

As an additional check of our results and to derive the surface gravity ($\log g$) for the target, we compare the target spectrum with a grid of synthetic spectra. In particular, we adopt synthetic BT-Settl spectra (Allard et al., 2011) with solar metallicity, such that $\log g$ is in the range from 3.0 to 5.0 (in steps of 0.5) and $T_{\rm eff}$ is equal to that of the best fit photospheric template using the SpT-$T_{\rm eff}$ relation from Luhman et al. (2003), and with a $T_{\rm eff}$ that corresponds to the next upper and lower spectral sub-classes.

The procedure used is the following. First, we correct the input spectrum for reddening using the best fit value of A_V. Subsequently, we remove the effect of veiling by subtracting the best fit slab model, which is rescaled with the constant $K_{\rm slab}$ derived in the fit, to the dereddened input spectrum. Then, we degrade the synthetic spectra to the same resolution of the observed one (R=17400 in the VIS), and we resample those to the same wavelength scale of the target. We then select a region, following Stelzer et al. (2013), with many strong absorption lines dependent only on the star $T_{\rm eff}$ and with small contamination from molecular bands and broad lines. This is chosen to derive the projected rotational velocity ($v\sin i$) of the target by comparison of its spectrum with rotationally broadened synthetic spectra. The region chosen is in the VIS arm from 960 to 980 nm and is characterized by several Ti I absorption lines and by some shallower Cr I lines. Then, we broaden the synthetic spectra to match the $v\sin i$ of the observed one, and we compare it with the reddened- and veiling-corrected target spectrum in two regions, which are chosen because they include absorption lines sensitive to both $T_{\rm eff}$ and $\log g$ of the star, following Stelzer et al. (2013, and references therein). One occurs in the wavelength range from 765 to 773 nm, where the K I doublet ($\lambda\lambda \sim$ 766-770 nm) exists, and another occurs in the range from 817 to 822 nm, where the Na I doublet ($\lambda\lambda \sim$ 818.3-819.5 nm) exists. The best fit $\log g$ occurs at the synthetic spectrum with smaller residuals from the observed-synthetic spectra in the line regions.

4.3.4 Stellar parameters

From the determined best fit parameters using the explained procedure in this section, we obtain $T_{\rm eff}$, A_V, and $L_{\rm acc}$. The first corresponds to the $T_{\rm eff}$ of the best fit photospheric template, which is converted from the SpT using the Luhman et al. (2003) relation, derived with the multicomponent fit and verified with the comparison to the synthetic spectra. The value of A_V is also derived in the multicomponent fit, while $L_{\rm acc}$ is calculated by integrating the total flux of the best fit slab model from 50 nm to 2500 nm. The flux is rescaled using the normalization constant $K_{\rm slab}$ derived before. This total accretion flux ($F_{\rm acc}$) is then converted in $L_{\rm acc}$ using the relation $L_{\rm acc} = 4\pi d^2 F_{\rm acc}$, where d is the distance of the target.

To derive $L_\star$ of the input spectrum, we use the values of $L_\star$ of the non-accreting YSOs used as a photospheric template for our analysis, which have been derived in Manara et al. (2013a). From the best fit result, we know that $f_{\rm obs,dereddened} = K_{\rm phot} \cdot f_{\rm phot} + K_{\rm slab} \cdot f_{\rm slab}$, where f is the flux of the spectrum of the dereddened observed YSO ($obs, dereddened$), of the photospheric template ($phot$), and of the slab model ($slab$). The photospheric emission of the input target is then given solely by the emission of the photospheric template rescaled with the constant $K_{\rm phot}$. Therefore, we use the relation:

$$L_{\star,\rm obs} = K_{\rm phot} \cdot (d_{\rm obs}/d_{\rm phot})^2 L_{\star,\rm phot}, \tag{4.2}$$

where d is the distance, $L_{\star,\rm phot}$ is the bolometric luminosity of the photospheric template, and $L_{\star,\rm obs}$ is that of the input object. With this relation, we derive $L_\star$ for the input YSO.

From $T_{\rm eff}$ and $L_\star$ we then derive $R_\star$, whose error is derived by propagation of the uncertainties on $T_{\rm eff}$ and $L_\star$. The target $M_\star$ and age are obtained by interpolation of evolutionary models (Siess et al., 2000; Baraffe et al., 1998; Palla & Stahler, 1999; D'Antona & Mazzitelli, 1994) in the position of the target on the HRD. Their typical uncertainties are determined by allowing their position on the HRD to vary according to the errors on $T_{\rm eff}$ and $L_\star$. Finally, we derive $\dot{M}_{\rm acc}$using the relation $\dot{M}_{\rm acc} = 1.25 \cdot L_{\rm acc} R_\star/(GM_\star)$ (Gullbring et al., 1998), and its error is determined propagating the uncertainties on the various quantities in the relation. We report the values derived using all the evolutionary models.

Another important quantity, which can be used to asses the young age of a PMS star, is the presence and the depth of the lithium absorption line at $\lambda \sim 670.8$. Given that veiling substantially modifies the equivalent width of this line (EW$_{\rm Li}$), we need to use the reddening- and veiling-corrected spectrum of the target to derive this quantity. On this

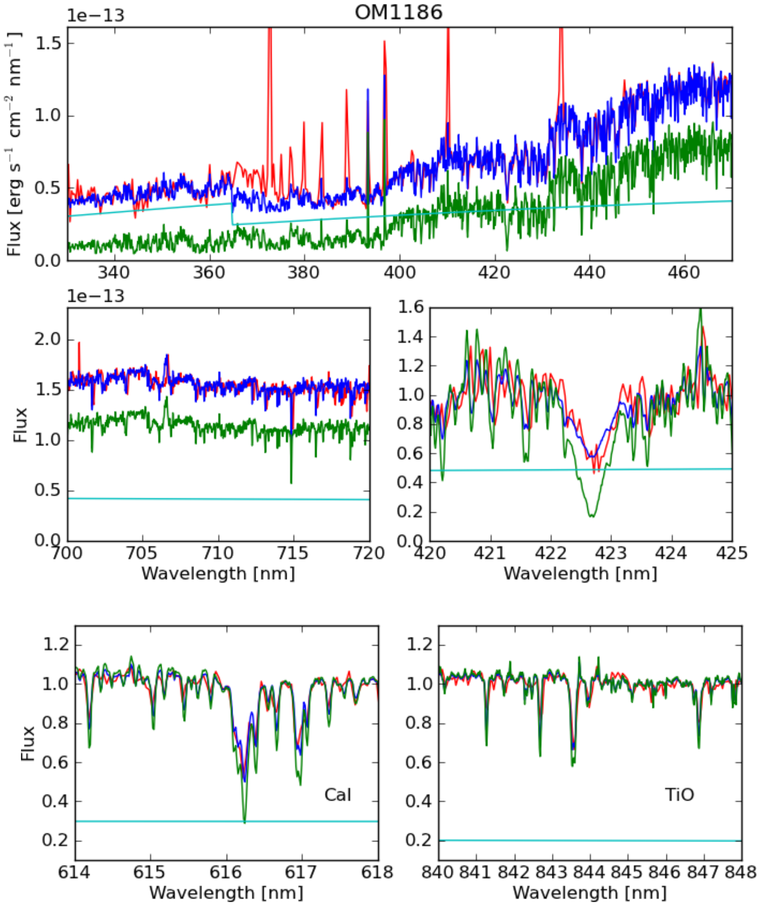

Figure 4.2: Best fit for the object OM1186. Balmer jump, normalization region, CaI absorption feature, and photospheric features used to check derived veiling.

corrected spectrum, we calculate EW_{Li}, integrating the Gaussian fit of the line, which is previously normalized to the local pseduo-continuum at the edges of the line. The statistical error derived on this quantity is given by the propagation of the uncertainty on the continuum estimate.

4.4 Results

In the following, we report the accretion and stellar properties of the two older PMS candidates obtained by using the procedure explained in Sect. 4.3.

4.4.1 OM1186

The best fit for OM1186 is shown in Fig.4.2: The red line is the observed spectrum, the green is the photospheric template, the cyan line is the slab model, and the blue is the best

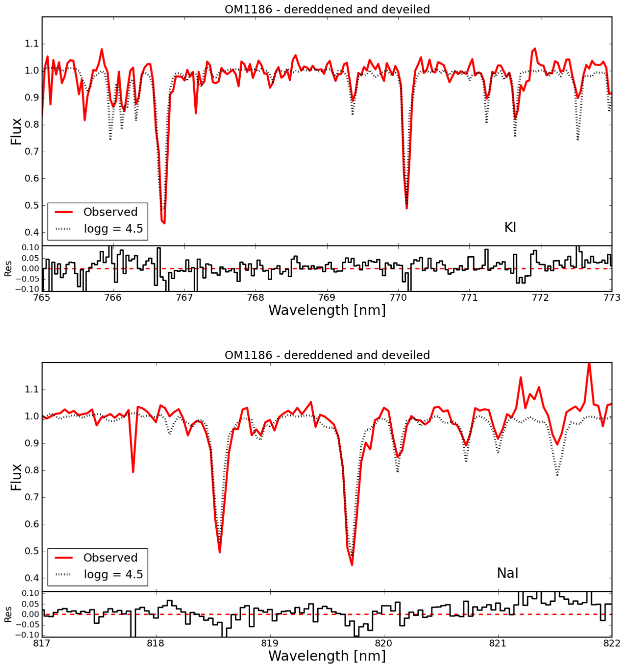

Figure 4.3: Comparison of the extinction- and veiling-corrected spectrum of OM1186 with a synthetic spectrum with T_{eff} = 4350 K and $\log g$=4.5.

fit. The region around the Balmer jump is shown in the upper plot. The other panels show the normalization region around ∼710 nm, the continuum normalized Ca I absorption line at ∼ 422 nm, and the photospheric features at $\lambda \sim$ 616 nm and $\lambda \sim$ 844 nm. We clearly see that the agreement between the observed and best fit spectra is very good in all the region analyzed. This is obtained using a photospheric template of SpT K5, which corresponds to T_{eff}=4350 K with an estimated uncertainty of 350 K, A_V = 0.9±0.4 mag, and slab parameters leading to a value of L_{acc}=0.20±0.09 $L_\odot$. We then confirm the SpT reported in the literature for this object, but we derive a different value for the extinction, which was found to be A_V=2.4 mag.

The result of the comparison of the input spectrum to the grid of synthetic spectra is shown in Fig. 4.3. The best agreement is found using a synthetic spectrum at the same nominal T_{eff} of the best fit photosphere: T_{eff} = 4350 K with $\log g$=4.5. In Fig. 4.3, both regions adopted for the $\log g$ analysis are shown, and the red line refers to the reddening- and veiling-corrected observed spectrum, while the black dotted line is the synthetic spectrum, which reproduces the observed one better. We also report the residuals in the bottom panel.

From the best fit, we derive a value of $L_\star$ = 1.15±0.36 $L_\odot$ for this object. With this value and using T_{eff} = 4350 K, we derive the mass and age for these objects with the evolutionary models of Siess et al. (2000), Baraffe et al. (1998), Palla & Stahler (1999), and D'Antona & Mazzitelli (1994). The values derived are, respectively, $M_\star$= {1.1±0.4, 1.4±0.3, 1.1±0.4, 0.6±0.3} $M_\odot$ and age = $\{3.2^{+4.8}_{-2.0}, 4.7^{+7.2}_{-2.5}, 2.8^{+2.9}_{-1.7}, 0.8^{+1.4}_{-0.4}\}$ Myr. Moreover, we derive $\dot{M}_{acc}$

with the parameters derived from the fit and from the evolutionary models, and we obtain $\dot{M}_{\rm acc}$={1.3 ±0.8, 1.1±0.6, 1.4±0.8, 2.4±1.8} $\cdot 10^{-8} M_{\odot}$/yr for this object, according to the different evolutionary tracks. From the reddening- and veiling-corrected spectrum, we derive EW$_{\rm Li}$ = 658 ± 85 mÅ. All the parameters derived from the best fit are reported in Table 4.3, while those derived using the evolutionary models are in Table 4.4.

4.4.2 OM3125

For OM3125, the values reported in the literature are SpT G8-K0 and A_V=1.47 mag. Using the same procedure, we obtain a minimum $\chi^2_{\rm like}$ value with a photospheric template of SpT K7, which corresponds to T$_{\rm eff}$=4060 K with an uncertainty of 250 K and A_V = 1.2±0.3 mag. With this best fit model, we do not reproduce the Ca I absorption feature at $\lambda \sim$616.5 nm very well, because the amount of veiling in this line is too high. Looking at the solutions with values of $\chi^2_{\rm like}$ similar to the minimum value, we find that the best agreement between the observed and fitting spectrum in this feature is with a value of A_V = 1.0 mag. Please note that the choice of this solution instead of the one with A_V = 1.2 mag implies the same derived parameters $L_\star$ and $L_{\rm acc}$ well within the errors. We show this adopted best fit in Fig. 4.4, using the same color-code as in Fig. 4.2. The slab model used here leads to a value of $L_{\rm acc}$= 1.25±0.60 $L_\odot$. The effect of veiling in this object is stronger than in OM1186, and this is clearly seen in both the Balmer jump excess and the Ca I absorption feature at $\lambda \sim$420 nm, which is almost completely veiled. The Ca I absorption features has also emission on reversal of the very faint absorption feature. Moreover, the other photospheric features are also much more veiled, as it is shown in the bottom panels of Fig. 4.4. In the bottom right panel, there are also hydrogen and helium emission lines due to accretion in correspondence with the TiO absorption features normally present in the photosphere of objects with this SpT (see Fig. 4.2 for comparison).

In Fig. 4.5 we show the synthetic spectrum analysis for this object, using the same color code as in Fig. 4.3. In this case, the best agreement is found with a synthetic spectrum with T$_{\rm eff}$ = 4000 K and log g=4.0.

The luminosity derived for this object from its best fit is $L_\star$ = 0.81±0.44 $L_\odot$. With this value and using T$_{\rm eff}$ = 4060 K, we derive the mass and age for these objects with the evolutionary models of Siess et al. (2000); Baraffe et al. (1998); Palla & Stahler (1999); D'Antona & Mazzitelli (1994). The values derived are $M_\star$= {0.8±0.3, 1.2±0.2, 0.8±0.2, 0.5±0.2} $M_\odot$ and age = {$2.2^{+6.6}_{-1.0}$, $4.32^{+8.7}_{-2.0}$, $2.4^{+4.3}_{-1.3}$, $0.8^{+2.7}_{-0.3}$} Myr, respectively. According to the different evolutionary models, this object has $\dot{M}_{\rm acc}$={1.2±0.9, 0.8±0.5, 1.2±0.7, 1.9±1.2} $\cdot 10^{-7} M_\odot$/yr, and EW$_{\rm Li}$ = 735 ± 42 mÅ. These results are also reported in Table 4.3 and 4.4.

4.5 Discussion

With the results presented in the previous section, we determine new positions for our target on the HRD. This is shown in Fig. 4.6 with green stars representing the two YSOs analyzed

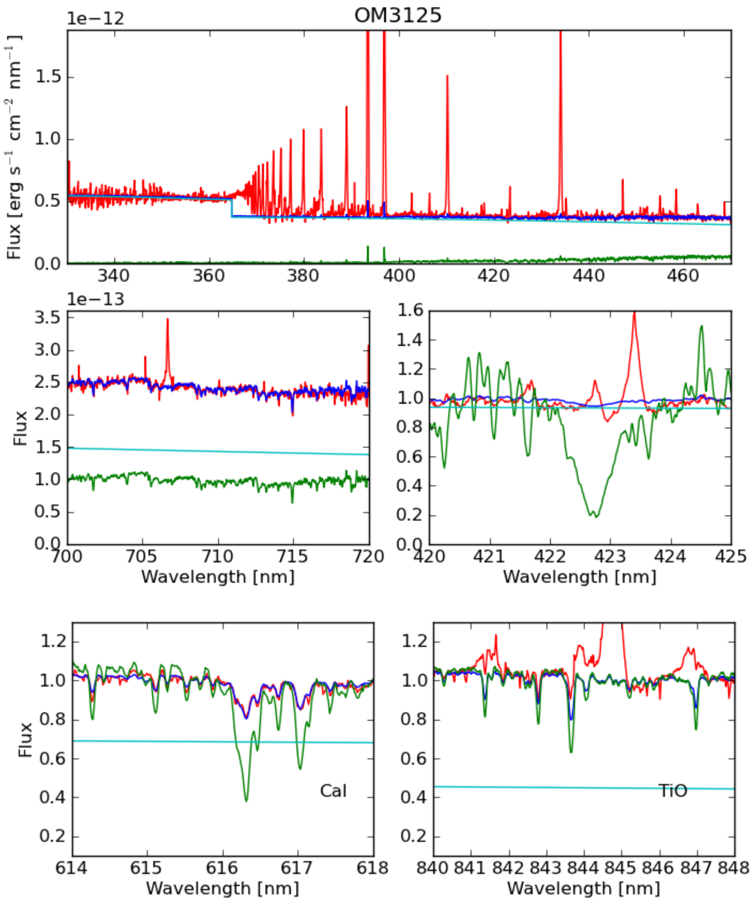

Figure 4.4: Best fit for the object OM3125. Same as Fig. 4.2.

Table 4.3: Newly derived parameters from the multicomponent fit

Name	SpT	T$_{\rm eff}$ [K]	A_V [mag]	L$_\star$ [L$_\odot$]	R$_\star$ [R$_\odot$]	$\log g$ [cm/s^2]	EW$_{\rm Li}$ [mÅ]	$L_{\rm acc}$ [L$_\odot$]
OM1186	K5	4350±350	0.9±0.4	1.15±0.36	1.9±0.4	4.5±0.5	658±85	0.20±0.09
OM3125	K7	4060±250	1.0±0.3	0.81±0.44	1.8±0.5	4.0±0.5	735±42	1.25±0.60

Table 4.4: Parameters derived from evolutionary models using the newly derived photospheric parameters

Evolutionary model	OM1186 M$_\star$ [M$_\odot$]	OM1186 age [Myr]	OM1186 $\dot{M}_{\rm acc}$ [$10^{-8} M_\odot$/yr]	OM3125 M$_\star$ [M$_\odot$]	OM3125 age [Myr]	OM3125 $\dot{M}_{\rm acc}$ [$10^{-8} M_\odot$/yr]
Siess et al. (2000)	1.1±0.4	$3.2^{+4.8}_{-2.0}$	1.3±0.8	0.8±0.3	$2.2^{+6.6}_{-1.0}$	12.0±8.6
Baraffe et al. (1998)	1.4±0.3	$4.7^{+7.2}_{-2.5}$	1.1±0.6	1.2±0.2	$4.3^{+8.7}_{-2.0}$	7.9±4.7
Palla & Stahler (1999)	1.1±0.4	$2.8^{+2.9}_{-1.7}$	1.4±0.8	0.8±0.2	$2.4^{+4.3}_{-1.3}$	11.6±7.5
D'Antona & Mazzitelli (1994)	0.6±0.3	$0.8^{+1.4}_{-0.4}$	2.4±1.8	0.5±0.2	$0.8^{+2.7}_{-0.3}$	18.6±12.3

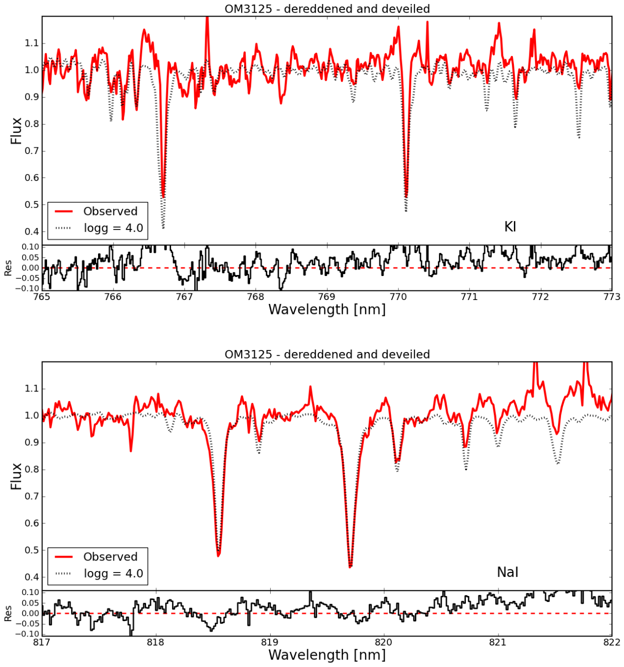

Figure 4.5: Comparison of the extinction- and veiling-corrected spectrum of OM3125 with a synthetic spectrum with $T_{\rm eff}$ = 4000 K and log g=4.0. Same as Fig. 4.3.

in this study and the other symbols representing the rest of the ONC population, as in Fig. 4.1. Their revised positions are compatible with the bulk of the population of the ONC, and their revised mean ages, ∼2.9 Myr for OM1186 and ∼2.4 Myr for OM3125, are typical ages for objects in this region, for which the mean age has been estimated around 2.2 Myr (Reggiani et al., 2011). We also check that the final results do not depend on the value that we have chosen for the reddening law, i.e. R_V=3.1. With a value of R_V=5.0, we obtain ages, which are systematically younger than the one obtained in our analysis by a factor ∼30% for OM1186 and ∼50% for OM3125. With the newly determined parameters, these objects are clearly not older than the rest of the population, and their status of candidate older PMS is due to an incorrect estimate of the photospheric parameters in the literature. Figure 4.6 also shows that most of the objects that then appear older than 10 Myr have small or negligible Hα excess (blue circles). Among the objects with age $\gtrsim$ 10 Myr, only eight objects actually show signatures of intense accretion (one red diamond visible in the plot; the other seven have $T_{\rm eff} < 3550$ K and are, therefore, outside the plot range) and at the same time of age older than 10 Myr. These objects should be observed in the future with techniques similar to the one we used here (see Sect. 4.5.3 for details) to understand their real nature. In the following, we analyze other derived parameters for these objects that confirm the age estimated with the HRD. Then, we address possible reasons which lead to misclassification of these targets in the literature.

4.5.1 Age related parameters

Lithium abundance: Using the values of $\mathrm{EW_{Li}}$ and the stellar parameters obtained in the previous section, we calculate the lithium abundance (log N(Li)) for the two targets by interpolation of the curves of growth provided by Pavlenko & Magazzu (1996). We derive log N(Li) = 3.324±0.187 for OM1186 and log$N$(Li)=3.196±0.068 for OM3125. These values are compatible with the young ages of the targets, according to various evolutionary models (Siess et al., 2000; D'Antona & Mazzitelli, 1994; Baraffe et al., 1998). Indeed, these models predict almost no depletion of lithium for objects with these $\mathrm{T_{eff}}$ at ages less than 3 Myr, which means that the measured lithium abundance for younger objects should be compatible with the interstellar abundance of log N(Li)$\sim$3.1-3.3 (Palla et al., 2007).

Surface gravity: The derived values of the surface gravity for the two targets are compatible with the theoretical values for objects with $\mathrm{T_{eff}}$ $\sim$4000-4350 K and an age between $\sim$1-4.5 Myr. Indeed, both models of Siess et al. (2000) and Baraffe et al. (1998) predict a value of $\log g\sim$ 4.0 for objects with these properties. Nevertheless, the derived value of $\log g$ for OM1186 is also typical of much older objects, given that models predict $\log g\sim$ 4.5 at ages $\sim$20 Myr with a very small increase in future evolutionary stages. However, the uncertainties on the determination of this parameter are not small, and the increase of this value during the PMS phase is usually within the errors of the measurements.

4.5.2 Sources of error in the previous classifications

Both targets have been misplaced on the HRD, but the reasons were different. For OM1186, we confirmed the SpT available from the literature, but we found different values of A_V and L_{acc} with respect to Da Rio et al. (2010a). In their work, they use a color-color BVI diagram to simultaneously derive A_V and L_{acc} with the assumption of the SpT. To model the excess emission due to accretion, they use a superposition of an optically thick emission, which reproduces the heated photosphere, and of an optically thin emission, which models the infalling accretion flow. From this model spectrum they derive the contribution of accretion to the photometric colors of the targets by synthetic photometry. Their method assumes that the positions of the objects on the BVI diagram are displaced from the theoretical isochrone due to a combination of extinction and accretion. With the assumption of the SpT, they can find the combination of parameters (A_V, L_{acc}), which best reproduces the positions of each target on the BVI diagram. With these values, they corrected the I-band photometry for the excess due to accretion, derived using the accretion spectrum model, and for reddening effects. Finally, they derived $L_\star$ from this corrected I-band photometry using a bolometric correction. Using this method, they found a solution for OM1186 with a large value of A_V and, subsequently, accretion. Given the large amount of excess due to accretion they derive in the I-band, they underestimated $L_\star$ and assigned an old age to this target. On the other hand, our revised photospheric parameters are compatible with those of Manara et al. (2012), who found A_V=1.16 mag, $L_\star$=0.77 $L_\odot$, and age$\sim$6 Myr. In their analysis, they used the same method as Da Rio et al. (2010a), but they also had U-band photometric data at their disposal, and thus used an UBI color-color diagram. Given

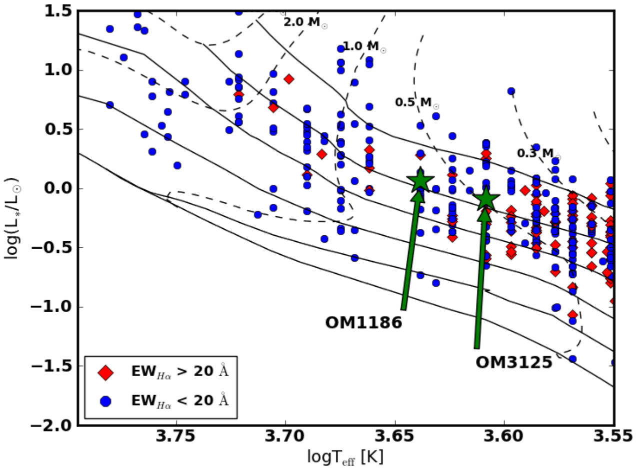

Figure 4.6: Hertzsprung-Russell diagram diagram of the ONC from Da Rio et al. (2012) with colored stars showing the new positions of the two targets of this study. The overplotted evolutionary tracks are from D'Antona & Mazzitelli (1994). We plot (from top to bottom) the 0.3, 1, 3, 10, 30, and 100 Myr isochrones.

that the excess emission due to accretion with respect to the photosphere in the U-band is much stronger, they were able to determine the accretion properties of the targets more accurately and to find a unique correct solution.

Regarding OM3125, we derived a different SpT with respect to the one usually assumed in the literature (G8-K0; Hillenbrand, 1997) with our analysis. This estimate was obtained using an optical spectrum covering the wavelength region from ∼500 nm to ∼900 nm, and their analysis did not consider the contribution of accretion to the observed spectrum. This was assumed not to be a strong contaminant for the photospheric features in this wavelength range. This is a reasonable assumption for objects with low accretion rates, but it was later shown not to be accurate for stronger accretors (Fischer et al., 2011), as we already pointed out for this target. In particular, strong veiling makes the spectral features shallower, which lead to an incorrect earlier classification of the target. Hillenbrand (1997) marked this SpT classification as uncertain, and they also reported the previous classification for this object from Cohen & Kuhi (1979), who classified it as being of SpT K6, a value which agrees with our finding. This previous classification is obtained using spectra at shorter wavelengths ($\lambda \sim$ 420-680 nm) with respect to Hillenbrand (1997) and with no modeling of the accretion contribution. The difference in the classification is most likely because some TiO features at $\lambda\lambda$ ∼476, 479 nm, which are typical of objects of spectral class late-K, were covered in the spectra of Cohen & Kuhi (1979). Given the large amount of veiling due to accretion that is present in the spectrum of this object, it represents a clear case where the detailed analysis carried out in our work is needed. We conclude that even optical spectra covering large regions of the spectra, like those used in Hillenbrand (1997) and in Cohen & Kuhi (1979), can lead to different and sometimes incorrect results, if the veiling contribution is not properly modeled.

4.5.3 Implications of our findings

Accretion veiling, extinction, and spectral type are difficult to estimate accurately from limited datasets, especially if they are mostly based on only few photometric bands. When classifying young stellar objects, the difficulty increases, given that accretion and extinction may substantially modify the observed spectra. For this reason, the use of few photometric bands, where accretion, extinction, and spectral type effects can be very degenerate (e.g., B-I band range), or of spectra that cover only small wavelength regions (e.g., λ ~500-900 nm), can lead to different solutions, which may be incorrect.

With our work, we show that an analysis of the whole optical spectrum, which includes a detailed modeling of the various components of the observed spectrum, leads to an accurate estimate of the stellar parameters. When good quality and intermediate resolution spectra with large wavelength coverage from λ ~330 nm to $\lambda \sim$ 1000 nm are not available, we suggest that a combination of photometric and spectroscopic data could also lead to a robust estimate of the stellar parameters of the targets independently of their SpT. In particular, the photometric data should cover the region around the Balmer jump (using both U- and B-band) and around λ ~700 nm (R- and I-band). With this dataset, it would be possible to derive accretion and veiling properties, extinction, and SpT by means of photometrical methods similar to those of Manara et al. (2012). This could be expanded to include different photospheric templates and different accretion spectra. At the same time, spectra in selected wavelength regions, where photospheric lines sensitive to $T_{\rm eff}$ and/or $\log g$ are present, are necessary to pin-down degeneracies on the SpT. Finally, the lithium absorption line should be included as another test of the age.

Our work also implies that single objects, which deviate from the bulk of the population in nearby young clusters (age $\lesssim$ 3 Myr), could be affected by an incorrect estimate of the photospheric parameters, especially in cases where the determination is based on few photometric bands and the effects of veiling due to accretion and extinction are strong. On the other hand, we have no reason to believe that also a large number of objects positioned along the isochrones that represents the bulk of the population in nearby regions should be affected by similar problems. We think that the vast majority of the estimates available are correct for the following reasons. First of all, objects with low or negligible accretion should be easier to classify, given that their spectral features are not affected by veiling. Then, there are small effects in various regions due to differential extinction. In particular, we expect the amount of misclassified objects to be particularly small when dealing with objects located in regions less affected by extinction effects, such as σ-Ori. Larger numbers of objects could be misclassified in very young regions (age$\lesssim$1 Myr, e.g., ρ-Oph), where both accretion and extinction effects are strong. We could have here both an underestimation of $L_\star$, as in the case of OM1186, due to an overestimation of $L_{\rm acc}$ and an overestimation of $L_\star$ due to an underestimation of $L_{\rm acc}$. These effects could contribute to the spread of $L_\star$, which is observed in almost all star forming regions. Finally, accretion variability effects should not substantially affect the properties of most of the targets, given that these effects are usually small (e.g., Costigan et al., 2012).

Even though any conclusion on the nature of the older populations observed in massive clusters cannot be drawn from this work, we suggest that the method explained here or the alternative approach suggested in this section should be used to study these objects in more detail.

4.6 Conclusion

We have observed two candidate old (age>10Myr) accreting PMS in the ONC with the ESO/VLT X-Shooter spectrograph to confirm previous accretion rate and age estimates. Using a detailed analysis of the observed spectra based on a multicomponent fit, that includes photospheric emission, the effect of reddening, and the continuum excess due to accretion, we derived revised accretion rates and stellar parameters for the two targets. We confirm that the objects are accretors as from previous studies, but the revised photospheric parameters place these objects in the same location as the bulk of the ONC young stellar population (age$\sim$2-3Myr). Therefore, they cannot be considered older PMS, but they are classical accreting YSOs. In particular, we confirmed the previously estimated SpT for OM1186, but we derived different values of A_V and $L_{\rm acc}$ with respect to previous works in the literature, finding that the real position of this object on the HRD leads to a mean age estimate of $\sim$2.9 Myr. On the other hand, we derived a different SpT for OM3125 with respect to the usually assumed value in the literature. With the other parameters, this moved this target to a position on the HRD leading to an age of $\sim$2.4 Myr. The analysis of the lithium abundance and that of the surface gravity confirm this finding, even if the uncertainties for the latter were large.

We showed that we are able to accurately determine the stellar parameters of YSOs with our analysis, while the use of few photometric bands alone (e.g., only the B- and I-band) or of only spectra covering small wavelength regions can lead to large errors in the derived position on the HRD. We thus suggest that single objects in nearby young clusters whose position on the HRD is not compatible with the bulk of the population in their region, could be misplaced, especially if there is the suspicion of high optical veiling connected to large values of the accretion rate. The nature of these individual objects will need to be verified using a detailed analysis similar to the one reported in this study to verify the existence and to study the properties of long-lived disks around young stellar objects.

Aknowledgements We thank the anonymous referee for providing useful comments which helped us to improve the paper. We thank the ESO Director General for awarding DDT time to this project and the ESO staff in Paranal for carrying out the observations in Service mode. We thank Andrea Banzatti for useful comments and discussion which helped to improve the fitting procedure. C.F.M. acknowledges the PhD fellowship of the International Max-Planck-Research School. G.B. acknowledges the European Community's Seventh Framework Programme under grant agreement no. 229517.

5

On the gas content of transitional disks: a VLT/X-Shooter study of accretion and winds

From Manara, Testi, Natta, Rosotti, Benisty, Ercolano, Ricci, submitted to A&A[*]

Abstract

Context: Transitional disks are thought to be a late evolutionary stage of protoplanetary disks whose inner regions have been depleted of dust. The mechanism responsible for this depletion is still under debate. To constrain the various models proposed to explain this phase it is mandatory to have a good understanding of the properties of the gas content in the inner part of the disk.
Aims: Using X-Shooter broad band - UV to NIR - medium resolution spectroscopy we derive the stellar, accretion, and wind properties of a sample of transitional disks. The analysis of these properties allows us to put strong constraints on the gas content in a region very close to the star ($\lesssim$ 0.2 AU) which is not accessible with any other observational technique.
Methods: We fit the medium-resolution broad-band spectra of 22 transitional disks with a self-consistent procedure to derive simultaneously spectral type, extinction, and accretion properties of the targets. These are determined from the fit of the whole broad-band spectrum, including the UV-excess and various absorption features at longer wavelengths. From the continuum excess at near-infrared wavelength we distinguish whether our targets have dust free inner holes. Analyzing forbidden emission lines present in the spectra we derive also the wind properties of the targets. We then compare our findings to results obtained in classical TTauri stars.
Results: The accretion rates and wind properties of 80% of the transitional disks in our sample are comparable to those of classical TTauri stars. We show that, in our sample, which is

---

[*] This chapter is the result of a collaborative work that I started and lead. In particular I wrote the two proposals to ask for the observing time to collect the data. I then prepared the observations that have been carried out in service mode. I also carried out all the data reduction of the spectra and I analyzed the data with various discussions with the coauthors. Finally, I was responsible of the composition of the manuscript, where the coauthors helped with several comments and suggestions.

strongly biased towards stongly accreting objects, there are (at least) some transitional disks with accretion properties compatible with those of classical TTauri stars, irrespective of the size of the dust inner hole. Only in 2 cases the mass accretion rates are much lower, while the wind properties remain similar. We do not see any strong trend of the mass accretion rates with the size of the dust depleted cavity, nor with the presence of a dusty optically thick disk very close to the star. These results suggest that, close to the central star, there is a gas rich inner disk. The density of gas in the inner region of these disks is similar to that of classical TTauri stars disks.
Conclusions: The sample analyzed here, that is biased towards known accreting transitional disks, suggests that, at least for some objects, the process responsible of the inner disk clearing should allow for a transfer of gas from the outer disk to the inner region. This should proceed at a rate that does not depend on the physical mechanism producing the gap seen in the dust emission and results in a gas density in the inner disk similar to that of unperturbed disks around stars of similar mass.

5.1 Introduction

At the beginning of their evolution, protoplanetary disks surrounding forming stars appear as a continuous distribution of gas and small dust particles. For the first few Myrs they evolve by viscous accretion (Hartmann et al., 1998), and in the meantime grain growth and planet formation take place. The observations show that, in a relatively small fraction of objects (∼10 %, e.g., Espaillat et al. 2014), a significant change in the disk morphology is detected: a dust-depleted region in the inner part of the disk appears in mm-interferometry observations (e.g. Andrews et al., 2011) and/or as a dip in the mid-IR spectral energy distribution (SED; e.g., Merín et al., 2010). This can be either a *hole* - absence of gas from the dust sublimation radius out to some much larger radius - or a *gap* - absence of gas in a relatively narrow region, like a ring. These disks are known as transitional disks (TDs; e.g., Calvet et al., 2005; Espaillat et al., 2014). In some cases an excess emission is detected at near-infrared wavelengths; this emission comes from a small annulus of warm dust close to the star (e.g., Benisty et al., 2010). These objects are commonly referred to as pre-transitional disks (PTDs; e.g., Espaillat et al., 2010, 2014).

Different processes have been proposed to explain the formation of these gaps/holes. The most plausible mechanisms so far are photoevaporation, grain growth, or planet formation (e.g., Espaillat et al., 2014). Still, none of these processes alone has been shown to be sufficient to explain all observations. Grain growth models explain the observed IR SEDs of TDs, but are unable to reproduce mm-observations (Birnstiel et al., 2012). The detection of large mass accretion rates ($\dot{M}_{\rm acc}$) in several TDs with large inner hole sizes is at odds with photoevaporative model predictions, which expect a very fast depletion of the gas mass reservoir for accretion by the inner disk onto the star (e.g. Owen et al., 2011, 2012). Moreover, planet formation models, which need to include multiple accreting planets to perturb sufficiently the inner disk surface density, still cannot explain TDs with large inner hole sizes and high mass accretion rates (Zhu et al., 2011). At the same time, the presence of a planet could explain the radial and azimuthal distribution of mm-sized grain particles in TDs (Pinilla et al., 2012). New attempts are being made to include various processes in one model. As an example, Rosotti et al. (2013) combined photoevaporation and planet formation, but they were still not able to explain the observed accretion properties of many TDs. Similar constraints arise from observations of winds in TDs. Analysis of forbidden line emission show that winds are emitted from the innermost region of the disk in various objects (Alexander et al., 2014), and these observations suggest that photoevaporation could play a role in the clearing of disks. At the same time, it is not yet clear what is the origin and what are the properties of these winds, and more studies are needed to have a clearer understanding of this aspect.

In this context, the combination of inner hole size, $\dot{M}_{\rm acc}$, and wind properties is a powerful observational diagnostic of disk evolution models. In particular, $\dot{M}_{\rm acc}$ and the wind properties allow us to place strong constraint on the gaseous content of the innermost region of these disks which can be compared with the models. As explained by magnetospheric accretion models (e.g. Hartmann et al., 1998), the process of accretion is related to the gaseous content of the innermost region of the disk at radii $\lesssim$ 0.2 AU. Similarly, forbidden lines are emitted in regions in the disk as close as $\sim$ 0.2 AU from the central star. The measurements of $\dot{M}_{\rm acc}$ for TDs available in the literature are mostly based on secondary indicators (such as the 10% Hα width) and have been obtained using different non-homogeneous techniques. In many cases these values are highly uncertain and, therefore, not reliable. At the same time, very few data on the wind properties for TDs are available. In order to remedy these deficiencies we have collected a sample of 22 spectra of TDs with the ESO VLT/X-Shooter spectrograph. We aim at deriving with an highly reliable method the stellar and accretion properties of these objects and to study simultaneously their wind properties from optical forbidden lines.

The analysis of this sample of TDs that we present here is focused firstly on deriving the values of $\dot{M}_{\rm acc}$ for these objects in order to verify the reliability of those reported in the literature. We use a very detailed and self-consistent analysis to derive accretion rates and simultaneously the spectral types and stellar properties of the objects from the fit of the whole spectrum from UV to NIR. In particular, we want to check the high values of $\dot{M}_{\rm acc}$ for objects with large inner hole sizes, that cannot be explained by current models. At the same time, we want to determine whether there is any dependence of the accretion properties of TDs with their disk morphology, in particular testing possible correlation with the inner hole size. Moreover, we investigate the differences and similarities in accretion and wind properties of TDs with respect to classical TTauri stars. Finally, we put constraint on the properties of the gaseous innermost regions of the disk in these objects from the derived values of $\dot{M}_{\rm acc}$ and from the wind properties.

The paper is organized as follows. In Sect. 5.2 we present the observations, the data reduction procedure, and the properties of the targets in our sample. In Sect. 5.3 we briefly describe the method used to derive the stellar and accretion properties of the objects, and we report the derived values. Then, in Sect. 5.4 we derive the wind properties of our targets. In Sect. 5.5 we discuss our results and describe the additional data from the literature collected to derive our conclusions, which we summarize in Sect. 5.6.

5.2 Observations

All the observations included in this work have been obtained with the ESO/VLT X-Shooter spectrograph. This medium resolution and high-sensitivity instrument covers simultaneously the wavelength range between $\sim$300 nm and $\sim$ 2500 nm, dividing the spectrum in three arms, namely the UVB arm in the region $\lambda\lambda \sim$ 300-560 nm, the VIS arm between $\lambda\lambda \sim$ 560-1020 nm, and the NIR arm from $\lambda \sim$ 1020 nm to $\lambda \sim$ 2500 nm (Vernet et al., 2011). In the following, we present the properties of the sample, the details of the observations, that are reported also in Table 5.1-5.2, and the data reduction procedure.

5.2.1 Sample description

The first criterion used to select the objects in our sample was to include all the targets with known inner hole sizes ($R_{\rm in}$) larger than $\sim$ 20 AU and large $\dot{M}_{\rm acc}$ ($\gtrsim 10^{-9} M_\odot$/yr). These were selected mainly from the sample of Andrews et al. (2011), where the value of $R_{\rm in}$ has been measured using resolved mm-interferometry observations. From this sample we selected the 8 objects with spectral type later than G2. For two of these objects (LkCa15, ISO-Oph 196) the X-Shooter spectra were available in the ESO archive, while we observed the remaining six targets (LkHα330, DM Tau, GM Aur, RX J1615-3255, SR21, and DoAr 44) during our programs (see Table 5.1). We added to these objects also four TDs for which $R_{\rm in}$ was derived from IR SED fitting by Merín et al. (2010) and Kim et al. (2009), namely SZ Cha, CS Cha, Sz 84, and Ser 34. Only for the latter the spectrum was not available in the ESO archive.

Then, we included some objects with smaller inner hole sizes and different values of $\dot{M}_{\rm acc}$, both as high as the object with large $R_{\rm in}$ and smaller than those. In particular, we included five targets whose spectra were not available in the ESO archive and with $R_{\rm in}\lesssim$ 15 AU and as small as 1 AU, namely Oph22, Oph24, and Ser29 from the sample of Merín et al. (2010), RX J1842.9 and RX J1852.3 from Hughes et al. (2010). Finally, we collected all the spectra of TDs classified by Kim et al. (2009) available in the ESO archive (four objects, CHXR22E, Sz 18, Sz 27, and Sz 45) and the spectrum of TWHya, whose $R_{\rm in}$ has been measured with resolved mm-observations by Hughes et al. (2007). In total the sample analyzed here comprises 22 objects.

For 9 of the objects analyzed here the value of $R_{\rm in}$ has been directly determined from resolved mm-interferometry observations (Hughes et al., 2007; Andrews et al., 2011), while for the remaining 13 targets the classification as TD and the size of the inner hole has been determined from IR SED fitting (Kim et al., 2009; Merín et al., 2010; Hughes et al., 2010; Espaillat et al., 2013). The list of targets, their distances, and the values of $R_{\rm in}$ available in the literature are reported in the first three columns of Table 5.3. The objects are located in different star forming regions (Perseus, Taurus, Chameleon, TW Hydrae, Lupus, ρ-Ophiucus, Serpens, Corona Australis) and have values of $R_{\rm in}$ between $\sim$1 to $\sim$ 70 AU, being representative of the whole range of measured values of $R_{\rm in}$. When both values of $R_{\rm in}$ obtained using IR SED fitting and mm-interferometry resolved observations are available we adopt in the analysis the mm-interferometry result. More information on individual objects in the sample are reported in Appendix 5.A.1.

Even if the sample is containing objects of different TD morphologies, such as various inner hole sizes, this is not statistically complete and it is in general biased toward accreting TDs. As explained before, our selection criteria were aimed at observing TDs with already known and high accretion rates, thus our own observations represent a biased sample. On the other hand, the targets collected in the literature were in some cases selected with different criteria that could mitigate our biases. Unfortunately, it is not possible to estimate completely the bias in its selection.

Class III properties

Here we present the properties of three non-accreting (Class III) YSOs, that we use as photospheric templates in our analysis (see Sect. 5.3) to enlarge the available sample of Class III YSOs observed with X-Shooter and presented in Manara et al. (2013a). We follow the same procedure as in Manara et al. (2013a) to derive their spectral types and stellar properties, which are reported in Table 5.2.

The YSO IC348-127 has spectral type (SpT) G4 (Luhman et al., 1998, 2003) and has been classified as Class III from Lada et al. (2006) using Spitzer photometry. This classification, with values of extinction $A_V \sim 6$ mag, has been confirmed by Cieza et al. (2007) and Dahm (2008). We confirm the spectral classification and the extinction, and we derive $L_\star$ = 12.9±5.9 $L_\odot$ for this object. Due to the very high A_V, the spectrum of this target at $\lambda \lesssim$350 nm is very noisy.

The second Class III YSO included in this work is T21, which has been classified as a Class III YSO with SpT G5 by Manoj et al. (2011, and references therein). The typical reddening law of the Chameleon I region in which this object is located is not well constrained (Luhman, 2008), and could be described using values of R_V (Cardelli et al., 1989) up to 5.5. By comparison of the dereddened spectrum with a blackbody at T=5770 K, which is the typical $T_{\rm eff}$ of a star with SpT G5, we obtain that the extinction towards this object is better represented using R_V = 3.1 and A_V = 3.2 mag. Adopting these values, the derived luminosity of the target is $L_\star$ = 18.5±8.5 $L_\odot$.

Finally, we include in the sample CrA75, which has been classified as a Class III YSO with SpT K2 from Forbrich & Preibisch (2007, and references therein). This has been later confirmed by Peterson et al. (2011) and Currie & Sicilia-Aguilar (2011), who suggested that the correct values of extinction for this object is A_V=1.5, assuming R_V=5.5, representative of objects in the Corona Australis region (Peterson et al., 2011; Chapman et al., 2009). With these parameters we derive for CrA75 $L_\star$ = 0.4±0.2 $L_\odot$.

The objects whose properties have been described in this section expand the coverage in SpT of our library of photospheric template. This, however, remains incomplete. In particular, the objects presented in Manara et al. (2013a) have an almost uniform coverage in the SpT range from K5 to M6.5. The three objects presented here, instead, do not cover entirely the range of SpT from G3 to K5. This incompleteness of photospheric templates in this range will be considered in the analysis.

5.2.2 Observational strategy

As explained before, we have included in the analysis both new observations and archival data. In the following, we describe separately our observational strategy and the settings used in the archival observations.

New observations

New observations with the ESO/VLT X-Shooter spectrograph have been carried out in service mode between April and November 2012 (ESO Pr.Id. 089.C-0840 and 090.0050, PI Manara). The targets have been observed in ABBA slit-nodding mode to achieve the best possible sky subtraction also in the NIR arm. The objects have been observed using different slit widths in the UVB arm. For the brightest objects the slit 0.5x11″, which leads to the highest spectral resolution in this arm (R=9100), has been adopted, while for the fainter objects - namely Oph22, Oph24, Ser29, and Ser34 - we have used the 1.0x11″slit, which leads to a lower resolution (R=5100) but allows to achieve an higher S/N. In the VIS and NIR arms the 0.4x11″slit has been adopted for all the targets. This slit width leads to the highest possible resolution (R= 17400, 10500 in the VIS and NIR arms, respectively) and to enough S/N in the spectra. The readout mode used was in all cases ``100,1x1,hg". To obtain a better flux calibration, we observed the targets of Pr.Id. 090.0050 with the large slit (5.0x11″) immediately after the exposure with the narrow slit. With the large slit we obtain spectra with a lower resolution but, at the same time, we avoid slit losses and we get a reliable flux calibration for this spectrum, which is then used to calibrate the narrow slit one (see Sect. 5.2.3). The names of the targets, their coordinates, observing date, and exposure times of the observations are summarized in Table 5.1.

We observed in our programs also two Class III YSOs (see Sect. 5.2.1 for details). We observed CrA 75 using the narrower slits in each arm - 0.5x11″ in the UVB arm, 0.4x11″ in the VIS and NIR arms - to obtain the highest possible spectral resolution. For IC348-127, we adopted the slit widths 1.6x11″, 1.5x11″, and 1.2x11″ in the UVB, VIS, and NIR arms, respectively. This was done in order to achieve enough S/N in the available observing time. We recap in Table 5.2 these information.

Archival data

The data included in our analysis collected from the ESO archive have been obtained using different observational strategies. The observational data are presented here and summarized in Table 5.1 and 5.2.

The transitional disk Sz 84 has been observed during the INAF GTO time in Pr.Id. 089.C-0143 (PI Alcalà). The adopted slits width for this object were 1.0x11″in the UVB arm and 0.9x11″in the VIS and NIR arms. More details on the observing procedure and on the data reduction for this targets are given in Alcalá et al. (2014).

The target ISO-Oph 196 was observed for the program Pr.Id. 085.C-0876 (PI Testi) using the same settings as the one adopted in our observations. We include in our analysis two targets - namely DoAr44 and TW Hya - from the program Pr.Id. 085.C-0764 (PI Guenther). Both targets have been observed with the narrow slits. For all these observations the readout mode used was ``100,1x1,hg", as in our programs, and for each object 4 exposures in the ABBA slit-nodding mode were taken.

We consider in our work also seven objects from the program Pr.Id. 084.C-1095 (PI Herczeg). Six of those - namely CS Cha, CHXR22E, Sz18, Sz27, Sz45, and Sz Cha - are TDs, while T21 is a Class III YSOs. These targets have been observed both with a narrow-slit setting (slit widths 1.0x11″in the UVB and 0.4x11″ in the VIS and NIR arms) and with the large slit to have a better flux calibration of the spectra. The narrow-slit observations have been carried out with the ``400,1x2,lg" mode with a AB slit-nodding mode. The large-slit exposures have been obtained in stare mode.

The data for the TD LkCa15 have been obtained in the program Pr.Id. 288.C-5013 (PI Huelamo). We use in our analysis only 4 exposures obtained in one epoch (2011-12-01), which correspond to an entire ABBA slit-nodding cycle. Observations have been made using the 0.8x11″ slit in the UVB arm, the 0.7x11″ one in the VIS arm, and the 0.9x11″ slit in the NIR arm. The readout mode used was ``100,1x1,hg". Using only 4 frames we obtain a spectrum with enough S/N for our purpose.

5.2.3 Data reduction

Data reduction has been carried out using the version 1.3.7 of the X-Shooter pipeline (Modigliani et al., 2010), run through the *EsoRex* tool. The spectra were reduced independently for the three spectrograph arms. The pipeline takes into account, together with the standard reduction steps (i.e. bias or dark subtraction, flat fielding, spectrum extraction, wavelength calibration, and sky subtraction), also the flexure compensation and the instrumental profile. We checked with particular care the flux calibration and telluric removal of the spectra.

Telluric removal has been performed using the standard telluric spectra that have been provided as part of the standard X-Shooter calibration plan on each night of observations. Spectra of telluric standard stars observed at similar airmasses right before or after the target have been selected. The correction has been accomplished using the IRAF[1] task *telluric* adopting the same procedure for telluric normalization in the VIS and for response-function preparation in the NIR as explained by Alcalá et al. (2014).

Flux calibration has been carried out within the pipeline. Then, for the targets where only narrow-slit observations were available, we checked the flux-calibrated pipeline products comparing them with the available photometry to quantify slit losses. These spectra were then rescaled to the photometric data, and a final check was performed to verify a correct conjunctions between the three arms. The overall final agreement is very good. On the other hand, in the cases where observations with the large slit were available, we

---

[1] IRAF is distributed by National Optical Astronomy Observatories, which is operated by the Association of Universities for Research in Astronomy, Inc., under cooperative agreement with the National Science Foundation.

first checked that the flux-calibration of the spectra obtained with this slit were compatible with the available photometry. Then, we rescaled the narrow-slit spectra to the large-slit flux-calibrated ones, thus achieving the best possible flux calibration. Also in this case the final products have very good conjunctions between the arms.

Table 5.1: Transitional disks observing log

Name	Other names	RA (2000)	DEC (2000)	OBS. DATE	T_{exp} (sec)			Pr.Id (PI)
		h m s	° ′ ″	YY-MM-DD	UVB	VIS	NIR	
LkHα330	...	03 45 48.29	32 24 11.9	2012-12-18	4x150	4x150	4x150	090.C-0050 (Manara)
DM Tau	...	04 33 48.74	18 10 09.7	2012-11-23	4x300	4x300	4x300	090.C-0050 (Manara)
LkCa15	...	04 39 17.79	22 21 03.4	2012-03-06	4x200	4x220	4x200	288.C-5013 (Huelamo)
GM Aur	...	04 55 10.98	30 21 59.3	2012-11-23	4x300	4x300	4x300	090.C-0050 (Manara)
SZ Cha	Ass Cha T 2-6	10 58 16.77	-77 17 17.0	2010-01-18	4x140	4x150	4x150	084.C-1095 (Herczeg)
TW Hya	...	11 01 51.91	-34 42 17.0	2010-05-03	4x150	4x60	4x100	085.C-0764 (Guenther)
CS Cha	ISO ChaI 3	11 02 24.91	-77 33 35.7	2010-01-18	2x55	2x60	2x60	084.C-1095 (Herczeg)
CHXR22E	...	11 07 13.30	-77 43 49.9	2010-01-19	2x280	2x300	2x300	084.C-1095 (Herczeg)
Sz18	Ass Cha T 2-25	11 07 19.15	-76 03 04.8	2010-01-17	2x60	2x53	2x60	084.C-1095 (Herczeg)
Sz27	Ass Cha T 2-35	11 08 39.05	-77 16 04.2	2010-01-18	2x410	2x420	2x420	084.C-1095 (Herczeg)
Sz45	Ass Cha T 2-56	11 17 37.00	-77 04 38.1	2010-01-17	2x45	2x40	2x45	084.C-1095 (Herczeg)
Sz84	...	15 58 02.53	-37 36 02.7	2012-04-18	2x350	2x300	2x115	089.C-0143 (Alcalà)
RX J1615-3255	2MASS J16152023-3255051	16 15 20.23	-32 55 05.1	2012-05-21	4x300	4x300	4x300	089.C-0840 (Manara)
Oph22	SSTc2d J162245.4-243124	16 22 45.40	-24 31 23.7	2012-04-25	4x600	4x600	4x600	089.C-0840 (Manara)
Oph24	SSTc2d J162506.9-235050	16 25 06.91	-23 50 50.3	2012-06-07	4x600	4x600	4x600	089.C-0840 (Manara)
SR 21	EM*SR21A, ISO-Oph 110	16 27 10.28	-24 19 12.7	2012-04-14	4x300	4x300	4x300	089.C-0840 (Manara)
ISO-Oph 196	WSB 60	16 28 16.51	-24 36 57.9	2010-07-28	4x750	4x750	4x750	085.C-0876 (Testi)
DoAr 44	...	16 31 33.46	-24 27 37.2	2010-05-03	4x300	4x140	4x150	085.C-0764 (Guenther)
Ser29	SSTc2d J182911.5+002039	18 29 11.50	00 20 38.6	2012-06-03	4x600	4x600	4x600	089.C-0840 (Manara)
Ser34	SSTc2d J182944.1+003356	18 29 44.11	00 33 56.0	2012-06-03	4x600	4x600	4x600	089.C-0840 (Manara)
RX J1842.9-3532	...	18 42 57.95	-35 32 42.7	2012-05-21	4x300	4x300	4x300	089.C-0840 (Manara)
RX J1852.3-3700	...	18 52 17.29	-37 00 11.9	2012-06-03	4x300	4x300	4x300	089.C-0840 (Manara)

Table 5.2: Class III YSOs properties and observing log

Name	Other names	RA (2000)	DEC (2000)	OBS. DATE	T_{exp} (sec)			SpT	T_{eff}	A_V	d	$L_\star$	Pr.Id (PI)
		h m s	° ′ ″	YY-MM-DD	UVB	VIS	NIR		[K]	[mag]	[pc]	[$L_\odot$]	
IC348-127	Cl* IC 348 CPS 127	03 45 07.9	32 04 01.8	2012-11-11	4x150	4x150	4x150	G4	5800	6.0	320	12.9±5.9	090.C-0050 (Manara)
T21	Ass Cha T 2-21	11 06 15.4	-77 21 56.9	2010-01-19	2x70	2x60	2x60	G5	5770	3.2	160	18.5±8.5	084.C-1095 (Herczeg)
CrA75	RX J190222.0-365541	19 02 22.1	-36 55 40.9	2012-05-17	2x300	2x300	2x300	K2	4900	1.5	130	0.4±0.2	089.C-0840 (Manara)

5.3 Accretion and photospheric parameters

In the following, we briefly describe the procedure adopted to derive self-consistently from the complete X-Shooter spectrum SpT, A_V, and the accretion luminosity ($L_{\rm acc}$) for our targets. The method is described in detail in Manara et al. (2013b) and is based on the fit of various parts of the observed spectra to derive these parameters. In particular, the analysis of the UV-excess together with that of absorption features at longer wavelengths allows us to determine properly the stellar properties and, at the same time, leads to an accurate and direct determination of the accretion properties. We then report the results obtained and compare these to the values derived in the literature.

5.3.1 Method description

Our method is based on a fitting procedure that considers the following three components to reproduce the observed spectrum. We include a range of photospheric template spectra - Class III YSOs from Manara et al. (2013a), augmented with some earlier SpT templates, as explained in Sect. 5.2.1 -. We consider a range of possible values for A_V, and we model the excess spectrum produced by the disk accretion process with a set of isothermal hydrogen slab emission spectra. The photospheric template spectrum and the slab model are normalized using two different normalization constants determined in the fitting procedure.

The best fit model is derived by minimizing a $\chi^2_{\rm like}$ function defined as the sum of the squared deviations (data - model) divided by the error. The $\chi^2_{\rm like}$ is computed in different regions of the UVB and VIS arms of the spectra, including the Balmer and Paschen continua region and some spectral regions around $\lambda \sim 700$ nm characterized by molecular features particularly strong in late-type stars. We also perform a visual check of the best fit in different photospheric features sensitive to the SpT of the target and veiled by the accretion emission.

The SpT of the best fit photospheric template is assumed for the input target with a typical uncertainty of one spectral sub-class. The best fit determined A_V has an uncertainty $\lesssim$0.4 mag, which takes into account both the uncertainty on the template A_V (0.3 mag; Manara et al., 2013a) and the one on the best-fit estimate ($\sim$ 0.2 mag; Manara et al., 2013b). We then derive $L_{\rm acc}$ by integrating the normalized best fit slab model spectrum from 50 nm to 2478 nm to include all the emission of the model. This value has an estimated uncertainty of $\sim$0.2 dex (Manara et al., 2013b). The value of $L_\star$ is obtained from the luminosity of the best fit photospheric template after properly taking into account the normalization factor. The uncertainty on $L_\star$, obtained considering the one on the $L_\star$ of the template ($\sim$ 0.2 dex; Manara et al., 2013a), on the best-fit, and on the distance, is $\sim$0.25 dex.

From the SpT of the photospheric template we derive the $T_{\rm eff}$ of the object using the SpT-$T_{\rm eff}$ relation from Luhman et al. (2003) for M-type stars and Kenyon & Hartmann (1995) for earlier SpT objects. The stellar mass ($M_\star$) is then derived by interpolating evolutionary models of Baraffe et al. (1998) in the position of the object on the HRD, and its uncertainty is computed perturbing the position on the HRD with the aforementioned uncertainty.

Finally, $\dot{M}_{\mathrm{acc}}$ is derived using the classical relation $\dot{M}_{\mathrm{acc}}$= $1.25 \cdot L_{\mathrm{acc}} R_\star/(GM_\star)$ (Hartmann et al., 1998), and this value has a typical uncertainty of $\sim$ 0.4 dex, obtained propagating the uncertainties on $R_\star$, $M_\star$, and L_{acc}.

We adopt the reddening curve from Cardelli et al. (1989). The value of R_V, which is usually uncertain in young star forming regions, is assumed to be R_V=5.5 for CrA (Peterson et al., 2011, and reference therein) and R_V=3.1 for the other regions. In particular, the analysis of the best fit results for the objects located in the ρ-Ophiucus region show that the use of the standard extinction curve at optical wavelength is more appropriate to reproduce the observations of our targets. Also for objects located in the Chameleon I region we find that the standard value R_V=3.1 better describes the observed spectrum of T21, as we reported in Sect. 5.2.1.

In addition to the fitting of the UVB and VIS arms of our spectra described above, we also perform a check of the best fit results using the NIR arm spectra, i.e. at $\lambda \gtrsim$ 1000 nm. For definition, TDs have low or negligible emission in excess to the photosphere at near-infrared wavelengths, and strong excess at mid-infrared and far-infrared wavelengths (e.g., Calvet et al., 2005). For this reason, we expect our best fit photospheric template to match the target spectrum also in the NIR arm. This does not apply when fitting PTDs, where the contribution of inner-disk emission at near-infrared wavelengths, which is not included in our models, is not negligible. In the latter case we expect the photospheric template spectrum to lay below the target one in the near-infrared. In this check we include also, when available, the 3.6 μm Spitzer magnitude of the object, after correcting it for extinction following the prescription of McClure (2009), and the magnitude of the template. The analysis of the IR color excess will be described in detail in Sect. 5.3.2. The best fit stellar and accretion parameters for the targets are reported in Table 5.3.

Finally, we use the relations between the luminosity of some emission lines (L_{line}) and L_{acc} calibrated by Alcalá et al. (2014) to verify our derived parameters. If the best fit L_{acc} and A_V are correct, we expect to derive compatible values of L_{acc} from the luminosity of emission lines located in different parts of the spectra with no particular wavelength dependence. We select for this check the following 5 emission lines spread along the whole spectrum: Hα (λ 656.3 nm), Hβ (λ 486.1 nm), Hγ (λ 434.0 nm), Paβ (λ 1281.8 nm), and Brγ (λ 2166.1 nm). We report the fluxes of these lines in Table 5.4. We collect in the same table also the equivalent width (EW) of the lithium line at λ 670.8 nm, that is an indicator of young ages and confirms the YSO status of all our objects.

In Manara et al. (2013b), Alcalá et al. (2014), and Rigliaco et al. (2012) the procedure described above has been tested on low-mass stars with SpT later than $\sim$K5. We show here its validity also for YSOs with early-K SpT. As reported in Sect. 5.2.1, we stress that the sample of Class III YSOs available is highly incomplete when considering objects with SpT in the interval from G5 to K5, given that we have at disposal only one Class III YSO with SpT K2. Finally, a more detailed analysis is needed for objects with G-type SpT, the so-called intermediate mass stars, because for these objects the excess emission due to accretion can be hardly detected in the wavelength region covered by X-Shooter (e.g. Calvet et al., 2004). We thus discuss in the following sections these three different types of objects separately.

Results for low mass stars

The best fits obtained for TDs with M SpT are shown in Fig. 5.1, while those for TDs with SpT later or equal to K5 in Fig. 5.2. The observed and reddening corrected spectra are shown with a red line, the green line represents the photospheric templates used, the light blue line the slab model, and the blue line the best fit, which is the sum of the photospheric template and the slab model. The best fit is plotted only in the regions where it is calculated, i.e. $\lambda\lambda$ $\sim$330-1000 nm. The agreement between the best fit and the observed spectrum in this wavelength range is always very good. At wavelengths longer than $\sim$ 1000 nm we plot only the photospheric template and the observed spectra, including also their 3.6 μm Spitzer magnitudes, when available. As mentioned earlier, we expect the photospheric template spectrum not to exceed the target one in this region. This is the case for most of the targets, but not for Oph22, Oph24, DM Tau, and GM Aur. For one object, Sz27, the excess emission at near-infrared wavelengths confirms the previous classification as PTD. According to our best fits, also CHXR22E and ISO-Oph 196 should be classified as PTD.

The stellar and accretion parameters obtained for these targets are reported in Table 5.3. For the objects considered in this section, i.e. with SpT later or equal to K5, the best fit SpT is the same within up to one or two spectral sub-class as the one reported in the literature. In most cases the difference with respect to the literature values is small also for the other stellar and accretion parameters. In particular, values of $\dot{M}_{\rm acc}$ agree within 0.3 dex with those reported in the literature. The objects with larger differences are Sz18, Sz45, RX J1615, Oph24, Ser29, and Ser34. We suggest that these differences are due to the different methodologies of previous studies with respect to our. Variability of accretion would result in a smaller difference. Recent studies showed that in most young accreting stars these variations are in general smaller than 0.3 dex (e.g., Costigan et al., 2012). For Ser29 we are only able to provide an upper limit on $L_{\rm acc}$ from the fitting due to the low signal-to-noise of the spectrum in the whole UVB arm. This value is compatible with the measurement of the Hα line, which is the only line seen in emission in the spectrum.

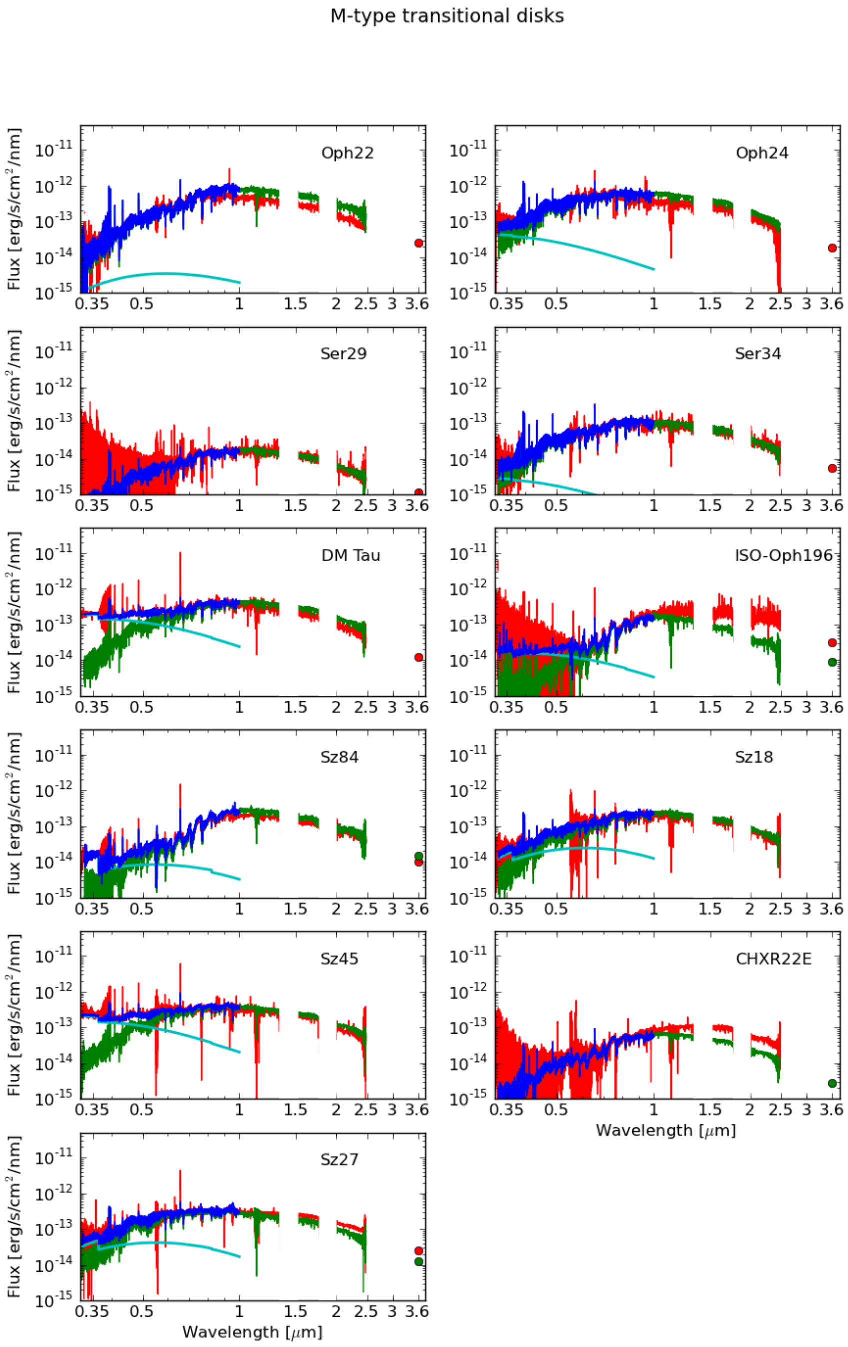

Figure 5.1: Best fit for M-type transitional disks. The red line is the observed dereddened spectrum, green line the photospheric template, light blue line the slab model, and blue line the best fit.

Table 5.3: Stellar, disk, and accretion parameters of the targets

Name	dist [pc]	R$_{\rm in}$ [AU]	SpT	T$_{\rm eff}$ [K]	A$_V$ [mag]	L$_\star$ [L$_\odot$]	log $L_{\rm acc}$ [L$_\odot$]	M$_\star$ [M$_\odot$]	log $\dot{M}_{\rm acc}$ [M$_\odot$/yr]	$R_\star$ [$R_\odot$]	Disk type	Ref	
LkHα330	250	68	G4	5800	3.0	14.40	-0.6	2.35±0.57	-7.8	3.74±1.08	PTD	1	D
DM Tau	140	19	M2	3560	1.1	0.36	-1.3	0.56±0.08	-8.2	1.57±0.46	TD	1	B
LkCa 15	140	50	K2	4900	1.2	1.21	-1.1	1.24±0.33	-8.4	1.52±0.44	PTD	1	B
GM Aur	140	28	K5	4350	0.6	0.99	-1.0	1.36±0.36	-8.3	1.75±0.51	PTD	1	B
Sz-Cha	160	29	K2	4900	1.3	1.17	-0.5	1.22±0.32	-7.8	1.50±0.43	PTD	2	B
TW Hya	55	4	K7	4060	0.0	0.18	-1.6	0.79±0.17	-8.9	0.85±0.25	TD	3	B
CS Cha	160	43	K2	4900	0.8	1.45	-1.0	1.32±0.37	-8.3	1.66±0.48	TD	4	B
CHXR22E	160	7	M4	3270	2.6	0.07	-4.1	0.24±0.06	-10.9	0.82±0.24	PTD	2	B
Sz18	160	8	M2	3560	1.3	0.26	-1.9	0.54±0.08	-8.9	1.34±0.39	TD	2	B
Sz27	160	15	K7	4060	2.9	0.33	-1.6	0.96±0.24	-8.9	1.16±0.34	PTD	2	B
Sz45	160	18	M0.5	3780	0.7	0.42	-1.2	0.85±0.11	-8.3	1.51±0.44	TD	2	B
Sz84	150	55	M5	3125	0.5	0.24	-2.3	0.24±0.06	-8.9	1.67±0.49	TD	5	B
RX J1615	185	30	K7	4060	0.0	0.89	-1.3	1.16±0.16	-8.5	1.90±0.55	TD	1	B
Oph22	125	1	M3	3415	3.0	0.56	-2.9	0.53±0.14	-9.7	2.13±0.62	TD	5	B
Oph24	125	3	M0	3850	4.0	0.42	-2.0	0.92±0.13	-9.2	1.45±0.42	TD	5	B
SR 21	125	36	G4	5800	6.0	8.11	-0.7^a	1.95±0.50	-7.9^a	2.81±0.81	PTD	1	D
ISO-Oph196	125	15	M5.5	3060	3.0	0.08	-2.3	0.14±0.04	-8.9	1.00±0.29	PTD	1	B
DoAr 44	125	30	K2	4900	1.7	0.64	-0.9	0.97±0.19	-8.2	1.11±0.32	PTD	1	B
Ser29	230	8	M2	3560	2.6	0.04	<-3.8	0.47±0.08	<-11.2	0.52±0.15	TD	5	B
Ser34	230	25	M1	3705	2.7	0.26	-2.7	0.71±0.08	-9.8	1.23±0.36	TD	5	B
RX J1842.9	130	5	K2	4900	0.4	0.56	-1.5	0.93±0.16	-8.8	1.03±0.30	PTD	6	B
RX J1852.3	130	16	K2	4900	1.0	0.77	-1.4	1.04±0.19	-8.7	1.21±0.35	TD	6	B

Notes. Reference for $R_{\rm in}$: (1) Andrews et al. (2011), (2) Kim et al. (2009), (3) Hughes et al. (2007), (4) Espaillat et al. (2013), (5) Merín et al. (2010), (6) Hughes et al. (2010), Evolutionary models used to derive $M_\star$ and $\dot{M}_{\rm acc}$: (B) Baraffe et al. (1998), (D) D'Antona & Mazzitelli (1994). ^{a}Highly uncertain value.

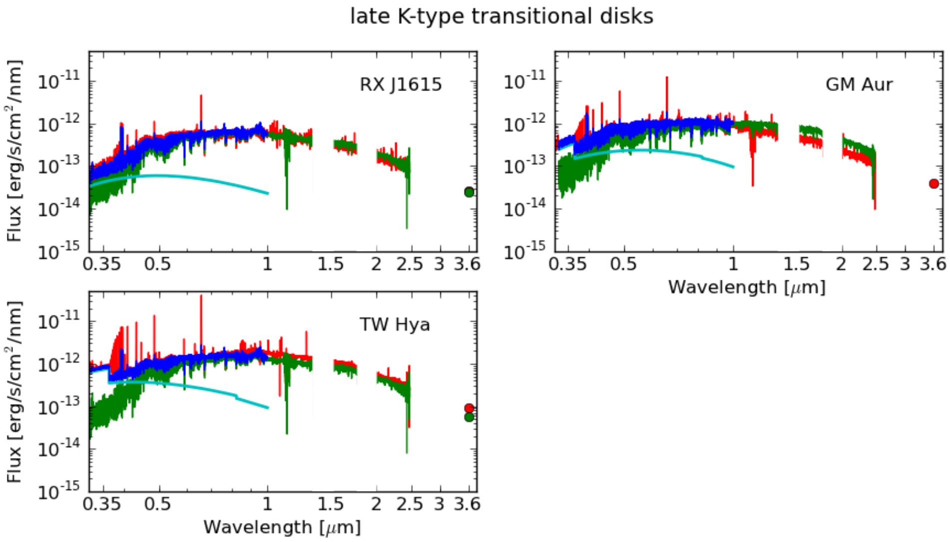

Figure 5.2: Best fit for late-K type transitional disks. Colors as in Fig. 5.1

Results for early K-type stars

For six of our objects we obtain a best fit using the Class III YSO template with SpT K2. These results are also reported in Table 5.3, while their best fit are shown in Fig. 5.3. In all these cases the best fit is very good with the only exception of RX J1852.3. With respect to the literature, typical differences of the SpT from the best fit K2 are of up to two spectral sub-classes apart from CS Cha, which was previously classified as K6. We adopt for all these targets SpT K2 in our analysis, with the caveat that the uncertainty on this parameter is larger for these objects with respect to later SpT targets due to the already mentioned incompleteness of photospheric templates of SpT late-G and early-K. Our best fits confirm that DoAr44, LkCa15, and SzCha are PTD (see also Sect. 5.3.2). We find a hint of excess in the K-band spectrum of RX J1842.9, which becomes clearer at the Spitzer [3.6] data point. This confirms the observations of infrared excess in this object reported in Hughes et al. (2010) and implies that also this object is a PTD. The largest difference in the derived values of $\dot{M}_{\rm acc}$ is for SzCha, which results to be a stronger accretor than previously determined.

Results for intermediate-mass stars

Two objects in our sample are of early-G SpT, namely LkHα330 and SR21. For these TDs we have not been able to detect excess emission with our fitter. As also Calvet et al. (2004) pointed out, the excess emission for intermediate-mass stars like these two is hard to be detected at λ >330 nm due to the similar temperatures of the accretion shock and the stellar photosphere. We have only been able to fit these spectra to derive their A_V and $L_\star$, and we show these best fits in Fig. 5.4. Their positions on the HRD are not covered by the evolutionary tracks of Baraffe et al. (1998), so we derive the values of $M_\star$ for these two targets using the models of D'Antona & Mazzitelli (1994). In both objects we detect

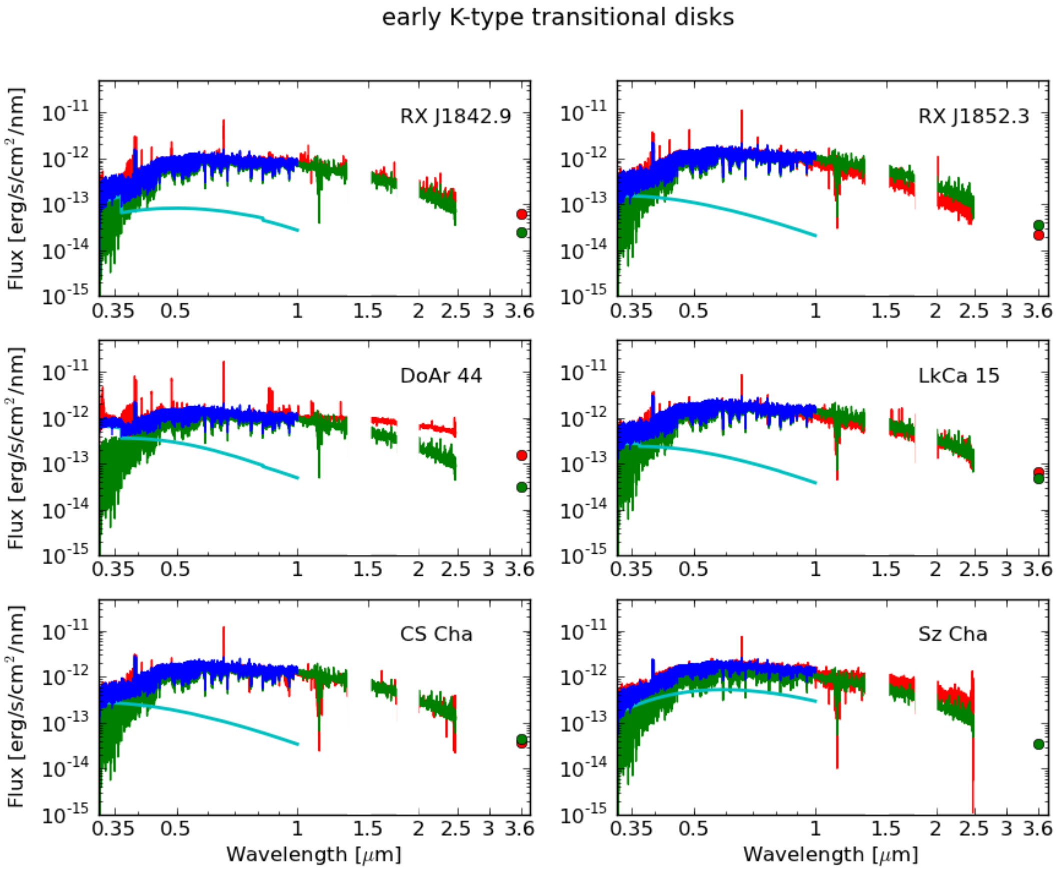

Figure 5.3: Best fit of early K-type transitional disks. Colors as in Fig. 5.1

an excess emission in the near-infrared wavelengths which could imply these objects are PTD.

In the spectrum of LkHα330 various emission lines are present, such as the Hα, Hβ, Paβ, and Brγ. The only L_{acc}-L_{line} relation available for this class of objects is the one reported in Calvet et al. (2004) for the Brγ line. We use this relation to derive a value of $L_{\text{acc}} \sim 0.23$ $L_\odot$ which leads to a value of $\dot{M}_{\text{acc}}$ consistent with those reported in the literature.

The hydrogen recombination lines of SR21 appear in absorption in the whole spectrum. The same is found when looking at the CaII IRT lines. Moreover, the photospheric lines of this object appear much broader than the corresponding Class III YSO spectrum. Nevertheless, the wings of the hydrogen lines, in particular those of the Hα line, appear in emission at very high velocities up to $\sim$ 250 km/s, thus suggesting that they originate in an accretion-related infall region. Therefore we classify this object as an accreting TD. Given that no Brγ emission is detected in this spectrum, we derive L_{acc} from the luminosity of the Hα line. This is derived from the dereddened spectrum corrected for the photospheric line contribution, which is estimated using a synthetic spectrum of the same T_{eff} and broaden to match photosferic lines close to the Hα. To convert the luminosity of the Hα line in L_{acc}

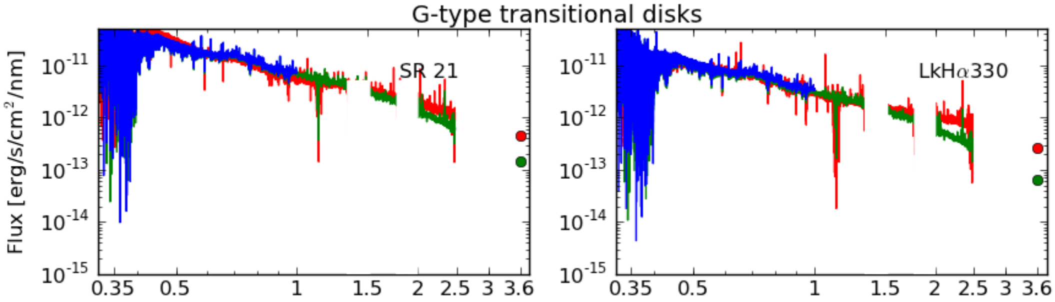

Figure 5.4: Best fit of G-type transitional disks. Colors as in Fig. 5.1.

we use the relation provided by Alcalá et al. (2014). Given all the assumptions adopted to estimate this value we consider the derived $L_{\rm acc}$ very uncertain.

Table 5.4: Derived properties of analyzed lines

Name	$F_{H\alpha}$ [erg s^{-1} cm^{-2}]	$F_{H\beta}$ [erg s^{-1} cm^{-2}]	$F_{H\gamma}$ [erg s^{-1} cm^{-2}]	$F_{Pa\beta}$ [erg s^{-1} cm^{-2}]	$F_{Br\gamma}$ [erg s^{-1} cm^{-2}]	$EW_{Li_{\lambda 670.8}}$ [mÅ]
LkHα330	$(1.11 \pm 0.02) \times 10^{-11}$	$(6.6 \pm 2.9) \times 10^{-13}$	$< 3.2 \times 10^{-13}$	$(6.5 \pm 0.3) \times 10^{-13}$	$(5.9 \pm 3.4) \times 10^{-14}$	110±2
DM Tau	$(4.48 \pm 0.02) \times 10^{-12}$	$(3.5 \pm 0.1) \times 10^{-13}$	$(2.2 \pm 0.1) \times 10^{-13}$	$(1.06 \pm 0.07) \times 10^{-13}$	$(1.4 \pm 0.2) \times 10^{-14}$	410±21
LkCa 15	$(3.1 \pm 0.1) \times 10^{-12}$	$(3.7 \pm 1.6) \times 10^{-13}$	$(1.5 \pm 0.1) \times 10^{-13}$	$(1.2 \pm 0.2) \times 10^{-13}$	$(1.9 \pm 1.5) \times 10^{-14}$	460±23
GM Aur	$(1.06 \pm 0.02) \times 10^{-11}$	$(2.1 \pm 0.07) \times 10^{-12}$	$(7.9 \pm 0.4) \times 10^{-13}$	$(1.01 \pm 0.02) \times 10^{-12}$	$(1.6 \pm 0.1) \times 10^{-13}$	440±22
Sz Cha	$(2.6 \pm 0.1) \times 10^{-12}$	$< 4.7 \times 10^{-14}$	$< 4.0 \times 10^{-14}$	$(1.9 \pm 0.3) \times 10^{-13}$	$< 1.3 \times 10^{-14}$	350±10
TW Hya	$(2.39 \pm 0.04) \times 10^{-11}$	$(4.52 \pm 0.07) \times 10^{-12}$	$(2.2 \pm 0.05) \times 10^{-12}$	$(2.21 \pm 0.04) \times 10^{-12}$	$(2.61 \pm 0.08) \times 10^{-13}$	430±21
CS Cha	$(5.23 \pm 0.09) \times 10^{-12}$	$(4.7 \pm 1.1) \times 10^{-13}$	$(2.2 \pm 0.4) \times 10^{-13}$	$(1.1 \pm 0.1) \times 10^{-13}$	$(2.6 \pm 1.1) \times 10^{-14}$	510±28
CHXR22E	$(1.1 \pm 0.1) \times 10^{-14}$	$(4.4 \pm 0.6) \times 10^{-15}$	$(9.1 \pm 4.9) \times 10^{-16}$	$< 9.1 \times 10^{-15}$	$< 2.4 \times 10^{-15}$	230±56
Sz18	$(3.8 \pm 0.2) \times 10^{-13}$	$(2.5 \pm 0.6) \times 10^{-14}$	$(7.9 \pm 0.9) \times 10^{-15}$	$(4.3 \pm 1.7) \times 10^{-15}$	$< 2.7 \times 10^{-15}$	590±77
Sz27	$(1.83 \pm 0.08) \times 10^{-12}$	$(7.8 \pm 0.6) \times 10^{-14}$	$(3.2 \pm 0.2) \times 10^{-14}$	$(4.9 \pm 0.5) \times 10^{-14}$	$(1.0 \pm 0.2) \times 10^{-14}$	510±29
Sz45	$(2.83 \pm 0.02) \times 10^{-12}$	$(4.6 \pm 0.1) \times 10^{-13}$	$(2.9 \pm 0.1) \times 10^{-13}$	$(1.17 \pm 0.08) \times 10^{-13}$	$(2.0 \pm 0.5) \times 10^{-14}$	440±32
Sz84	$(7.0 \pm 0.1) \times 10^{-13}$	$(5.59 \pm 0.09) \times 10^{-14}$	$(2.7 \pm 0.04) \times 10^{-14}$	$(3.1 \pm 0.3) \times 10^{-14}$	$(1.1 \pm 0.5) \times 10^{-14}$	460±20
RX J1615	$(2.24 \pm 0.05) \times 10^{-12}$	$(2.5 \pm 0.3) \times 10^{-13}$	$(6.9 \pm 1.1) \times 10^{-14}$	$(7.5 \pm 1.6) \times 10^{-14}$	$(1.5 \pm 0.7) \times 10^{-14}$	550±32
Oph22	$(1.9 \pm 0.09) \times 10^{-13}$	$(5.4 \pm 0.1) \times 10^{-14}$	$(2.8 \pm 0.1) \times 10^{-14}$	$< 1.7 \times 10^{-14}$	$< 7.3 \times 10^{-15}$	570±40
Oph24	$(3.2 \pm 0.2) \times 10^{-13}$	$(1.08 \pm 0.03) \times 10^{-13}$	$(7.7 \pm 0.3) \times 10^{-14}$	$< 6.4 \times 10^{-14}$	$(5.0 \pm 1.5) \times 10^{-15}$	570±37
SR 21^{a}	...	...	...	...	...	140±2
ISO−Oph196	$(3.54 \pm 0.01) \times 10^{-13}$	$(8.8 \pm 0.6) \times 10^{-14}$	$(8.8 \pm 0.8) \times 10^{-14}$	$< 7.4 \times 10^{-14}$	$(2.2 \pm 0.3) \times 10^{-14}$	370±31
DoAr 44	$(9.4 \pm 0.1) \times 10^{-12}$	$(2.66 \pm 0.08) \times 10^{-12}$	$(1.04 \pm 0.06) \times 10^{-12}$	$(1.12 \pm 0.01) \times 10^{-12}$	$(2.6 \pm 0.1) \times 10^{-13}$	420±19
Ser29	$(1.3 \pm 0.1) \times 10^{-14}$	$< 1.7 \times 10^{-15}$	$< 8.0 \times 10^{-15}$	$< 1.9 \times 10^{-15}$	$< 4.8 \times 10^{-17}$	380±199
Ser34	$(1.02 \pm 0.05) \times 10^{-13}$	$(7.8 \pm 0.7) \times 10^{-15}$	$(5.9 \pm 1.1) \times 10^{-15}$	$< 1.6 \times 10^{-15}$	$(1.8 \pm 0.4) \times 10^{-15}$	630±40
RX J1842.9	$(3.41 \pm 0.08) \times 10^{-12}$	$(4.6 \pm 0.6) \times 10^{-13}$	$(2.0 \pm 0.2) \times 10^{-13}$	$(1.2 \pm 0.1) \times 10^{-13}$	$(1.5 \pm 0.7) \times 10^{-14}$	440±21
RX J1852.3	$(5.67 \pm 0.09) \times 10^{-12}$	$(1.01 \pm 0.07) \times 10^{-12}$	$(2.8 \pm 0.4) \times 10^{-13}$	$(2.0 \pm 0.2) \times 10^{-13}$	$(4.0 \pm 2.5) \times 10^{-14}$	510±30

Notes. Fluxes are reported in the format (flux ± err) multiplied by the order of magnitude. ^{a}The estimate of the flux of the emission lines of SR21 is very uncertain, thus we do not report these values for this object.

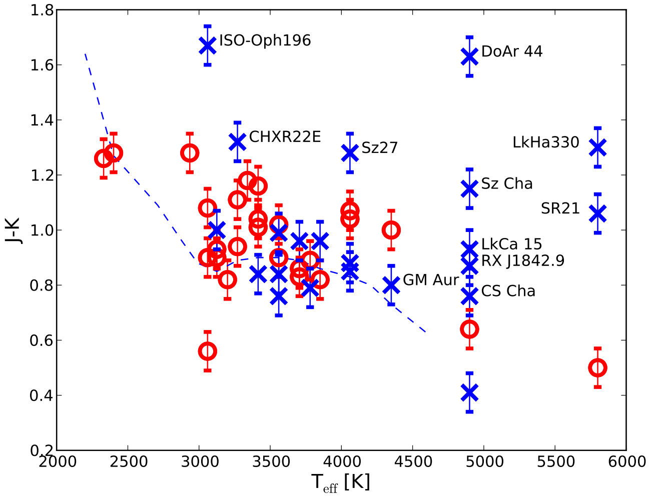

Figure 5.5: ($J - K$) color calculated with synthetic photometry on the best fit dereddened TD spectra (*blue crosses*) vs T_{eff} of the targets. The *red circles* represent the Class III YSOs colors derived with synthetic photometry on their spectra. The dashed line represents the photospheric color of YSOs according to Luhman et al. (2010).

5.3.2 Infrared color excess

From the best fit derived as explained above we analyze the color excess in the IR colors in order to detect emission from the innermost dusty disk. We perform synthetic photometry on the dereddened TD spectra and on the Class III YSO spectra. We then plot in Fig. 5.5-5.6 the $J-K$ and $J-$[3.6] colors as a function of T_{eff} both for the Class III YSOs (*red circles*) and the TDs (*blue crosses*). These colors trace the presence of an inner disk, which would result in an excess emission with respect to the photosphere in the K band and at 3.6 μm. As a reference, we plot with a dashed line the photospheric color locus of diskless YSOs derived by Luhman et al. (2010). We see that the colors of the Class III YSOs are distributed on these plots around this empirically calibrated locus with a small dispersion. Also most of the TDs have colors compatible with the Class III YSOs at the same T_{eff}, meaning that their IR colors are compatible with photospheric ones, thus they have no dust-rich inner disk. In some cases, however, the excess is detectable and the objects should be classified as PTD. This is the case for the objects already listed in the previous sections, namely ISO Oph 196, CHXR22E, Sz 27, DoAr 44, Sz Cha, LkCa15, RX J1842.9, LkHα330, and SR21, and for GM Aur, given the excess in the $J-$[3.6] color (see Fig. 5.6). This object was also previously classified as PTD by Calvet et al. (2005) and Espaillat et al. (2010). For one object, CS Cha, the excess is detected in the $J - K$ color but not in the J-[3.6] one, and in the former it is compatible with the Class III YSOs color. We thus classify this object as TD. We report this classification in Table 5.3. The objects classified as PTD have R_{in} values that range smoothly from 5 to 68 AU. The presence of a dusty innermost region of the disk is thus uncorrelated with the size of the dust-depleted gap.

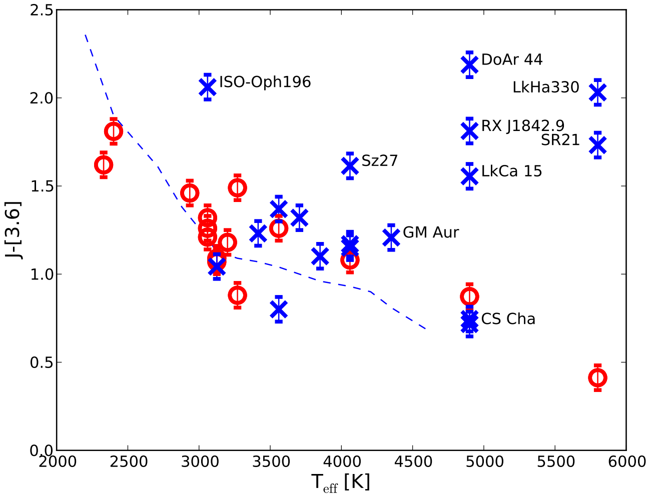

Figure 5.6: ($J-[3.6]$) color vs $T_{\rm eff}$ of the targets. The J magnitude is calculated on the best-fit dereddened TD spectra (*blue crosses*), while the [3.6] magnitude is derived from the literature. Colors and symbols are the same as in Fig. 5.5.

5.4 Wind signatures

The most prominent forbidden line present in the spectra of our TDs is the [OI] λ 630 nm line. This line has been detected in many accreting YSOs (e.g., Hartigan et al., 1995) and can present two distinct components. The high-velocity component (HVC, $\Delta v \sim$ 100-200 km s^{-1}) of this line is known to trace collimated jets. The origin of the low-velocity component (LVC, $\Delta v \sim$ 2-3 km s^{-1}), instead, is still unclear. It is believed to originate in the disk or from the base of a slow disk wind (Hartigan et al., 1995), but there are suggestions that it can be originated in a photoevaporative wind (Rigliaco et al., 2013, and references therein). We detect the LVC of this line in 17 ($\sim$80 %) of the spectra of our TDs, with a clear detection of the HVC only in ISO-Oph 196.

We derive the flux and the peak velocity of the LVC of the [OI]λ 630 nm line in the following way. We firstly refine the wavelength calibration by fitting the photospheric Li I line at λ 670.78 nm and shifting the spectra to match the nominal central wavelength of this line. This line is detected in all the objects and its EW are reported in Column 7 of Table 5.4. Then, we fit with a gaussian profile on the dereddend spectrum the LVC of the [OI]λ630 nm line and we integrate the flux of the best fit to derive the line flux. The error on the flux is derived from the standard deviation of the continuum estimated around the line. The derived flux, error, peak velocity (v_0), and FWHM of the gaussian fit is reported in Table 5.5. The lines and their best fits are shown in Fig. 5.7. In all the objects with detected [OI]λ630 nm line, with the exception of LkHα330, the line is slightly blueshifted, with values of v_0 ranging from $\sim$ -2 km/s to $\sim$ -8 km/s in most cases, and only two objects (Oph24 and ISO-Oph 196) with $v_0 <$ -10 km/s. Even if the exact value of v_0 in each object is still uncertain also after the procedure to correct the wavelength calibration described

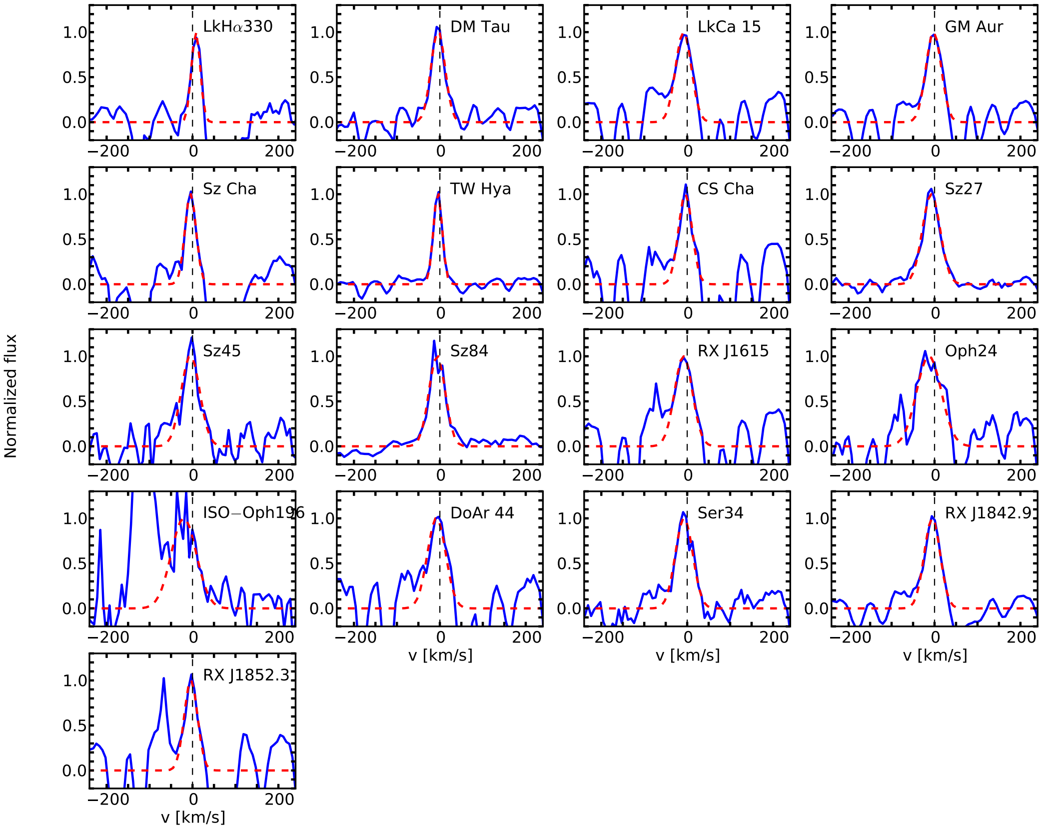

Figure 5.7: Normalized [OI] 630 nm line for the transitional disks in our sample where this line has been detected. The red dashed line is the best gaussian fit of the low-velocity component of the line.

above, we see that the [OI]λ630 nm line is systematically blueshifted, meaning that it is originated in some kind of wind. The mean value of the FWHM of the [OI]λ630 nm line derived from the spectra of our targets is $\sim$ 40 km/s. We note, however, that the values of FWHM $\lesssim$ 30 km/s should be considered with caution, as these values are close to the nominal resolution of the instrument.

5.5 Discussion

In this section we discuss the accretion and wind properties of our targets and we estimate the amount of gaseous material in their inner disks. It should be kept in mind that our sample is composed mostly by objects already known to be strong accretors and it is *not* an unbiased sample. Nevertheless, the properties of these strong-accreting TDs have important consequences on our understanding of the TDs formation and evolution, as we

Table 5.5: Derived properties of [OI] line at λ 630 nm

Name	$F_{[OI]\lambda630}$ [erg s^{-1} cm^{-2}]	$v_{0,[OI]\lambda630}$ [km/s]	$FWHM_{[OI]\lambda630}$ [km/s]
LkHα330	$(6.1 \pm 1.9) \times 10^{-14}$	7.7	24
DM Tau	$(9.1 \pm 1.8) \times 10^{-15}$	-4.3	38
LkCa 15	$(4.6 \pm 1.9) \times 10^{-14}$	-8.7	43
GM Aur	$(3.9 \pm 1.0) \times 10^{-14}$	-2.2	42
Sz Cha	$(2.4 \pm 0.9) \times 10^{-14}$	-4.7	30
TW Hya	$(9.0 \pm 0.8) \times 10^{-14}$	-4.8	24
CS Cha	$(2.8 \pm 1.5) \times 10^{-14}$	-4.4	37
CHXR22E	$< 8.0 \times 10^{-16}$	...	...
Sz18	$< 2.6 \times 10^{-15}$	...	...
Sz27	$(5.4 \pm 0.3) \times 10^{-14}$	-7.6	49
Sz45	$(1.8 \pm 0.5) \times 10^{-14}$	-4.8	50
Sz84	$(2.4 \pm 0.2) \times 10^{-15}$	-6.5	44
RX J1615	$(1.7 \pm 0.8) \times 10^{-14}$	-8.7	49
Oph22	$< 7.3 \times 10^{-15}$	...	...
Oph24	$(3.0 \pm 1.3) \times 10^{-14}$	-13.0	67
SR 21	$< 6.4 \times 10^{-14}$	...	...
ISO−Oph196	$(1.4 \pm 0.4) \times 10^{-15}$	-20.4	68
DoAr 44	$(2.6 \pm 1.2) \times 10^{-14}$	-7.7	50
Ser29	$< 4.2 \times 10^{-16}$	...	...
Ser34	$(4.1 \pm 0.8) \times 10^{-15}$	-7.3	47
RX J1842.9	$(5.0 \pm 0.8) \times 10^{-14}$	-5.5	43
RX J1852.3	$(2.6 \pm 1.3) \times 10^{-14}$	-3.8	36

Notes. Fluxes are reported in the format (flux ± err) multiplied by the order of magnitude.

discuss in the following.

5.5.1 Accretion properties

Here we aim at understanding whether there is a dependence of the accretion properties of our objects with the morphology of the disk, in particular with $R_{\rm in}$, and whether there are differences with respect to accretion properties in cTTs.

In Fig. 5.8 we show the logarithmic values of $\dot{M}_{\rm acc}$ determined in Sect. 5.3 as a function of the values of $R_{\rm in}$ reported in the literature (see Table 5.3). We represent these values using different symbols to differentiate measurement of $R_{\rm in}$ derived with resolved mm-interferometry observations (*red circles*) from those obtained by modeling the optical to mid-infrared SEDs (*blue squares*). The uncertainties on the values of $R_{\rm in}$ are various and depend strongly on the assumptions on the models. In particular, values of $R_{\rm in}$ determined with SED fitting are strongly model-dependent and can be an overestimation of the real gap size (Rodgers-Lee et al., 2014). We do not find any strong trend of $\dot{M}_{\rm acc}$ increasing with $R_{\rm in}$ over the whole range of $R_{\rm in}$ we have explored. If we compare our results with more complete samples of TDs, e.g., Kim et al. (2013), we see that our results agree with the upper boundary of their sample, and that indeed there is an increase of $\dot{M}_{\rm acc}$ with $R_{\rm in}$

up to values of $R_{\rm in}\sim$ 20 AU. At $R_{\rm in}$ larger than about 20 AU, however, $\dot{M}_{\rm acc}$ is essentially constant in our sample. In fact, a similar trend is also present in the upper envelope of the TDs considered in Kim et al. (2013), where, however, there are just two accreting TDs with $\dot{M}_{\rm acc}> 10^{-8}M_\odot$/yr for $R_{\rm in}\gtrsim$ 20 AU and none for $R_{\rm in}\gtrsim$30-40 AU. All objects in our sample have $\dot{M}_{\rm acc}$ in the range $10^{-9}-10^{-8}M_\odot$/yr, independently of the value of $R_{\rm in}$. Therefore, the density of their innermost gaseous disk, which accretes onto the star, does not depend on the mechanism that produces the gap or the hole, and must be high enough to sustain the observed accretion rates.

We want now to compare the derived values of $\dot{M}_{\rm acc}$ for our sample of TDs with a sample of classical TTauri stars (cTTs) to determine whether the accretion properties are different in these two classes of objects. It is well established that the values of $\dot{M}_{\rm acc}$ in cTTs depend on $M_\star$ with a power of ~1.6-1.8 (e.g., Muzerolle et al., 2003; Rigliaco et al., 2011a; Manara et al., 2012; Alcalá et al., 2014; Ercolano et al., 2014). A comparison of the values of $\dot{M}_{\rm acc}$ between different samples should be based on a comparison of this relation and not on the values of $\dot{M}_{\rm acc}$ alone. Another well known dependence is the one between $\dot{M}_{\rm acc}$ and the age of the targets (e.g., Hartmann et al., 1998; Sicilia-Aguilar et al., 2010; Manara et al., 2012), which is a consequence of the viscous evolution of protoplanetary disks. Therefore, a comparison should be carried out between objects of similar mean age. Finally, different methodology and evolutionary models can lead to different values of $\dot{M}_{\rm acc}$; it is thus needed to compare samples analyzed with a similar methodology. For these reasons we select as a comparison sample the objects studied by Alcalá et al. (2014). These are located in the Lupus I and III clouds and have ages $\sim$ 3 Myr, similar to the objects in our sample. The analysis of that sample was carried out with the same methodology as the one we used here. We show in Fig. 5.9 the logarithmic relation between $\dot{M}_{\rm acc}$ and $M_\star$ for these two samples. Our data are reported as blue circles, while data from Alcalá et al. (2014) as green diamonds. The solid line on the plot is the best fit relation from Alcalá et al. (2014), and the dashed lines represent the dispersion of 0.4 dex around this best fit relation. The typical errors on the quantities are shown as a black cross. We see that ~80% of the TDs have values of $\dot{M}_{\rm acc}$ consistent with the values found by Alcalá et al. (2014) for Lupus objects of the same $M_\star$. Therefore, for these objects we do not see any difference in the accretion properties with respect to those in cTTs. We also perform on these two samples a Kolmogorov-Smirnof statistical test (K-S test). When restricting to objects in the same $M_\star$ range the probability that the two samples are drawn from the same distribution is 80%. We can then conclude that for our sample, the amount of accretion depends on the mass of the central object, and not on the evolutionary stage (cTTs or TD) of the system.

This result differs from what found in the literature. For example, Najita et al. (2007) noted that TDs have a sistematically smaller value of $\dot{M}_{\rm acc}$ at any given value of the mass of the disk (M_d). They inferred that the accretion rates for TDs are in general smaller than for cTTs. Similarly, various further analyses of larger samples of TDs found values of $\dot{M}_{\rm acc}$ typically lower than those of cTTs by a factor ~10 (e.g., Kim et al., 2009, 2013; Muzerolle et al., 2010; Espaillat et al., 2012). A critical review of these results by Espaillat et al. (2014) found somehow different results with respect to Najita et al. (2007), as they report values of $\dot{M}_{\rm acc}$ for 3 TDs in ρ-Ophiucus which are compatible with the locus of cTTs in the same

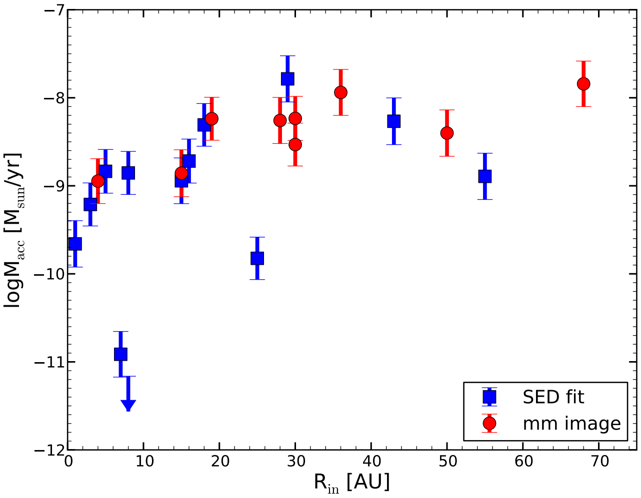

Figure 5.8: Logarithm of the mass accretion rate vs inner hole size for our sample. Different symbols are used to distinguish the methods used in the literature to derive the size of the inner hole. *Blue squares* are adopted when this has been derived using IR-SED fitting, while *red circles* when the values are derived from resolved mm-interferometry observations. Downward arrows are upper limits. The two lowest points are, from left to right, CHXR22E and Ser29. The object at $R_{\rm in}$=25 AU and log$\dot{M}_{\rm acc}$=−9.8 is Ser34.

region and in Taurus on the $\dot{M}_{\rm acc}$-M_d plane. They suggest that different results may arise from different sample selection and/or different methods to estimate $\dot{M}_{\rm acc}$. To avoid this possible systematic bias, we have shown here only the comparison between our sample of TDs and the sample of cTTs in Lupus, which is analyzed in the same way as our objects. We stress here again that our TDs have been selected to be mostly strong accretors, and that we do not derive conclusions for the whole TD population. Nevertheless, our results prove that there are TDs that accrete at the same rate of cTTs.

The two main outliers in Fig. 5.8-5.9 are the object with an upper limit on $L_{\rm acc}$, Ser29, and CHXR22E. The lower intensity of accretion for these targets implies that the gas density in the inner disk is substantially depleted with respect to the one of cTTs. These objects do not have any peculiar property reported in the literature. From Fig. 5.9 we note that in the same range of $M_\star$ of these objects there are other TDs with values of $\dot{M}_{\rm acc}$ comparable or even higher than cTTs. Therefore, these objects are not peculiar in their stellar properties. We will discuss in more detail about these objects later after considering their wind and dusty inner disk properties. It is possible that these objects are part of a population of TDs with lower values of $\dot{M}_{\rm acc}$ not included in our sample.

5.5.2 Wind properties

As discussed in Sect. 5.4, we have measured the flux of the LVC of the [OI]λ630 nm line, which is a tracer of winds in YSOs. To determine whether the wind properties of our objects depend on the disk morphology we compare in Fig. 5.10 the logarithmic luminosity

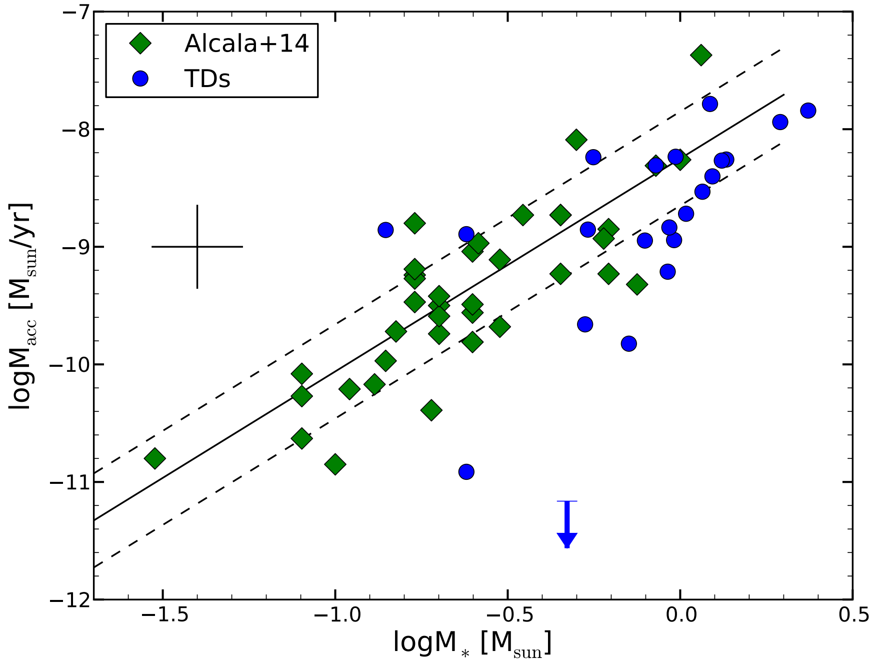

Figure 5.9: Logarithm of the mass accretion rate vs logarithm of the stellar mass for our sample of transitional disks and for a sample of classical TTauri stars from Alcalá et al. (2014). Our targets are shown as *blue circles*, while data from the literature are reported with *green diamonds*. The lines are the best fit to the data reported in Alcalá et al. (2014) (solid line) and the 0.4 dex spread reported in that study. Downward arrows are upper limits. The two lowest points are, from left to right, CHXR22E and Ser29. Typical errors are shown with the black cross.

of this line with the values of R_{in} available from the literature. We do not see any clear correlation between these quantities. The luminosity of the LVC of the [OI]λ630 nm line ($L_{\text{[OI]630}}$) appears constant regardless the size of the dust depleted cavity in the disk with values between $\sim 10^{-6}$ and $\sim 10^{-4}$ $L_\odot$. This implies that the properties of the wind traced by the [OI]λ630 nm line - that can be a disk wind, an accretion-driven wind, or a photoevaporative wind - are similar in most of the TDs in our sample. The question then is where in the disk the wind is originated. With the data in our hands we cannot put any constraint on the emitting region. Analysis of higher-resolution spectra of this line (e.g., Rigliaco et al., 2013) showed that, in cTTs, the emission region can be as close to the star as $\sim$ 0.2 AU, which is well within the dust depleted cavity in all our objects. Models of X-ray photoevaporation (Ercolano & Owen, 2010) predict that the luminosity of this line is insensitive to the size of the inner hole and depend mostly on the EUV and X-ray luminosity (L_X) of the central star. The X-ray photons are responsible for driving the wind in the first place, while the EUV photons heat up the inner region of the wind and excite the [OI] line. In this context, the correlation of L_{acc} with $L_{\text{[OI]}}$ (see discussion in the next paragraph and Fig. 5.11) could be due to the heating of the wind by the UV photons. Therefore a lack of

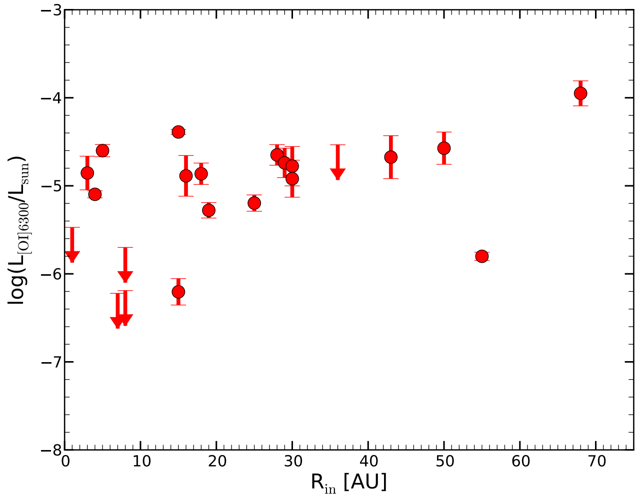

Figure 5.10: Logarithmic luminosity of the low-velocity component of the [OI] 630 nm line vs inner hole size for the transitional disks in our sample. Downward arrows are upper limits.

correlation of $L_{[OI]}$ with L_X, that is found when comparing our data with the data reported in the literature for L_X (see Table 5.9), is not at all surprising, as the emission measure of this line is determined by the UV luminosity, which is instead correlated to L_{acc}. For this reason $L_{[OI]}$ cannot be used as a quantitative tracer of the photoevaporated wind. Higher resolution spectra and more complete grids of models are needed to better constraint the origin of this line.

It is then important to compare the properties of this line in our TDs and in cTTs to understand whether they are similar in the two classes of objects. As comparison samples we select the objects studied by Rigliaco et al. (2013, and references therein) and those observed with X-Shooter and analyzed by Natta et al. (in prep.). These two samples are representative of different stellar, accretion, and wind properties of cTTs. In particular, the sample of Rigliaco et al. (2013, and references therein) comprises mostly strong accretors with low to intermediate stellar mass, while Natta et al. (in prep.) has a sample of low- and very low-mass YSOs with lower accretion rates. Here we compare only the luminosity of the LVC of the [OI]λ630 nm line derived in our work and in the comparison samples. The best way to compare these values is to analyze the $L_{[OI]630}$-L_{acc} relation, which is well characterized in the literature (see e.g., Rigliaco et al., 2013, and references therein). This is shown in Fig. 5.11, where we plot log $L_{[OI]630}$ as a function of log L_{acc} for our sample of TDs (*red filled circles*) and for the two samples of cTTs (*blue empty circles* for data from Rigliaco et al. 2013 and *green empty circles* for those from Natta et al. in prep.). The relation between these two quantities spans over $\sim$ 7 orders of magnitude in both axes with a typical spread of $\sim$ 1 dex for the cTTs, and our objects follow it very well in all the cases. The location of our TDs right in the middle between the two comparison samples reflects the fact that their accretion rates are typical of $\sim$0.5-1 $M_\odot$ YSOs, i.e. smaller than

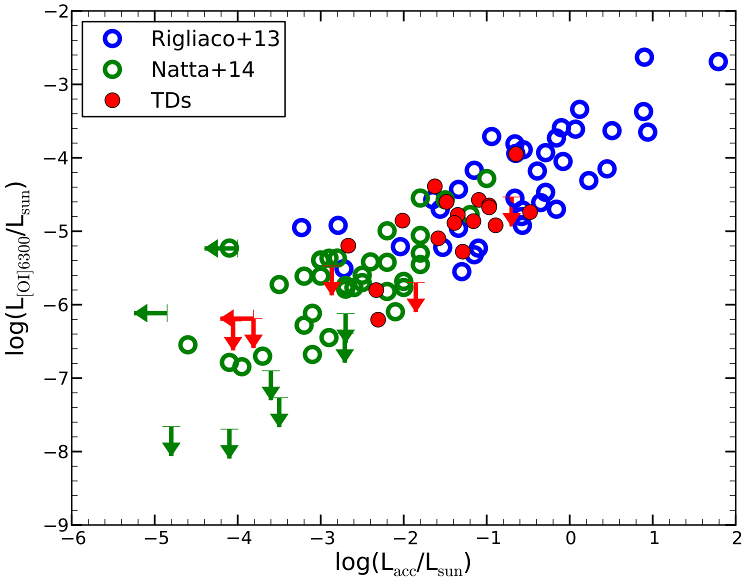

Figure 5.11: Logarithmic luminosity of the low-velocity component of the [OI] 630 nm line vs the logarithm of the accretion luminosity of our objects (*red filled symbols*) and for two samples of classical TTauri stars (*blue empty circles* from Rigliaco et al. 2013, *green empty symbols* from Natta et al. in prep.). Downward arrows are upper limits.

those in the sample of Rigliaco et al. (2013) and larger than low-mass YSOs. At the same time, this implies that their wind properties traced by the [OI]λ630 nm line scale with the accretion properties in the same fashion as in cTTs. Therefore, the process responsible for the formation of this line should be the same in objects surrounded by dust-rich disks and in TDs.

[NeII] from the literature

To better understand the properties of the winds in our objects we include also data from the literature on the [NeII]λ12.8 μm, which is a well know tracer of disk wind. This line has been detected in emission in the mid-infrared spectra of protoplanetary disks using *Spitzer* (e.g. Pascucci et al., 2007; Güdel et al., 2010; Espaillat et al., 2013, and reference therein) or ground-based observations (e.g., Pascucci & Sterzik, 2009; Pascucci et al., 2011; Sacco et al., 2012). This line is of interest to study the inner gaseous disk properties as it traces warm gas ($T \sim$ 5000 K) and the effects of extreme ultraviolet (EUV) and X-ray emission from the star on the disk (Glassgold et al., 2007). High-resolution spectroscopic studies constrained the emitting region of this line within 20-40 AU from the central star (Sacco et al., 2012). High resolution observations of TW Hya, in particular, showed that most ($\gtrsim$80%) of the [NeII] emission arises from the region where the disk is still optically thick, but still within $\sim$10 AU from the central star (Pascucci et al., 2011).

Among the objects in our sample, 13 have been observed with MIR spectroscopy and

Table 5.6: Properties of [NeII] $\lambda 12.8\mu$m line from the literature

Name	$F_{\text{[NeII]\_hires}}$	FWHM	v_0	$F_{\text{[NeII]\_Spitzer}}$	Ref
LkHα330	...	...	...	0.38 ± 0.19	G10
DM Tau	...	...	...	0.55	G10
LkCa 15	< 0.5	...	...	0.28 ± 0.02	S12
GM Aur	...	...	...	1.2 ± 0.06	G10
Sz Cha	...	...	...	1.62 ± 0.20	E13
TW Hya	3.8 ± 0.3	14.6	-6.2	5.9 ± 1.1	P09,G10
CS Cha	2.3 ± 0.2	27	-3.3	3.63 ± 0.07	P09,E13
CHXR22E	...	...	...	...	...
Sz18	...	...	...	...	...
Sz27	...	...	...	0.63 ± 0.07	E13
Sz45	...	...	...	...	...
Sz84	...	...	...	...	...
RX J1615	1.4 ± 0.2	20.5	-7.5	2.76 ± 0.46	S12
Oph22	...	...	...	...	...
Oph24	...	...	...	...	...
SR 21	0.5 ± 0.1	15.1	-8.3	< 3.0	S12,G10
ISO-Oph196	...	...	...	...	...
DoAr 44	< 0.3	...	...	0.68 ± 0.33	S12,G10
Ser29	...	...	...	...	...
Ser34	...	...	...	...	...
RX J1842.9	< 0.2	...	...	0.43 ± 0.13	S12,G10
RX J1852.3	...	...	...	0.72 ± 0.04	G10

References. P11: Pascucci et al. (2011); P09: Pascucci & Sterzik (2009); S12: Sacco et al. (2012); E13: Espaillat et al. (2013); G10: Güdel et al. (2010)

Notes. Fluxes are reported in units of 10^{-14} erg s^{-1} cm^{-2}; v_0 and FWHM in units of km/s.

all of them have a [NeII] line detection, as we report in Table 5.6. In all these objects we detected also the [OI] λ 630 nm line, with the only exception being SR21.

5.5.3 Accretion and wind properties in objects with inner disk emission

Following the analysis described in Sect. 5.3, we divide the sample in two classes of objects: we refer to objects with no near-infrared color excess as TD, while those with excess are referred to as PTD, as reported in Table 5.3. The morphological difference between these two classes is the presence of warm dust in the inner region of the disk of PTD, which could be a small ring of dust at few tenths of AU from the star (e.g., Benisty et al., 2010; Espaillat et al., 2010). This difference in the inner disk morphology could be due to different evolutionary stages of these two classes of objects or to different dust depleting mechanisms. Here we compare the accretion and wind properties of the objects in these two classes present in our sample to verify whether we see any difference among these objects.

The comparison of the accretion properties of TDs and PTDs is carried out using the logartithmic $\dot{M}_{\text{acc}}$-$M_\star$ relation, which is shown in Fig. 5.12. In this figure different symbols

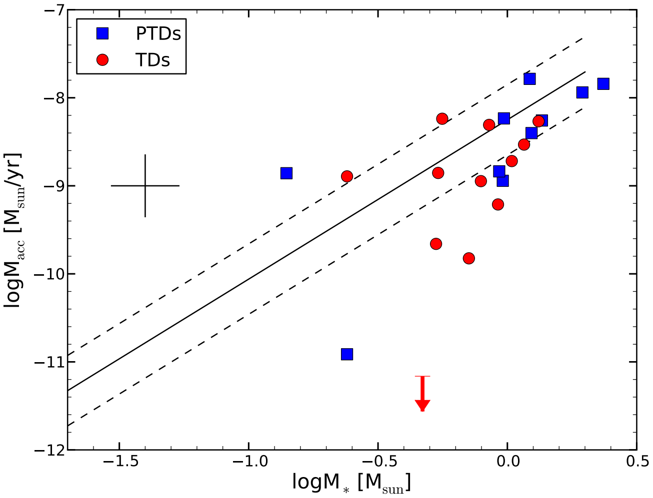

Figure 5.12: Logarithm of the mass accretion rate vs logarithm of the stellar mass of our sample. Different symbols are used to distinguish objects with inner disk emission (*blue squares*) from TDs with no IR-excess (*red circles*).

are used to plot TDs (*red circles*) and PTDs (*blue squares*). We overplot here the best fit relation from Alcalá et al. (2014) as in Fig. 5.9 that is used as a reference. We clearly see that there is not a significant difference between the two classes of objects. Similarly to what we discuss in Sect. 5.5.1, also this result is apparently at odd with previous studies, which showed that PTDs accrete at a lower rate than TDs (e.g., Espaillat et al., 2010; Kim et al., 2013). This implies that the accretion properties in our sample of TDs are independent on the dusty inner disk morphology.

We proceed with this analysis by comparing in Fig. 5.13 the logarithmic relation between L_{acc} and $L_{\mathrm{[OI]630}}$ for our sample, using different symbols for TDs (*red circles*) and for PTDs (*blue squares*) to see whether wind properties depend on the inner disk properties. Also in this case there is no correlation between the position on the plot and the inner disk morphology. The wind properties traced by the [OI] λ 630 nm line are thus independent of the presence of dust in the innermost region of the disk.

5.5.4 Constraint on the gas content of the inner disk

Here we present additional constraint on the region in the inner disk where gas is present and on its properties. From observations obtained in the literature we have measurement on the emission from CO from the inner part of the disk, which we discuss in the next subsection. Then, using the information on the accretion properties of our targets we derive the extent of the gas-rich inner disk, which extends down to the magnetospheric radius (R_m) at few stellar radii. We then also derive the density of gas in the inner disk needed to sustain the observed $\dot{M}_{\mathrm{acc}}$ if the disk is assumed in ``steady-state''. We also discuss possibilities to explain the observed $\dot{M}_{\mathrm{acc}}$, and thus for a gas-rich inner disk, allowing for a significant gas

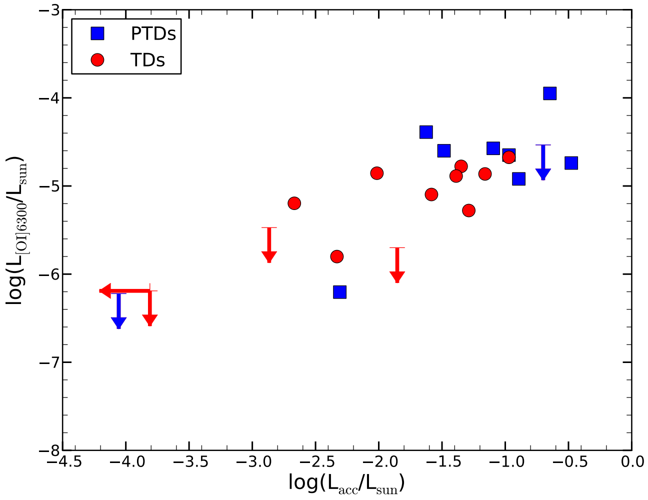

Figure 5.13: Logarithmic luminosity of the low-velocity component of the [OI] 630 nm line vs the logarithm of the accretion luminosity of our objects. Symbols and colors are the same as in Fig. 5.12.

depletion in the disk gaps. Finally, we give a complete view of the gas content of the inner disk adding to these informations also the wind properties of our TDs.

CO emission from the literature

The fundamental (Δv = 1) rovibrational line of CO at 4.7 μm is an important diagnostic to constraint the presence of gas in the inner region of TDs. This is sensitive to gas temperatures of 100-1000 K, which correspond to radii of 0.1-10 AU in typical protoplanetary disks around solar-mass stars YSOs, assuming that it originates in the so-called ``warm molecular layer" of the disk. Study of high-resolution spectra of this line have determined with high precision its emitting region within the disk (Najita et al., 2003; Salyk et al., 2007; Pontoppidan et al., 2008; Salyk et al., 2009; Pontoppidan et al., 2011). These studies observed 7 objects included in this work, and detected the line in all of them besides DM Tau. We report in Table 5.7 the inner radius of the CO emission in the disks ($R_{\rm in,CO}$) derived from the studies in the literature. Additional studies on three other objects of our sample have detected this line in RX J1842.9, while non-detection are obtained in the spectra of Sz Cha and RX J1852.3 (A. Carmona, personal communication). Seven out of the ten objects where this line has been studied are classified as PTD, so this emission could arise from the dusty inner disk. However, we also see that CO can be emitted in the dust-depleted inner disk of some TDs, such as TW Hya or RX J1852.3. A possible explanation for the emission of CO in the case of TW Hya is local warming due to the presence of a companion orbiting in the gap (Arnold et al., 2012). In any case, the detection of CO emission in the aforementioned objects confirms that their inner disk is gas-rich, confirming the results obtained by detecting ongoing accretion in the same targets.

Table 5.7: Properties of CO fundamental transition from the literature

Name	$R_{\text{in,CO}}$ [AU]	Ref
LkHα330	4±1	P11
DM Tau	...^{a}	S09
LkCa 15	0.093	N03
GM Aur	0.5±0.2	S09
Sz Cha	...^{c}	...
TW Hya	0.11±0.07	P08
CS Cha	...	...
CHXR22E	...	...
Sz18	...	...
Sz27	...	...
Sz45	...	...
Sz84	...	...
RX J1615	...	...
Oph22	...	...
Oph24	...	...
SR 21	7.6±0.4	P08
ISO-Oph196	...	...
DoAr44	0.4±0.1	S09
Ser29	...	...
Ser34	...	...
RX J1842.9	...^{b}	...
RX J1852.3	...^{c}	...

References. S09: Salyk et al. (2009); N03: Najita et al. (2003); P08: Pontoppidan et al. (2008); P11: Pontoppidan et al. (2011). ^{a} Non detection. Personal communications from A. Carmona: ^{b} detection of CO line, ^{c} non detection of CO line.

Magnetospheric radius

In the context of magnetospheric accretion models (e.g., Hartmann et al., 1998) the position in the disk from where the gas is accreted onto the star is determined by R_m. This is the radius where the external torque due to star-disk magnetic interaction dominates over the viscous torque. Following Armitage (2010), this can be derived by equating the expressions representing the two timescales involved in this process, namely the magnetospheric accretion timescale:

$$t_m \sim 2\pi \frac{\Sigma\sqrt{GM_\star r}}{B_z^s B_\phi^s r}, \tag{5.1}$$

where r is the radial distance in the disk from the central star, B is the magnetic field, the superscript s stands for magnetic field evaluated at the disk surface, and Σ is the surface density of the gas, and the viscous timescales:

$$t_\nu \sim \frac{r^2}{\nu}, \tag{5.2}$$

where ν is the disk viscosity. We assume the steady-state disk relation for the viscosity:

$$\nu\Sigma = \frac{\dot{M}_{\rm acc}}{3\pi}, \tag{5.3}$$

that implies a constant $\dot{M}_{\rm acc}$ in the disk, and we consider the simple case where the stellar magnetic field is bipolar and oriented in the same direction as the rotation axis of the star. With these assumptions, we derive the usual relation for R_m (e.g. Hartmann, 2009):

$$R_m \sim \left(\frac{3B_\star^2 R_\star^6}{2\dot{M}_{\rm acc}\sqrt{GM_\star}}\right)^{2/7}. \tag{5.4}$$

It is important to note that this quantity depends weakly on $\dot{M}_{\rm acc}$, $M_\star$, and to $B_\star$. The stronger dependence is on $R_\star$. Using this relation we are able to derive the values of R_m for all the accreting TDs in our sample using the values of $\dot{M}_{\rm acc}$[2], $M_\star$, and $R_\star$ derived in Sect. 5.3, and assuming a typical value for the magnetic field of the star $B_\star \sim 1$ kG (e.g. Johnstone et al., 2014). The effect of the arbitrary choice of the value of $B_\star$ is the prominent source of uncertainty in our estimate of R_m. We have to adopt a typical value for $B_\star$ since only for two targets in our sample this quantity has been measured. This is the case of TW Hya and GM Aur, where $B_\star$ is 1.76 kG and 1 kG, respectively (Johns-Krull, 2007). By varying the values of $B_\star$ from 2 kG to 0.5 kG we estimate a relative uncertainty on R_m of less than 0.5. This is then the assumed uncertainty of our estimate.

The values of R_m we have derived are reported in Table 5.8. In all the objects $R_m > 5R_\star$, in accordance with magnetospheric accretion models. This radius is always located at a distance from the central star much smaller than $R_{\rm in}$. The detection of ongoing accretion implies that gas is present in the disk at this distance from the star. The gas density in the region of the disk at radii $\sim R_m$ can be estimated as we explain in the next subsection.

Density of gas in the inner disk

Assuming steady-state disk condition the surface density of the gas is related to the accretion disk viscosity and $\dot{M}_{\rm acc}$ by the relation reported in Eq. (5.3). We describe the viscosity using the α viscosity prescription ($\nu = \alpha c_s H$, Shakura & Sunyaev, 1973) and we assume that the disk is vertically isothermal, so that $H = c_s/\Omega(r)$, where $c_s = (kT/\mu m_p)^{1/2}$ is the sound speed, μ=2.3 is the mean molecular weight, m_p is the mass of the proton, and $\Omega = (GM_\star/r^3)^{1/2}$ is the angular velocity of the disk. We then derive the following relation for the surface density of the gas in the disk:

$$\Sigma(r) \sim \frac{2m_p}{3\pi\alpha k_B T(r)}\dot{M}_{\rm acc}\sqrt{\frac{GM_\star}{r^3}}. \tag{5.5}$$

---

[2] The values of $\dot{M}_{\rm acc}$ derived previously have been obtained assuming R_m = 5 $R_\star$. This is the usual assumption made in the literature, thus this value is the appropriate one to derive $\dot{M}_{\rm acc}$ consistently to previous analyses. The same values of $\dot{M}_{\rm acc}$ can be adopted here because of the weak dependence of R_m on $\dot{M}_{\rm acc}$ ($R_m \propto \dot{M}_{\rm acc}^{-2/7}$). By re-deriving $\dot{M}_{\rm acc}$ using the newly determined R_m we obtain values of $\dot{M}_{\rm acc}$ with a typical difference of ~0.05 dex and always smaller than 0.1 dex. This translates in relative uncertainties on the value of R_m of less than 0.06.

Table 5.8: Derived properties of the gas

Name	R_m [$R_\star$]	R_m [AU]	Σ_{1AU} [g cm^{-2}]
LkHα330	10.05	0.175	411.36
DM Tau	7.94	0.058	106.87
LkCa 15	8.35	0.059	82.81
GM Aur	7.46	0.061	174.28
Sz Cha	5.54	0.039	337.56
TW Hya	8.37	0.033	19.17
CS Cha	8.07	0.062	116.45
CHXR22E	35.18	0.134	0.12
Sz18	10.88	0.068	23.91
Sz27	9.73	0.052	24.61
Sz45	7.50	0.053	118.54
Sz84	14.55	0.113	15.01
RX J1615	9.49	0.084	92.24
Oph22	24.22	0.240	4.63
Oph24	13.13	0.089	15.08
SR 21	8.97	0.117	299.26
ISO−Oph196	11.51	0.054	9.45
DoAr 44	6.28	0.032	102.45
Ser29	...	...	...
Ser34	18.61	0.106	2.95
RX J1842.9	8.88	0.043	25.22
RX J1852.3	9.08	0.051	34.91

We estimate the surface density of the gas at a distance of 1 AU from the central star (Σ_{1AU}). This radius is chosen because it is much larger than R_m but still within $R_{\rm in}$ for all our targets. Assuming $\alpha = 10^{-2}$ and T(1AU) = 200 K (representative value derived from Andrews & Williams, 2007), we derive the values of Σ_{1AU} from the central star reported in Table 5.8. These values vary from few g cm^{-2} to $\sim 4 \times 10^2$ g cm^{-2} for our objects, and represent the expected densities of gas in the disk inner region needed to sustain the observed accretion rates assuming steady state viscous inner disk. Another possibility is that the density of the gas in the cavity is lower than the one derived here if the radial inflow of gas is at high velocity, approaching free-fall (Rosenfeld et al., 2014). Finally, episodic events that replenish the gas content of the inner disk from the outer disk could also possibly explain our observed $\dot{M}_{\rm acc}$ with a significantly gas depleted hole for most of the TD lifetime.

5.5.5 Discussion on the gas content of the inner disk

We now want to put together all the information collected from our spectra and from the literature on the objects in our sample to understand what is the morphology of their gaseous inner disk. The discussion is divided between accreting and non-accreting objects. All the objects analyzed in this work besides Ser 29 have accretion detected with our method. Also CHXR22E has a measured value of $\dot{M}_{\rm acc}$ lower than other objects with similar stellar properties, as we pointed out when discussing the result of Fig. 5.9. We discuss these two objects in Sect. 5.5.5, while the other 20 accreting objects are discussed in the next subsection.

Accreting transitional disks

As discussed in the introduction, the detection of measurable accretion rates in young stellar objects implies that the innermost region of the disk is gas rich. This is the case for our accreting TDs, and we derived in Sect. 5.5.4 and 5.5.4 the inner boundary of the gaseous disk in these objects and the densities of the gas in the inner disk needed to sustain the observed accretion rates assuming a steady-state viscous disk. We constrain with our analysis that gas is present in these disks in regions as close to the star as $\sim$ 0.03 - 0.3 AU, that are the values of R_m. The evidence of gas presence in this region is confirmed in 17 of the 20 accreting TDs with the detection of the [OI] λ 630 nm line in their spectra, which is originated as close as $\sim$ 0.2 AU from the star. At similar disk radii ($\sim$ 0.1-0.5 AU) the CO emission is detected in 4 objects (LkCa15, GM Aur, TW Hya, and DoAr 44, see Table 5.7), confirming the presence of gas in their inner disk. For TW Hya this region is known to be strongly dust-depleted. On the other hand, it is plausible that the CO emission arises from the dusty inner disk in the other three objects, known to be PTDs. To these objects we should add RX J1842.9 where the CO line is also detected, but no analysis has yet been carried out to determine the distance to the star of the region emitting this line. For LkHα330 and SR21 the emission of the CO line arises from larger radii ($R_{\rm CO} \geq$ 4 AU) due to the higher temperature of the disk related to the larger $L_\star$ of these objects compared to the rest of the sample. Finally, in 13 of the 20 accreting TDs we could find a detection of the [NeII] in the literature. This line is also originated in a wind coming from a gas rich region of the disk inside a distance from the central star of ~20-40 AU. In only 9 of the 20 accreting TDs we found evidence of infrared excess, a signature of the presence of a dusty inner disk.

The picture of these accreting TDs coming from our analysis is then the following. These are objects with a gas rich disk well within the observed $R_{\rm in}$, i.e. at the inner disk edge. Given that we do not find any correlation between the dust-depleted hole and the accretion or wind properties, and that we see both accreting TDs with dusty inner disks and without, the model needed to explain the formation of the dust-depleted inner region should leave almost unaltered the gas properties of the innermost region. From the point of view of the gas content of the inner disk there is no observable difference between accreting TDs and cTTs.

Non-accreting transitional disks

The two objects we discuss here (Ser 29 and CHXR22E) have a gas-depleted inner region of the disk. The non-detection of accretion signatures in these objects or the very low detected $\dot{M}_{\rm acc}$ of CHXR22E imply that the density of the gas in this region of the disk is smaller in these objects by at least one order of magnitude than in any other accreting object. This is clearly seen in the value of $\Sigma_{1\text{AU}}$ = 0.1 g cm^{-2} reported for CHXR22E in Table 5.8, smaller by a factor $\sim$ 30-40 than the one computed for Oph 22 and Ser 34, that have similar stellar properties. With the addition of the non-detection of the [OI] λ 630 nm in the spectra of both objects we conclude that the region around $\sim$ 0.1-0.3 AU is significantly gas-depleted in these non-accreting TDs. No further information on the gas content of the inner disk of Ser 29 and CHXR22E are available. These two targets should be observed in the future with the aim of detecting [NeII] and/or CO emission in the inner parts of these objects, in order to constraint the inner boundary of the gas-rich disk.

5.6 Conclusions

In this work we analyzed a sample of 22 X-Shooter spectra of TDs. This sample comprises objects with different outer disk morphologies, in particular with values of R_{in} ranging from $\sim$1 AU to $\sim$ 70 AU, and includes mainly TDs with previous accretion rate estimates. This sample cannot provide a conclusive statistical result on the general properties of the TD class, but it is a good benchmark to study with an highly reliable method these objects. We used a multi-component fitting method to derive simultaneously the SpT, A_V, and L_{acc} of the objects fitting our broad-band spectra. At the same time we derived from the same spectra the intensity of the [OI]λ 630 nm line. From the analysis of the results we derived the following conclusions:

- The dependence of the accretion properties of our sample of strongly accreting TDs with the size of the dust-depleted cavity (R_{in}) is small, in particular there is no evidence for increasing $\dot{M}_{\text{acc}}$ with R_{in} at values of $R_{\text{in}} \gtrsim 20-30$ AU;

- There are strongly accreting TDs, like the majority of the objects in our sample, whose accretion properties are consistent with those reported in the literature for cTTs;

- The wind properties of the TDs analyzed here have no dependence with the size of the dust-depleted cavity (R_{in}) and are consistent with the wind properties of cTTs;

- There are no differences in the accretion and wind properties between the objects in our sample with inner disk emission (PTD) or without (TD);

- Strongly accreting TDs such as those analyzed here are gas-rich down to distances from the central star as small as $\sim$0.03-0.3 AU as can be obtained from the derivation of the values of R_m, from the detection of the [OI] λ 630 nm line, and from the detection of the CO and [NeII] lines. This distance is always smaller than the values of R_{in} reported in the literature for these objects, meaning that there is a gaseous inner disk much closer to the star than the dusty one;

- Non-accreting TDs have gas depleted inner disks. The gaseous disk is significantly depleted of gas at a distance from the star of at least $\sim$0.03-0.3 AU. Also for these objects the inner extent of gas and dust in the disk are uncoupled;

- The process needed to explain the formation of TDs should act differently on the gas and the dust components of the disk.

Future studies aimed at understanding the process responsible for the formation of the dust depleted cavity in TDs should aim at:

- conducting a similar analysis on a larger and more complete sample of TDs, including a larger amount of objects known to accrete at lower rates than those included in this work;

- determining the process responsible for the formation of the forbidden lines - photoevaporation, disk wind, or other possibilities - from the analysis of high-resolution and high-signal to noise forbidden lines and the comparison with theoretical models covering more completely the parameter space of stellar properties;

- determining the extent of the region emitting the [OI] and [NeII] line and the density of gas in this region in order to put stronger constraint on the distance from the central star at which gas is present;

- studying the CO line with high-resolution spectroscopy in non-accreting TDs to verify the decoupling of the gas-rich and dust-rich disk in these objects.

Aknowledgements We thank the ESO staff in Paranal for carrying out the observations in Service mode. We thank J. Alcala and the ``JEts and Disk at Inaf'' (JEDI) team for providing the reduced spectrum of Sz84. We thank A. Carmona for sharing the information on the CO line detection. C.F.M. acknowledges the PhD fellowship of the International Max-Planck-Research School.

5.A Comments on individual objects

5.A.1 Sample properties

LkCa 15: this object has been resolved with 880 μm interferometric observations by Andrews et al. (2011), and its cavity was previously resolved at 1.3 mm by Piétu et al. (2006). The modelling of this target carried out by Andrews et al. (2011) has a discrepancy with the observed 880 μm flux inside the cavity probably due to dust emission.
Sz Cha: we observed only the primary component of this wide binary system with separation 5.122″. The companion of this object is not a confirmed member of the Cha I association (Luhman, 2008).
CS Cha: Guenther et al. (2007) classified this objects as a spectroscopic binary with a period of more than 2482 days. The minimum mass of the companion is 0.1 $M_{\odot}$.
Sz 84: It is under debate whether this object should be classified as TD. Merín et al. (2010), who classified it as a TD in first place, derived $R_{\rm in}$ = 55±5 AU, but they pointed out that the classification was rather uncertain due to possible extended emission contamination. Also Matrà et al. (2012) suggest that this classification is dubious. They point out that this object has no 10 μm silicate feature in the spectrum, which is a typical feature in the spectra of TDs. Then, they report that it has a SED very similar to the one of T54, which they propose is not a TD due to extended emission in the *Herschel* images.
RX J1615-3255: different distances for this object are reported in the literature. Merín et al. (2010) consider this object to be located in the ρ-Ophiuci cloud, thus at d=125 pc. Andrews et al. (2011), instead, adopt a distance to this object of 185 pc because they assume it is located in the Lupus cloud. This location is then adopted also by Sacco et al. (2012), but they use a distance of 150 pc for the object. We decide to adopt the distance of 185 pc

used by Andrews et al. (2011) for consistency with the values of $R_{\rm in}$ derived in that work. We then correct the value of $R_{\rm in}$ derived in Merín et al. (2010) to the distance adopted here. This is the value of $R_{\rm in,SED}$ reported in Table 5.9.

SR21: this object is known to be a wide binary with a separation of $\sim 6.4'' \sim$ 770 AU. We observed only the primary component of the system, which is the one observed by Andrews et al. (2011). Regarding the dust emission of this object, Andrews et al. (2011) report a poor matching of the observations which may indicate that a small amount of ~mm-sized dust particles is present in the cavity.

ISO-Oph196: the inner dust depleted cavity has been barely resolved with SMA by Andrews et al. (2011). Looking at the SED of this object there is no signature of dust depletion, i.e. there is no dip in the MIR SED. This suggests that the dust is not strongly depleted in the inner disk of this object.

5.B Additional literature data

We report in Table 5.9 additional data collected in the literature on our targets. These data have not been used in this work but are useful for further analysis. The spectral type and $\dot{M}_{\rm acc}$ reported here have not been used in our analysis.

Table 5.9: Stellar and disk parameters available in the literature

Name	Spectral type	$\dot{M}_{\text{acc}}$ [10^{-8} $M_{\odot}$/yr]	$R_{\text{gap,in,SED}}$ [AU]	$R_{\text{in,SED}}$ [AU]	$R_{\text{in,mm}}$ [AU]	i [°]	logL_X [erg/s]	Disk Type	Ref
LkHα330	G3	0.20	0.8	50	68	35	...	...	1,12,22,26
DM Tau	M1	0.60	...	3	19	35	30.30	TD	1,10,20,21,28
LkCa15	K3	0.30	4	48	50	49	<29.6	PTD	1,15,16,21,24
GM Aur	K5	1.00	1	24	28	55	30.20	TD	6,9,10,20,21,28
SZ Cha	K0	0.24	...	29	...	...	29.90	PTD	16,17,21,25
TW Hya	K7	0.20	...	4	4	4	30.32	...	10,14,23,27
CS Cha	K6	0.53	...	43	...	45	30.56	TD	10,16,24,25,30
CHXR22E	M3.5	...	...	7	...	...	29.41	TD	16,19
Sz18	M3	1.5e-10	...	8	...	...	...	TD	16,19
Sz27	M0	1.2e-9	...	15	...	...	29.76^{a}	PTD	16,19
Sz45	M0.5	7.6e-10	...	18	...	...	...	WTD	16,19
Sz84	M5.5	1.00	...	55	...	...	...	...	8
RX J1615	K5	0.04	...	3^{b}	30	41	30.40	...	1,2,8
Oph22	M2	...	...	1	...	...	...	...	8
Oph24	M0.5	1.00	...	3	...	...	...	...	8
SR 21	G3	<0.1	0.45	18	36	22	30.00	...	1,3,4,5,18,26
ISO-Oph 196	M4	0.20	...	...	15	28	...	...	1,18
DoAr 44	K3	0.90	...	27	30	35	29.9	PTD	1,13,29
Ser29	M0	30.00	...	8	...	...	...	...	8
Ser34	M0	0.25	...	25	...	...	...	...	8
RX J1842.9	K2	0.10	...	5	...	...	30.34	...	6,7,19
RX J1852.3	K3	0.05	...	16	...	...	30.41	...	6,7,19

References. (1) Andrews et al. (2011), (2) Krautter et al. (1997), (3) Brown et al. (2009), (4) Andrews et al. (2009), (5) Grosso et al. (2000), (6) Hughes et al. (2010), (7) Neuhäuser et al. (2000), (8) Merín et al. (2010), (9) Hughes et al. (2008), (10) Güdel et al. (2010), (11) König et al. (2001), (12) Brown et al. (2008), (13) Montmerle et al. (1983), (14) Hughes et al. (2007), (15) Neuhaeuser et al. (1995), (16) Kim et al. (2009), (17) White et al. (2000), (18) Natta et al. (2006), (19) Pascucci et al. (2007), (20) Ingleby et al. (2009), (21) Espaillat et al. (2010), (22) Salyk et al. (2009), (23) Herczeg & Hillenbrand (2008), (24) Ingleby et al. (2013), (25) Espaillat et al. (2013), (26) Brown et al. (2007), (27) Calvet et al. (2002), (28) Calvet et al. (2005), (29) Kim et al. (2013), (30) Pascucci & Sterzik (2009) ----- $R_{\text{gap,in,SED}}$ is the inner radius of the gap in PTDs obtained from MIR SED fitting, whereas R_{in} is the inner radius of the dusty outer disk, i.e. the outer radius of the gap in PTDs and of the hole in TDs. ^{a} Highly uncertain parameter. ^{b} Value corrected for the different distance as explained in Appendix 5.A.1.

6

Accretion as a function of stellar properties in nearby star forming regions

To be included in Manara, Testi et al., to be submitted to A&A[*]

6.1 Introduction

To address the questions raised in Section 1.4.2 I collect here a large sample of 88 accreting YSOs in various star forming regions (ρ-Ophiucus, ONC, Lupus, σ-Orionis, Upper Scorpius, and others). This dataset covers a range of stellar masses of more than 2 dex, and nominal age of the regions from $\sim$1 to $\sim$10 Myr. The basic data and reference for each dataset included in this Chapter are reported in Table 6.1. All the targets have been observed with the VLT/X-Shooter spectrograph and analyzed, when possible, with the method described in Chapter 4 or with similar procedures described in the following. The range of stellar properties covered, the use of the same instrument, and of the same analysis method make this sample a unique benchmark to study the properties of accretion in YSOs.

A significant fraction of the data analyzed here have been obtained during guaranteed time observations (GTO) of the INAF collaboration (e.g., Alcalá et al., 2011). Other data have been collected in independent programs, such as the ρ-Ophiucus data (ESO Pr.Id. 085.C-0876, PI Testi), the Upper Scorpius data (ESO Pr.Id. 085.C-0482, PI Montesinos), and the data discussed in Chapters 4 and 5.

In this Chapter I will mainly report on the analysis of each dataset and on the derivation of the mass accretion rates for the targeted Class II YSOs. This will allow me to discuss the dependence of accretion with mass of the central object, with age, and with the luminosity of the central star in Sect. 6.6. I refer to the published papers (e.g., Rigliaco et al., 2012; Alcalá et al., 2014; Manara et al., in prep.) for more details on the observations and the data reduction of each dataset and on more general discussion on the properties of the

---

[*] This chapter includes work done in collaboration with other scientists and also work interely carried out by me. When including the adapted text of a published paper I will clarify my contribution to that specific work. With regards to the ρ-Ophiucus and the Upper Scorpius datasets, I have carried out all the data reduction and analysis work that is reported here. Finally, the discussion and analysis of the properties of the full dataset is reported for the first time in this Thesis.

targets. In any case, for all the objects discussed here the reduction has been carried out using the same procedures as in Chapters 3, 4, and 5, while the observing strategies have always been similar, with small differences, such as different slit widths or exposure times, mostly due to the brightness of the targets.

The structure of this Chapter is as follows. In Sect. 6.2 I report on the analysis of the accretion properties of 36 Class II YSOs in the Lupus clouds, and in Sect. 6.3 those of 8 Class II YSOs in the σ-Ori cluster. Then, in Sect. 6.4 I will show for the first time the analysis and results on the accretion properties of 17 accreting YSOs in the ρ-Ophiucus cloud, and in Sect. 6.5 for 3 Class II YSOs in the Upper Scorpius association. Finally, in Sect. 6.6 I collect together these data and those analyzed in Chapters 4 and 5 to analyze the accretion properties of the whole sample of this Thesis.

Table 6.1: Data included in this study

Region	dist [pc]	Age [Myr]	ClassII [#]	Reference
ρ-Ophiucus	125	1	17	Manara et al. (in prep.)
Orion Nebula Cluster	420	2	2	Manara et al. (2013b)
Lupus	150-200	2-3	36	Alcalá et al. (2014)
σ-Orionis	360	3-5	8	Rigliaco et al. (2012)
Upper Sco	145	$\gtrsim$5	3	Montesinos et al. (in prep.)
Transitional disks	various	~1-10	22	Manara et al. (2014a)
TOTAL	-	1-10	88	Manara et al. (in prep.)

6.2 Accretion in the Lupus clouds

Based on Alcalà, Natta, Manara et al. 2014, A&A, 561, A2[†]

The Lupus cloud complex (RA 15h to 16h and DEC −43d to −33d) is one of the low-mass star-forming regions located closest (d <200 pc) to the Sun (see Comerón, 2008, for a review). Similarly to other regions (e.g., Taurus, Chamaeleon, and ρ-Ophiucus), a large variety of objects in various stages of evolution are present in this region. The stellar population of this complex is composed of ~250 YSOs (e.g., Evans et al., 2009) and is dominated by mid M-type PMS objects, while several substellar objects have also been discovered in the region (Comerón, 2008; López Martí et al., 2005). With an age of ~2-4 Myr, Lupus lies between the epoch when most stars are still embedded in the parental cloud or surrounded by optically thick disks (Class I/II, 1-2 Myr) and the epoch where stars are not surrounded by an optically thick disk (Class III, ~10 Myr). The YSO population

---

[†] In this work I have personally carried out all the analysis of the UV-excess of the targets and the derivation of the accretion rates. I have also contributed significantly to the text of the manuscript, both in the analysis and in the discussion sections. Here I report only the parts of this work more relevant for this Thesis modifying substantially the text of the original paper.

in this complex is mainly distributed in five clouds (Lupus I, III, IV, V and VI) which are substantially different from each other in the stellar content. In particular, the Lupus III cloud contains the largest and most concentrated YSO population, followed by Lupus I with a filamentary structure and by the smaller Lupus IV, where a very high density core with little star formation activity has been found. In these three clouds the large majority of the objects are found to be Class II ($\sim$50%) or Class III (28%) YSOs, with only 12% of the targets being Class I sources (Merín et al., 2008). The remaining two clouds, Lupus V and VI, show a significantly different picture to the previously mentioned ones , with the large majority of the YSOs being surrounded by optically thin disks (Class III; 79% in Lupus V and 87% in Lupus VI, Spezzi et al. 2011). The reason for this difference could be an age gradient in the region, but further studies that go beyond the aim of this work are needed to understand this. In this section I report on the work carried out on a large fraction ($\sim$50%) of the YSO population of the Lupus I and III clouds to derive stellar parameters and accretion rates for these objects.

6.2.1 Sample

The sample analyzed here comprises 36 YSOs mainly located in the Lupus I and III clouds that satisfy the following criteria as closely as possible: i) YSOs with infrared class II characteristics and low extinction to take full advantage of the broad X-Shooter spectral range from UV to near-infrared (NIR); ii) targets extensively surveyed in as many photometric bands as possible: mainly Spitzer (IRAC & MIPS) surveys and complementary Wide-field Infrared Survey Explorer (WISE; Wright et al., 2010) data, as well as optical photometry available; and iii) mostly very low mass (VLM, $M_\star < 0.3\,M_\odot$) objects, but also a number of more massive ($M_\star \lesssim 1\,M_\odot$) stars to explore a wider range of accretion luminosity.

The two main bibliographic sources from which this sample was compiled are Allen et al. (2007) and Merín et al. (2008). The former reported several new VLM YSOs with Spitzer colors, while the latter provided a clearly characterised sample in terms of spectral energy distribution (SED) and SED spectral index, based on the Spitzer c2d criteria (Evans et al., 2009). Additional class II YSOs in Lupus III that extend the sample to a broader mass range and eventually to higher accretion luminosity were selected from Hughes et al. (1994), following criteria i) and ii) above as closely as possible, although several of these targets do not possess Spitzer fluxes because they were not covered by the c2d or other Spitzer surveys. Thus, the available WISE data were used.

Among the selected objects, there are two visual binaries, namely Sz 88 and Sz 123, where both components were observed. In another eight of the Lupus YSOs the Spitzer images revealed objects with separations between 2.″0 and 10.″0 (see Table 6.2). Among these, six have separations larger than 4.″0 (see Table 1 in Merín et al. 2008 and Table 9 in Comerón 2008). The spatial resolution of X-Shooter is sufficiently high, allowing the observation of all the targets without light pollution from any of those nearby objects. None of these targets has been reported as a spectroscopic binary in previous investigations using high-resolution spectroscopy (e.g. Melo, 2003; Guenther et al., 2007). The sample also

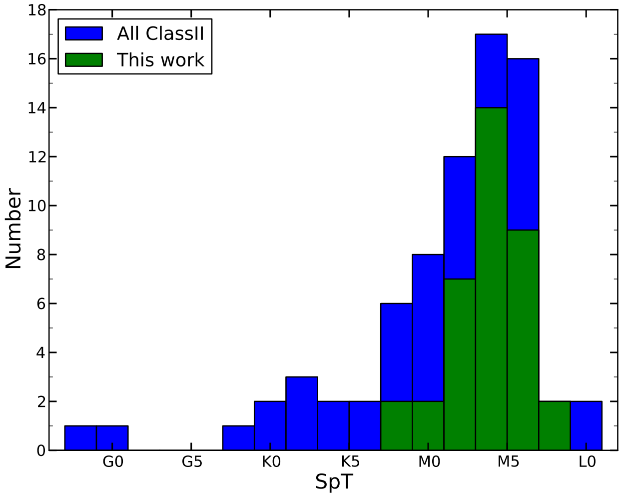

Figure 6.1: Histogram comparing the number of objects in the Lupus I and III clouds analyzed here with the total Class II YSO population of the region. The histogram of SpT of the objects analyzed here is shown in green, while the total population of Class II YSOs from Merín et al. (2008) and Mortier et al. (2011) is shown with a blue histogram.

includes Par-Lup3-4, one of the lowest-mass YSOs in Lupus known to host an outflow (Comerón et al., 2003).

This sample covers a mass range between ∼0.05 $M_\odot$ and ∼1 $M_\odot$ rather well (40% with $M_\star < 0.2\,M_\odot$, 35% with $M_\star$ in the range 0.2-0.5 $M_\odot$, and 25% with $M_\star > 0.5 M_\odot$). Nevertheless, this is incomplete at each mass bin. However, it represents about 50% of the total population of Class II YSOs in the Lupus I and Lupus III clouds (see Fig. 6.1), being thus a representative sample to study the accretion properties of this region.

Table 6.2 provides the list of the targets. The observations and data reduction procedure are explained in detail in Alcalá et al. (2014).

6.2.2 Stellar and substellar properties

A first estimate of the SpT of the Lupus targets was derived using various spectral indices from Riddick et al. (2007) for optical wavelengths (the details of these indices are also reported in Table 3.5), and the H2O-K2 index from Rojas-Ayala et al. (2012) for the NIR spectra (see Table 3.9). The Riddick et al. (2007) spectral indices in the VIS are almost independent of extinction[1]. The SpT assigned to a given object was estimated as the average SpT resulting from the various indices in the VIS. From the dispersion over the average of all the available spectral indices we obtain an uncertainty of half a spectral subclass.

The NIR indices provide SpTs that are consistent with the VIS results typically within one spectral subclass. Therefore, the SpTs derived from the VIS were adopted for the ana-

---

[1] Note that the spectral indices may be affected by high extinction (A_V >5 mag). None of the Lupus targets has such high A_V.

Table 6.2: Selected YSOs in the Lupus region

Object/other name	RA(2000) h :m :s	DEC(2000) ° ′ ″	Lupus cloud
Sz66†	15:39:28.28	−34:46:18.0	I
AKC2006-19	15:44:57.90	−34:23:39.5	I
Sz69 / HW Lup†	15:45:17.42	−34:18:28.5	I
Sz71 / GW Lup	15:46:44.73	−34:30:35.5	I
Sz72 / HM Lup	15:47:50.63	−35:28:35.4	I
Sz73	15:47:56.94	−35:14:34.8	I
Sz74 / HN Lup	15:48:05.23	−35:15:52.8	I
Sz83 / RU Lup	15:56:42.31	−37:49:15.5	I
Sz84	15:58:02.53	−37:36:02.7	I
Sz130	16:00:31.05	−41:43:37.2	IV
Sz88A (SW) / HO Lup (SW)	16:07:00.54	−39:02:19.3	I
Sz88B (NE) / HO Lup (NE)	16:07:00.62	−39:02:18.1	III
Sz91	16:07:11.61	−39:03:47.1	III
Lup713†	16:07:37.72	−39:21:38.8	III
Lup604s	16:08:00.20	−39:02:59.7	III
Sz97	16:08:21.79	−39:04:21.5	III
Sz99	16:08:24.04	−39:05:49.4	III
Sz100†	16:08:25.76	−39:06:01.1	III
Sz103	16:08:30.26	−39:06:11.1	III
Sz104	16:08:30.81	−39:05:48.8	III
Lup706	16:08:37.30	−39:23:10.8	III
Sz106	16:08:39.76	−39:06:25.3	III
Par-Lup3-3	16:08:49.40	−39:05:39.3	III
Par-Lup3-4†	16:08:51.43	−39:05:30.4	III
Sz110 / V1193 Sco	16:08:51.57	−39:03:17.7	III
Sz111 / Hen 3-1145	16:08:54.69	−39:37:43.1	III
Sz112	16:08:55.52	−39:02:33.9	III
Sz113	16:08:57.80	−39:02:22.7	III
2MASS J16085953-3856275†	16:08:59.53	−38:56:27.6	III
SSTc2d160901.4-392512	16:09:01.40	−39:25:11.9	III
Sz114 / V908 Sco	16:09:01.84	−39:05:12.5	III
Sz115	16:09:06.21	−39:08:51.8	III
Lup818s†	16:09:56.29	−38:59:51.7	III
Sz123A (S)	16:10:51.34	−38:53:14.6	III
Sz123B (N)	16:10:51.31	−38:53:12.8	III
SST-Lup3-1†	16:11:59.81	−38:23:38.5	III

Notes. † : nearby ($2.''0 < d < 10.''0$) object detected in Spitzer images (see Merín et al., 2008; Comerón, 2008).

lysis, consistently with the SpT assignment for the class III templates (Manara et al., 2013a, and Chapter 3). The SpTs are listed in Table 6.3. For the two earliest-type stars in this sample (Sz73 and Sz83), an accurate SpT of K7 is reported in the literature (see Herczeg & Hillenbrand, 2008; Comerón, 2008). All these estimates are checked using the fitting procedures of Chapter 4 as described in the following.

Some difference in determining the SpT in the literature can be ascribed to the different spectral ranges used in the different investigations (Comerón et al., 2003; Hughes et al., 1994; Mortier et al., 2011). With the wide spectral range of X-Shooter and the accurate fitting procedure adopted this problem is overcome. Generally, the SpT derived here are consistent within ±0.5 subclass with those in the literature, with a few exceptions that are discussed in the following. The SpTs of this sample range from K7 to M8, with an overabundance of M4-M5 objects.

To derive the first estimate of $A_{\rm V}$ for a given Class II YSO, its VIS spectrum was compared with the Class III templates (Manara et al., 2013a, and Chapter 3) that best match the Class II SpT. All the Class III templates have a low extinction ($A_{\rm V} < 0.5$). The templates were then artificially reddened by $A_{\rm V}$ =0...4.0 mag in steps of 0.25 mag, until the best match to the Class II YSO was found. The procedure simultaneously provided an additional test for the correct assignment of the template to derive the accretion luminosity (see Sect. 6.2.3). The $A_{\rm V}$ values derived in this way are listed in Table 6.3. This procedure confirms that the majority of the targets possess zero extinction because they were selected with this criterion. The highest values, 2.2 mag and 3.5 mag, are found for Par-Lup3-3 and Sz73, respectively.

The combined effect of uncertainties in SpT and A_V leads generally to an error of <0.5 mag. However, another important source of uncertainty may be introduced by strong veiling, which makes the YSOs spectra intrinsically bluer than the templates. This has not strong impacts on the estimates of stellar parameters for low-accreting late-type YSOs like those analyzed here. For earlier-type stars (<K7) with much higher levels of veiling than those in this sample, the fitting method explained in Chapter 4 must be used to derive SpT, extinction, and accretion properties simultaneously. Here this fitting method is used to verify and validate the estimates derived as just explained.

To check the self-consistency of the extinction derived in another spectral range the same procedure was repeated on the NIR spectra. The result is that the $A_{\rm V}$ values are consistent within the 0.5 mag uncertainty, but are affected by a larger error (~0.75 mag). The latter is mainly due to the higher uncertainty in the SpT provided by the spectral indices in the NIR than in the VIS. Therefore the values derived from the VIS are adopted for the following analysis. Another obvious reason for preferring the extinction in the VIS is that the extinction in the NIR is low and one needs to multiply it (and its uncertainty) by a large factor to derive $A_{\rm V}$.

The SpT and extinction determinations reported here agree well with the literature values except for a few cases. For Sz 69, Hughes et al. (1994) reported a SpT M1 with a visual extinction of 3.20 mag, while it is shown here that the M4 template with zero extinction fits the entire X-Shooter spectrum much better. For Sz 110, Hughes et al. (1994) reported M2, while Mortier et al. (2011) claimed M3, more consistent with the M4 determination reported here. In the case of Sz 113, the M4 SpT reported by Hughes et al. (1994) agrees with the M4.5 determination of this study, while Mortier et al. (2011) reported M1 and Comerón et al. (2003) M6. The visual extinction values in the literature for Par-Lup3-4 range from 2.4 to 5.6 mag (Comerón et al., 2003). The confirmed under-luminosity and edge-on geometry of this object (Comerón et al., 2003; Huélamo et al., 2010) suggest that the zero extinction adopted here can be interpreted as wavelength-independent, that is, gray extinction, rather than as a null extinction (see also Whelan et al., 2014). Interestingly, a null extinction is consistent with the value derived off-source using the [Fe II] lines at 1.27, 1.32, and 1.64 μm (Bacciotti et al., 2011; Giannini et al., 2013), which trace jet emission (Nisini et al., 2005).

On the other hand, it is worth mentioning that the zero extinction derived for Sz 83 agrees with the value derived by Herczeg et al. (2005) from the profile of the Lyα line. The fitting procedure as in Chapter 4 also confirms the SpT of this YSO, despite its strong veiling (see Section 6.2.3). The $A_{\rm V}$ determination for Sz 113, the most veiled among the M-type YSOs in this sample, also agrees with that reported by Hughes et al. (1994).

The effective temperature, $T_{\rm eff}$, was derived using the temperature scales given by Kenyon & Hartmann (1995) for the two K-type stars, and by Luhman et al. (2003) for the M-type YSOs. The latter scale is intermediate between the dwarf and giant temperature scales, and more appropriate for young objects than temperature scales derived for field M-dwarfs (e.g. Testi, 2009). The stellar luminosity and radius were computed using the methods described in Spezzi et al. (2008), adopting the extinction and distance values given in Table 6.3. The stellar radius was also determined using the flux-calibrated X-Shooter spectra as explained in Alcalá et al. (2011). The good agreement between the radius calculated with the two methods (cf. Figure 5 in Alcalá et al., 2011) also confirms the reliability of the flux calibration of the spectra. Mass and age were derived by comparison with theoretical PMS evolutionary tracks (Baraffe et al., 1998) on the HRD. The physical parameters of the targets are listed in Table 6.3. Uncertainties in luminosity, radius, and mass take into account the error propagation of about half a spectral subclass in spectral typing, as well as errors in the photometry and uncertainty on extinction.

The luminosity of four objects, namely Par-Lup3-4, Lup706, Sz 123B, and Sz 106, is significantly lower than for the other YSOs of similar SpT or mass, hence their ages are apparently older than 15 Myr. The much lower luminosity of these objects as compared to the others is evident in Figure 6.2, where the HRD for the sample is shown. It is not entirely clear whether the relatively low luminosity of these objects is due to evolution or to obscuration effects because of a particular disc geometry. Sz 106 and Par-Lup3-4 have been reported to be subluminous (Comerón et al., 2003), and for the latter it has been shown that the disc is edge-on (Huélamo et al., 2010). No evidence of significantly low luminosity for the other two objects is found in the literature. I refer to Alcalá et al. (2014) for arguments suggesting that the low luminosity of these objects is most likely due to geometrical effects.

The average age of 3±2 Myr for the Lupus sample, excluding the subluminous objects, is consistent with previous age estimates for Lupus YSOs (Comerón, 2008, and references therein). Finally, the Li I λ670.78nm absorption line is detected in all the spectra analyzed

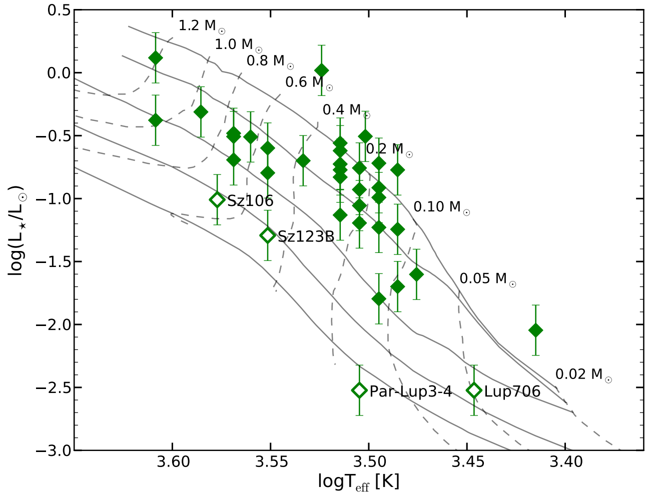

Figure 6.2: Hertzsprung-Russell diagram for the Lupus sample. The four subluminous objects described in the text are represented with open symbols and labelled. The continuous lines show the 1 Myr, 3 Myr, 10 Myr, 30 Myr, and 100 Myr isochrones, reported by Baraffe et al. (1998), while the dashed lines show the low-mass pre-main sequence evolutionary tracks by the same authors as labelled. Adapted from Alcalá et al. (2014).

here.

6.2.3 Accretion rate determination

The procedure explained in Chapter 4 is used to determine $L_{\rm acc}$ from the continuum excess luminosity and to confirm and validate the SpT and A_V derived as described in Sect. 6.2.2. Being the Lupus objects analyzed here not strongly veiled, low-extincted, and mostly M-type, the results obtained as explained in the previous section are reliable and confirmed by the fitting procedure of Chapter 4. Examples of the best fit of the Balmer jump region for the Lupus targets are shown in Figure 6.3, while the complete set of plots showing the best fits for all targets can be found in Alcalá et al. (2014).

The adopted Class III templates and the derived $L_{\rm acc}$ values corresponding to each Class II YSO are reported in Table 6.4. The uncertainties on $L_{\rm acc}$ are dominated by the uncertainty in the extinction and by the choice of the Class III template (Manara et al., 2013b). An additional, non-negligible uncertainty for low values of $L_{\rm acc}$ comes from the uncertainty on the Paschen continuum excess emission, especially in objects with a poor signal-to-noise ratio (e.g. Rigliaco et al., 2012). In general, the uncertainty on $L_{\rm acc}$ is estimated to be ~0.2 dex. The Balmer and Paschen continua as well as the Balmer jump are well reproduced by the fits. Only in one case, namely Sz123B, the slope of the Balmer continuum is not exactly reproduced by any combination of the free parameters. This is not caused by data reduction problems (e.g. flat-field correction or incorrect spectrum extraction), but perhaps to slit-loss effects. Small differences between the observed and best-fit spectra in the Paschen continuum are present in some objects (e.g. AKC2006-19, Sz115),

Table 6.3: Spectral types, extinction, and physical parameters of the Lupus Class II YSOs

Object	SpT	$T_{\rm eff}$ [K]	$A_{\rm V}$ [mag]	d [pc]	$L_\star$ [$L_\odot$]	$R_\star$ [$R_\odot$]	$M_\star$ [$M_\odot$]	Age [Myr]
Sz66	M3.0	3415	1.00	150	0.200±0.092	1.29±0.30	$0.45^{+0.05}_{-0.15}$	4
AKC2006-19	M5.0	3125	0.00	150	0.016±0.008	0.44±0.10	$0.10^{+0.03}_{-0.02}$	13
Sz69	M4.5	3197	0.00	150	0.088±0.041	0.97±0.22	$0.20^{+0.00}_{-0.03}$	3
Sz71	M1.5	3632	0.50	150	0.309±0.142	1.43±0.33	$0.62^{+0.02}_{-0.17}$	4
Sz72	M2.0	3560	0.75	150	0.252±0.116	1.29±0.30	$0.45^{+0.12}_{-0.00}$	3
Sz73	K7	4060	3.50	150	0.419±0.193	1.35±0.31	$1.00^{+0.00}_{-0.00}$	9
Sz74	M3.5	3342	1.50	150	1.043±0.480	3.13±0.72	$0.50^{+0.10}_{-0.10}$	1
Sz83	K7	4060	0.00	150	1.313±0.605	2.39±0.55	$1.15^{+0.25}_{-0.05}$	2
Sz84	M5.0	3125	0.00	150	0.122±0.056	1.21±0.28	$0.17^{+0.08}_{-0.02}$	1
Sz130	M2.0	3560	0.00	150	0.160±0.074	1.03±0.24	$0.45^{+0.05}_{-0.00}$	6
Sz88A (SW)	M0	3850	0.25	200	0.488±0.225	1.61±0.37	$0.85^{+0.10}_{-0.10}$	4
Sz88B (NE)	M4.5	3197	0.00	200	0.118±0.054	1.12±0.26	$0.20^{+0.05}_{-0.03}$	2
Sz91	M1	3705	1.20	200	0.311±0.143	1.36±0.31	$0.62^{+0.13}_{-0.08}$	4
Lup713	M5.5	3057	0.00	200	0.020±0.009	0.52±0.12	$0.08^{+0.05}_{-0.00}$	4
Lup604s	M5.5	3057	0.00	200	0.057±0.026	0.83±0.19	$0.11^{+0.04}_{-0.02}$	2
Sz97	M4.0	3270	0.00	200	0.169±0.078	1.34±0.28	$0.25^{+0.05}_{-0.00}$	2
Sz99	M4.0	3270	0.00	200	0.074±0.034	0.89±0.20	$0.17^{+0.08}_{-0.00}$	3
Sz100	M5.5	3057	0.00	200	0.169±0.078	1.43±0.33	$0.17^{+0.00}_{-0.04}$	1
Sz103	M4.0	3270	0.70	200	0.188±0.087	1.41±0.30	$0.25^{+0.05}_{-0.00}$	1
Sz104	M5.0	3125	0.00	200	0.102±0.047	1.11±0.26	$0.15^{+0.02}_{-0.02}$	1
Lup706†	M7.5	2795	0.00	200	0.003±0.001	0.22±0.05	$0.06^{+0.03}_{-0.02}$	32
Sz106†	M0.5	3777	1.00	200	0.098±0.045	0.72±0.17	$0.62^{+0.00}_{-0.05}$	32
Par-Lup3-3	M4.0	3270	2.20	200	0.240±0.110	1.59±0.37	$0.25^{+0.05}_{-0.05}$	1
Par-Lup3-4†	M4.5	3197	0.00	200	0.003±0.001	0.17±0.04	$0.13^{+0.02}_{-0.00}$	>50
Sz110	M4.0	3270	0.00	200	0.276±0.127	1.61±0.37	$0.35^{+0.05}_{-0.05}$	1
Sz111	M1	3705	0.00	200	0.330±0.152	1.40±0.32	$0.75^{+0.05}_{-0.13}$	6
Sz112	M5.0	3125	0.00	200	0.191±0.088	1.52±0.35	$0.25^{+0.00}_{-0.08}$	1
Sz113	M4.5	3197	1.00	200	0.064±0.030	0.83±0.19	$0.17^{+0.03}_{-0.04}$	3
2MASS J16085953-3856275	M8.5	2600	0.00	200	0.009±0.004	0.47±0.11	$0.03^{+0.01}_{-0.01}$	1
SSTc2d160901.4-392512	M4.0	3270	0.50	200	0.148±0.068	1.25±0.29	$0.20^{+0.10}_{-0.05}$	1
Sz114	M4.8	3175	0.30	200	0.312±0.144	1.82±0.42	$0.30^{+0.05}_{-0.10}$	1
Sz115	M4.5	3197	0.50	200	0.175±0.080	1.36±0.31	$0.17^{+0.08}_{-0.08}$	1
Lup818s	M6.0	2990	0.00	200	0.025±0.011	0.58±0.13	$0.08^{+0.02}_{-0.02}$	3
Sz123A (S)	M1	3705	1.25	200	0.203±0.093	1.10±0.25	$0.60^{+0.20}_{-0.03}$	7
Sz123B (N)†	M2.0	3560	0.00	200	0.051±0.024	0.58±0.13	$0.50^{+0.00}_{-0.10}$	40
SST-Lup3-1	M5.0	3125	0.00	200	0.059±0.027	0.85±0.19	$0.13^{+0.02}_{-0.04}$	2

Notes.

† objects classified as subluminous YSO by Alcalá et al. (2014).

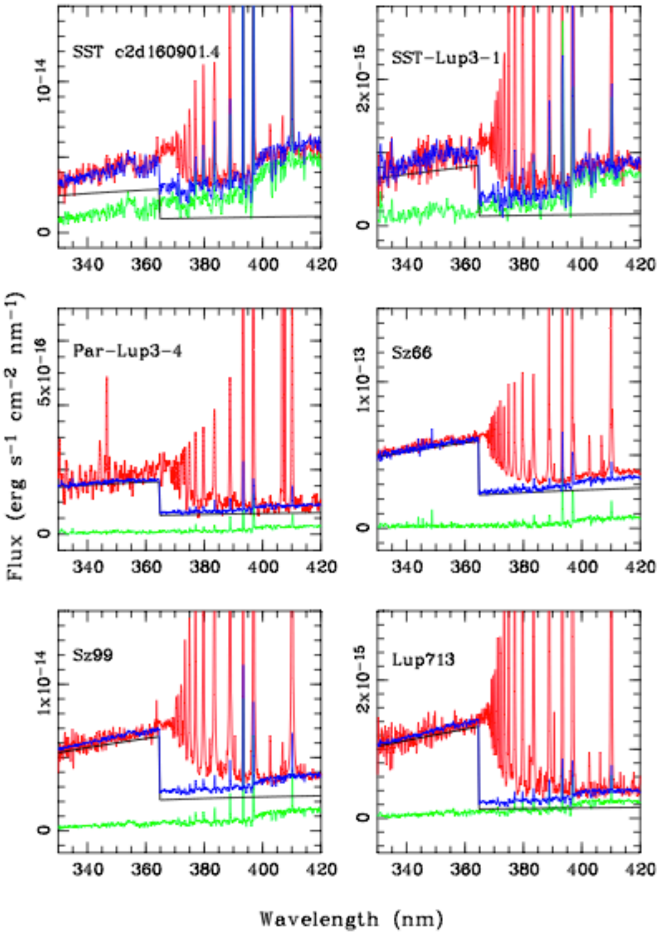

Figure 6.3: Examples of the best fit of X-Shooter spectra of Class II YSOs in Lupus in the region of the Balmer jump (red lines). The spectrum of the adopted Class III templates are overplotted with green lines. The continuum emission from the slab is shown by the black continuous line. The best fit with the emission predicted from the slab model added to the template is given by the blue lines. From Alcalá et al. (2014).

but differences are small compared with the excess emission in the Balmer continuum region.

The accretion luminosities are converted into $\dot{M}_{\rm acc}$ using the relation of Eq. (1.2) and adopting for $R_\star$ and $M_\star$ the values reported in Table 6.3. The results on $\dot{M}_{\rm acc}$ are listed in column 7 of Table 6.4. The calculated $\dot{M}_{\rm acc}$ values range from $2\times10^{-12}\,M_\odot$ yr^{-1} to $4\times10^{-8}\,M_\odot$ yr^{-1}. The sources of error in $\dot{M}_{\rm acc}$ are the uncertainties on $L_{\rm acc}$, stellar mass and radius (see Table 6.3). Propagating these, the estimated average error is of ∼0.35 dex in $\dot{M}_{\rm acc}$. However, additional errors on these quantities come from the uncertainty in distance, as well as from differences in evolutionary tracks, which could affect significantly the M_* estimates, and thus $\dot{M}_{\rm acc}$. The uncertainty on the Lupus YSOs distance is estimated to be ∼20% (see Comerón, 2008, and references therein), yielding a relative uncertainty of about

0.26 dex in $\dot{M}_{\rm acc}$[2]. On the other hand, using the D'Antona & Mazzitelli (1994) tracks, the difference in M_* ranges from 10% to 70% (with an average of 30%) with respect to the Baraffe et al. (1998) tracks, leading to uncertainties of 0.04 dex to 0.3 dex in $\dot{M}_{\rm acc}$. The cumulative relative uncertainty in $\dot{M}_{\rm acc}$ is then estimated to be of about 0.5 dex.

With $\dot{M}_{\rm acc}$=3.4×10^{-8} $M_\odot$ yr^{-1} , the strongest accretor in the Lupus sample is Sz 83. A variety of $\dot{M}_{\rm acc}$ estimates for this star exist in the literature that range from 10^{-7} to a few 10^{-8} $M_\odot$ yr^{-1} and may be as high as 10^{-6} (Comerón, 2008). The $\dot{M}_{\rm acc}$ estimate derived here agrees very well with that calculated by Herczeg & Hillenbrand (2008) (1.8×10^{-8} $M_\odot$ yr^{-1}). There are large discrepancies between $\dot{M}_{\rm acc}$ determined here and those derived by Comerón et al. (2003) for Sz 100, Sz 106, Sz 113, and Par-Lup3-4. The Comerón et al. (2003) estimates, which are based on the flux of the calcium λ854.2 nm line, are higher by up to 1 dex. Although part of the discrepancies may in principle be ascribed to variable accretion, this variability must be enormous over timescales of years to explain the differences. Costigan et al. (2012) and Costigan et al. (2014) have observed variable accretion over years, but their results show that it is very rare to have YSOs that vary $\dot{M}_{\rm acc}$ by large factors. Most of the variability they found occurs on rotational timescales, suggesting asymmetric and not strongly variable accretion flows.

Emission lines as tracer of accretion

In the spectra of the Lupus YSOs there are a large number of permitted and forbidden emission lines that display a variety of profiles. The detected emission lines include several from the Balmer and Paschen series, the Brγ line, and several helium and calcium lines.

Balmer lines are detected up to H25 in six objects (Lup 713, Sz 113, Sz 69, Sz 72, Sz 83, Sz 88A). One of these (Lup 713) is at the hydrogen-burning limit, with its spectrum resembling that of the young brown dwarf J 053825.4−024241 reported in Rigliaco et al. (2011b). In Sz 88A Balmer line emission is detected up to H27 at the 2σ level. The Pa 8, Pa 9, and Pa 10 lines are located in spectral regions of dense telluric absorption bands. Although the telluric correction was performed as accurately as possible, some residuals from the correction still remain. Thus, the detection and analysis of these three Paschen lines is more uncertain and lead to larger errors, in particular for Pa 8.

Other lines detected in these spectra are the nine He I lines with the highest transition strength. Of these, the He I λ1082.9nm has been found to be also related to winds and outflows (Edwards et al., 2006). Thus, the line may include both accretion and wind contributions. In most cases the He I λ492.2 nm is blended with the Fe I λ492.1 nm line.

The Ca II H & K lines are detected in all YSOs. The Ca II H-line is partially blended with Hϵ. The Ca II IRT $\lambda\lambda\lambda$ 849.8, 854.2, 866.2 nm, and the D-lines of the Na I $\lambda\lambda$ 589.0,589.6 nm doublet are very well resolved in all the spectra. In several objects both the Ca II IRT and the Na I lines are detected as an emission reversal superposed on the broad photospheric absorption lines. Therefore the strength of these lines was corrected for the photospheric contribution for the complete sample.

---

[2] Note that $\dot{M}_{\rm acc} \propto$ d^3, as $L_{\rm acc} \propto$ d^2 and $R_\star \propto$ d.

Table 6.4: Accretion properties of Lupus YSOs

Object	Template	$\log L_{\rm acc}$ $[L_\odot]$	$\log \dot{M}_{\rm acc}$ $[M_\odot\ {\rm yr}^{-1}]$	WHα(10%) [km s^{-1}]
Sz66	SO797	−1.8	−8.73	460
AKC2006-19	SO641	−4.1	−10.85	228
Sz69	SO797	−2.8	−9.50	403
Sz71	TWA15A	−2.2	−9.23	350
Sz72	TWA9B	−1.8	−8.73	455
Sz73	SO879	−1.0	−8.26	504
Sz74	TWA15A	−1.5	−8.09	401
Sz83	SO879	−0.3	−7.37	604
Sz84	SO641	−2.7	−9.24	456
Sz130	TWA2A	−2.2	−9.23	266
Sz88A (SW)	TWA25	−1.2	−8.31	597
Sz88B (NE)	SO797	−3.1	−9.74	405
Sz91	TWA13A	−1.8	−8.85	374
Lup713	Par-Lup3-2	−3.5	−10.08	378
Lup604s	SO925	−3.7	−10.21	264
Sz97	Sz94	−2.9	−9.56	452
Sz99	TWA9B	−2.6	−9.27	373
Sz100	SO641	−3.0	−9.47	251
Sz103	Sz94	−2.4	−9.04	426
Sz104	SO641	−3.2	−9.72	201
Lup706†	TWA26	−4.8	−11.63	328
Sz106†	TWA25	−2.5	−9.83	459
Par-Lup3-3	TWA15A	−2.9	−9.49	240
Par-Lup3-4†	SO641	−4.1	−11.37	393
Sz110	Sz94	−2.0	−8.73	498
Sz111	TWA13A	−2.2	−9.32	455
Sz112	SO641	−3.2	−9.81	160
Sz113	SO797	−2.1	−8.80	392
2MASS J16085953-3856275	TWA26	−4.6	−10.80	147
SSTc2d160901.4-392512	Sz94	−3.0	−9.59	447
Sz114	Sz94	−2.5	−9.11	222
Sz115	SO797	−2.7	−9.19	338
Lup818s	SO925	−4.1	−10.63	200
Sz123A (S)	TWA2A	−1.8	−8.93	487
Sz123B (N)†	TWA15B	−2.7	−10.03	519
SST-Lup3-1	SO641	−3.6	−10.17	254

Notes.
† objects classified as subluminous YSO by Alcalá et al. (2014).

Finally, the two O I lines at 777.3 nm and 844.6 nm are clearly detected in 14 and 18 YSOs, respectively. These lines are seen in the objects with the strongest Balmer, He I, and Ca II lines.

The flux in permitted lines was computed by directly integrating the flux-calibrated and extinction-corrected spectra using the *splot* package under IRAF[3]. Three measurements per line were made, considering the lowest, highest, and the middle position of the local continuum, depending on the local noise level of the spectra. The flux and its error were then computed as the average and standard deviation of the three measurements, respectively. The extinction-corrected fluxes, equivalent widths, and their errors are reported in Alcalá et al. (2014). In the cases where the lines were not detected, 3σ upper limits were estimated using the relationship $3 \times \mathrm{F}_{\mathrm{noise}} \times \Delta\lambda$, where $\mathrm{F}_{\mathrm{noise}}$ is the rms flux-noise in the region of the line and $\Delta\lambda$ is the expected average line width, assumed to be 0.2 nm.

The contribution of the photospheric absorption lines of the Na I D lines and the Ca II IRT, strongest in the late-K and early-to-mid M-type objects, were removed in all spectra by using the synthetic BT-Settl spectra by Allard et al. (2011) of the same T_{eff} and $\log g$ as the YSOs, binned at the same resolution of X-Shooter, and were rotationally broadened at the same $v \sin i$ as the YSOs. For this purpose, we applied the ROTFIT code (Frasca et al., 2006), specifically modified for X-Shooter data (see Stelzer et al., 2013, for details).

The luminosity of the different emission lines was computed as $L_{\mathrm{line}} = 4\pi d^2 \cdot f_{\mathrm{line}}$, where d is the YSO distance in Table 6.3 and f_{line} is the extinction-corrected absolute flux of the lines.

In units of $L_{\odot}$, the dynamical range of L_{acc} for the Lupus sample covers more than four orders of magnitude, while the luminosity of the line diagnostics discussed in the previous section spans more than five orders of magnitude. Therefore, it is possible to investigate the relationships between continuum excess emission and the emission in individual permitted lines. A detailed discussion on this L_{acc}-L_{line} relationship for most of the aforementioned permitted emission lines is presented in Alcalá et al. (2014). Here I report only the results and the relationships derived for the brighter emission lines usually present in the spectra of TTauri stars. These were calculated as linear fits of the $\log L_{\mathrm{acc}}$ vs. $\log L_{\mathrm{line}}$ relationships using the package ASURV (Feigelson & Nelson, 1985) under the IRAF environment. ASURV includes censoring of upper or lower limits in the fits. In the various relationships the upper limits in the independent variable L_{line} are well consistent with the trends seen in the L_{acc} vs. L_{line} plots. The results of the fits including and excluding upper limits are consistent within the errors. The errors in the computed relationships also account for upper limits when included. The relations derived for the principal emission lines are the

---

[3] IRAF is distributed by the National Optical Astronomy Observatory, which is operated by the Association of the Universities for Research in Astronomy, inc. (AURA) under cooperative agreement with the National Science Foundation

following:

$$
\begin{aligned}
\log(L_{\rm acc}/L_\odot) &= (1.12 \pm 0.07) \cdot \log(L_{\rm H\alpha}/L_\odot) + (1.50 \pm 0.26) \\
\log(L_{\rm acc}/L_\odot) &= (1.11 \pm 0.05) \cdot \log(L_{\rm H\beta}/L_\odot) + (2.31 \pm 0.23) \\
\log(L_{\rm acc}/L_\odot) &= (1.09 \pm 0.05) \cdot \log(L_{\rm H\gamma}/L_\odot) + (2.50 \pm 0.25) \\
\log(L_{\rm acc}/L_\odot) &= (1.06 \pm 0.06) \cdot \log(L_{\rm H\delta}/L_\odot) + (2.50 \pm 0.28) \\
\log(L_{\rm acc}/L_\odot) &= (1.04 \pm 0.08) \cdot \log(L_{\rm Pa\beta}/L_\odot) + (2.45 \pm 0.39) \\
\log(L_{\rm acc}/L_\odot) &= (1.18 \pm 0.06) \cdot \log(L_{\rm Pa\gamma}/L_\odot) + (3.17 \pm 0.31) \\
\log(L_{\rm acc}/L_\odot) &= (1.18 \pm 0.10) \cdot \log(L_{\rm Pa\delta}/L_\odot) + (3.33 \pm 0.47) \\
\log(L_{\rm acc}/L_\odot) &= (1.16 \pm 0.07) \cdot \log(L_{\rm Br\gamma}/L_\odot) + (3.60 \pm 0.38) \\
\log(L_{\rm acc}/L_\odot) &= (1.13 \pm 0.06) \cdot \log(L_{\rm HeI\lambda587.6nm}/L_\odot) + (3.51 \pm 0.30) \\
\log(L_{\rm acc}/L_\odot) &= (1.16 \pm 0.08) \cdot \log(L_{\rm HeI\lambda667.8nm}/L_\odot) + (4.12 \pm 0.45) \\
\log(L_{\rm acc}/L_\odot) &= (0.96 \pm 0.05) \cdot \log(L_{\rm CaII\lambda393.4nm}/L_\odot) + (2.06 \pm 0.27)
\end{aligned}
\tag{6.1}
$$

The reported $L_{\rm acc}$ vs. $L_{\rm line}$ relationships generally agree with those found in previous investigations (Muzerolle et al., 1998a; Calvet et al., 2004; Natta et al., 2004; Herczeg & Hillenbrand, 2008; Ingleby et al., 2013). The slopes and zero points of the $L_{\rm acc}$ vs. $L_{\rm line}$ relations derived here are consistent within the errors with those reported in Herczeg & Hillenbrand (2008) (see their Table 16[4]). Also the relationships of Eq. (6.1) for the Hα, Hβ, and Ca II K lines are practically identical to those of Ingleby et al. (2013), which were derived by fitting UV and optical spectra with multiple accretion components. Also the $L_{\rm acc}$-$L_{\rm Pa\beta}$ and $L_{\rm acc}$-$L_{\rm Br\gamma}$ relations are similar to those in previous works by Muzerolle et al. (1998a), Natta et al. (2004), Calvet et al. (2000), and Calvet et al. (2004), but extend to much lower values of $L_{\rm acc}$, toward the very low-mass regime. However, because of the different methodologies adopted in deriving $L_{\rm acc}$ (Hα line profile modelling, veiling in the FUV, UV, and VIS, etc.), systematic differences may exist at different mass regimes (e.g., Herczeg & Hillenbrand, 2008). Therefore, except for the YSOs in σ-Ori (Rigliaco et al., 2012, and Sect. 6.3), whose $L_{\rm acc}$ and $L_{\rm line}$ values were computed in the same way as here, no other literature data were combined to derive $L_{\rm acc}$-$L_{\rm line}$ relationships. It should be noted also that the Lupus sample comprises $L_{\rm acc} \leq 1\ L_\odot$, while literature data extend to higher accretion luminosities.

While the accretion luminosity is well correlated with the luminosity of all the emission lines, the scatter in the correlations differs for the various lines. Among the relationships of Eq. (6.1) the one with the larger scatter is that of the Hα line. This is expected because it is well known that several other processes (e.g. outflows, hot spots, chromospheric activity, complex magnetic field topology and geometry, stellar rotation) in addition to accretion may contribute to the strength of the line. All these processes have an important impact on the line profile, in particular on its width. The least scattered $L_{\rm acc}$-$L_{\rm line}$ relations are those of the Balmer lines with $n > 3$, the Brγ line, and the He I lines. The Paβ and the Brγ

---

[4] Note that the slope and zero points in the Herczeg & Hillenbrand (2008) relationships are swapped in their Table 16.

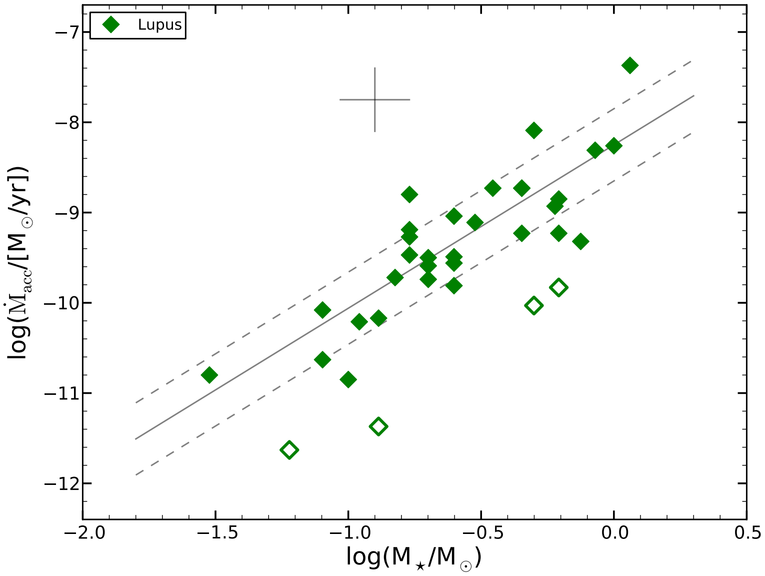

Figure 6.4: Mass accretion rate as a function of mass for the Lupus sample. The open symbols are used for the low-luminosity YSOs. The continuous line represents the linear fit of Equation 6.3, that is, it does not include the subluminous objects. The dashed lines represent the 1 σ deviation from the fit. Average error bars are shown in the upper left corner. Adapted from Alcalá et al. (2014).

relations are recommended because these lines are the least affected from chromospheric emission, as shown also by the analysis of Class III YSO spectra (Manara et al., 2013a, and Chapter 3). Finally, as also noted by Rigliaco et al. (2012), accretion luminosity derived using simultaneously various emission lines lead to results compatible within the errors with those obtained from the UV-excess fitting and with a much better agreement than using a single emission line.

6.2.4 Accretion properties of stellar and substellar objects in Lupus

As I discussed in Sect. 1.4.1 of this Thesis, previous investigations (Muzerolle et al., 2003; Mohanty et al., 2005; Natta et al., 2006; Herczeg & Hillenbrand, 2008; Rigliaco et al., 2011a; Antoniucci et al., 2011; Biazzo et al., 2012; Manara et al., 2012, and references therein) have found that $\dot{M}_{\rm acc}$ goes roughly as the square of $M_\star$ although with a significant scatter (up to 3 dex) in $\dot{M}_{\rm acc}$ for a given YSO mass.

Figure 6.4 shows the $\dot{M}_{\rm acc}$ versus $M_\star$ diagram for the Lupus YSOs studied here. The scatter is significantly increased by the four subluminous YSOs. A linear fit to the complete Lupus sample yields to the following relation:

$$\log \dot{M}_{\rm acc} = 1.89(\pm 0.26) \cdot \log M_\star - 8.35(\pm 0.18), \tag{6.2}$$

with a standard deviation of 0.6. The scatter decreases if the subluminous objects are

Table 6.5: Coordinates, spectral types, physical and accretion parameters of the σ-Ori Class II YSOs

Object	RA	DEC	SpT	$T_{\rm eff}$ [K]	$L_\star$ $[L_\odot]$	$R_\star$ $[R_\odot]$	$M_\star$ $[M_\odot]$	log$L_{\rm acc}$ $[L_\odot]$	log$\dot{M}_{\rm acc}$ $[M_\odot$/yr]
SO397	05:38:13.18	−02:26:08.63	M4.5	3200	0.19	1.45	0.20	–2.71	–9.42
SO490	05:38:23.58	−02:20:47.47	M5.5	3060	0.08	1.02	0.14	–3.10	–9.97
SO500	05:38:25.41	−02:42:41.15	M6	2990	0.02	0.47	0.08	–3.95	–10.27
SO587	05:38:34.04	−02:36:37.33	M4.5	3200	0.28	1.73	0.20	<-4.00	<–10.41
SO646	05:38:39.01	−02:45:31.97	M3.5	3350	0.10	0.97	0.30	–3.00	–9.68
SO848	05:39:1.938	−02:35:02.83	M4	3270	0.02	0.46	0.19	–3.50	–10.39
SO1260	05:39:53.63	−02:33:42.88	M4	3270	0.13	1.12	0.26	–2.00	–8.97
SO1266	05:39:54.22	−02:27:32.87	M4.5	3200	0.06	0.84	0.20	<–4.85	<–11.38

excluded from the fit, and the best fit relation becomes in this case:

$$\log \dot{M}_{\rm acc} = 1.81(\pm0.20) \cdot \log M_\star - 8.25(\pm0.14), \tag{6.3}$$

with a standard deviation of 0.4. The slope and zero point of the $\dot{M}_{\rm acc}$- $M_\star$ fit do not change significantly in either cases because the subluminous objects represent only 11% of the sample. It is thus reasonable to conclude that for the Lupus sample $\dot{M}_{\rm acc} \propto {M_\star}^{1.8(\pm0.2)}$, which agrees with previous studies (Natta et al., 2006; Muzerolle et al., 2005; Herczeg & Hillenbrand, 2008; Rigliaco et al., 2011a; Antoniucci et al., 2011; Biazzo et al., 2012; Manara et al., 2012), but is inconsistent with the results by Fang et al. (2009) ($\dot{M}_{\rm acc} \propto {M_\star}^3$) for their subsolar mass sample in the Lynds 1630N and 1641 clouds in Orion. I will discuss in Sect. 6.6.2 the reasons of this difference.

In this sample of Lupus Class II YSOs the power-law index of the $\dot{M}_{\rm acc}$-$M_\star$ relation is $\sim$2 similarly to previous investigations, but the scatter is considerably smaller than in previous data sets (cf. the standard deviation for the Lupus fit is a factor 2 lower than for the Taurus sample in Herczeg & Hillenbrand, 2008). As pointed out in Section 6.2.1, this sample represents about 50% of the complete population of Class II YSOs in the Lupus I and Lupus III clouds. It is therefore unlikely that the wide range of $\dot{M}_{\rm acc}$ ($>$ 2 dex) at a given mass observed in other data sets will be also detected in Lupus, in a more complete sample. However, it would be worthwhile to study YSOs more massive than those in this sample, using spectra of the same quality as these. In addition, although the number statistics of this sample is low, there is no evidence for a double power-law as suggested by Vorobyov & Basu (2009), supporting the conclusion that the apparent bi-modal relations suggested in the literature between $\dot{M}_{\rm acc}$ and other YSOs properties are probably the result of mixing $\dot{M}_{\rm acc}$ derived with different methods.

6.3 Accretion in the σ-Orionis region

Based on Rigliaco, Natta, Testi et al. 2012, A&A, 548, A56[†]

The σ-Orionis cluster (RA 5h40m DEC -2d36′) is located at a distance of $\sim$360 pc (Hipparcos distance 352^{+166}_{-85}pc, Brown et al. 1994; Perryman et al. 1997) and has an age of $\sim$3 Myr (Zapatero Osorio et al., 2002; Fedele et al., 2010). It contains more than 300 YSOs, ranging in mass from the bright, massive multiple system σ-Ori itself (the spectral type of the brightest star is O9.5V, Caballero 2008) to brown dwarfs. The region has negligible extinction (Béjar et al., 1999; Oliveira et al., 2004), and has been extensively studied in the optical, X-rays, and infrared (e.g., Rigliaco et al., 2011a; Kenyon et al., 2005; Zapatero Osorio et al., 2002; Jeffries et al., 2006; Franciosini et al., 2006; Hernández et al., 2007).

The sample of objects in σ-Ori observed with X-Shooter comprises 8 Class II YSOs and 4 Class III YSOs which have been discussed in Chapter 3 and Manara et al. (2013a). Here I report on the accretion rates derived for the 8 Class II YSOs, that have been selected from the sample of Rigliaco et al. (2011a) and cover a range of masses from $M_\star \sim 0.08 M_\odot$ to $\sim 0.3 M_\odot$.

Spectral types for the σ-Ori sample were estimated by averaging the results obtained using the various indices by Riddick et al. (2007) on the flux calibrated spectra, similarly to the other data-sets discussed in this Thesis (see e.g., Chapter 3 and Sect. 6.2.2). The SpT was then converted in $T_{\rm eff}$ using the temperature scale of Luhman et al. (2003). Stellar luminosities were then computed from the I-band magnitudes, and the bolometric correction for zero age main sequence (ZAMS) stars as reported by Luhman et al. (2003). The typical uncertainty in $L_\star$ for these targets is estimated to be of $\sim$0.2 dex. The stellar masses and ages were derived comparing the location of the targets on the HR diagram with the evolutionary models by Baraffe et al. (1998). The adopted stellar parameters for the targets are reported in Table 6.5.

The accretion luminosity was then derived for these objects by fitting the UV-excess with the same set of models as the fitting procedure described in Chapter 4, i.e. with a Class III YSO template (see Chapter 3) of the same SpT of the Class II target and the slab model to describe the excess flux due to accretion (see Chapter 2). I stress that it was assumed $A_V \sim 0$ for all the targets in this region. In 6 out of the 8 objects analyzed here the excess luminosity is clearly detected; in two cases (SO587 and SO1266) only upper limits could be determined. The derived values are reported in Table 6.5, while the best fits of the Balmer jump are shown in Fig. 6.5.

Figure 6.6 shows the values of $\dot{M}_{\rm acc}$ vs $M_\star$ for the 8 targets discussed in this section. The overplotted relation is the best fit of the $\dot{M}_{\rm acc}$-$M_\star$ relation derived by Alcalá et al. (2014) for the Lupus sample, shown as reference. The values for all the six Class II YSOs

---

[†] In this work I had a marginal contribution. However, the accretion rates for these targets have been derived with the same slab model as the one I have been using and have been checked and validated with my fitting procedure. Given that these results are obtained with a methodology compatible to that of the other works discussed in this Thesis, these can be included in the final sample. For these reasons I include here a short section describing this work to report the results that I will use in the next sections.

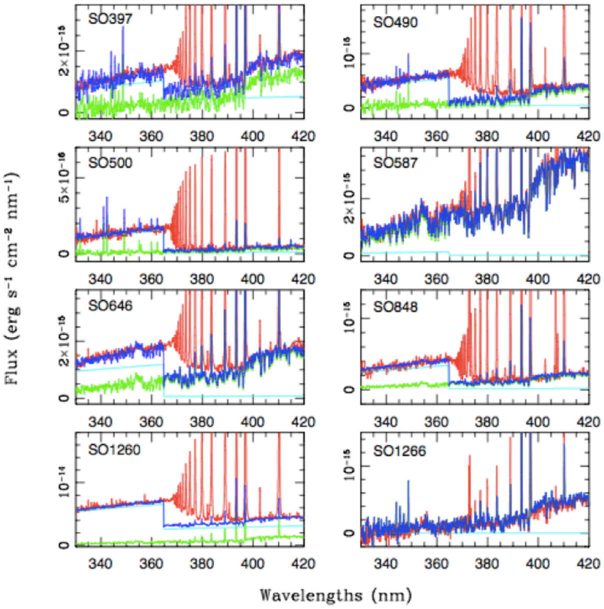

Figure 6.5: Best fit of the UV-excess for the σ-Ori Class II YSOs. The spectrum of the target is shown in red, the Class III template in green, the slab model in cyan, and the best fit in blue. From Rigliaco et al. (2012).

with detected $\dot{M}_{\rm acc}$ are compatible with this best fit relation. For SO1266 the upper limit on $\dot{M}_{\rm acc}$ is significantly smaller than the measurements for Class II YSOs of similar $M_\star$. As discussed in detail in Rigliaco et al. (2012), this object has probably a significantly depleted gaseous inner disk, and is an example of low-accreting TD. Interestingly, the luminosity of the emission lines for this object would imply an higher value of $L_{\rm acc}$. However, Rigliaco et al. (2012) suggest that most (~80%) of the emission in the lines is due to chromospheric emission, as discussed also in Manara et al. (2013a).

6.4 New data in the ρ-Ophiucus embedded complex

The Ophiucus molecular cloud (RA 16h25m DEC -24d20′) is a well known low-mass star forming region. It is located at the edge of the Upper Scorpious subgroup in the Sco-Cen OB association. This complex is composed of series of filamentary dark clouds that extend from cores of dense molecular gas (de Geus, 1992). It is composed of three main dark clouds, L1688, L1689, and L1709 located at a distance $d \sim 125$ pc (Lombardi et al., 2008; Loinard et al., 2008). This region is still highly embedded in the parental cloud, with values of A_V up to 50 mag in the densest core (Wilking & Lada, 1983), and with a rather high value of total-to-selective extinction ratio $R_V \sim 5.6$ (e.g., Kenyon et al., 1998; Chapman et al., 2009; McClure et al., 2010; Comerón et al., 2010). This region has been extensively studied in the past at various wavelengths from optical, near- and far-infrared, millimeter, radio, to X-ray (e.g., Greene & Meyer, 1995; Luhman & Rieke, 1999; Wilking et al., 2005; Alves de Oliveira et al., 2010, 2012; Bontemps et al., 2001; McClure et al., 2010; Gagné

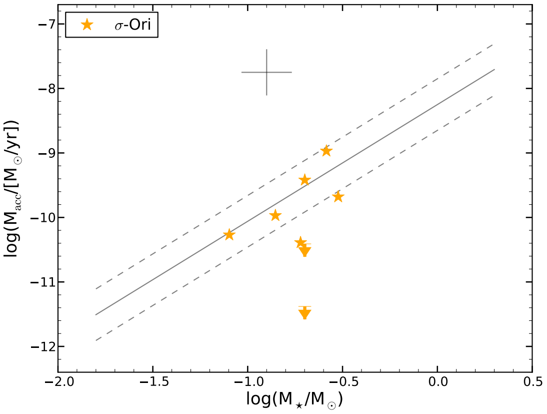

Figure 6.6: Mass accretion rate $\dot{M}_{\rm acc}$ as a function of mass for the σ-Ori sample analyzed by Rigliaco et al. (2012). The continuous line represents the linear fit of this relation for the Lupus sample (see Equation 6.3) shown here as a reference. The dashed lines represent the 1 σ deviation from the fit. Average error bars are shown in the upper left corner.

et al., 2004) and the total population of the region is estimated to be of around 300 YSOs (Evans et al., 2009), with ∼200 YSOs located in the central cluster ρ-Oph (or L1688). One possible scenario for the formation of the dense ρ-Oph core is triggered formation from the OB stars in the Upper Scorpius subgroup (de Geus, 1992; Preibisch & Mamajek, 2008). The age of this region is estimated to be $\lesssim$1 Myr as suggested by the fact that it is still highly embedded. Various works aimed at understanding the accretion properties of YSOs at early ages have targeted ρ-Oph. In particular, Natta et al. (2004, 2006) have studied a significant fraction of the Class II YSOs in this cluster, selected from the ISO sample of Bontemps et al. (2001), using near-infrared emission lines (Paβ and Brγ). Their results, corrected for the newly determined distance as explained by Rigliaco et al. (2011a), showed an increase of $\dot{M}_{\rm acc}$ with $M_\star$ with an exponent of the power law of 1.3±0.2 using the evolutionary tracks of Baraffe et al. (1998), but also a large scatter of $\dot{M}_{\rm acc}$ (roughly two order of magnitudes, independent of $M_\star$). When compared with results in Taurus from Muzerolle et al. (2003, 2005), the values of $\dot{M}_{\rm acc}$ derived in ρ-Oph showed a similar trend but significantly larger values of $\dot{M}_{\rm acc}$ at lower $M_\star$ ($\lesssim 0.1 M_\odot$). The latter could be due to incompleteness at lower masses in the sample of Class II YSOs of Bontemps et al. (2001).

In this section I will report on new data collected with X-Shooter (Pr.Id.085.C-0876, PI Testi) on a small sample of ∼20 very low mass stars (VLM) and BDs analyzed here for the first time. I will focus only on the Class II objects, while the Class III targets will be discussed in a following paper (Manara et al., in prep.) and the TD object ISO-Oph196 has been discussed in Manara et al. (2014a).

Table 6.6: Selected YSOs in the ρ-Ophiucus region and observing log

Object/other name	RA(2000) h :m :s	DEC(2000) ° ′ ″	Obs. date YY-MM-DD	Exp. Time [s]
ISO−Oph023 / SKS1	16:26:18.821	−24:26:10.52	2010-08-20	4×750s
ISO−Oph030 / GY5	16:26:21.528	−24:26:00.96	2010-08-20	4×750s
ISO−Oph032 / GY3	16:26:21.899	−24:44:39.76	2010-06-01	4×750s
ISO−Oph033 / GY11	16:26:22.269	−24:24:07.06	2010-08-26	4×1800s
ISO−Oph037 / LFAM3 / GY21	16:26:23.580	−24:24:39.50	2010-08-21	4×750s
ISO−Oph072 / WL18	16:26:48.980	−24:38:25.24	2010-04-06	4×480s
ISO−Oph087	16:26:58.639	−24:18:34.66	2010-08-28	4×750s
ISO−Oph094	16:27:03.591	−24:20:05.45	2010-08-28	4×750s
ISO−Oph102 / GY204	16:27:06.596	−24:41:48.84	2010-07-23	4×750s
ISO−Oph115 / WL11 / GY229	16:27:12.131	−24:34:49.14	2010-07-30	4×750s
ISO−Oph117 / WLY2-32b / GY235	16:27:13.823	−24:43:31.66	2010-06-08	4×480s
ISO−Oph123	16:27:17.590	−24:05:13.70	2010-08-27	4×750s
ISO−Oph160 / B162737-241756	16:27:37.422	−24:17:54.87	2010-08-27	4×750s
ISO−Oph164 / GY310	16:27:38.631	−24:38:39.19	2010-06-08	4×750s
ISO−Oph165 / GY312	16:27:38.945	−24:40:20.67	2010-06-08	4×750s
ISO−Oph176 / GY350	16:27:46.291	−24:31:41.19	2010-08-21	4×750s
ISO−Oph193 / B162812-241138	16:28:12.720	−24:11:35.60	2010-08-21	4×750s

Notes. Exposure times are the same in the three X-Shooter arms (UVB, VIS, and NIR).

6.4.1 Sample, observations, and data reduction

The sample of ρ-Oph targets comprises 17 Class II YSOs observed with X-Shooter. All these targets were included in the ISO sample compiled by Bontemps et al. (2001) and have been previously studied by Natta et al. (2004, 2006). Their ISO number, other names, coordinates, observing dates, and exposure times are reported in Table 6.6. The sample was selected from the sample of Natta et al. (2006) to cover as many of the objects with estimated mass <0.1 $M_\odot$ and measured $\dot{M}_{\rm acc}$ as possible. ISO-Oph072 was reported by McClure et al. (2010) to be member of a binary system with a separation of 3.62″. In the X-Shooter spectrum analyzed here there is only the primary component of the system, while the secondary is not in the slit.

All the objects have been observed in service mode using the 1.0″ slit in the UVB arm and the 0.9″ slits in the VIS and NIR arms, which lead to resolution R$\sim$ 4350, 7450, and 5300 in the three arms, respectively. Different exposure times have been adopted for each target depending on their estimated fluxes. The low mass of most of the targets and the high extinction of the region result in a low SNR for most spectra at least in the UVB arm. The only spectra with SNR greater than $\sim$5 at 400 nm are those of ISO-Oph032 and ISO-Oph123. Some objects have also very low SNR in the VIS spectra at $\lambda \lesssim$ 600-700 nm, or even more. The NIR spectra of all targets have a good SNR.

Data reduction has been carried out using the X-Shooter pipeline Modigliani et al. (2010) version 1.3.7 and the same procedure as in the rest of this Thesis (see, e.g, Chapters 3, 4, 5, and Manara et al., 2013a,b, 2014a; Alcalá et al., 2014). The flux calibration of the spectra reduced with the pipeline has been compared with available photometry and a good agreement was found in most cases. Indeed, these spectra have all been obtained with quite large slits, so slit losses are small. Only in four cases a small correction factor was applied ($\sim$ 1.2-1.5) to adjust the flux-calibrated spectra to the photometric data. The only spectrum where the conjunction between the arms are not very good is ISO-Oph102. In this object the flux calibration of the last $\sim$100 nm of the VIS arm is not good, and this results in a bad matching of the VIS and NIR arms.

6.4.2 Stellar and substellar properties

As explained in the previous section, most of the spectra have SNR$\sim$0 in the UVB arm, therefore the fitting procedure explained in Chapter 4 and used in the analyses discussed in this Thesis cannot be used. For this reason I derive SpT and A_V from the spectra of the targets following a procedure similar to that discussed in Sect. 6.2.2 for all the objects in ρ-Oph but ISO-Oph032 and ISO-Oph123, as I explain later in this section. Moreover, given that the SNR is low in most spectra also in the VIS arm (at least at $\lambda \gtrsim$ 600-700 nm), I smooth all of them in the VIS to enhance the SNR. This is done using the *boxcar smoothing* procedure included in the IRAF *splot* package. This procedure convolves the spectrum with a rectangular box, whose width is set to 7 or 11 bins depending on the initial SNR of the spectra. This smoothing procedure results in a broadening of the narrower absorption and emission lines and features, but preserves their fluxes and equivalent widths.

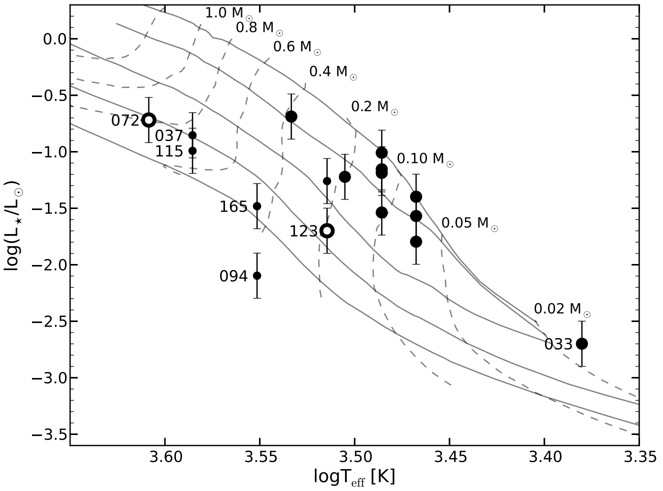

Figure 6.7: Hertzsprung-Russell diagram for the ρ-Oph Class II YSOs analyzed here. Smaller symbols are used for the objects with uncertain stellar parameters, while empty symbols for the strongly veiled ones. The continuous lines show the 1 Myr, 3 Myr, 10 Myr, 30 Myr, and 100 Myr isochrones, reported by Baraffe et al. (1998), while the dashed lines show the low-mass pre-main sequence evolutionary tracks by the same authors as labelled. ISO numbers are reported for the objects with estimated ages greater than 10 Myr and for ISO-Oph033.

To derive SpT and A_V I first use the indices of Riddick et al. (2007) discussed in Chapter 3 and in Manara et al. (2013a). These are independent of extinction if A_V is low, which is not the case for most of the objects included in this sample. They are also valid only for objects with SpT later than M2-M3, as discussed by, e.g., Manara et al. (2013a). Therefore, these are used only to have a first estimate of the SpT. Then, I compare the VIS arm of the observed spectra with the Class III YSO spectra of Chapter 3 (Manara et al., 2013a) of similar SpT to the one predicted from the indices or to that reported in the literature for the object. The Class III YSO spectrum is reddened using the reddening law of Cardelli et al. (1989) and R_V = 5.6[5] with increasing amount of A_V until a best match is found. This visual comparison, which aims at finding a good matching of target and Class III spectra in the absorption features discussed in Chapter 3, leads to a determination of the SpT of the targets. Starting from this estimate, the NIR arm of the observed spectra is compared with the reddened Class III YSO spectra to validate the SpT determination and to derive an accurate value of A_V. Indeed, veiling due to accretion makes the observed spectrum bluer and leads to underestimate the value of A_V when using the VIS arm alone. Veiling is, instead, smaller in the NIR, in particular in the J-band, where the effects of the presence of a circumstellar disk are still small. In most cases A_V derived from the VIS spectra is confirmed or a value of A_V larger by less than a factor ∼1.2-1.3 is found.

From the values of SpT and A_V derived with this procedure I then determine $L_\star$ comparing the extinction corrected spectrum of the Class II YSO target with that of the best matching Class III YSO. First I derive the factor K to rescale the observed Class III spectrum to the exinction corrected Class II YSO by matching the two spectra at λ = 1030 nm. This factor K corresponds to the squared ratio of the stellar radii of the two targets. Then, I compute the Class II YSO bolometric luminosity from the one of the Class III YSO taking into account the distance of the latter and the distance of ρ-Oph, assumed to be 125 pc, using the formula:

$$L_{\star,\mathrm{ClassII}} = K \cdot (d_{\rho-\mathrm{Oph}}/d_{\mathrm{ClassIII}})^2 \cdot L_{\star,\mathrm{ClassIII}}, \tag{6.4}$$

as done in, e.g., Chapter 4 (Manara et al., 2013b). Converting the SpT in $T_{\rm eff}$ using the SpT-$T_{\rm eff}$ relation of Luhman et al. (2003) for M-type stars and of Kenyon & Hartmann (1995) for earlier type objects I am able to assign to each object a position on the HRD and derive the stellar parameters ($M_\star$, age) using the evolutionary tracks of Baraffe et al. (1998). This is shown in Fig. 6.7. In the following paragraphs I present the results obtained with this analysis, which are reported in Table 6.7. Finally, the comparison between the observed spectra and the corresponding Class III YSO template is shown in Figs. 6.8 to 6.12.

Spectra with good VIS arms

For 10 out of the 17 targets (ISO-Oph023,030,032,033,102,117,160,164,176,193) the analysis explained in the previous paragraphs leads to a firm estimate of the SpT and A_V.

---

[5] This analysis was carried out also adopting $R_V = 3.1$, but a better agreement between the reddened spectra of the Class III and the targets is found using $R_V = 5.6$, especially in the region of the VIS spectra at $\lambda \gtrsim$ 900 nm and in the NIR J- and H-bands. The final $\dot{M}_{\rm acc}$ values derived using the two different values of R_V differ by a factor ∼2-3, at most.

Table 6.7: Spectral types, extinction, and physical parameters of the ρ-Oph Class II YSOs

Object	SpT	$T_{\rm eff}$ [K]	A_V [mag]	$L_\star$ [$L_\odot$]	$R_\star$ [$R_\odot$]	$M_\star$ [$M_\odot$]	Age [Myr]
ISO−Oph023	M6.5	2935	8.5	0.027	0.64	0.07	2
ISO−Oph030	M5.5	3060	5.8	0.098	1.12	0.14	1
ISO−Oph032	M6.5	2935	1.9	0.040	0.77	0.08	1
ISO−Oph033	M9	2400	5.5	0.002	0.28	0.02	∼1
ISO−Oph037†	M0	3850	15.0	0.140	0.84	0.74	28
ISO−Oph072*	K7	4060	10.5	0.191	0.88	0.81	33
ISO−Oph087†	M4	3270	13.0	0.055	0.73	0.23	6
ISO−Oph094†	M2	3560	11.0	0.008	0.23	0.40	>100
ISO−Oph102	M5.5	3060	3.7	0.070	0.94	0.14	1
ISO−Oph115†	M0	3850	15.5	0.102	0.72	0.68	43
ISO−Oph117	M3	3415	10.0	0.205	1.30	0.38	2
ISO−Oph123*	M4	3270	5.0	0.020	0.44	0.19	20
ISO−Oph160	M5.5	3060	7.0	0.029	0.61	0.11	4
ISO−Oph164	M6.5	2935	3.0	0.016	0.49	0.07	4
ISO−Oph165†	M2	3560	13.0	0.033	0.48	0.45	69
ISO−Oph176	M5.5	3060	8.3	0.065	0.91	0.14	2
ISO−Oph193	M4.5	3200	8.4	0.060	0.80	0.20	4

Notes. M_* and age are derived using the evolutionary tracks of Baraffe et al. (1998). † Objects with uncertain stellar parameters due to the low SNR of the spectra and the strong extinction. * Object with uncertain stellar parameters due to the strong veiling.

In these objects the VIS spectra have always good SNR at least for $\lambda \gtrsim$650-700 nm, thus in the wavelength region where most of the absorption features are. In all these targets but two the best fit SpT derived confirms the first estimate done using the indices from Riddick et al. (2007), with differences of less than 0.5 spectral subclasses. The largest differences with the values derived using the indices are for ISO-Oph033 and ISO-Oph117. In the former the indices suggest a SpT M6.1 while I derive SpT M9, and the difference is probably due to the low SNR of the spectrum at $\lambda \lesssim$ 800 nm. In the latter, the SpT assigned to this object is M3, while the indices suggest a SpT between M3.5 and M4, but closer to M4. Among the targets analyzed in this paragraph this one is the more extincted one (A_V=10 mag), and this could be the reason for the discrepancy. Indeed, the indices of Riddick et al. (2007) are extinction independent for $A_V \lesssim 5$, but may be affected by larger extinctions.

The SpT derived here agree in most cases with those reported in the literature within 0.5 spectral subclasses. In some cases, such as ISO-Oph033, the difference of 0.5 subclasses is due to the incompleteness of the set of photospheric templates used. This object has been classified as M8.5 by Natta et al. (2002), Testi et al. (2002), and Comerón et al. (2010), while I classify it as M9 because the grid I am using has no spectra between M6.5 and M9 (see Fig. 3.4). The largest difference with SpT available in the literature is found for ISO-Oph032 and ISO-Oph193. The former has been classified as M7.5 by Natta et al. (2002) and as M8 by Wilking et al. (2005), while I derive a spectral type M6.5 for this target. Also in this case this could be due to incompleteness of the grid of template spectra, but

I rely on my result which is also validated by the spectral indices result and by the fitting procedure discussed later. For the latter the SpT reported in the literature is M6 (Natta et al., 2002), while I derive M4.5 both with the spectral indices and with the visual comparison. In this case, this is not due to incompleteness of the template grid, as this is complete until M6.5. Using the X-Shooter spectra I am able to determine the SpT for ISO-Oph117 and ISO-Oph164, whose classification was debated in the literature. For ISO-Oph117 Gatti et al. (2006) derived SpT K8, while Wilking et al. (2005) found SpT M5. My analysis leads to a SpT of M3, while it is clear that this object can be neither late-K or M5, as the molecular features at $\lambda \sim$ 700-800 nm are too strong for a late-K star, and too shallow for an M5 YSO. Regarding ISO-Oph164, the spectral types determined in the literature vary from M8.5 (Wilking et al., 1999), to M6 (Natta et al., 2002), and even to M4 (Wilking et al., 2005). The spectral indices suggest a SpT M5.9 for this target, while the best match determined with the X-Shooter spectra is found to be M6.5. However, the observed spectrum cannot be well reproduced with any of the templates available, and further analysis are needed on this target.

The age determined with the stellar parameters determined here and using the evolutionary tracks of Baraffe et al. (1998) is always between ~1 Myr and ~4 Myr for these objects, as one would expect given the young age of the region and, at the same time, the uncertainty in the age determination with isochrone interpolation. Only ISO-Oph033 has stellar parameters that correspond to a position on the HRD where there are no evolutionary tracks. I extrapolate the stellar mass and report an age ~1 Myr.

Spectra with stong veiling and/or good UVB spectra

Two spectra, ISO-Oph072 and ISO-Oph123, are too strongly veiled to get SpT from the procedure explained in the previous paragraphs. The first one has a spectrum with SNR~0 in the UVB arm due to the high extinction ($A_V \sim$ 10.5 mag), so I cannot use the procedure explained in Chapter 4 to determine its properties. Using the procedure described above I determine a best estimate of SpT, M0.5, and A_V=10.5 mag. However, this value is rather uncertain as the strong veiling could modify substantially the stellar parameters (see, e.g., Manara et al., 2013b; Herczeg & Hillenbrand, 2014). The SpT determined here is compatible with that available in the literature (K6.5 Wilking et al., 2005), but the age determined with these stellar parameters is rather high (~33 Myr), suggesting that the stellar luminosity is underestimated or the SpT is incorrect, similarly to the objects discussed in Chapter 4 (Manara et al., 2013b).

For ISO-Oph123 the UVB spectrum has enough SNR to use the fitting procedure discussed in Chapter 4. Particular care is used when fitting this object in selecting the correct wavelength ranges to determine the stellar continuum in the Balmer and Paschen continua regions. Indeed, this spectrum shows a multitude of emission lines at all wavelengths which make the continuum estimate more difficult. Even if particular care is taken, the best fit does not reproduce well the slope of the Balmer continuum and probably overestimates the excess emission at $\lambda \lesssim$ 320 nm, thus the accretion luminosity. This will be discussed in Sect. 6.4.3 when I will compare the $L_{\rm acc}$ obtained from the luminosity of the emission lines with that determined by this fitting procedure. The SpT determined here agrees well with that suggested by the spectral indices and found in the literature. At the same time, the stellar parameters derived (SpT M4, A_V=5 mag, $L_\star$= 0.02 $L_\odot$) result in an estimated age of $\sim$ 20 Myr, much older than the actual age of the region. I then use the $M_\star$ derived from the evolutionary tracks for the rest of the analysis, but I caution that the age is probably over-estimated due to an underestimation of the stellar luminosity for the strong veiling and the presence of many emission lines in the observed spectrum.

Finally, the fitting procedure is used also for ISO-Oph032, whose UVB spectrum is good. In this object the best fit is obtained with the same SpT as determined before (M6.5) but with a slightly higher A_V due to the fact that with this methodology the effects of veiling due to accretion are taken into account. I adopt the value of A_V determined with this method in the following analysis.

Spectra with low SNR in the VIS arm

Five objects included in this sample have a very low SNR in the VIS arm due to their strong extinction, always $A_V > 10$ mag. The spectral classification for these targets is difficult, and should be carried out in the NIR, and the results are rather uncertain. The procedure I follow is similar to that carried out earlier on with the VIS arm of spectra with good SNR. Starting from the SpT(s) reported in the literature and checking also other SpTs, I vary A_V until a best visual match is found. This leads to reasonable agreements, but not for all the targets, as I discuss in the following. However, in all the cases the stellar parameters determined result in an estimated age much older than the real age of ρ-Oph, thus suggesting that the stellar luminosity is underestimated for these targets. Only for ISO-Oph087 I derive age $\sim$6 Myr, but the result is still rather uncertain. In the following I discuss the five objects separately.

The NIR spectrum of ISO-Oph037 looks like that of an object at a very early stage of evolution. It is raising due to the strong disk/envelope contribution and has no clear spectral features. McClure et al. (2010) classify this object as ``disk'' but report that this could be a flat spectrum, as well. The SpT determined here (M0) is the same as that determined by McClure et al. (2010), while Gatti et al. (2006) reported a SpT K5 for this target. However, the SpT I determine is only a best guess for this target.

For ISO-Oph087 no previous estimates of SpT are reported in the literature. This is an object known to be variable, with two strong flares reported by Parks et al. 2014. Natta et al. (2006) derived $T_{\rm eff}$ = 3090 K for this objects assuming a single isochrone and deriving the stellar luminosity from the NIR photometric colors. This corresponds to SpT M5-M5.5 according to the SpT-T$_{\rm eff}$ relation by Luhman et al. (2003). The best matching of the NIR spectrum is found with the template of SpT M4, and this value leads to a reasonable age estimate of $\sim$6 Myr. However, also in this case the stellar parameters should be considered uncertain.

Alves de Oliveira et al. (2010) already analyzed a NIR spectrum of ISO-Oph094, and suggested that this object could have a SpT M3, but with high uncertainty. In the X-Shooter spectra only the NIR arm has a reasonable SNR, while the VIS arm has almost no flux. I derive SpT M2 for this object, but with high uncertainty. The stellar parameters determined here result in a position of this object on the HRD well below the main sequence. This suggests that the parameters are incorrect, or that this object is under-luminous.

Both for ISO-Oph115 and ISO-Oph165 I determine the same SpT as reported in the literature. For the former I get M0 as reported by Gatti et al. (2006), while for the latter I get M2 as obtained by McClure et al. (2010). In both cases, however, the stellar parameters lead to a position on the HRD corresponding to objects with age$\gtrsim$40 Myr, suggesting that the luminosity is underestimated or that these targets are under-luminous.

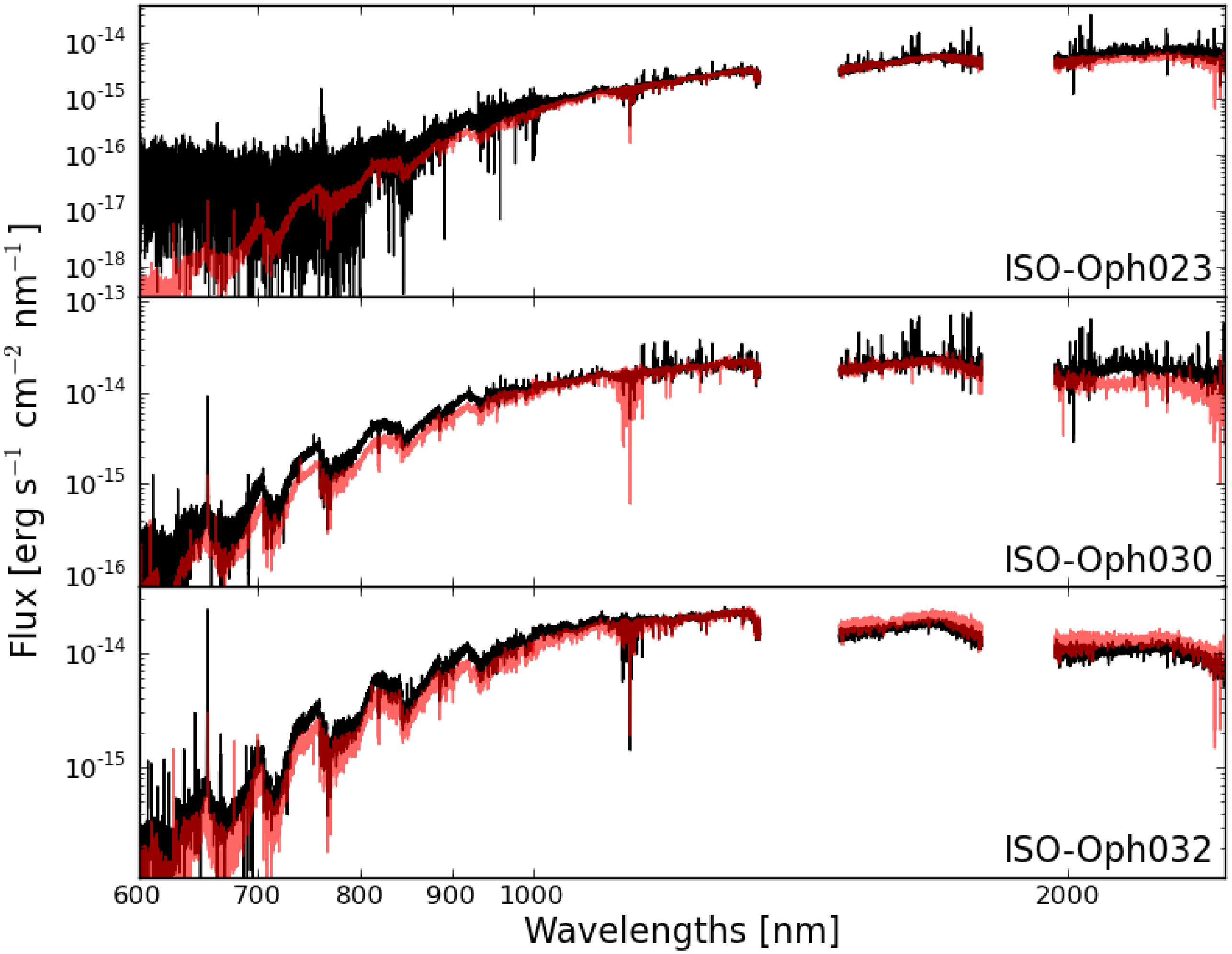

Figure 6.8: Spectra of ρ-Oph targets from 600 to 2450 nm. The observed spectra are shown in black. In red I report the Class III YSO spectrum with the same SpT of the observed target. This is exincted and normalized at λ=1250 nm to match the observed spectrum. Veiling due to accretion or disk emission is not included.

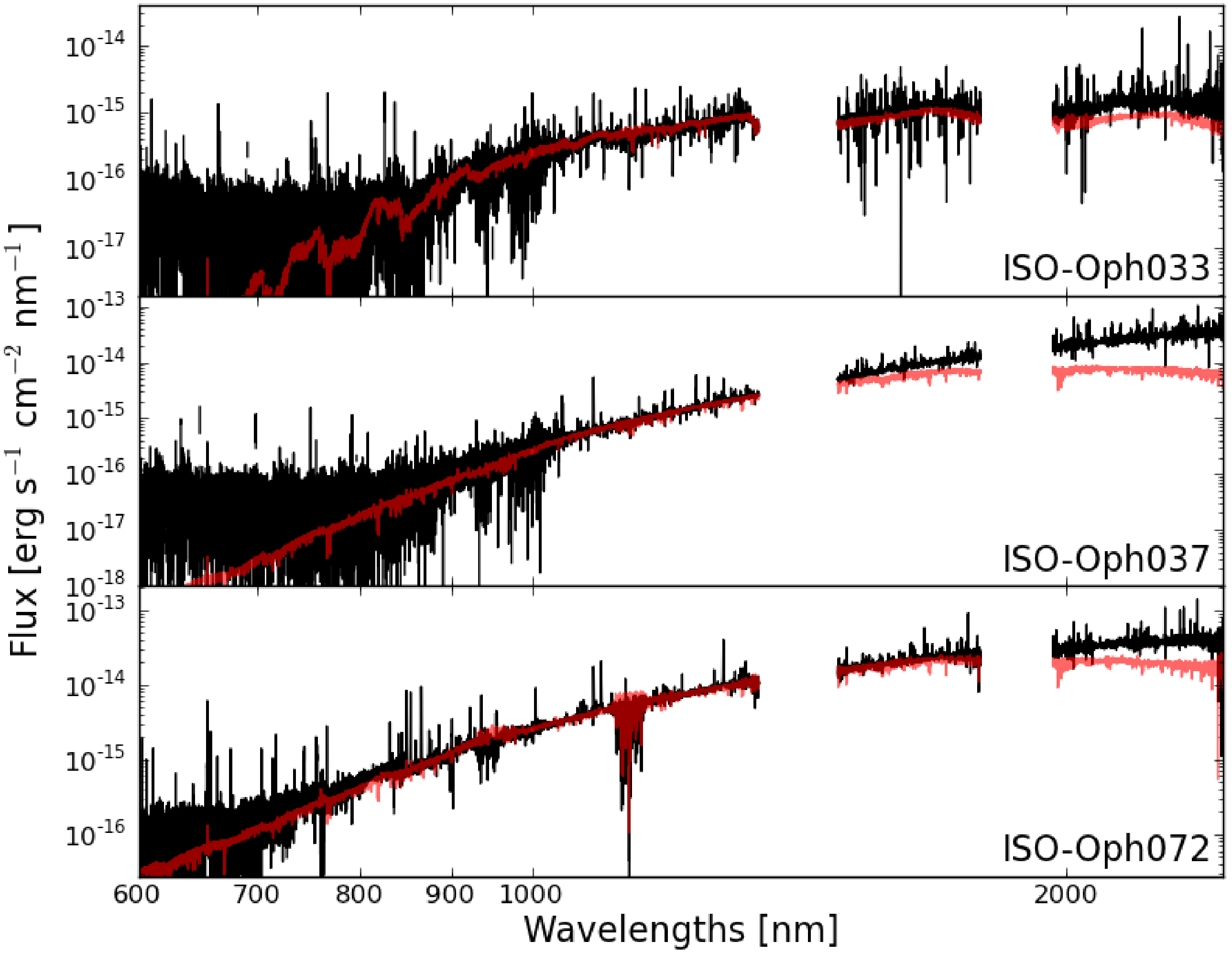

Figure 6.9: Spectra of ρ-Oph targets from 600 to 2450 nm. Same as Fig. 6.8.

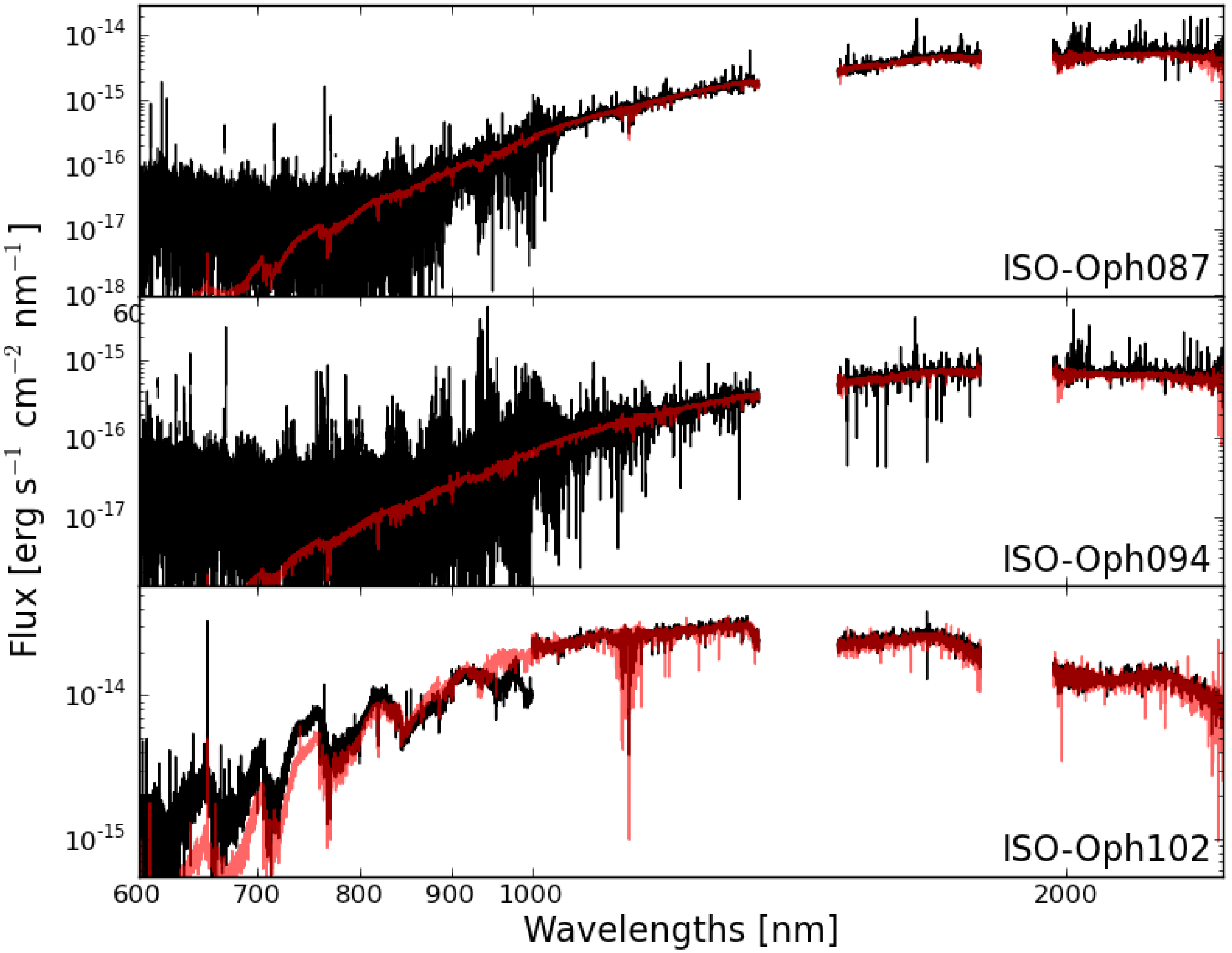

Figure 6.10: Spectra of ρ-Oph targets from 600 to 2450 nm. Same as Fig. 6.8.

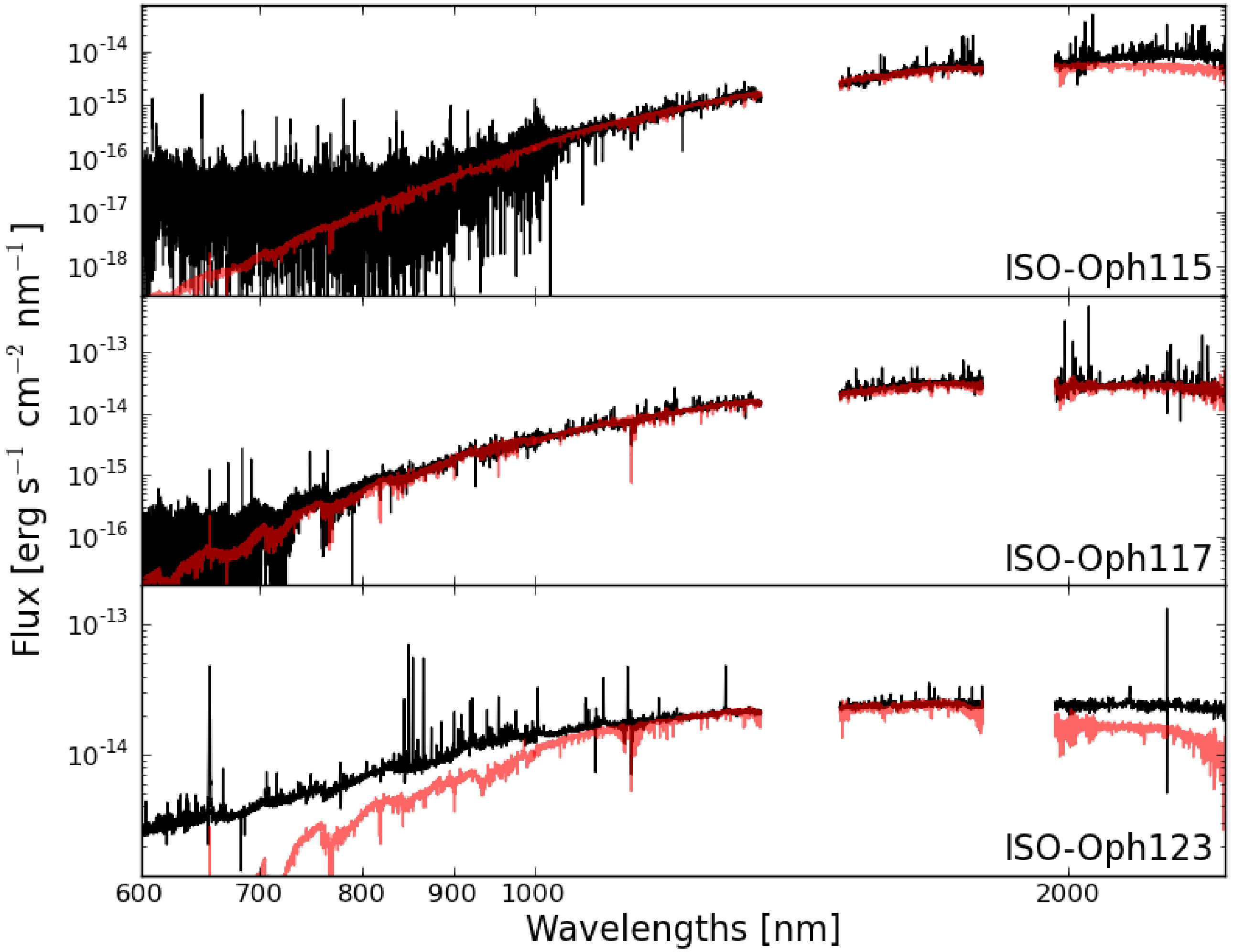

Figure 6.11: Spectra of ρ-Oph targets from 600 to 2450 nm. Same as Fig. 6.8.

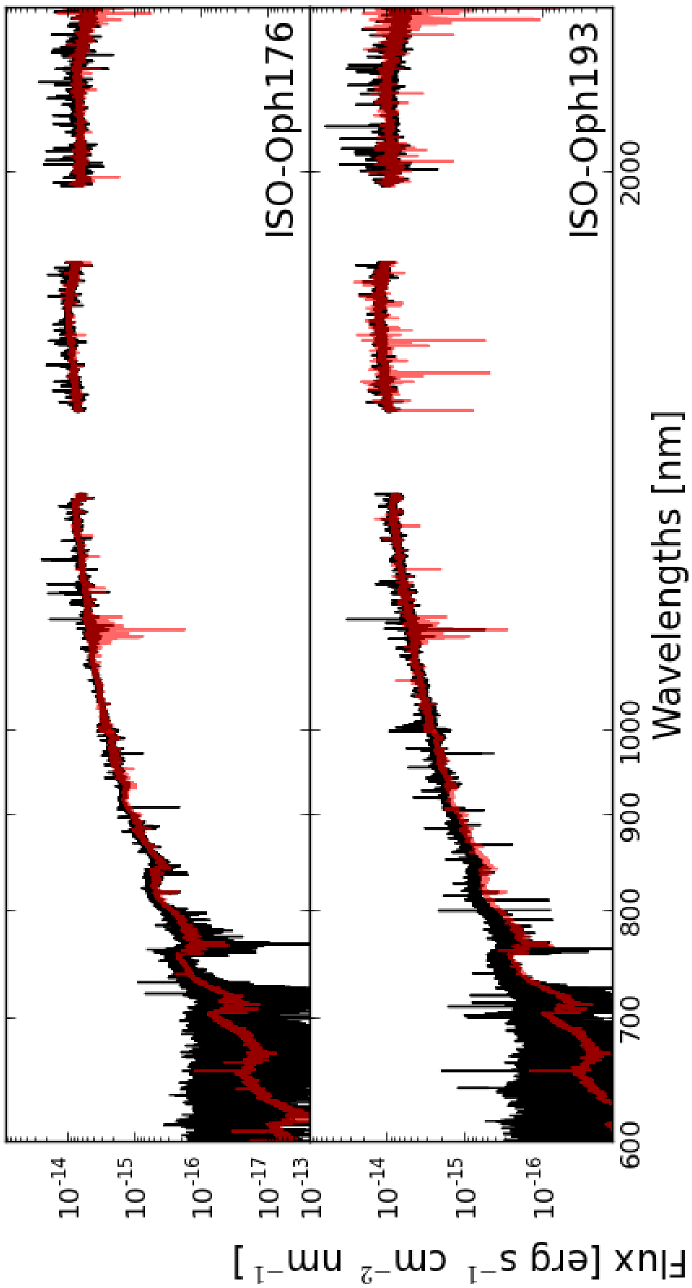

Figure 6.12: Spectra of ρ-Oph targets from 600 to 2450 nm. Same as Fig. 6.8.

Table 6.8: Accretion luminosity and mass accretion rates of the ρ-Oph Class II YSOs

Object	$\log L_{\rm acc}$ [L$_\odot$]	$\log \dot{M}_{\rm acc}$ [M$_\odot$/yr]	Detected lines [#]
ISO−Oph023	-3.76	-10.22	4
ISO−Oph030	-2.85	-9.34	6
ISO−Oph032	-3.82	-10.21	9
ISO−Oph033	-5.10	-11.38	1
ISO−Oph037	-1.78	-9.12	4
ISO−Oph072	-0.97	-8.33	8
ISO−Oph087	<-3.10	<-9.99	0
ISO−Oph094	-3.70	-11.33	1
ISO−Oph102	-2.71	-9.28	7
ISO−Oph115	-2.13	-9.50	2
ISO−Oph117	-2.56	-9.43	3
ISO−Oph123	-1.93	-8.97	11
ISO−Oph160	-3.24	-9.88	4
ISO−Oph164	-3.75	-10.30	8
ISO−Oph165	-3.00	-10.38	2
ISO−Oph176	-4.45	-11.04	1
ISO−Oph193	-2.75	-9.54	3

Notes. M_* and age are derived using the evolutionary tracks of Baraffe et al. (1998). The last column reports the number of detected emission lines in the spectra used to derive $L_{\rm acc}$.

6.4.3 Accretion properties of ρ-Ophiucus young stellar objects

The accretion luminosity for the ρ-Oph targets is derived using the luminosity of various emission lines present in their spectra. This is converted into $L_{\rm acc}$ using the $L_{\rm line}$-$L_{\rm acc}$ relations of Alcalá et al. (2014) and reported here in Eq. (6.1). As previously discussed, this indirect method is not as accurate as direct fitting of the UV-excess, but $L_{\rm acc}$ determined in this way are consistent with direct measurements of $L_{\rm acc}$ when multiple lines are used (e.g., Rigliaco et al., 2012; Alcalá et al., 2014). Given the high extinction and the low SNR of the UVB spectra of the targets, this is the only available method to determine $L_{\rm acc}$ for this sample.

Similarly to Sect. 6.2.3 and Alcalá et al. (2014), the flux of the emission lines is determined from the flux-calibrated and extinction-corrected spectra using the *splot* package under IRAF by direct integration of the line. The line flux is the average of three measurements of the integrated flux considering the lowest, highest, and the middle position of the local continuum, depending on the local noise level of the spectra. The error is the standard deviation of these three measurements. For non detected lines, I calculate the 3σ upper limits with the relationship $3 \times F_{\rm noise} \times \Delta\lambda$, where $F_{\rm noise}$ is the rms flux-noise in the region of the line and $\Delta\lambda$ is the expected average line width, assumed to be 0.2 nm. The luminosity of the lines is calculated as $L_{\rm line} = 4\pi d^2 \cdot f_{\rm line}$, where d is the distance of ρ-Oph (125 pc) and $f_{\rm line}$ the flux of the line determined as explained in this paragraph. The line luminosity is converted in $L_{\rm acc}$ with the relations of Eq. (6.1), and the final value of $L_{\rm acc}$ is determined as the average of the values of the detected lines, while the error is the standard

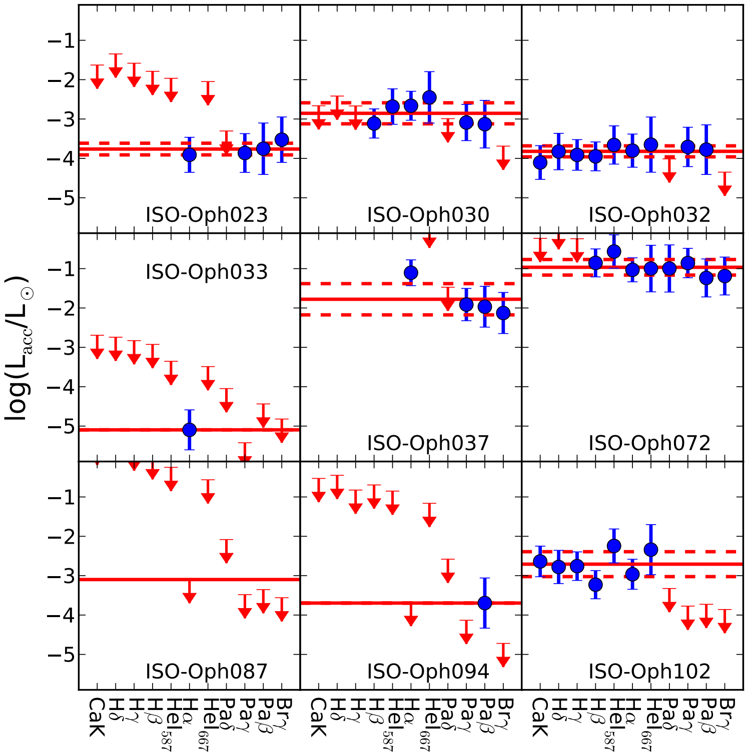

Figure 6.13: Accretion luminosity derived from various emission lines luminosity for the ρ-Oph targets. Each subplot shows the value of $\log(L_{\rm acc}/L_\odot)$ derived using the various indicators reported on the x-axis (CaK, Hδ, Hγ, Hβ, He$_{\lambda 587\rm nm}$, Hα, He$_{\lambda 667\rm nm}$, Paδ, Paγ, Paβ, Brγ). The red solid line is the average values obtained from the detected lines, while the dashed lines are the 1σ standard deviation of this value.

deviation of these values. Figures 6.13-6.14 show the value of $L_{\rm acc}$ determined with each line for all the targets. The accretion luminosity for the targets are reported in the second column of Table 6.8, while the number of detected emission lines used to calculate $L_{\rm acc}$ is available in the last column.

I use the value of $L_{\rm acc}$ determined using the emission lines as the final value also for ISO-Oph032 and ISO-Oph123, for which my fitting procedure could determine directly $L_{\rm acc}$ from the fit of the UVB spectrum. This choice is done to keep the results for the targets consistent. Moreover, the value of $L_{\rm acc}$ determined for ISO-Oph032 from the fitting procedure ($\log(L_{\rm acc}/L_\odot)$=-3.87) is compatible with that determined with the emission lines ($\log(L_{\rm acc}/L_\odot)$=-3.82). For ISO-Oph123, the value determined from the fit of the UV-excess ($\log(L_{\rm acc}/L_\odot)$=-1.22) is much higher than the one obtained from the luminosity of the emission lines ($\log(L_{\rm acc}/L_\odot)$=-1.93). However, as I discussed in the previous section, this difference could be due to the bad fit of the Balmer continuum and to an underestimation of the stellar luminosity with the fitting procedure.

In the spectrum of ISO-Oph087 there are no emission lines. Therefore it is not possible

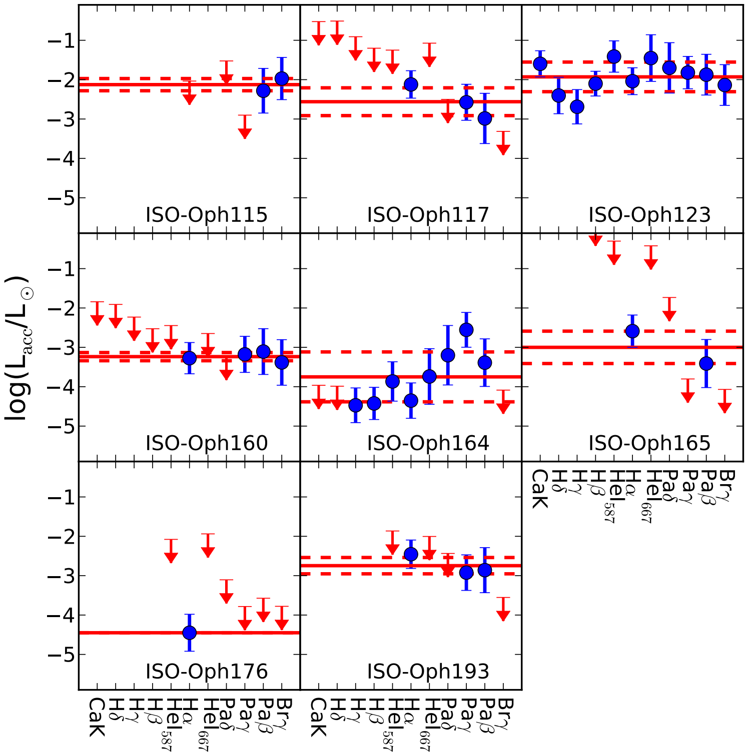

Figure 6.14: Accretion luminosity derived from various emission lines luminosity for the ρ-Oph targets. Same as Fig. 6.13.

to determine the accretion rate of this object. I estimate an upper limit on the accretion rate from the upper limit on the Hα line and use this value in the analysis.

From the values of $L_{\rm acc}$ and the stellar parameters $M_\star$ and $R_\star$ derived as in the previous section and reported in Table 6.7, I derive $\dot{M}_{\rm acc}$ using Eq. (1.2). This is reported for every object in the third column of Table 6.8. In Fig. 6.15 I show the values of $\dot{M}_{\rm acc}$ vs $M_\star$ derived here (*black points*) and those from Natta et al. (2004, 2006) and corrected for distance by Rigliaco et al. (2011a) (*gray points*). I also report the best fit of the $\dot{M}_{\rm acc}$-$M_\star$ relation for the Lupus targets derived by Alcalá et al. (2014) as a reference. The values derived here for the ρ-Oph sample are reported with *small filled circles* for targets with uncertain stellar parameters and with *open circles* for objects with strong veiling. In Fig. 6.16, instead, I show only the data for the targets in common, with *red crosses* reporting the values from the literature. With respect to the results of Natta et al. (2004, 2006), the values of $M_\star$ are different in many cases, and this is due to the more precise derivation of stellar parameters done here. In general, the values of $\dot{M}_{\rm acc}$ derived here are lower, and this could be due in part to the different $L_{\rm acc}$-$L_{\rm line}$ relations adopted here, and in part to the better derivation of the extinction. The values of $M_\star$ derived here are, instead, larger than those in the literature for many targets. However, the newly estimated values of $M_\star$ are compatible with those

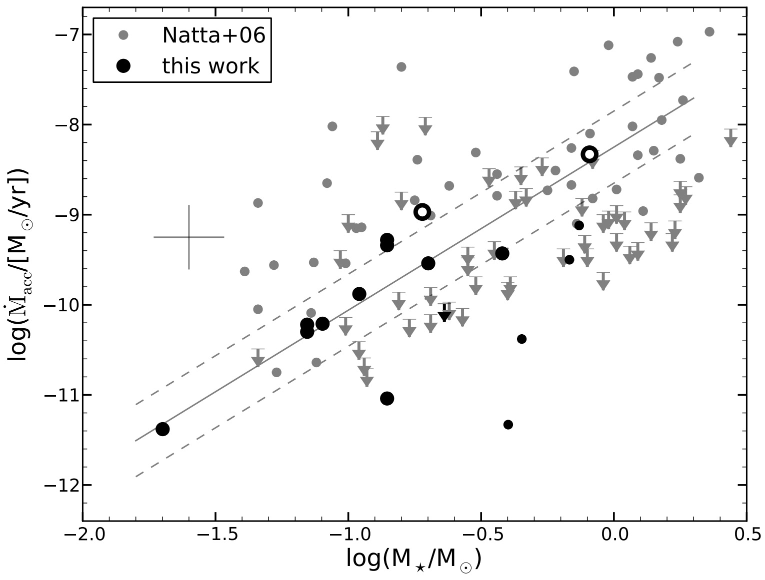

Figure 6.15: Mass accretion rate as a function of mass for the ρ-Oph sample. Values derived for the objects analyzed here are reported with *black* markers, where *big filled circles* are used for objects with reliable stellar properties estimates, *small filled circles* for those with uncertain stellar parameters, and *open circles* for targets with strong veiling. Values from the literature for ρ-Oph (Natta et al., 2004, 2006, corrected for distance as in Rigliaco et al. 2011a) are shown with gray symbols. Downward arrows are used for upper limits. The continuous line represents the linear fit of this relation for the Lupus sample (see Equation 6.3). The dashed lines represent the $1\,\sigma$ deviation from the fit. Average error bars are shown in the upper left corner.

of Natta et al. (2004, 2006) for the vast majority of objects with reliable stellar parameters estimate derived in my analysis. The largest differences are found for objects with highly uncertain SpT, as expected. In one case, ISO-Oph176, the spectrum analyzed here present a detected emission line (Hα) and I am able to measure a value of $\dot{M}_{\rm acc}$ lower than the upper limit reported by Natta et al. (2004, 2006). This object, however, has a value of $\dot{M}_{\rm acc}$ significantly lower than the one expected by the $\dot{M}_{\rm acc}$-$M_\star$ relation of Lupus for objects with the same mass. This measurement is probably strongly affected by chromospheric emission contribution in the line luminosity and thus uncertain, as the value of $L_{\rm acc}$ is compatible to the value of $L_{\rm acc,noise}$ determined in Chapter 3 from the luminosity of the emission lines of Class III YSOs. However, this object could also possibly be a low-accreting object with a significantly gas-depleted disk. On the other hand, I do not detect any line in the spectrum of ISO-Oph087, for which Natta et al. (2004, 2006) report a value of $L_{\rm acc}$ from the measurement of the Paβ line. One possibility is that this object is variable, and the large difference in the value could be in part due to variability and in part to the low luminosity derived here for this target.

Interestingly, the newly derived values of $\dot{M}_{\rm acc}$ are compatible on the $\dot{M}_{\rm acc}$-$M_\star$ plane with the best fit relation of the Lupus sample at least for nine of the ten spectra with good

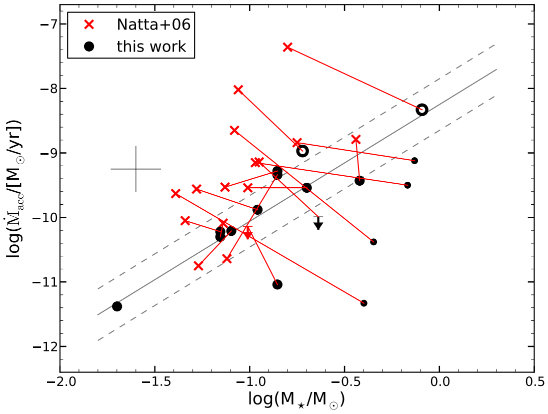

Figure 6.16: Comparison of mass accretion rate as a function of mass for the ρ-Oph sample with the literature data. Values from the literature for ρ-Oph (Natta et al., 2004, 2006, corrected for distance as in Rigliaco et al. 2011a) for the targets analyzed here are shown with *red crosses*. The red lines connect these values with those derived here for the same targets. The other symbols are as in Fig. 6.15.

SNR and not strong veiling and for the two strongly veiled ones. In particular, the spread of values on this plot at any mass decreases with respect to the one of the same objects with the values derived by Natta et al. (2004, 2006). The five objects with uncertain stellar parameters (four small black circles and one black upper limit) are all located below the 1σ deviation from the best-fit line. However, given the uncertainties on their stellar parameters, the values of $\dot{M}_{\rm acc}$ derived for these targets are probably not accurate, and possibly underestimated, given that their $L_\star$ are probably underestimated, as well.

The smaller spread of $\dot{M}_{\rm acc}$ at any $M_\star$ found with the new X-Shooter spectra and the analysis described in this section suggest that most of the spread observed in the past was due to the methodology used. In particular, in the case of ρ-Oph the uncertain stellar parameter and the possibility to use only one or two emission lines to derive $L_{\rm acc}$ was a severe limitation of previous investigations. However, the small sample analyzed in this section does not allow to make final statements on this. I refer to Sect. 6.6 for a more detailed discussion including all the samples analyzed in this Chapter and in this Thesis.

6.5 New data in the Upper Scorpius association

The Scorpius-Centaurus or Sco OB2 association is the OB association located closer to the Sun. It is divided in three distinct groups with different ages: Upper Scorpius (US), Upper Centaurus-Lupus (UCL), and Lower Centaurus-Crux (LCC). Their ages are estimated to be of about 5, 17, and 16 Myr (Preibisch & Mamajek, 2008). In the whole Sco OB2 association there is no sign of ongoing star formation, thus this is an ideal region to study properties of protoplanetary disks after the completion of the star formation process. Strictly related to this, there is almost no gas and dust clouds in the region, so the members show only very

Table 6.9: YSOs in the Upper Scorpius association analyzed here: coordinates and observing log

Object	RA(2000) h :m :s	DEC(2000) ° ' ''	Obs. date YY-MM-DD	Exp. Time [s]
J160525.5-203539	16:05:25.5	−20:35:39	2010-09-17	750x2
J160702.1-201938	16:07:02.1	−20:19:38	2010-09-18	750x4
J161420.2-190648	16:14:20.2	−19:06:48	2010-09-19	400x4

Notes. Names are from Preibisch et al. (2002). Exposure times are the same in the three X-Shooter arms (UVB, VIS, and NIR).

moderate extinction, typically $A_V \lesssim 2$ mag. This gas and dust free environment is possibly the consequence of several supernova explosions and massive stars winds, that cleared the region from diffuse matter. The evolution of these massive stars also created a huge system of loop-like H I structures around the association, with a total mass of about $3 \times 10^5 M_\odot$. These loops are thought to be the remnants of the original giant molecular cloud in which the OB subgroups formed (e.g., de Geus, 1992; Preibisch & Mamajek, 2008).

The younger subgroup, and object of study here, is Upper Scorpius (RA 16h DEC -21d), which is located at a distance of ~145 pc (Blaauw, 1991; de Geus et al., 1989; Preibisch et al., 1999; de Zeeuw et al., 1999). The age of this region has been determined to be ~5-6 Myr by de Geus et al. (1989) using the main sequence turnoff in the HRD for the B-type stars of this subgroup. The total population of PMS members of this association has been discussed in Preibisch et al. (2002) and Preibisch & Mamajek (2008) and comprises 364 members. Preibisch et al. (2002) have shown that, using D'Antona & Mazzitelli (1994) models, the whole population of this region, from low-mass stars to high-mass stars, is located on the HRD around the 5 Myr isochrone with an observational dispersion of 1-2 Myr. In the Upper Scorpius association only ~19% of the whole sample of PMS stars are still surrounded by protoplanetary disks (Carpenter et al., 2006), as one would expect given the age of the region and the known disk dispersal timescale (see Sect. 1.1). Finally, 20 disks in this region have been recently observed with ALMA to determine their masses (Carpenter et al., 2014). The average disk mass in this region has been found to be lower than in younger regions such as Taurus, even though the significance of this result is below 3σ.

Here I present for the first time the analysis of the X-Shooter spectra of three objects located in the Upper Scorpius association and still surrounded by a protoplanetary disk. These have been observed during Pr.Id.085.C-0482 (PI Montesinos) using the 1.0″, 1.2″, and 0.9″slits in the UVB, VIS, and NIR arms, respectively. The coordinates, date of observation, and exposure times are reported in Table 6.9.

Data reduction has been carried out using the same procedure as in the rest of the Thesis. The flux calibration of the pipeline has been found to underestimate systematically the flux of the targets obtained from the available photometry by a factor ~2. This could be due to the bad seeing of the three nights of the observations (~2-2.5″). Therefore, the flux-calibrated spectra reduced using the pipeline have been multiplied by a factor 2 in all

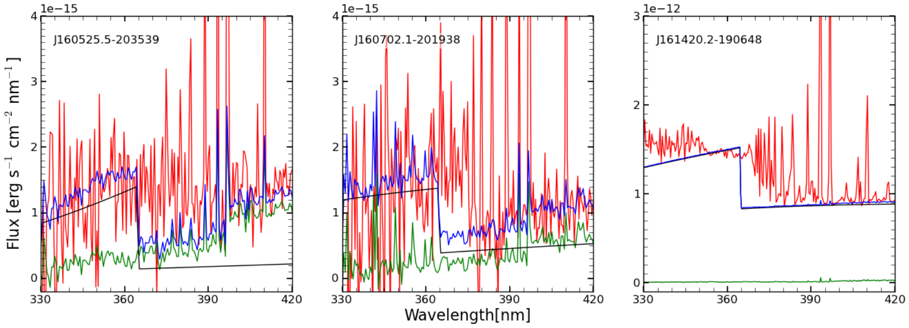

Figure 6.17: Best fit of the UV-excess for the targets located in Upper Scorpius.

Table 6.10: Stellar and accretion parameters for the Upper Scorpius YSOs

Object	SpT	T$_{\rm eff}$ [K]	A_V [mag]	$L_\star$ [$L_\odot$]	$M_\star$ [$M_\odot$]	age [Myr]	$L_{\rm acc}$ [$L_\odot$]	$\dot{M}_{\rm acc}$ [$M_\odot$/yr]
J160525.5-203539	M5	3125	0.9	0.05	0.16	3.63	2.16e-04	4.20e-11
J160702.1-201938	M5.5	3060	1.2	0.03	0.11	3.59	4.13e-04	9.60e-11
J161420.2-190648	K7	4060	3.0	0.12	0.68	62.37	4.13e-01	1.69e-08

Notes. $M_\star$ and age are determined using the Baraffe et al. (1998) evolutionary tracks.

cases.

The three spectra are analyzed using the method described in Chapter 4 assuming $R_V = 3.1$. In the case of J160525.5-203539 and J160702.1-201938 a good fit is found (see Fig. 6.17) and the best fit parameters, which are reported in Table 6.10, are compatible with those derived in the literature (Preibisch et al., 2002). On the opposite, the best fit for J161420.2-190648, shown in Fig. 6.17 as well, does not reproduce the Balmer continuum well and results in a significantly underestimated $L_\star$, thus in a very old age, for this target. Similarly to the Class II YSO ISO-Oph123 discussed in the previous section, also this target has a spectrum with many emission lines that make it more difficult to estimate accurately the value of the continuum in the spectrum. For the time being, I adopt the stellar parameters of the best fit in the analysis but I stress that these are uncertain. I refer to Montesinos et al. (in prep.) for a more detailed analysis of this target.

I refer to the next section for a discussion on the values of the accretion rates derived here, as the sample available in this region is too small to be discussed on its own.

6.6 Discussion

As reported in Table 6.1, in this Thesis I have collected stellar and accretion properties for a total of 88 accreting YSOs, including objects in different star forming regions and in two different evolutionary states, i.e. Class II YSOs and transitional objects. All these objects have been observed with X-Shooter and analyzed using the procedure explained in Chapter 4, or with similar procedures (e.g., Sect. 6.4). This sample is therefore homogeneous in the analysis method, and thus there should be no systematic differences in the subsamples due to different methods. In particular, the targeted objects have different stellar properties, covering a wide range of $L_\star$, $M_\star$, and age, and different accretion properties ($L_{\rm acc}$, $\dot{M}_{\rm acc}$). In this section I discuss the dependence of accretion on the stellar properties to derive general properties of the accretion process and of the inner disk properties. As noted above, I include in the sample analyzed here both Class II YSOs, thus PMS objects still surrounded by full disks, and the TDs analyzed in Chapter 5. The latter are known to be a different evolutionary stage of disk evolution, but, at least for the sample analyzed in this Thesis, I have shown that the gas content of the innermost region of the disk, which is related to the accretion rate, is the same in these objects as in Class II. Moreover, for some objects considered here as Class II the classification as TD or Class II is still under debate, thus it could be possible that some objects in the sample have different outer disk properties than it is thought. Therefore, I consider all the objects altogether stressing that I am analyzing the properties of the inner disk, and not of the outer disk, for the entire sample[6].

The sample analyzed here is, I stress, homogeneously analyzed but is not complete. Each of the subsamples does not represent the entire population of its region, and the vast majority of targets included here were known accretors. This possibly makes the sample, in general, biased towards higher accretion rate objects. Nevertheless, this sample is a good ensemble to study the general properties of accreting YSOs, as it is representative of these objects by various means. Indeed, it contains PMS stars covering a large stellar parameter space, i.e. with SpT ranging from M9 to G3, $L_\star$ from $\sim 1 L_\odot$ to $\sim 10^{-3} L_\odot$, $M_\star$ from $\sim 2 M_\odot$ to $\sim 0.01 M_\odot$, and located in regions with age from $\sim$ 1 Myr to $\sim$ 10 Myr. However, incompleteness could affect some of the results I will derive, and I will discuss this in detail in each of the following subsections.

6.6.1 Accretion luminosity and stellar luminosity relation

The stellar and accretion parameters derived more independently on evolutionary models are $L_\star$ and $L_{\rm acc}$. The former is determined from the derived parameters (SpT, A_V), from the absolute flux calibration of the spectrum (or from photometry), and from the knowledge of the distance of the target. The latter is obtained measuring the flux due to accretion in excess to the photosphere plus a bolometric correction to account for the not observed flux in the UV part of the spectrum (see Chapters 2 and 4), or converting the flux of various emission lines into $L_{\rm acc}$ using calibrated relations (see Sect. 6.2.3). Neither is based on models of PMS stellar evolution, thus these quantities can be considered as ``purely observational''. For these reasons, it is interesting to analyze the observed relation between those. This is shown in Fig. 6.18, where the accreting objects from the various samples are shown with different symbols (cf. legend in the plot and caption). The dashed lines on the plot represent different $L_{\rm acc}/L_\star$ ratios, going downwards from 1, to 0.1, to 0.01. The *gray*

---

[6] The only object present in different samples is Sz84, a TD located in Lupus. For this target I use in the following analysis only the results obtained in Chapter 5, which do not differ substantially from those derived as in Sect. 6.2.

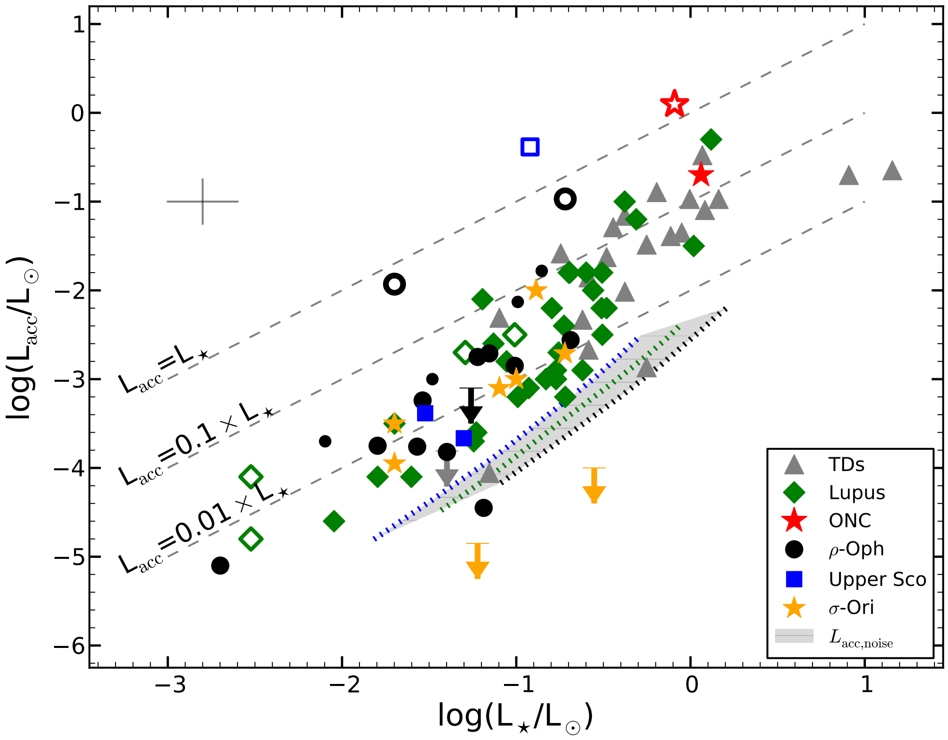

Figure 6.18: Accretion luminosity vs stellar luminosity for the whole sample. Data from the different samples are reported with various symbols as in the legend. Upper limits are shown as downward arrows. Green empty diamonds represent the Lupus sub-luminous objects. The red empty star, black empty circles, and the blue empty square are the targets with strong veiling. The small black circles represent the targets in ρ-Oph with highly uncertain stellar properties. The gray shaded region shows the values of $L_{\rm acc,noise}$ derived using Class III YSOs line luminosities in Chapter 3, and is shown here as a reference. The three dotted lines are the values of $L_{\rm acc,noise}$ at 10 Myr (blue), 3 Myr (green), and 1 Myr (black), respectively. On the upper left side the typical errors on the two quantities are shown. Finally, the dashed lines are for different $L_{\rm acc}/L_{\star}$ ratios, going downwards from 1, to 0.1, to 0.01, as labeled.

shaded region shows the values of $L_{\rm acc,noise}$ derived using Class III YSOs line luminosities in Chapter 3, and is shown here as a reference. The three dashed lines on that region are then the values of $L_{\rm acc,noise}$ at 10 Myr (blue), 3 Myr (green), and 1 Myr (black), respectively.

Most of the targets ($\sim$50%) lie on the log$L_{\rm acc}$-log$L_{\star}$ plane between the $L_{\rm acc}/L_{\star}$= 0.1 and $L_{\rm acc}/L_{\star}$= 0.01 lines, while only the 4 strongly veiled targets lie close to the $L_{\rm acc}/L_{\star}$=1 line. All the Class III YSOs are located below the $L_{\rm acc}/L_{\star}$= 0.01, where also several accreting objects ($\sim$30%) are found. Previous studies (e.g., Natta et al., 2006; Clarke & Pringle, 2006; Rigliaco et al., 2011a; Manara et al., 2012) on (almost) complete samples of Class II YSOs in different star forming regions have shown a correlation, although with a large scatter, of $L_{\rm acc}$ with $L_{\star}$. The results reported here are similar to those found in the literature regarding the observed upper boundary at $L_{\rm acc}$$\sim$$L_{\star}$, and about the fact that most of the targets happen to have $L_{\rm acc}/L_{\star}$ ratios between 0.1 and 0.01. With respect to previous works, such as Natta et al. (2006) or Manara et al. (2012), I find a smaller spread of values of $L_{\rm acc}$ at any $L_\star$, which could in part be due to incompleteness of my sample, but is mostly a consequence of the more robust methodology used in this Thesis. It is also evident from Fig. 6.18 that the distribution of targets on the log$L_{\rm acc}$-log$L_\star$ plane has a slope larger than 1, i.e. not parallel to the dashed lines. I compute the linear best fit relation using all the accreting objects (i.e. excluding the Class III YSOs) and including upper limits using the ASURV package (Feigelson & Nelson, 1985) under the IRAF environment[7] and I derive a slope of 1.5±0.1 with a standard deviation of 0.6 excluding the four sub-luminous objects in the Lupus sample, the five highly uncertain ones in the ρ-Oph sample, for which $L_\star$ is unreliable, and the four strongly veiled Class II YSOs. This relation is, however, dominated by the two targets with $L_\star \gtrsim L_\odot$ (LkHα330 and SR21) and by ISO-Oph033, the only point at $L_\star < 0.009 L_\odot$. If I exclude also these three points I obtain $L_{\rm acc} \propto {L_\star}^{1.7\pm0.1}$ and the same standard deviation as before. The same result is found when excluding only the two targets with $L_\star \gtrsim L_\odot$, as well. This value is in agreement with what found for the sole Lupus sample (Alcalá et al., 2014) and for the complete sample in the ONC of Manara et al. (2012). Also a non-parametric fit of the log$L_{\rm acc}$-log$L_\star$ data leads to a best fit which is compatible with the linear fit both in the slope and in the shape.

It is interesting to note that $L_{\rm acc,noise}$ derived for the Class III YSOs in Chapter 3 is located on the $L_{\rm acc}$-$L_\star$ plane right at the lower boundary of my targets. Only five objects have measurements in or below this chromospheric threshold. For four of the five, however, $L_{\rm acc}$ is measured from the UV-excess, while for ISO-Oph176 this is derived from the Hα line luminosity alone. This suggests that $L_{\rm acc}$ for this object is highly uncertain, as this measurement could be significantly contaminated by chromospheric contribution in the line. The upper boundary of the $L_{\rm acc}$-$L_\star$ relation seen here, instead, seems to be a real feature and not an observational bias. Indeed, I expect my sample to be incomplete of low accreting objects, rather than of strong accretors. Moreover, contrary to Natta et al. (2006), most of the ρ-Oph targets in common between their and my sample and with $L_\star \lesssim 0.1 L_\odot$ are not found here to have values of $L_{\rm acc}$>0.1$L_\odot$. Similar to Fig. 6.15, the targets in common are now found to be consistent with those in the other regions, i.e. to follow the $L_{\rm acc} \propto {L_\star}^{1.7}$ slope. This suggest that the objects found in the past with high $L_{\rm acc}$ at low $L_\star$ were misclassified, i.e. $L_{\rm acc}$ was probably overestimated, or $L_\star$ underestimated, and this caused a larger spread of values o $L_{\rm acc}$ at low $L_\star$. Thus, I believe that the upper boundary of the $L_{\rm acc}$-$L_\star$ relation present in Fig. 6.18 is real.

Starting from these observational conclusions more theoretical work should be carried out to understand the $L_{\rm acc}$-$L_\star$ relation. So far, the only study of this relation has been carried out by Tilling et al. (2008) using simplified PMS stellar evolution models. They derived a slope of 1.7 for this relation, assuming $\dot{M}_{\rm acc}$ to decrease with time with an exponent 1.5, and using the evolutionary models of D'Antona & Mazzitelli (1994) in the analysis. Tilling et al. (2008) also suggest that unpopulated regions on the $L_{\rm acc}$-$L_\star$ plane could be used to constrain disk models directly from this purely observational relation. This is what I

---

[7] All the linear fits done with ASURV in this chapter are obtained using the **emmethod** task. Results from this task and from the task **buckleyjames** are compatible. Other tasks, such as **schmittbin**, are not used as they have many drawbacks (cf. IRAF user manual) and the sample analyzed here comprises censored data only on one variable.

find in the upper envelope of my data. However, their simplified evolutionary model cannot describe the region in the plane at $L_\star$<$0.1 L_\odot$, so more detailed PMS stellar evolution calculations are needed to explain my findings.

6.6.2 Accretion as a function of stellar mass

As discussed in Sect. 1.4.1 and 6.2.4 of this Thesis, various previous works (Muzerolle et al., 2003; Mohanty et al., 2005; Natta et al., 2006; Herczeg & Hillenbrand, 2008; Rigliaco et al., 2011a; Antoniucci et al., 2011; Biazzo et al., 2012; Manara et al., 2012, and references therein) studied the $\dot{M}_{\rm acc}$-$M_\star$ relation in different samples of accreting YSOs and found that $\dot{M}_{\rm acc} \propto M_\star{}^2$, but with a significant scatter (up to 3 dex) in $\dot{M}_{\rm acc}$ at any given $M_\star$. In Sect. 6.2.4, in particular, I showed that the dependence of $\dot{M}_{\rm acc}$ with $M_\star$ is confirmed from the data I analyze here using the Lupus sample alone. The slope obtained using these objects is $\dot{M}_{\rm acc} \propto M_\star{}^{1.8}$, and this relation is found to have a significantly smaller scatter of the data around the best fit, with a standard deviation of 0.4 dex. In Fig. 6.19 I show the values of log$\dot{M}_{\rm acc}$ vs log$\dot{M}_{\rm acc}$ for the whole sample of accreting objects analyzed here (cf. caption and legend for explanation of the symbols). With respect to the Lupus sample (Fig. 6.4) the scatter of values of $\dot{M}_{\rm acc}$ at any $M_\star$ is not substantially increased. In particular, there are no objects significantly above the $\dot{M}_{\rm acc}$-$M_\star$ locus of the Lupus Class II YSOs, and this suggests that the upper boundary of this relation is constrained by the data shown here. This could be the case as this sample is composed mostly by known accretors, thus it is most probably missing objects in the lower part of the $\dot{M}_{\rm acc}$-$M_\star$ relation, rather than in the upper envelope. On the other side, various objects seem to have values of $\dot{M}_{\rm acc}$ at their $M_\star$ lower than the Lupus targets, and even as low as the sub-luminous objects in Lupus. However, also in this case this does not change substantially the spread of values.

Considering the whole sample and linearly fitting the points with ASURV, the standard deviation around the linear fit with slope 1.7±0.2 is of 0.7. This becomes smaller (0.6) while leaving unaltered the slope when excluding sub-luminous Lupus targets and highly uncertain ρ-Oph YSOs. The latter is the best fit relation reported in Fig. 6.19, whose analytic form is:

$$\log \dot{M}_{\rm acc} = 1.71(\pm 0.16) \cdot \log M_\star - 8.45(\pm 0.11). \qquad (6.5)$$

Different slopes, but always compatible within the uncertainty, are found when excluding the veiled objects or the two higher mass stars (slope~1.6). The exact value of the slope, however, is uncertain and depends on many parameters. In particular, the choice of the evolutionary model used to derive $M_\star$ is crucial, as this can lead to different slopes, and even to different spread of values. Here I have been using one evolutionary model (Baraffe et al., 1998) for all the subsamples, in order to have results compatible among each other, but the exact values of the slope reported here depend strongly on the choice of this particular model. Also for the $\dot{M}_{\rm acc}$-$M_\star$ fit a non-parametric analysis leads to a best fit compatible with a linear one. However, the slope derived here is compatible with those derived in the past (e.g., Natta et al., 2006; Rigliaco et al., 2011a; Manara et al., 2012; Biazzo et al., 2012; Alcalá et al., 2014), apart from that derived by Fang et al. (2009) ($\dot{M}_{\rm acc} \propto M_\star{}^3$). The

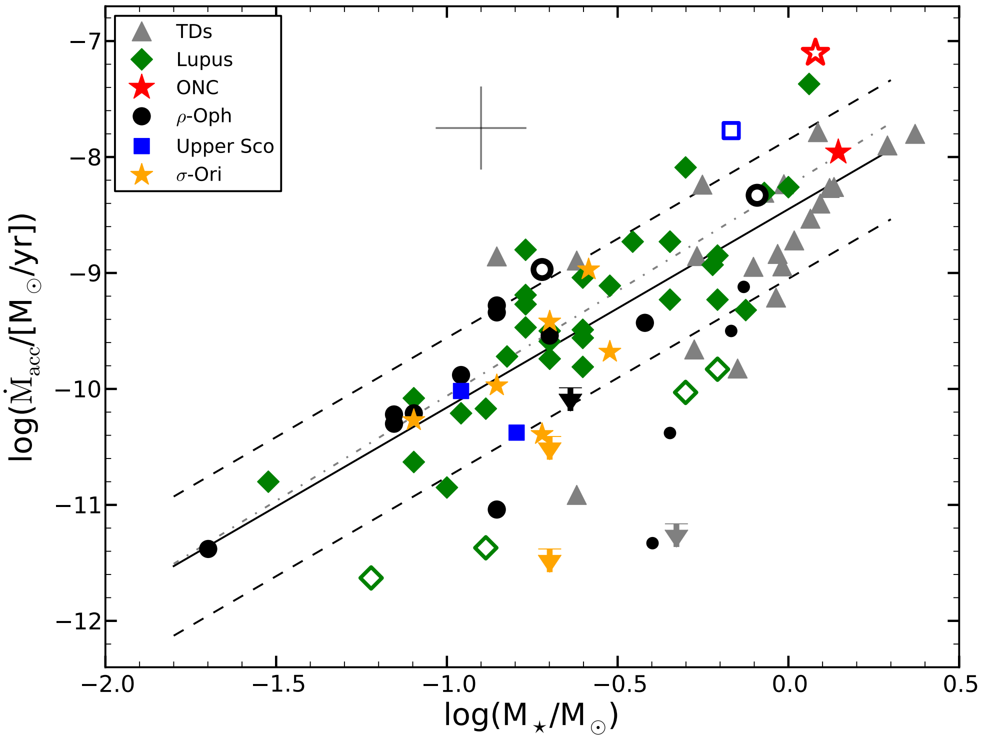

Figure 6.19: Mass accretion rate as a function of mass for the whole sample. Symbols are as in Fig. 6.18. The solid line is the linear fit obtained excluding only the sub-luminous and highly uncertain targets, and the dashed lines represent the 1σ deviation from the fit. The black dot-dashed line is the best fit for the Lupus sample by Alcalá et al. (2014). Typical error bars are shown in the upper part of the plot.

difference with the latter is to be ascribed to the different evolutionary model and analysis method used in that work.

The slightly larger spread of values of $\dot{M}_{\rm acc}$ around the best fit in the whole sample with respect to the Lupus one could be explained as an effect of age, as here I include also younger and older objects, or to a difference in the intrinsic properties of the various regions. This cannot be determined with this sample, as effects of incompleteness could modify the results. However, the fact that the spread in the whole sample remains significantly smaller than in previous investigation suggests that the methodology used in previous analyses was one of the main reasons for the observed scatter of values. Indeed, even studies carried out using broad-band spectroscopy including the observation and modeling of the UV-excess in the past (e.g., Herczeg & Hillenbrand, 2008) were affected by uncertainties due to the non-simultaneous observations at different wavelengths and to the low resolution of the spectra. This, as also discussed by Herczeg & Hillenbrand (2014), could lead to an erroneously estimate of the SpT, A_V, and veiling of the targets. All these will result in a larger scatter in the observed $\dot{M}_{\rm acc}$ at any given $M_\star$.

In Fig. 6.20 I report the values of $\dot{M}_{\rm acc}$ and $M_\star$ for the whole sample as in Fig. 6.19,

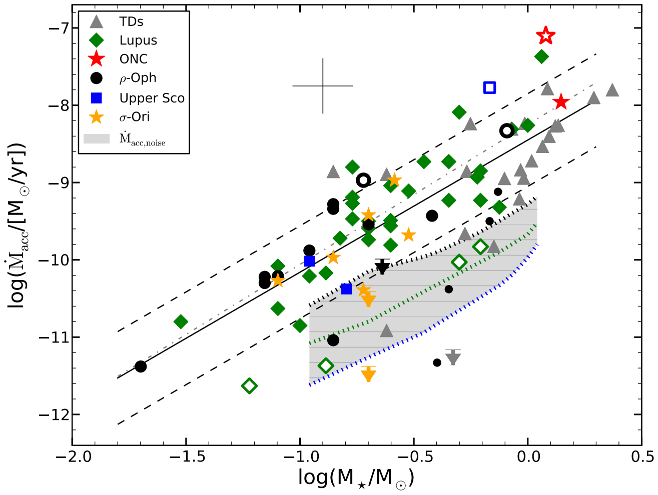

Figure 6.20: Mass accretion rate as a function of mass for the whole sample. Symbols are as in Fig. 6.18 and Fig. 6.19. The gray shaded region shows the values of $\dot{M}_{\rm acc,noise}$ derived using Class III YSOs line luminosities in Chapter 3, and is shown here as a reference. The three dotted lines are the values of $L_{\rm acc,noise}$ at 1 Myr (black), 3 Myr (green), and 10 Myr (blue), respectively.

but I also show as a reference the values of $\dot{M}_{\rm acc,noise}$ derived in Chapter 3 as a gray shaded area. This is located right at the bottom of the distribution of most of the targets on the $\dot{M}_{\rm acc}$-$M_\star$ plane. Most of the targets which are in this region happen to be sub-luminous or highly uncertain ones. In any case, among the targets analyzed here only those located in the ρ-Oph cluster have $L_{\rm acc}$ measured from line emission. Apart from the two highly uncertain values, only ISO-Oph176 is located in a region of the plane which suggests that its measured accretion is strongly contaminated from chromospheric emission, as discussed previously.

The analysis carried out here shows that the scatter of $\dot{M}_{\rm acc}$ at any $M_\star$ is significantly reduced using the method described in this Thesis. If this relation is due to the initial conditions at disk formation (e.g., Dullemond et al., 2006), then this would imply that the spread of initial core rotation rates is small, as well. Then, I have derived a slope of this relation which is clearly not 1 and is smaller than 2. When comparing with models predicting that the $\dot{M}_{\rm acc}$-$M_\star$ relation is driven by photoevaporation, my data are in agreement with the proposed slope of Ercolano et al. (2014) obtained using X-ray photoevaporation, and not with that of Clarke & Pringle (2006) derived from EUV photoevaporation. As discussed early on when considering the Lupus sample alone, there is in the data analyzed here no evidence of the double power-law behavior suggested by Vorobyov & Basu (2009), and the apparent bi-modality of past data could be ascribed to mixing $\dot{M}_{\rm acc}$ determined with different methods and evolutionary models. Finally, the upper envelope of my measurements has a slope similar to the bulk of the population and larger than 1, contrary to the prediction of Hartmann et al. (2006), which describes the $\dot{M}_{\rm acc}$-$M_\star$ relation as a consequence of layered disk accretion. A more complete view of this relation will be available when applying my method to larger and complete samples of data.

6.6.3 Accretion as a function of age

In Sect. 1.3.1 I have discussed how the evolution of $\dot{M}_{\rm acc}$ with the age of the central object is important to put constraints on the properties of the protoplanetary disk. However, from an observational point of view the measurement of the $\dot{M}_{\rm acc}$-age relation is problematic.

As I discussed in this Thesis, estimates of $\dot{M}_{\rm acc}$ in PMS stars are not trivial and are affected by various uncertainties. However, I have also shown how the methodology developed here lead to reliable derivations of $\dot{M}_{\rm acc}$, and how the sample discussed here is a good sample to study properties of accretion.

On the other hand, determining the exact ages of the targets is not possible at present days with the precision needed to study the $\dot{M}_{\rm acc}$-age relation (e.g., Soderblom et al., 2014). Indeed, ages are determined from comparison of the derived position of PMS stars on the HRD with theoretical PMS evolutionary models (e.g., Baraffe et al., 1998; D'Antona & Mazzitelli, 1994; Palla & Stahler, 1999; Siess et al., 2000). These models are simplified, for example they do not include different accretion histories of the targets, and lead to systematically different values of ages one with respect to the others. This effect is smaller in the estimated $M_\star$, which are then more reliable, and this lead to privilege the study of the $\dot{M}_{\rm acc}$-$M_\star$ relation in accreting YSOs over the $\dot{M}_{\rm acc}$-age one. Moreover, as I also discuss in this chapter (e.g., Sect. 6.4.2 and Sect. 6.5) and in Chapter 4, uncertainties in the stellar parameters can lead to estimated positions on the HRD corresponding to extremely old isochronal ages which are, in fact, unrealistic. Even placing the objects correctly on the HRD, the intrinsic uncertainties on $L_\star$ and $T_{\rm eff}$ (thus on $M_\star$ and age) generate correlated uncertainties on the $\dot{M}_{\rm acc}$-age plane that lead to significantly underestimate (i.e. by a factor $\sim$3) the slope of the decay of $\dot{M}_{\rm acc}$ with age (Da Rio et al., 2014).

As estimates of the age of each YSO independent on the evolutionary models are not possible, here I make the choice to assume all the targets in each region to be coeval, therefore I assume the mean age of the cluster as the age of each object. Discussion has been ongoing since many years whether star forming regions are really coeval, and no final answer has been found yet, mainly due to the large uncertainties in the age estimates discussed also here. It is plausible that a real age spread of $\sim$1-2 Myr is present in each region (e.g., Reggiani et al., 2011; Da Rio et al., 2014; Soderblom et al., 2014), but the choice of using the mean assumed age appear to be the more reasonable given the uncertainties on the individual isochronal ages. However, I will not attempt to fit the distribution of objects on the $\dot{M}_{\rm acc}$-age plane but only to show some general properties.

The values of $\dot{M}_{\rm acc}$ vs age are shown in Fig. 6.21 for all the objects in my sample (cf. legend and caption for explanation of the symbols). As explained above, the mean age of each region is used to plot the targets here. No clear relation between the two quantities is evident in this plot, and I do not attempt to fit the points here. A similar scattered plot is found when plotting the isochronal ages instead of the mean age of the cluster. However, a possible explanation for the large scatter is that I am plotting objects with very different

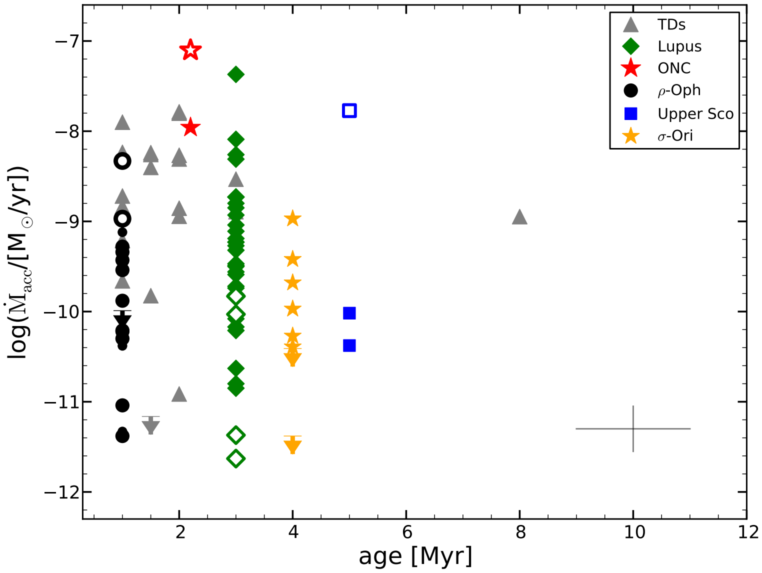

Figure 6.21: Mass accretion rate as a function of age for the whole sample. The mean age of the region in which the targets are located is used. Symbols are as in Fig. 6.18. Typical uncertainties on the two quantities are shown in the lower right corner.

$M_\star$. As I discussed in the previous section, $\dot{M}_{\rm acc}$ varies steeply with $M_\star$, and in my sample the values of $\dot{M}_{\rm acc}$ are spread over ∼4 dex from one side to the other of the $\dot{M}_{\rm acc}$-$M_\star$ plane (cf. Fig. 6.19). In the following, I first consider two subsamples comprising objects in smaller stellar mass ranges to show the typical set of parameters that should be explored to reproduce the observations through viscous evolution models, then I analyze the whole sample normalizing the values of $\dot{M}_{\rm acc}$ for the known dependence on $M_\star$ (see Sect. 6.6.2) as done by, e.g., Caratti o Garatti et al. (2012).

The two mass bins I consider here are that in the range of $M_\star$ from 0.1 $M_\odot$ to 0.3 $M_\odot$, and the one with $M_\star$ ranging from 0.5 $M_\odot$ to 1.0 $M_\odot$. These are chosen to have a narrow mass range but with enough targets in different star forming regions to sample enough stellar ages. The $\dot{M}_{\rm acc}$-age relation for these two subsamples is shown in Fig. 6.22. As expected, the spread of values of $\dot{M}_{\rm acc}$ at any age is significantly reduced when considering the two subsamples with respect to the total sample. Also in this case, however, I do not attempt to fit the data, as the uncertainties on the age would make the results unreliable. Instead, I try to find under which disk physical conditions the position of the data on these $\dot{M}_{\rm acc}$-age plots could be represented using the similarity solution obtained assuming a viscous disk. As I discussed in Sect. 1.3.1, Hartmann (2009) derived simple expressions to describe the evolution of accreting YSOs under the assumption of similarity solution and of a dependence of the the disk viscosity (ν) to the disk radius (R) as $\nu \propto R$, which implies that $\dot{M}_{\rm acc} \propto t^{-1.5}$. In particular, the evolution of $\dot{M}_{\rm acc}$ with age under the assumptions discussed in the aforementioned section is expressed using Eq. (1.23) and calculating $\dot{M}(R)$

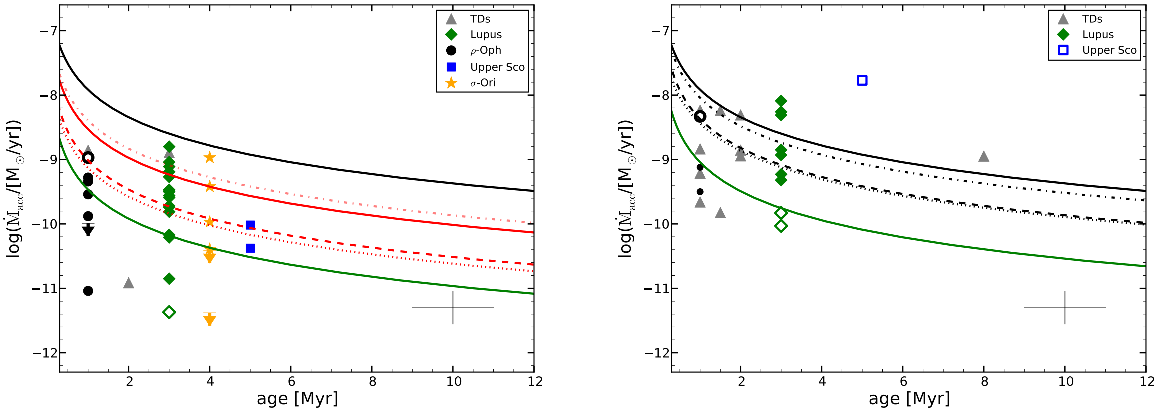

(a) 0.1 $M_\odot \leq M_\star \leq$ 0.3 $M_\odot$

(b) 0.5 $M_\odot \leq M_\star \leq$ 1.0 $M_\odot$

Figure 6.22: Mass accretion rate as a function of age for two subsamples with a smaller stellar mass range. The mean age of the region in which the targets are located is used. Symbols are as in Fig. 6.18. The range of masses are reported in the caption of each plot. In both panels the *black solid line* is the similarity solution model obtained using the fiducial parameters of Hartmann (2009). The *red solid line* in panel (a) is obtained rescaling the fiducial parameters to the lower stellar mass and radius as discussed in the text. *Dotted lines* are obtained diminishing by a factor of $\sim$3 the initial disk mass of the rescaled fiducial model in panel (a) and of the fiducial model in panel (b) while leaving the other parameters unaltered. Similarly, the *dashed-dotted lines* refer to a $\sim$3 times smaller radius and the *dashed lines* to a 10 times larger value of the viscosity parameter α. Finally, the *green solid lines* are the similarity solution obtained when the three aforementioned parameters are modified altogether.

at $R = 5R_\star$. According to this description, the evolution of $\dot{M}_{\rm acc}$ with age is determined by the following parameters: the initial disk radius inside which $\sim$60% of the initial disk mass is contained (R_0), the initial disk mass ($M_d(0)$), the viscosity parameter (α), the stellar mass ($M_\star$), and the disk temperature at 100 AU (T_{100}). In this expression the dependence of $\dot{M}_{\rm acc}$ on $M_\star$ is much shallower than that on the other parameters.

The solution using the fiducial parameters of Eq. (1.23) - $M_d(0)$=0.1$M_\odot$, R_0=10 AU, α=10^{-2}, $M_\star$=0.5$M_\odot$, T_{100}=10 K, and $R_\star$=2$R_\odot$ - suggested by Hartmann (2009) is shown on both panel of Fig. 6.22 as a *black solid line*. These parameters are representative of a typical cTTs with $M_\star\sim$ 0.5 $M_\odot$, and, indeed, seem to represent the values of $\dot{M}_{\rm acc}$ for some targets in panel (b) of Fig. 6.22, i.e. for targets with 0.5$M_\odot \leq M_\star \leq$1.0$M_\odot$. However, there are various YSOs in the same plot whose $\dot{M}_{\rm acc}$ are smaller than those predicted by the fiducial model. In order to reproduce these observed $\dot{M}_{\rm acc}$, I calculate $\dot{M}_{\rm acc}$ using Eq. (1.23) with one parameter at a time different from the fiducial model. I firstly assume a $\sim$3 times smaller initial disk mass ($M_d(0)$=0.03$M_\odot$, *black dotted line*), then a $\sim$2 times smaller initial radius (R_0=5 AU, *black dashed-dotted line*), and finally a 10 times larger value of α ($\alpha = 10^{-1}$, *black dashed line*). Each of these three assumptions leads to smaller estimated values of $\dot{M}_{\rm acc}$ at the ages of my targets and allows to reproduce the observed values of $\dot{M}_{\rm acc}$ for some other objects. When modifying these three parameters altogether (*green solid line*) I obtain even smaller values of $\dot{M}_{\rm acc}$ in the observed age range and this model is able to reproduce the observed $\dot{M}_{\rm acc}$ of most of the remaining targets. Thus, with a combination of these variations of the parameters or with other values of the parameters in the same range I can reproduce most of the data.

I proceed in a similar way to reproduce the observed $\dot{M}_{\rm acc}$ of panel (a) of Fig. 6.22, i.e. of objects with $0.1M_\odot \leq M_\star \leq 0.3M_\odot$. The fiducial model is clearly overestimating $\dot{M}_{\rm acc}$ in this case, as it is calculated for more massive objects. I rescale the stellar mass to $0.2M_\odot$ and, accordingly, $M_d(0)$ to 0.04 AU, the stellar radius to 1 $R_\odot$ and, accordingly, the initial disk radius to 5 AU, while using the same value for α and for T_{100}. This rescaled fiducial model is shown on the plot with a *red solid line* and represents with good agreement the behavior of most of the stronger accreting objects in this subsample. If I would modify less one of the aforementioned parameters I would obtain a better agreement with some of the stronger accretors in this subsample. As an example, I shown with a *red dashed-dotted line* the rescaled fiducial model with initial disk radius R_0=10 AU, which would make the values of $\dot{M}_{\rm acc}$ at any age larger. I then calculate the solution varying one parameter at a time using the same ratios as before to the rescaled fiducial model - a $\sim$3 times smaller initial disk mass ($M_d(0)$=0.01$M_\odot$, *red dotted line*) and a 10 times larger value of α ($\alpha = 10^{-1}$, *red dashed line*) - and also varying the two parameters altogether (*green solid line*). Also in this case with these assumptions I am able to reproduce the observed $\dot{M}_{\rm acc}$ vs age dependence for most of the targets.

The typical set of parameters that can be used to reproduce the observations is then used to compare the whole sample with viscous evolution models. I shown in Fig. 6.23 the values of $\dot{M}_{\rm acc}$ normalized for the known dependence $\dot{M}_{\rm acc} \propto {M_\star}^{1.7}$ (see Sect. 6.6.2) as a function of age. If compared with Fig. 6.21, the spread of values on this plot is significantly smaller ($\lesssim$ 2 dex). Moreover, with this representation I can compare the observed data with the viscous evolution models without the need to rescale the disk parameters to those of typical objects in different mass bins. Indeed, the fiducial model and the rescaled fiducial model for lower mass stars (cf. Fig. 6.22b, black and red solid lines) would overlap in Fig. 6.23, i.e. when dividing the predicted $\dot{M}_{\rm acc}$ by the assumed $M_\star^{1.7}$. I can then compare the observations with a set of similarity solution viscous evolution models with values of α ranging from 10^{-3} to 10^{-1}, $M_d(0)$ from 0.005 $M_\odot$ to 0.1 $M_\odot$, and R_0 from 5 AU to 15 AU. The region covered by these models is shown in Fig. 6.23 as a cyan region, while the fiducial model is shown as a black line. With this set of parameters viscous evolution models can reproduce the whole range of observed $\dot{M}_{\rm acc}$ normalized to their dependence with $M_\star$.

Even if my sample is incomplete, I have shown here that viscous evolution can reproduce the general observed dependence of $\dot{M}_{\rm acc}$ with age with some variations of the fiducial parameters. This confirms that the general evolution of disks can be described in first approximation with these models.

However, viscous evolution models alone still fail to explain some observables. As an example, the presence of objects surrounded by optically thin disks (Class III) at all ages (cf. Chapter 3) or the properties of transitional disks (cf. Chapter 5) is not described by these models. The clearing of disks at young ages could be explained with disk lifetimes

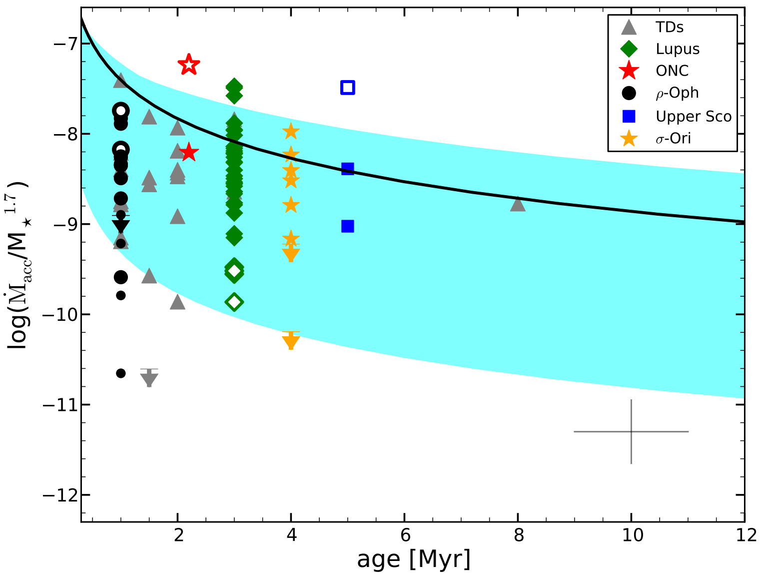

Figure 6.23: Mass accretion rate normalized to the stellar mass as a function of age for the whole sample. The values of the mass accretion rates are divided for each object by the stellar mass to the power of 1.7, which is the dependence that I derived in Sect. 6.6.2. The mean age of the region in which the targets are located is used. Symbols are as in Fig. 6.18. The cyan region represents the region of this plot that can be reproduced using viscous evolution similarity solution models from Hartmann (2009) and with reasonable assumptions on the disk physical parameters. The black solid line is the model with fiducial parameters suggested by Hartmann (2009).

very different from one object to another, which, according to Eq. (1.22), could be due to significantly smaller initial disks or significantly more viscous disks. However, other mechanisms are known to play an important role in the evolution and can lead to a faster dispersal of some disks at young ages. Possible mechanisms responsible of this fast dispersal could be internal or external photoevaporation, or dynamical disruption of the disk in binary systems or in crowded environments, or even planet formation itself. This Thesis has shown that, instead, Class II objects with detectable accretion rates, i.e. with $L_{\rm acc} \gtrsim L_{\rm acc,noise}$, have properties compatible with those predicted by viscous accretion models.

6.7 Conclusions

In this chapter, I have discussed the derived accretion properties for a total of almost 90 accreting YSO located in various star forming regions. This sample covers a large range of stellar properties, such as luminosity and mass, and regions with different ages. With my analysis method I have derived consistently for the whole sample the stellar and accretion properties for the whole sample and I derived a significantly smaller spread of accretion rates at any value of the central star stellar properties (e.g., $L_\star$, $M_\star$) than in the past. I have shown why this is probably not an effect of incompleteness in my sample, but rather a result of the more sophisticated and reliable analysis method developed here. I have determined that $\dot{M}_{\rm acc} \propto M_\star{}^{-1.7}$, which is compatible with the predictions of X-ray photoevaporation models. The small observed spread of values of $\dot{M}_{\rm acc}$ at any $M_\star$ could also be explained by a small spread of initial conditions of the parental cloud cores at the beginning of the star formation process. Thanks to the well determined $\dot{M}_{\rm acc}$-$M_\star$ relation I have been able to remove the dependence of the accretion rates with the stellar mass and to search for a purely evolutionary trend of accretion. I have then shown that, in general, the derived accretion are compatible with those predicted by viscous evolution models using reasonable assumptions on the disk properties. In particular, small changes on the assumed initial disk mass or radius, and on the viscosity parameter α can explain the observed values and their spread. However, I have also discussed how viscous evolution models alone fall short of explaining some observables, such as the presence of disk-less YSOs at any age in any star forming region.

7

Conclusions

Here I summarize the main achievements and findings of this Thesis, and I discuss some of possible follow-up investigations and developments of this work.

During my Thesis, I have worked on various samples of accreting YSOs, developing my own analysis method to study their properties. I have determined stellar and accretion properties of YSOs to ultimately constrain the current models of disk evolution. My method is based on fitting various continuum and absorption features of observed Class II YSO X-Shooter spectra at various wavelengths to determine simultaneously and automatically SpT, A_V, and $L_{\rm acc}$. I coded the slab model used to reproduce the emission due to accretion, and collected a large sample of spectra of non accreting (Class III) YSOs that I have been using as photospheric templates in my analysis. This method represents a big leap forward in the field as it allows for the first time to determine stellar and accretion properties of PMS stars with no prior assumptions. This important development was made possible also thanks to the spectra obtained with X-Shooter, a second generation ESO/VLT instrument with medium-resolution, broad-band coverage, and great sensitivity also in the UV part of the spectrum. In the future it would be profitable to include a disk model in the grid to study the stellar, accretion, and inner dusty disk properties simultaneously. This would be possible already with the data analyzed in this Thesis, as the X-Shooter spectra extends to the K-band in the NIR, where the contribution of the dusty inner disk to the observed flux is already important. Furthermore, a more complete grid of Class III YSO spectra would help to study the lower mass objects and the higher mass ones.

The study of two objects with an apparently old age in the Orion Nebula Cluster (ONC) has shown that the fitting procedure developed in this Thesis leads to correct stellar and accretion parameters for objects where photometric studies or spectroscopic studies with small wavelength coverage found degenerate solutions. This also suggests that other targets with anomalous age in this and other regions could be misclassified in the literature, but the real extent of this effect is unknown. To quantify these effects, I am leading an international team that has proposed an extensive X-Shooter survey of the ONC.

I have also studied, in this Thesis, the accretion properties of a more evolved class of objects, the transitional disks (TDs), whose inner disk is significantly depleted of dust. I have shown that at least some of these objects have inner gaseous disk properties similar to those of cTTs disks. This is due to the fact that their accretion, and also wind properties, are very similar to those of Class II YSOs. This allowed me to derive the properties of the gas content of their inner disk, such as the density and the radial extent. To explain this observations under steady-state assumptions, an efficient mechanism to transport gas from the outer disk to the inner regions of the system through the dust depleted gap is needed. The question now is whether this is true only for this relative small sample of objects or for the entire class of TDs. Future complete surveys of TDs done with X-Shooter will finally answer this question. Moreover, a better understanding of the mechanism driving the wind traced by the forbidden lines detected in these targets will help to constrain the current models explaining the evolution from Class II to TD and to better constrain the extent and density of the gaseous inner disk in TDs. For this reason, I have already collected with other collaborators higher-resolution spectra with the VLT/UVES instrument to study the line profile of various forbidden lines in the spectra of the TDs analyzed in this Thesis.

The large amount of data collected in this Thesis, meaning the stellar and accretion properties for almost 90 accreting YSO located in various regions, allowed me to study the dependence of accretion with various stellar parameters. The first result of this analysis is that the spread of accretion rates at any value of the central star stellar properties (e.g., $L_\star$, $M_\star$) observed in the past is significantly smaller when derived using my more accurate analysis. This is probably not an effect of incompleteness in my sample, but rather a result of the more sophisticated and reliable analysis method developed here. The derived slope of the $\dot{M}_{\rm acc}$-$M_\star$ relation is compatible with the predictions of X-ray photoevaporation models, while the small observed spread of values could also be explained as similar initial conditions of the parental cloud core. With my data I was also able to show that the general properties of accretion are compatible with those predicted by viscous evolution models using reasonable assumptions on the disk properties. According to my analysis, some of the spread of $\dot{M}_{\rm acc}$ at any given $M_\star$ and in a given region could be ascribed to different initial disk mass and radius or to different values of the viscosity parameter α. However, I have also discussed how viscous evolution models alone fall short of explaining some observables, such as the presence of disk-less YSOs at any age in any star forming region. The data presented here are also a great benchmark for future theoretical studies, even though this is not a complete sample of accreting YSO. In the future, with my collaborators, I plan to continue to collect data in these and other star forming regions in order to get complete samples of YSOs to be studied with my method, and to better constrain the accretion disk physics.

To conclude, I have shown that the current picture of disk evolution is able to reproduce some of the observed properties of disks. However, my analysis has also showed that current observations allow to better constrain the models as they show significantly smaller spread of values. With complete samples in various star forming regions I could be able to offer an even better observational benchmark to theorists. At the same time I have also shown that the general picture of disk evolution still cannot explain everything. A better observational and theoretical understanding of the importance of other mechanisms driving the evolution of disks, such as photoevaporation or dynamical interaction, is needed to firmly understand the evolution of protoplanetary disks and its connection with planet formation. The future and present large surveys will give us the possibility to constrain the various models with more accuracy. Future X-Shooter surveys of accretion in complete samples will surely be crucial. At the same time, on-going surveys such as the GAIA-ESO survey will help as they will provide properties for complete and unbiased samples of YSOs to the community. GAIA itself will help the field substantially, as it will drastically lower the uncertainties affecting the present day studies due to the poor knowledge of the distance of the objects. Finally, surveys of star forming regions with ALMA will give us for the first time the possibility to compare stellar and disk properties in large samples of data. For example, I am involved in a survey of the Lupus I and III clouds aimed at studying the dust and gas content of the disks present in that region. This will provide a great sample to compare with the objects located in Lupus observed with X-Shooter and discussed in this Thesis.

The wealth of data with unprecedented details, the new analysis method developed, and the knowledge acquired will make it possible to have an even more complete and precise understanding of the whole disk evolution process, and thus of the formation of planets like ours.

Bibliography

Alcalá, J. M., Stelzer, B., Covino, E., et al. 2011, Astronomische Nachrichten, 332, 242

Alcalá, J. M., Natta, A., Manara, C. F., et al. 2014, A&A, 561, A2

Alexander, R. D., & Armitage, P. J. 2006, ApJ, 639, L83

Alexander, R., Pascucci, I., Andrews, S., Armitage, P., & Cieza, L. 2014, arXiv:1311.1819

Allard, F., Homeier, D., & Freytag, B. 2011, Astronomical Society of the Pacific Conference Series, 448, 91

Allen, L. E., & Strom, K. M. 1995, AJ, 109, 1379

Allen, P. R., Luhman, K. L., Myers, P. C., et al. 2007, ApJ, 655,1095

Allers, K. N., Jaffe, D. T., Luhman, K. L., et al. 2007, ApJ, 657, 511

Alves de Oliveira, C., Moraux, E., Bouvier, J., et al. 2010, A&A, 515, A75

Alves de Oliveira, C., Moraux, E., Bouvier, J., & Bouy, H. 2012, A&A, 539, A151

André, P. 2002, EAS Publications Series, 3, 1

Andrews, S. M., & Williams, J. P. 2007, ApJ, 659, 705

Andrews, S. M., Wilner, D. J., Hughes, A. M., Qi, C., & Dullemond, C. P. 2009, ApJ, 700, 1502

Andrews, S. M., Wilner, D. J., Espaillat, C., et al. 2011, ApJ, 732, 42

Antoniucci, S., Garcia Lopez, R., Nisini, B., et al. 2011, A&A, 534, 32

Armitage, P. J. 2010, Astrophysics of Planet Formation, by Philip J. Armitage, pp. 294. ISBN 978-0-521-88745-8 (hardback). Cambridge, UK: Cambridge University Press, 2010.,

Arnold, T. J., Eisner, J. A., Monnier, J. D., & Tuthill, P. 2012, ApJ, 750, 119

Bacciotti, F., Whelan, E. T., Alcalá, J. M., et al. 2011, ApJ, 737, 26

Banzatti, A., Meyer, M. R., Bruderer, S., et al. 2012, ApJ, 745, 90

Banzatti, A., Meyer, M. R., Manara, C. F., Pontoppidan, K. M., & Testi, L. 2014, ApJ, 780, 26

Baraffe, I., Chabrier, G., Allard, F., & Hauschildt, P. H. 1998, A&A, 337, 403

Baraffe, I., & Chabrier, G. 2010, A&A, 521, A44

Baraffe, I., Vorobyov, E., & Chabrier, G. 2012, ApJ, 756, 118

Barentsen, G., Vink, J. S., Drew, J. E., et al. 2011, MNRAS, 415, 103

Barrado Y Navascués, D. 2006, A&A, 459, 511

Basri, G., & Bertout, C. 1989, ApJ, 341, 340

Beccari, G., Spezzi, L., De Marchi, G., et al. 2010, ApJ, 720, 1108

Béjar, V. J. S., Zapatero Osorio, M. R., & Rebolo, R. 1999, ApJ, 521, 671

Bell, C. P. M., Naylor, T., Mayne, N. J., Jeffries, R. D., & Littlefair, S. P. 2013, MNRAS, 434, 806

Benisty, M., Tatulli, E., Ménard, F., & Swain, M. R. 2010, A&A, 511, A75

Bergin, E. A., Cleeves, L. I., Gorti, U., et al. 2013, Nature, 493, 644

Biazzo, K., Alcalá, J. M., Covino, E., et al. 2012, A&A, 547, A104

Birnstiel, T., Andrews, S. M., & Ercolano, B. 2012, A&A, 544, A79

Blaauw, A. 1991, NATO ASIC Proc. 342: The Physics of Star Formation and Early Stellar Evolution, 125

Bontemps, S., André, P., Kaas, A. A., et al. 2001, A&A, 372, 173

Bouvier, J., Alencar, S. H. P., Boutelier, T., et al. 2007, A&A, 463, 1017

Brown, A. G. A., de Geus, E. J., & de Zeeuw, P. T. 1994, A&A, 289, 101

Brown, J. M., Blake, G. A., Dullemond, C. P., et al. 2007, ApJ, 664, L107

Brown, J. M., Blake, G. A., Qi, C., Dullemond, C. P., & Wilner, D. J. 2008, ApJ, 675, L109

Brown, J. M., Blake, G. A., Qi, C., et al. 2009, ApJ, 704, 496

Brown, J. M., Pontoppidan, K. M., van Dishoeck, E. F., et al. 2013, ApJ, 770, 94

Burningham, B., Naylor, T., Littlefair, S. P., & Jeffries, R. D. 2005, MNRAS, 356, 1583

Caballero, J. A. 2008, MNRAS, 383, 750

Caballero, J. A. 2008, A&A, 478, 667

Caballero, J. A., Albacete-Colombo, J. F., & López-Santiago, J. 2010, A&A, 521, A45

Calvet, N., & Gullbring, E. 1998, ApJ, 509, 802

Calvet, N., Hartmann, L., & Strom, S. E. 2000, in Protostars and Planets IV, 377

Calvet, N., D'Alessio, P., Hartmann, L., et al. 2002, ApJ, 568, 1008

Calvet, N., Muzerolle, J., Briceño, C., et al. 2004, AJ, 128, 1294

Calvet, N., D'Alessio, P., Watson, D. M., et al. 2005, ApJ, 630, L185

Caratti o Garatti, A., Garcia Lopez, R., Antoniucci, S., et al. 2012, A&A, 538, A64

Cardelli, J. A., Clayton, G. C., & Mathis, J. S. 1989, ApJ, 345, 245

Carpenter, J. M., Mamajek, E. E., Hillenbrand, L. A., & Meyer, M. R. 2006, ApJ, 651, L49

Carpenter, J. M., Ricci, L., & Isella, A. 2014, arXiv:1404.0387

Chapman, N. L., Mundy, L. G., Lai, S.-P., & Evans, N. J., II 2009, ApJ, 690, 496

Cieza, L., Padgett, D. L., Stapelfeldt, K. R., et al. 2007, ApJ, 667, 308

Clarke, C. J., & Pringle, J. E. 2006, MNRAS, 370, L10

Cohen, M., & Kuhi, L. V. 1979, ApJS, 41, 743

Comerón, F., Fernández, M., Baraffe, I., Neuhäuser, R., & Kaas, A. A. 2003, A&A, 406, 1001

Comerón, F. 2008, Handbook of Star Forming Regions, Volume II, 295

Comerón, F., Testi, L., & Natta, A. 2010, A&A, 522, A47

Costigan, G., Scholz, A., Stelzer, B., et al. 2012, MNRAS, 427, 1344

Costigan, G., Vink, J. S., Scholz, A., Ray, T., & Testi, L. 2014, arXiv:1403.4088

Currie, T., & Sicilia-Aguilar, A. 2011, ApJ, 732, 24

Cutri, R. M., Skrutskie, M. F., van Dyk, S., et al. 2003, VizieR Online Data Catalog, 2246, 0

Dahm, S. E. 2008, AJ, 136, 521

Dahm, S. E. 2010, AJ, 140, 1444

D'Antona, F., & Mazzitelli, I. 1994, ApJS, 90, 467

Da Rio, N., Robberto, M., Soderblom, D. R., et al. 2010a, ApJ, 722, 1092

Da Rio, N., Gouliermis, D. A., & Gennaro, M. 2010b, ApJ, 723, 166

Da Rio, N., Robberto, M., Hillenbrand, L. A., Henning, T., & Stassun, K. G. 2012, ApJ, 748, 14

Da Rio, N., Jeffries, R. D., Manara, C. F., & Robberto, M. 2014, MNRAS, 439, 3308

de Geus, E. J., de Zeeuw, P. T., & Lub, J. 1989, A&A, 216, 44

de Geus, E. J. 1992, A&A, 262, 258

De Marchi, G., Panagia, N., & Romaniello, M. 2010, ApJ, 715, 1

De Marchi, G., Paresce, F., Panagia, N., et al. 2011, ApJ, 739, 27

DENIS Consortium 2005, VizieR Online Data Catalog, 2263, 0

de Zeeuw, P. T., Hoogerwerf, R., de Bruijne, J. H. J., Brown, A. G. A., & Blaauw, A. 1999, AJ, 117, 354

Draine, B. T. 2011, Physics of the Interstellar and Intergalactic Medium by Bruce T. Draine. Princeton University Press, 2011. ISBN: 978-0-691-12214-4,

Dullemond, C. P., Natta, A., & Testi, L. 2006, ApJ, 645, L69

Edwards, S., Fischer, W., Hillenbrand, L., & Kwan, J. 2006, ApJ, 646, 319

Ercolano, B., & Owen, J. E. 2010, MNRAS, 406, 1553

Ercolano, B., Mayr, D., Owen, J. E., Rosotti, G., & Manara, C. F. 2014, MNRAS, 178

Erickson, K. L., Wilking, B. A., Meyer, M. R., Robinson, J. G., & Stephenson, L. N. 2011, AJ, 142, 140

Espaillat, C., D'Alessio, P., Hernández, J., et al. 2010, ApJ, 717, 441

Espaillat, C., Ingleby, L., Hernández, J., et al. 2012, ApJ, 747, 103

Espaillat, C., Ingleby, L., Furlan, E., et al. 2013, ApJ, 762, 62

Espaillat, C., Muzerolle, J., Najita, J., et al. 2014, arXiv:1402.7103

Evans, N. J., II, Dunham, M. M., Jørgensen, J. K., et al. 2009, ApJS, 181, 321

Fang, M., van Boekel, R., Wang, W., et al. 2009, A&A, 504, 461

Fedele, D., van den Ancker, M. E., Henning, T., Jayawardhana, R., & Oliveira, J. M. 2010, A&A, 510, A72

Feigelson, E. D., & Nelson, P. I. 1985, ApJ, 293, 192

Fischer, W., Edwards, S., Hillenbrand, L., & Kwan, J. 2011, ApJ, 730, 73

Forbrich, J., & Preibisch, T. 2007, A&A, 475, 959

Franchini, M., Morossi, C., & Malagnini, M. L. 1998, ApJ, 508, 370

Franciosini, E., Pallavicini, R., & Sanz-Forcada, J. 2006, A&A, 446, 501

Frank, A., Ray, T. P., Cabrit, S., et al. 2014, arXiv:1402.3553

Frasca, A., Guillout, P., Marilli, E., et al. 2006, A&A, 454, 301

Gagné, M., Skinner, S. L., & Daniel, K. J. 2004, ApJ, 613, 393

Gammie, C. F. 1996, ApJ, 457, 355

Gatti, T., Testi, L., Natta, A., Randich, S., & Muzerolle, J. 2006, A&A, 460, 547

Giannini, T., Nisini, B., Antoniucci, S., et al. 2013, ApJ, 778, 71

Glassgold, A. E., Najita, J. R., & Igea, J. 2007, ApJ, 656, 515

Gómez, M., & Mardones, D. 2003, AJ, 125, 2134

Greene, T. P., & Meyer, M. R. 1995, ApJ, 450, 233

Grosso, N., Montmerle, T., Bontemps, S., André, P., & Feigelson, E. D. 2000, A&A, 359, 113

Güdel, M., Briggs, K. R., Arzner, K., et al. 2007, A&A, 468, 353

Güdel, M., Lahuis, F., Briggs, K. R., et al. 2010, A&A, 519, A113

Guenther, E. W., Esposito, M., Mundt, R., Covino, E., Alcalá, J. M., et al. 2007, A&A, 467, 1147

Gullbring, E., Hartmann, L., Briceno, C., & Calvet, N. 1998, ApJ, 492, 323

Gullbring, E., Calvet, N., Muzerolle, J., & Hartmann, L. 2000, ApJ, 544, 927

Haisch, K. E., Jr., Lada, E. A., & Lada, C. J. 2001, ApJ, 553, L153

Hartigan, P., Kenyon, S. J., Hartmann, L., et al. 1991, ApJ, 382, 617

Hartigan, P., Edwards, S., & Ghandour, L. 1995, ApJ, 452, 736

Hartmann, L., Calvet, N., Gullbring, E., & D'Alessio, P. 1998, ApJ, 495, 385

Hartmann, L. 2003, ApJ, 585, 398

Hartmann, L., D'Alessio, P., Calvet, N., & Muzerolle, J. 2006, ApJ, 648, 484

Hartmann, L. 2009, Accretion Processes in Star Formation: Second Edition, by Lee Hartmann. ISBN 978-0-521-53199-3. Published by Cambridge University Press, Cambridge, UK, 2009., Henry, T. J., Kirkpatrick, J. D., & Simons, D. A. 1994, AJ, 108, 1437

Herczeg, G., Walter, F. M., Linsky, J. L., et al. 2005, AJ, 129, 2777

Herczeg, G. J., & Hillenbrand, L. A. 2008, ApJ, 681, 594

Herczeg, G. J., & Hillenbrand, L. A. 2014, ApJ, 786, 97

Hillenbrand, L. A. 1997, AJ, 113, 1733

Hernández, J., Hartmann, L., Megeath, T., et al. 2007, ApJ, 662, 1067

Høg, E., Fabricius, C., Makarov, V. V., et al. 2000, A&A, 355, L27

Houdebine, E. R., Mathioudakis, M., Doyle, J. G., & Foing, B. H. 1996, A&A, 305, 209

Huélamo, N., Bouy, H., Pinte, C., et al. 2010, A&A, 523, A42

Hughes, J., Hartigan, P., Krautter, J., & Kelemen, J. 1994, AJ, 108, 1071

Hughes, A. M., Wilner, D. J., Calvet, N., et al. 2007, ApJ, 664, 536

Hughes, A. M., Wilner, D. J., Qi, C., & Hogerheijde, M. R. 2008, ApJ, 678, 1119

Hughes, A. M., Andrews, S. M., Wilner, D. J., et al. 2010, AJ, 140, 887

Ingleby, L., Calvet, N., Bergin, E., et al. 2009, ApJ, 703, L137

Ingleby, L., Calvet, N., Bergin, E., et al. 2011, ApJ, 743, 105

Ingleby, L., Calvet, N., Herczeg, G., et al. 2013, ApJ, 767, 112

Jayawardhana, R., Ardila, D. R., Stelzer, B., & Haisch, K. E., Jr. 2003a, AJ, 126, 1515

Jayawardhana, R., Mohanty, S., & Basri, G. 2003b, ApJ, 592, 282

Jeffries, R. D., Maxted, P. F. L., Oliveira, J. M., & Naylor, T. 2006, MNRAS, 371, L6

John, T. L. 1988, A&A, 193, 189

Johns-Krull, C. M. 2007, ApJ, 664, 975

Johnstone, C. P., Jardine, M., Gregory, S. G., Donati, J.-F., & Hussain, G. 2014, MNRAS, 437, 3202

Kenyon, S. J., & Hartmann, L. 1995, ApJS, 101, 117

Kenyon, S. J., Lada, E. A., & Barsony, M. 1998, AJ, 115, 252

Kenyon, M. J., Jeffries, R. D., Naylor, T., Oliveira, J. M., & Maxted, P. F. L. 2005, MNRAS, 356, 89

Kim, K. H., Watson, D. M., Manoj, P., et al. 2009, ApJ, 700, 1017

Kim, K. H., Watson, D. M., Manoj, P., et al. 2013, ApJ, 769, 149

Kirkpatrick, J. D., Reid, I. N., Liebert, J., et al. 1999, ApJ, 519, 802

Kirkpatrick, J. D., Cruz, K. L., Barman, T. S., et al. 2008, ApJ, 689, 1295

König, B., Neuhäuser, R., & Stelzer, B. 2001, A&A, 369, 971

Krautter, J. 1992, Low Mass Star Formation in Southern Molecular Clouds, 127

Krautter, J., Wichmann, R., Schmitt, J. H. M. M., et al. 1997, A&AS, 123, 329

Lada, C. J., Muench, A. A., Luhman, K. L., et al. 2006, AJ, 131, 1574

Lynden-Bell, D., & Pringle, J. E. 1974, MNRAS, 168, 603

Lodato, G. 2008, New A Rev., 52, 21

Loinard, L., Torres, R. M., Mioduszewski, A. J., & Rodríguez, L. F. 2008, ApJ, 675, L29

Lombardi, M., Lada, C. J., & Alves, J. 2008, A&A, 480, 785

Looper, D. L., Burgasser, A. J., Kirkpatrick, J. D., & Swift, B. J. 2007, ApJ, 669, L97

López Martí, B., Eislöffel, J., & Mundt, R. 2005, A&A, 440, 139

Luhman, K. L., Rieke, G. H., Lada, C. J., & Lada, E. A. 1998, ApJ, 508, 347

Luhman, K. L., & Rieke, G. H. 1999, ApJ, 525, 440

Luhman, K. L., Stauffer, J. R., Muench, A. A., et al. 2003, ApJ, 593, 1093

Luhman, K. L. 2004, ApJ, 602, 816

Luhman, K. L. 2008, Handbook of Star Forming Regions, Volume II, 169

Luhman, K. L., Allen, P. R., Espaillat, C., Hartmann, L., & Calvet, N. 2010, ApJS, 189, 353

Mayor, M., & Queloz, D. 2012, New A Rev., 56, 19

Mamajek, E. E. 2005, ApJ, 634, 1385

Manara, C. F., Robberto, M., Da Rio, N., et al. 2012, ApJ, 755, 154

Manara, C. F., Testi, L., Rigliaco, E., et al. 2013a, A&A, 551, A107

Manara, C. F., Beccari, G., Da Rio, N., et al. 2013b, A&A, 558, A114

Manara, C. F., Testi, L., Natta, A., Rosotti, G., et al. 2014a, A&A, submitted

Manara, C. F., Testi, L., Natta, A., Alcalà, J., et al. 2014b, A&A, in prep.

Manoj, P., Kim, K. H., Furlan, E., et al. 2011, ApJS, 193, 11

Matrà, L., Merín, B., Alves de Oliveira, C., et al. 2012, A&A, 548, A111

McClure, M. 2009, ApJ, 693, L81

McClure, M. K., Furlan, E., Manoj, P., et al. 2010, ApJS, 188, 75

Megeath, S. T., Gutermuth, R., Muzerolle, J., et al. 2012, AJ, 144, 192

Melo, C. 2003, A&A, 410, 269

Menten, K. M., Reid, M. J., Forbrich, J., & Brunthaler, A. 2007, A&A, 474, 515

Mentuch, E., Brandeker, A., van Kerkwijk, M. H., Jayawardhana, R., & Hauschildt, P. H. 2008, ApJ, 689, 1127

Merín, B., Jørgensen, J., Spezzi, L., et al. 2008, ApJS, 177, 551

Merín, B., Brown, J. M., Oliveira, I., et al. 2010, ApJ, 718, 1200

Messina, S., Desidera, S., Tutatto, M., Lanzafame, A. C., & Guinan, E. F. 2010, VizieR Online Data Catalog, 352, 9015

Miotello, A., Testi, L., Lodato, G., et al. 2014, arXiv:1405.0821

Modigliani, A., Goldoni, P., Royer, F., et al. 2010, Proc. SPIE, 7737

Mohanty, S., Jayawardhana, R., & Basri, G. 2005, ApJ, 626, 498

Montes, D. 1998, Ap&SS, 263, 231

Montmerle, T., Koch-Miramond, L., Falgarone, E., & Grindlay, J. E. 1983, ApJ, 269, 182

Morrison, J. E., Röser, S., McLean, B., Bucciarelli, B., & Lasker, B. 2001, AJ, 121, 1752

Mortier, A., Oliveira, I., & van Dishoeck, E. F. 2011, MNRAS, 418, 1194

Muzerolle, J., Calvet, N., & Hartmann, L. 1998a, ApJ, 492, 743

Muzerolle, J., Hartmann, L., & Calvet, N. 1998b, AJ, 116, 455

Muzerolle, J., Hillenbrand, L., Calvet, N., Briceño, C., & Hartmann, L. 2003, ApJ, 592, 266

Muzerolle, J., Luhman, K., Briceño, C., et al. 2005, ApJ, 625, 906

Muzerolle, J., Allen, L. E., Megeath, S. T., Hernández, J., & Gutermuth, R. A. 2010, ApJ, 708, 1107

Najita, J., Carr, J. S., & Mathieu, R. D. 2003, ApJ, 589, 931

Najita, J. R., Strom, S. E., & Muzerolle, J. 2007, MNRAS, 378, 369

Natta, A., & Testi, L. 2001, A&A, 376, L22

Natta, A., Testi, L., Comerón, F., et al. 2002, A&A, 393, 597

Natta, A., Testi, L., Muzerolle, J., et al. 2004, A&A, 424, 603

Natta, A., Testi, L., & Randich, S. 2006, A&A, 452, 245

Natta, A., Testi, L., et al. A&A, in prep.

Neuhaeuser, R., Sterzik, M. F., Schmitt, J. H. M. M., Wichmann, R., & Krautter, J. 1995, A&A, 297, 391

Neuhäuser, R., Walter, F. M., Covino, E., et al. 2000, A&AS, 146, 323

Nisini, B., Bacciotti, F., Giannini, et al. 2005, A&A, 441, 159

Oliveira, J. M., Jeffries, R. D., & van Loon, J. T. 2004, MNRAS, 347, 1327

Oliveira, J. M., Jeffries, R. D., van Loon, J. T., & Rushton, M. T. 2006, MNRAS, 369, 272

Owen, J. E., Ercolano, B., & Clarke, C. J. 2011, MNRAS, 412, 13

Owen, J. E., Clarke, C. J., & Ercolano, B. 2012, MNRAS, 422, 1880

Padoan, P., Kritsuk, A., Norman, M. L., & Nordlund, Å. 2005, ApJ, 622, L61

Palla, F., & Stahler, S. W. 1999, ApJ, 525, 772

Palla, F., Randich, S., Pavlenko, Y. V., Flaccomio, E., & Pallavicini, R. 2007, ApJ, 659, L41

Parks, J. R., Plavchan, P., White, R. J., & Gee, A. H. 2014, ApJS, 211, 3

Pascucci, I., Hollenbach, D., Najita, J., et al. 2007, ApJ, 663, 383

Pascucci, I., & Sterzik, M. 2009, ApJ, 702, 724

Pascucci, I., Sterzik, M., Alexander, R. D., et al. 2011, ApJ, 736, 13

Pavlenko, Y. V., & Magazzu, A. 1996, A&A, 311, 961

Perryman, M. A. C., Lindegren, L., Kovalevsky, J., et al. 1997, A&A, 323, L49

Peterson, D. E., Caratti o Garatti, A., Bourke, T. L., et al. 2011, ApJS, 194, 43

Piétu, V., Dutrey, A., Guilloteau, S., Chapillon, E., & Pety, J. 2006,A&A, 460, L43

Pinilla, P., Benisty, M., & Birnstiel, T. 2012, A&A, 545, A81

Pontoppidan, K. M., Blake, G. A., van Dishoeck, E. F., et al. 2008, ApJ, 684, 1323

Pontoppidan, K. M., Blake, G. A., & Smette, A. 2011, ApJ, 733, 84

Preibisch, T., Balega, Y., Hofmann, K.-H., Weigelt, G., & Zinnecker, H. 1999, New A, 4, 531

Preibisch, T., Brown, A. G. A., Bridges, T., Guenther, E., & Zinnecker, H. 2002, AJ, 124, 404

Preibisch, T., Kim, Y.-C., Favata, F., et al. 2005, ApJS, 160, 401

Preibisch, T., & Mamajek, E. 2008, Handbook of Star Forming Regions, Volume II, 235

Preibisch, T. 2012, Research in Astronomy and Astrophysics, 12, 1

Reggiani, M., Robberto, M., Da Rio, N., et al. 2011, A&A, 534, A83

Reid, I. N., Cruz, K. L., Kirkpatrick, J. D., et al. 2008, AJ, 136, 1290

Riaz, B., Gizis, J. E., & Harvin, J. 2006, AJ, 132, 866

Riaz, B., Martín, E. L., Tata, R., et al. 2012, MNRAS, 419, 1887

Riddick, F. C., Roche, P. F., & Lucas, P. W. 2007, MNRAS, 381, 1067

Rigliaco, E., Natta, A., Randich, S., Testi, L., & Biazzo, K. 2011a, A&A, 525, A47

Rigliaco, E., Natta, A., Randich, S., et al. 2011b, A&A, 526, 6

Rigliaco, E., Natta, A., Testi, L., et al. 2012, A&A, 548, A56

Rigliaco, E., Pascucci, I., Gorti, U., Edwards, S., & Hollenbach, D. 2013, ApJ, 772, 60

Robberto, M., Song, J., Mora Carrillo, G., et al. 2004, ApJ, 606, 952

Robberto, M., Soderblom, D. R., Bergeron, E., et al. 2013, ApJS, 207, 10

Rodgers-Lee, D., Scholz, A., Natta, A., & Ray, T. 2014, arXiv:1405.3833

Rojas-Ayala, B., Covey, K. R., Muirhead, P. S., & Lloyd, J. P. 2012, ApJ, 748, 93

Rosenfeld, K. A., Chiang, E., & Andrews, S. M. 2014, ApJ, 782, 62

Rosotti, G. P., Ercolano, B., Owen, J. E., & Armitage, P. J. 2013, MNRAS, 430, 1392

Sacco, G. G., Franciosini, E., Randich, S., & Pallavicini, R. 2008, A&A, 488, 167

Sacco, G. G., Flaccomio, E., Pascucci, I., et al. 2012, ApJ, 747, 142

Salyk, C., Blake, G. A., Boogert, A. C. A., & Brown, J. M. 2007, ApJ, 655, L105

Salyk, C., Blake, G. A., Boogert, A. C. A., & Brown, J. M. 2009, ApJ, 699, 330

Samus', N. N., Goranskii, V. P., Durlevich, O. V., et al. 2003, Astronomy Letters, 29, 468

Scholz, A., Muzic, K., Geers, V., et al. 2012, ApJ, 744, 6

Sciculuna, P., Rosotti, G., and Testi, L. 2014, A&A, submitted

Seaton, M. J. 1960, Reports on Progress in Physics, 23, 313

Skelly, M. B., Unruh, Y. C., Collier Cameron, A., et al. 2008, MNRAS, 385, 708

Shakura, N. I., & Sunyaev, R. A. 1973, A&A, 24, 337

Sherry, W. H., Walter, F. M., & Wolk, S. J. 2004, AJ, 128, 2316

Shkolnik, E. L., Liu, M. C., Reid, I. N., Dupuy, T., & Weinberger, A. J. 2011, ApJ, 727, 6

Shu, F. H., Adams, F. C., & Lizano, S. 1987, ARA&A, 25, 23

Shu, F., Najita, J., Ostriker, E., et al. 1994, ApJ, 429, 781

Sicilia-Aguilar, A., Hartmann, L. W., Hernández, J., Briceño, C., & Calvet, N. 2005, AJ, 130, 188

Sicilia-Aguilar, A., Henning, T., & Hartmann, L. W. 2010, ApJ, 710, 597

Siess, L., Dufour, E., & Forestini, M. 2000, A&A, 358, 593

Soderblom, D. R., Stauffer, J. R., Hudon, J. D., & Jones, B. F. 1993, ApJS, 85, 315

Soderblom, D. R. 2010, ARA&A, 48, 581

Soderblom, D. R., Hillenbrand, L. A., Jeffries, R. D., Mamajek, E. E., & Naylor, T. 2014, arXiv:1311.7024

Spezzi, L., Alcalá, J. M., Covino, E., et al. 2008, ApJ, 680, 1295

Spezzi, L., Vernazza, P., Merín, B., et al. 2011, ApJ, 730, 65

Spezzi, L., de Marchi, G., Panagia, N., Sicilia-Aguilar, A., & Ercolano, B. 2012, MNRAS, 421, 78

Spitzer, L. 1978, New York Wiley-Interscience, 1978. 333 p.,

Stassun, K. G., Mathieu, R. D., Mazeh, T., & Vrba, F. J. 1999, AJ, 117, 2941

Stelzer, B., Frasca, A., Alcalá, J. M., et al. 2013, A&A, 558, A141

Teixeira, R., Ducourant, C., Chauvin, G., et al. 2008, A&A, 489, 825

Testi, L., D'Antona, F., Ghinassi, F., et al. 2001, ApJ, 552, L147

Testi, L., Natta, A., Oliva, E., et al. 2002, ApJ, 571, L155

Testi, L. 2009, A&A, 503, 639

Tilling, I., Clarke, C. J., Pringle, J. E., & Tout, C. A. 2008, MNRAS, 385, 1530

Tobin, J. J., Hartmann, L., Chiang, H.-F., et al. 2013, ApJ, 771, 48

Torres, C. A. O., Quast, G. R., da Silva, L., et al. 2006, A&A, 460, 695

Torres, C. A. O., Quast, G. R., Melo, C. H. F., & Sterzik, M. F. 2008, Handbook of Star Forming Regions, Volume II, 757

Turner, N. J., Fromang, S., Gammie, C., et al. 2014, arXiv:1401.7306

Valenti, J. A., Basri, G., & Johns, C. M. 1993, AJ, 106, 2024

Vernet, J., Dekker, H., D'Odorico, S., et al. 2011, A&A, 536, A105

Vorobyov, E. I., & Basu, S. 2008, ApJ, 676, L139

Vorobyov, E. I., & Basu, S. 2009, ApJ, 703, 922

Webb, R. A., Zuckerman, B., Platais, I., et al. 1999, ApJ, 512, L63

Weinberger, A. J., Anglada-Escudé, G., & Boss, A. P. 2013, ApJ, 762, 118

Whelan, E. T., Bonito, R., Antoniucci, S., et al. 2014, A&A, 565, A80

White, N. E., Giommi, P., & Angelini, L. 2000, VizieR Online Data Catalog, 9031, 0

White, R. J., & Ghez, A. M. 2001, ApJ, 556, 265

White, R. J., & Basri, G. 2003, ApJ, 582, 1109

White, R. J., & Hillenbrand, L. A. 2005, ApJ, 621, L65

Wilking, B. A., & Lada, C. J. 1983, ApJ, 274, 698

Wilking, B. A., Greene, T. P., & Meyer, M. R. 1999, AJ, 117, 469

Wilking, B. A., Meyer, M. R., Robinson, J. G., & Greene, T. P. 2005, AJ, 130, 1733

Williams, J. P., & Cieza, L. A. 2011, ARA&A, 49, 67

Wolf, S., Malbet, F., Alexander, R., et al. 2012, A&A Rev., 20, 52

Wright, E. L., Eisenhardt, P. R. M., Mainzer, A. K., Ressler, M. E., Cutri, R. M. et al. 2010, AJ, 140, 1868

Zapatero Osorio, M. R., Béjar, V. J. S., Pavlenko, Y., et al. 2002, A&A, 384, 937

Zhu, Z., Nelson, R. P., Hartmann, L., Espaillat, C., & Calvet, N. 2011, ApJ, 729, 47

Zuckerman, B., Webb, R. A., Schwartz, M., & Becklin, E. E. 2001, ApJ, 549, L233

Zuckerman, B., & Song, I. 2004, ARA&A, 42, 685

Acknowledgments

First of all I sincerely want to thank Leonardo for his supervision during these years. You kept me motivated, on path, and taught me a lot about the practical aspects and the spirit of this job. You showed me that you have to follow your ideas, that you have to put all yourself in what you do. And many things more. Also thanks to your supervision I will never regret to have done my PhD in Munich and not in Honolulu!

A special thanks also to Antonella, for her patience, her guidance, and her suggestions. I am also very grateful to Juan, for his availability and his detailed explanations. I thank Barbara for her help and enthusiasm, and Nina for arriving right in time for my defense!

I want to acknowledge the support, suggestions, and comments from a great many people, including Thomas Preibisch, Giacomo Beccari, Luca Ricci, Massimo Robberto, Giovanni Rosotti, Nicola Da Rio, Lee Hartmann, Greg Herczeg, Beate Stelzer, and Andrea Banzatti. I am also grateful for the discussions I had at the Accretion/Star Formation coffee at ESO.

A special thanks for my travel mate Grainne Costigan, in particular for her availability, her proof read, and the great daily discussions we had. And that we will have.

I thank ESO, and in particular Eric Emsellem, for the support, and my fellow mentors Giacomo and Izaskun for their suggestions. I am grateful for the office mates I had, Carolina, Carina, Leticia, Julian, Karina, and also Dominika, even if for a short time. I would also like to thank all the students and fellows that have come to ESO in the last years. It has been a great company! In particular, a special thank you to Anna Feltre, the best next-office mate I have ever had, and also to Grainne, Leticia, Dominika, Margherita, Sebastian, Roberto, Peter, Alvaro, Leo, Anja, Anna McLeod, Marco(s), and many more.

I also want to thank the institutes that I visited in the last years, in particular Arcetri, DIAS, and STScI. A special thanks to Luca, Lorenzo, Rachel, Andrea, and Giulia for their support in Florence, Dublin, and Baltimore.

Finally, I want to thank my friends in these years in Munich, in particular Lorenzo, Jack, Massi, Tommi, Dome, Vito, Marco, Anna, Thomas, Berno, Davide, Veronica, Michi, die Vero, die Franci, Paolo, Diego, Andrea, Beppe e Titta, Fede and many others, including those around the world. And a particular thanks to my two girls: Anna, for sustaining me every day, and Caterina, for making us smile at the beginning of every new day.

Referred publications

[11] ``*On the gas content of transitional disks: a VLT/X-Shooter study of accretion and winds*''
Manara, C.F., Testi, L., Natta, A., Rosotti, G., Benisty, M., B. Ercolano, Ricci, L., **A&A, submitted**

[10] ``*Strong Biases in Estimating the Time Dependence of Mass Accretion Rates in Young Stars*''
Da Rio,N., Jeffries,R.D., **Manara,C.F.**, Robberto,M., **2014, MNRAS, 439, 3308**

[9] ``*The* $\dot{M}$*-*$M_\star$ *relation of pre-main sequence stars: a consequence of X-ray driven disc evolution*"
Ercolano, B., Mayr, D., Owen, J., Rosotti, G., **Manara, C.F.**, **2014, MNRAS, 439, 256**

[8] ``*Time monitoring of radio jets and magnetospheres in the nearby young stellar cluster R Coronae Australis*''
H. B. Liu, R. Galvan-Madrid, J. Forbrich, et al. (incl. **Manara, C.F.**), **ApJ, 780, 155**

[7] ``*A simultaneous UV-to-MIR monitoring of DR Tau to explore how water vapor in the disk is affected by accretion variability during the T Tauri phase*''
Banzatti, A., Meyer, M., **Manara, C.F.**, Pontoppidan, K., Testi, L., **2014, ApJ, 780, 26**

[6] ``*X-Shooter spectroscopy of young stellar objects: IV. Accretion in low-mass and sub-stellar objects in Lupus*''
Alcala, J., Natta, A., **Manara, C.F.**, Spezzi, L., Stelzer, B., Frasca, A., Biazzo, K., Covino, E., Randich, S., Rigliaco, E., Testi, L., et al., **2014, A&A, 561, A2**

[5] ``*X-Shooter spectroscopy of young stellar objects: III. Photospheric and chromospheric properties of Class III objects*''
B. Stelzer, A. Frasca, J.M. Alcala, **Manara, C.F.**, K. Biazzo, E. Covino, E. Rigliaco, L. Testi, S. Covino, V. D'Elia, **2013, A&A, 558, 141**

[4] ``*Accurate determination of accretion and photospheric parameters in Young Stellar Objects: the case of two candidate old disks in the Orion Nebula Cluster*''
Manara, C.F., Beccari, G., Da Rio, N., De Marchi, G., Natta, A., Ricci, L., Robberto, M., Testi, L., **2013, A&A, 558, 114**

[3] ``*The Hubble Space Telescope Treasury Program on the Orion Nebula Cluster*''
M. Robberto, D. Soderblom, E. Bergeron, V. Kozhurina-Platais, R. Makidon, et al. (incl. **Manara, C.F.**), **2013, ApJS, 207, 10**

[2] ``*X-Shooter spectroscopy of young stellar objects: II. Impact of chromospheric emission on accretion rate estimates*''
Manara, C.F., Testi, L., Rigliaco, E., Alcala, J., Natta, A., Stelzer, B., Biazzo, K., Covino, E., Covino, S., Cupani, G., DElia, V., Randich, S., **2013, A&A, 551, 107**

[1] ``*HST measurements of Mass Accretion Rates in the Orion Nebula Cluster*''
Manara, C.F., Robberto, M., Da Rio, N., Lodato, G., Hillenbrand, L., A., Stassun, K., Soderblom, D., **2012, ApJ, 755, 154**

Conference contributions

[13] ``*Accretion in young stellar objects: a complete view with the VLT/X-Shooter spectrograph.*'', **Manara, C.F.**; **talk** at the conference: *"Cool Stars 18"*, Lowell Observatory, Flagstaff, USA, June 2014.

[12] ``*On the gas content of transitional disks: a VLT/X-Shooter study of accretion and winds.*'', **Manara, C.F.**; *poster* at the conference: *"Cool Stars 18"*, Lowell Observatory, Flagstaff, USA, June 2014.

[11] ``*The evolution of protoplanetary disks in young stellar clusters.*'', **Manara, C.F.**; **talk** at the conference: *"The formation of the solar system"*, Max Planck Institute of Radioastronomy, Bonn, Germany, May 2014.

[10] ``*The Orion Nebula Cluster as a benchmark for the study of the accretion process.*'', **Manara, C.F.**; **talk** at the conference: *"The Orion Nebula Cluster as a paradigm for star formation"*, STScI, Baltimore, USA, October 2013.

[9] ``*The imprint of accretion on the UV spectrum of YSOs: an X-Shooter view.*'', **Manara, C.F.**; **talk** at the conference: *"UV-challenges in Astronomy"*, ESO, Garching, October 2013.

[8] ``*A VLT/X-Shooter study of accretion and photoevaporation in Transitional Disks*'', **Manara, C.F.**, Testi, L., Natta, A., Ricci, L., et al.; *poster* at the conference: *"Protostars & Planets VI"*, Heidelberg, Germany, July 2013.

[7] ``*A VLT/X-Shooter study of accretion and photoevaporation in Transitional Disks*'', **Manara, C.F.**, Testi, L., Natta, A., Ricci, L., et al.; *poster* at the conference: *"IAU symposium 299: Exploring the formation and evolution of planetary systems"*, Victoria, British Columbia, Canada, June 2013.

[6] ``*The timescales of protoplanetary disk evolution. New scenario opening?*'', **Manara, C.F.**, Beccari, G., Testi, L., Ricci, L., et al.; *poster* at the conference: *"Planet Formation and Evolution"*, Munich, Germany, September 2012.

[5] ``*Understanding star formation with the VLT/X-Shooter eye*", **Manara, C.F.**, **talk** at the conference: *"30 years of Italian participation to ESO"*, Rome, Italy, July 2012.

[4] ``*An X-Shooter analysis of chromospheric activity of Class III low mass sources* '', **Manara, C.F.**, Testi, L., Natta, A., et al.; *poster* at the conference: *"The Labyrinth of Star Formation"*, Crete, Greece, June 2012.

[3] ``*The HST Treasury Program on the ONC: Mass Accretion Rates Estimates*'', **Manara, C.F.**, **talk** at the conference: *"Formation and evolution of Very Low Mass Stars and Brown Dwarfs"*, Garching, Germany, October 2011.

[2] ``*HST measurements of mass accretion rates in the Orion Nebula Cluster* '', **Manara, C.F.**, Robberto, M., Da Rio, N. et al.; *poster* at the conference: *"Transport Processes and Accretion in YSOs"*, Schloss Ringberg, Germany, February 2011.

[1] ``*The HST Treasury Program on the ONC - Mass Accretion Rates Determination*'', Robberto, M., **Manara, C.F.**, Da Rio, N.; *poster* at the conference: ``*Science with the Hubble Space Telescope III. Two decades and counting*'', Venice, Italy, October 2010.

Accepted proposals

[16] *``Disk Demographics in Lupus.''*, Proposal 2013.1.00220.S, 6 hrs, ALMA, PI Williams.

[15] *``ALMA measurements of disk turbulence.''*, Proposal 2013.1.00601.S, 3 hrs, ALMA, PI Isella.

[14] *``A VLT/UVES detailed study to understand wind emission in transitional disks.''*, Pr.Id.093.C-0658, 9 hrs, VLT/UVES, **PI Manara**.

[13] *``The Jet-Accretion Connection in Young Stellar Objects: Coordinated Observations with KMOS and the JVLA. ''*, Pr.Id.093.C-0657, 12 hrs, VLT/KMOS, CoI, PI Galvan-Madrid.

[12] *``The Jet-Accretion Connection in Young Stellar Objects''*, Pr.Id.VLA/14A-120, 18 hrs, VLA, CoI, PI Liu.

[11] *``Spectroscopic followup of long living circumstellar discs in the star clusters NGC3572 and NGC3590 discovered with WFI''*, Pr.Id.092.C-0820, 8 hrs, VLT/FLAMES, CoI, PI Beccari.

[10] *``The Jet-Accretion Connection in YSOs: KMOS Mapping of Near-Infrared Lines.''*, Pr.Id.060.A-9463, 2 hours, VLT/KMOS (Science Verification), CoI, PI Galvan-Madrid.

[9] *``The embedded stellar population of ρ-Oph.''*, Pr.Id.060.A-9459, 4 hours, VLT/KMOS (Science Verification), CoI, PI Fedele.

[8] *``Connecting Accretion Variations to Stellar Rotation.''*, Pr.Id.060.A-9453, 5 hours, VLT/KMOS (Science Verification), CoI, PI Costigan.

[7] *``Monitoring Magnetic Fields: Searching for the Connection Between Variable Magnetic Fields and Accretion Variability.''*, Pr.Id.091.C-0768, 4 nights, VLT/CRIRES, CoI, PI Costigan.

[6] *``Circumstellar discs and star formation history in the massive cluster Trumpler 14.''*, Pr.Id.091.C-0876, 4 hours, VLT/FLAMES, CoI, PI Beccari.

[5] *``Constraining the evolution and dispersal of Transitional Disks through X-Shooter signatures of accretion and photoevaporation''*, Pr.Id.090.C-0050, 3 hours, VLT/X-Shooter, **PI Manara**.

[4] *``WFI survey of circumstellar discs in nearby star clusters.''*, Pr.Id.090.C-0647, 7 nights, ESO/MPG 2.2m/WFI, CoI, PI Beccari.

[3] *``Characterizing the mass accretion rates in young low-mass stars at low metallicity''*, 4 orbits, HST/ACS-WFC3, CoI, PI Da Rio.

[2] *``Constraining the evolution and dispersal of Transitional Disks through X-Shooter signatures of accretion and photoevaporation''*, Pr.Id.089.C-0840, 8 hours, VLT/X-Shooter, **PI Manara**.

[1] *``Can planet formation happen on very long timescales? Preparation of an ALMA massive and long-lived disk confirmation.''*, Pr.Id.288.C-5038, 1.5 hours, VLT/X-Shooter, DDT, **PI Manara**.